Non-linear optics and plasma : Electric field characterization and Terahertz generation

Farah Aljammal

To cite this version:

Farah Aljammal. Non-linear optics and plasma : Electric field characterization and Terahertz generation. Optics / Photonic. Université Grenoble Alpes [2020-..], 2021. English. NNT : 2021GRALT089 . tel-03612011

HAL Id: tel-03612011
https://theses.hal.science/tel-03612011

Submitted on 17 Mar 2022

THÈSE

Pour obtenir le grade de

DOCTEUR DE L'UNIVERSITÉ GRENOBLE ALPES
Spécialité : **Optique et Radiofréquences**
Arrêtée ministériel : 25 mai 2016

Présentée par

Farah ALJAMMAL

Thèse dirigée par **Gwenaël Gaborit**
et co-encadrée par **Maxime Bernier**

préparée au sein du **l'Institut de Microélectronique, Electromagnétisme et Photonique - Laboratoire d'hyperfréquences et de caractérisation**
dans **l'École Doctorale EEATS**

Optique non-linéaire et plasma: caractérisation du champ électrique et génération des ondes THz

Thèse soutenue publiquement le **17 Décembre 2021**,
devant le jury composé de :

M. Laurent PECASTAING
Professeur, Université de Pau et pays de l'Adour, Président

M. Christophe VOLAT
Professeur, Université du Québec, Rapporteur

Mme Nadège BODIN-COURJAL
Maître de conférence HDR, Université Franche-Comté, Examinateur

M. Lionel DUVILLARET
Professeur, Kapteos CEO, Examinateur

M. Gwenaël GABORIT
Maître de conférence HDR, Université de Savoie Mont-Blanc, Directeur de thèse

M. Maxime BERNIER
Maître de conférence, Université de Savoie Mont-Blanc, Co-encadrant de thèse

M. Sylvain ISENI
Chargé de Recherche CNRS, Université d'Orléans, Invité

Acknowledgments

This thesis work was carried out at IMEP-LAHC laboratory in collaboration with Kapteos company which develops solutions of electric field measurement in severe environment. First of all, I would like to thank all the actors of these entities. I thank Mr. Frédéric Garet and Mr. Lionel Duvillaret, for their welcome in the IMEP LAHC laboratory and in the Kapteos company, respectively. I would like to take the advantage of this space area to sincerely thank all the people who accompanied me during these years. Four years of adventure and discovery of the research world!

I would like to express my deepest thanks to my thesis director Gwenaël, who launched my research four years ago and who has been a pillar of support for me ever since. I would like to say that I benefited from the best possible supervision to carry out this hard work that is the thesis. During these years, you knew how to bring me your knowledge, your great availability, your extreme patience, your humor, your kindness, and especially your unfailing support from the beginning to the end of this thesis. Shoukran Gwen!!

I would also like to sincerely thank my thesis supervisor Maxime. Thanks for having supervised me, guided me, helped me and advised me. Thanks for the time you devoted to bring me the methodological tools essential to the conduct of this research. Your requirement has greatly stimulated me!

Im very grateful for the Jury members in particular Prof. Laurent Pecastaing and Prof. Christophe Volat for having accepted the heavy task of being the reviewers of this manuscript as well as to Dr. Nadége Courjal for having accepted to take part in my defense as an examiner. I would also like to thank Dr. Sylvain Iséni of the GREMI laboratory for his interesting collaboration which helped and guided me during this journey.

Thanks to all the people of the IMEP-LAHC, Fernanda, Magali, Emilie, Jean François, Jean Louis... for their advice and experiences. Thanks to Dongwei and Bastien for their indispensable support. Thanks to Gizem, for all the moments shared, her support, her understanding, her friendship.

I had the pleasure, during these three years, to teach at the University Savoie Mont Blanc as a temporary teacher. As such, I would like to thank all the teachers with whom I had the opportunity to exchange.

And what would those years have been like without the support of my family and friends? Friends can turn bad times into good memories and good times into great memories! A huge thank you to my friends : Samah, Houssein, Rim, Sara, Marwa, Amal, Malak, Zahraa, Ali, Wassim, Abbass... who believe in me and help me to move forward and with whom I had the pleasure of interacting.

I want to thank my family, my brothers Mohammad and Ali and my sister Batoul, for supporting me. Unfortunately, the distance did not allow us to see each other often, thank you for always being there to support me.

These last lines will allow me to show my deepest love and gratitude to my dear mother and father who have allowed me to carry out these studies and to do a job that I adore! Thank you for

your devotion to me and for all the sacrifices made to get me here. Shoukran Mom and Dad!

Contents

General introduction

The notion of field was introduced by physicists to try to explain how two objects can interact at a distance, without anything connecting them. Newton's law of universal gravitation and Coulomb's law of electrostatics both imply such interaction at a distance. There is no wire connecting the earth to the sun; the sun exerts its attraction at a distance. Similarly, two electric charges attract or repel each other in a vacuum without anything connecting them, without any material support. To try to explain this phenomenon, Michael Faraday introduced the notion of **electric field (E-field)**[1]. Among the technological solutions that allow the more or less complete characterization of an E-field, we find today mainly : antennas, calorimeters and bolometers, infrared thermography and **electro-optical (EO) sensors**.

E-field is an essential parameter in several domains. Particularly, the E-field is of crucial importance for the characterization of a complex medium like plasma. The characterization of this field remains a challenge, and experimental data sets are still rare [1]; this is the aim of my thesis work. Nowadays, plasmas are used in various fields and are an active and innovative branch of applied physics. It is an electrically conductive medium in which there is an approximately equal number of positively and negatively charged particles produced when the atoms of a gas are ionized. Most of the matter in the universe is in the form of plasma, primarily in the Sun and stars (an example of dense plasma), as well as in the solar wind in interplanetary space (an example of diluted plasma). Auroras, lightning and welding arcs are also plasmas. The Earth itself is immersed in a tenuous plasma called the solar wind and is surrounded by a dense plasma called the ionosphere. Actually, there is a lack of available tool allowing the actual measurement of E-field in the vicinity or within the plasma. Following the request and the needs of research plasma laboratories and taking advantage of our collaboration with Kapteos company, through its innovative E-field probes, we decided to study for the first time in our laboratory the ability of these probes to measure the E-field associated to plasma. To characterize the plasma, our laboratory **IMEP-LaHC** has developed an original and non-invasive **EO technique** that have allowed to measure in **real time** (up to 100 GHz) the absolute E-field and its evolution in time.
The present work is an attempt to improve the characterization and quantification of the E-field associated to plasmas, which are induced by **dielectric barrier discharges (DBD)** and by **cold atmospheric pressure plasma jet (CAPPJ)**. Through a parametric analysis (voltage, inter-electrode spacing, electrode geometry, electric current, nature of the gas), we study these plasmas in order to open up new application perspectives in the field of medical and water treatment.

On the other hand, taking advantage of the expertise of our laboratory at higher frequency range, and using plasma as a method to generate **TeraHertz (THz)** waves from laser-induced air breakdown, we studied the ability of an external plasma jet to control the polarization state of the generated THz field. For this goal, an innovative detection setup, which permits to perform **polarimetric analysis** of THz pulses has been developed. So it makes the links existing between plasma and optics. Either the optics to characterize the plasma, or the plasma for the **nonlinear interaction** between pulsed optical wave for the parametric generation of **terahertz (THz) waves**.

---

[1] It is well known that all matter is composed of positively and negatively charged electric particles. When there is an abundance of one polarity in a certain area, an E-field is produced.

In order to carry out this study, we have divided our work into three parts. A summary of the experimental work is given in Table 1.

Part I is dedicated to **"Plasma as an intense field source and electro-optic detection"**. We seek on the one hand to review the state of knowledge on plasmas (brief overview of plasma physics, focus on cold plasmas at low frequencies, applications and principle of characterization (chapter 1)) and covers the different methods used to E-fields measurement in the literature , on the other hand, and especially describe the one based on the electro-optic (EO) detection. Specific details on the EO probe developped by the French company Kapteos are given as it has been used in all measurement campaign during this thesis. Then, chapter 2 is devoted to the study at high frequency. We present the THz pulse generation technique used and we also describe the detection technique, which is based on the EO effect using femtosecond laser pulses. Finally, we will present the experimental setup developed during this thesis to make the link between plasma and THz wave generation, which is the expertise of our laboratory. In chapter 3, we show the different contributions of the electro-optic effects, their origins and their behaviors. This will provide the knowledge necessary for the interpretation of the experimental results and the theoretical calculations. Then we present the real time EO measurement from low to high frequency.

Part II is dedicated to **"Vectorial and real time characterization of plasmas by electro-optical method"** and divided into two chapters. The aim of this experimental part is the complete analysis (especially a polarimetric analysis), the characterization (highly accurate characterization by EO method of new cold plasma sources), and the evaluation of the E-field associated to a DBD and a CAPPJ (developed for the first time in our laboratory) via an EO probe. We propose in this part, a vectorial characterization of the Laplacian field as well as for the E-field induced by the plasma in two different configurations, which have been characterized : The chapter 4 is devoted to the vectorial measurement of the E-field induced by the DBD. It is followed by an in-depth study of the CAPPJ in chapter 5.

Part III is dedicated to **"Non-linear optics for THz generation (different aspects involving fast optics and plasmas)"**. The objective of this part is to study the non-linear optics at high frequency as a tool for plasma analysis. Chapter 6 studies the interactions between the plasma jet and an optical plasma in aim to control the THz generation. In parallel, studies in this chapter will be carried out on the polarization state modulation of the THz radiation induced by the presence of the plasma jet.

Finally, a general conclusion takes stock of the thesis work described here. An additional experimental work concerning the nonlinear optical behavior of a Langatate crystal to generate THz waves by optical rectification of a fs laser pulse was presented in Appendix.

Comparison between experimental analysis works of this thesis

Differences and similarities in this thesis works	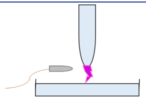 DBD	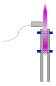 Plasma Jet	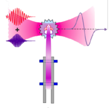 Plasma/He - THz
Generation and detection of E-field	✓	✓	✓
Non-linear optics	✓	✓	✓
Electro-Optics	✓	✓	✓
Polarimetric & vectorial measurement	✓	✓	✓
Pigtailed sensor	✓	✓	✗
High-Voltage source	✓	✓	✗
Measurement system frequency	30 Hz - 1 GHz	30 Hz - 1 GHz	100 GHz - 3 THz
Operating frequency	50 Hz	18 kHz	100 GHz - 3 THz
Laser	CW	CW	Amplified system (fs laser)
Time domain	Real time	Real time	Equivalent time
Optical power	mW	mW	W
Peak power	mW	mW	> 1 GW
Detected E-field range	MV/m	MV/m	V/m
Gas	Air	Helium	Air, Helium or Nitrogen
Spatial resolution	Sub-millimetric	Sub-millimetric	N/A
Dynamic range	120 dB	120 dB	50 dB
Crystal thickness	5 mm	5 mm	1 mm
Crystal (detection)	BSO (cubic)	BSO (cubic)	ZnTe (cubic)

Table 1: Sum up of different works done during this thesis.

Part I

Plasma as intense field source and electro-optic detection

1

Overview of plasmas and focus on low frequency plasmas

Sommaire

Nowadays, plasmas are used in various fields and are an active and innovative branch of applied physics. This chapter is divided into two sections : Section 1.1 provides a brief overview concerning plasma physics and describes the basic physic, applications and principle of the characterization of plasma. We will recall the various parameter and physical processes, which intervene within plasmas and which thus make it possible to classify them (Section 1.2). A focus is dedicated to **Dielectric Barrier Discharge (DBD)** and **Cold Atmospheric Pressure Plasma Jet (CAPPJ)**. Subsequently, Section 1.3 covers the different methods used to measure electric fields in the literature and especially describe the one based on the electro-optic (EO) detection. Specific details on the EO probe developped by the French company *Kapteos* are given as it has been used in all measurement campaigns during this thesis.

1.1 Generalities and sources of plasmas

It was in 1879 that **plasma** was originally discovered and identified for the first time in a Crookes tube[1] by Sir William Crookes who described it as " radiant matter " [2, 3]. It was in 1928 that the term " plasma " was coined and used by Irving Langmuir, the Nobel laureate who pioneered the scientific study of ionized gases produced in an electric discharge and characterized by the behavior of charged particles (electrons and ions) [4, 5].

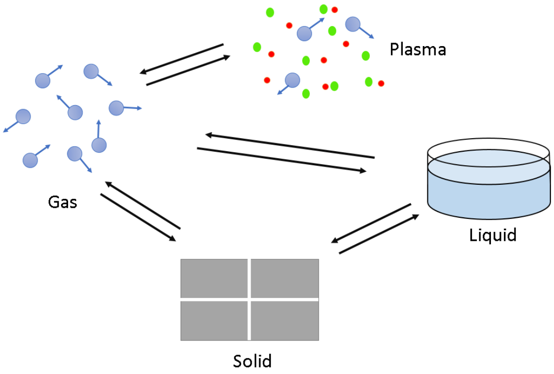

Figure 1.1: Different states of matter.

It is an ionized gas obtained from the excitation of this gas by means of a contribution of a warm vitality, radiative or electrical structure. In reality, the electrons created crash into particles and gas atoms and initiate them. At that point it happens an ionization. The comparison of properties between the four states of matter *i.e.* solid, liquid, gas and plasma is resumed from these two Ref. [6] and [7] and tabulated here after (Table 1.1) :

When a solid is heated enough for the thermal motion of atoms to break the structure of the crystal lattice, it usually forms a liquid. When a liquid is enough heated, surface atoms are vaporized faster than they re-condense : a gas is formed. When a gas is enough heated for atoms to collide and destroy their electrons in the process, a plasma is formed : the so-called **fourth state of matter** like shown in Figure 1.1, largely described in litterature [7–9].

This plasma state, which is found in the "natural" state in the most celestial objects, such as the surface of the Sun, interstellar gas clouds, stars and comets, constitutes the majority of our universe (around 99 %). On the other hand, on Earth, we do not encounter it in its natural state, except

---

[1] Crookes tube is an experimental electrical discharge tube in which air is ionized by the application of a high voltage through a voltage coil.

PROPERTIES	**PLASMA**	**GAS**	**LIQUID**	**SOLID**
Mass	Stable mass	Stable mass	Stable mass	Stable mass
Volume and shape	No fixed shape or volume	No fixed shape or volume	Definite volume but no fixed shape	Fixed shape and volume
Independently acting species	Two or three	One	Atoms/molecules behave the same way	Atoms/molecules behave the same way
Electrical conductivity	Very high	Very low	Low	Very high in solid conductors
Velocity distribution	Maxwellian	Often non-Maxwellian	Eddy and Laminar velocities	Vibrate about a fixed position
Energy	Extremely high	High	Medium	Low
Fluidity	Flow in all directions	Flow in all directions	Flow from a higher to lower level	Cannot flow from one place to another

Table 1.1: Generalities about physical characteristics of the four states of matter.

in the lightning or aurora Borealis and flames. Nevertheless it can be "artificially" produced in the laboratory by applying electric fields strong enough to separate the electrons from their nucleus in the gases [10].

Subsequently, plasmas have always aroused great interest for applications both in industry (micro-electronics, plasma torch, etc.) [11–14] and in everyday life (flat screen TVs [15–18]), the most common of which is the neon tube that lights our rooms. Nevertheless, this discipline comes up against a rather complex theoretical study. This is why we will limit ourselves thereafter to giving and describing some fundamental elements, which will allow us to situate the general framework of electric discharges (**Dielectric Barrier Discharge** and **Cold Atmospheric Pressure Plasma Jet**) studied and characterized during this thesis.

1.2 Classification of plasmas

1.2.1 Physical parameters of plasmas

According to Hollahan and Bell [19], and at macroscopic scales, the plasmas are generally electrically quasi-neutral. Unlike a classical gas where the particle interactions are of short ranges, the charged particles of the plasma can interact with each other at a long distance. Indeed, the Coulomb attraction/repulsion being the main one between particles (force which varies as $\frac{1}{r^2}$), even though the concentrations of positive and negative charges are roughly equal. However, this is not necessarily the case at microscopic scales. Physically, the definition of plasma is linked to the so-called Debye length[2] "λ_D" (Eq. 1.1). Thus, an ionized gas can be considered as a plasma if λ_D around a charged particle is smaller than the dimensions (l_g) of the gas container.

$$\lambda_D = \sqrt{\frac{\varepsilon_0 k T_e}{n_e e^2}}, \tag{1.1}$$

where $\varepsilon_0 = 8.854 \times 10^{-12}$ C/(Vm) is the dielectric permittivity of the free space, $k = 1.381 \times 10^{-23}$ J/K is Boltzmanns constant, T_e is the kinetic electron temperature, n_e is the electron density and $e = 1.602 \times 10^{-19}$ C is the elementary charge.

Unlike a gas, in a plasma, certain electrons are no longer linked to their atom, they can move freely. These free electrons leave the attractive potential of the atom if sufficient energy is supplied to them. But it is not enough for a gas to have free electrons to be called plasma. The electron density must be large enough relatively to the total density of species so that a collective behavior and a certain reactivity occur [5,20]. The parameter representing this relationship is the ionization coefficient, which is one of the important parameters of the plasma called ionization degree[3] α. It refers to the proportion of neutral particles that are ionized, which is defined by :

$$\alpha = \frac{n_i}{n_i + n_n}, \tag{1.2}$$

where n_i is the density of ionized particles and n_n the density of neutral species. If $\alpha \ll 1$ then the plasma is said to be "weakly" ionized and if $\alpha \approx 1$ then it is said to be "strongly" ionized[4].

1.2.2 Types of plasma

In his book [10], which is known as an important reference in the study of gas discharges, Raizer offers us a very understandable reference for beginners and also makes it useful for the specialist. There are many varieties of plasmas classified according to certain precise parameters, which depend essentially on their electronic density, their ionization degree, their temperature (or energy) etc.. Such a classification is sketched in Figure 1.2 based on diagrams from Boeuf [21], Braithwaite [22], Hollahan and Bell [19], Jolibois [23] and Smirnov [24].

The plasma states cover an extremely wide range of particle densities and temperatures. Besides the plasmas occurring in nature, laboratory plasmas play an important role in science and technology. **Our research is focused on non-equilibrium and low-temperature plasmas** of electrical discharges. Most plasmas are hot, like the surface of the sun, Tokamaks etc.. While a candle flame, with a temperature of around 1000 K, is considered as a cold plasma (Figure 1.2).

At present, plasmas are increasingly studied and used in various fields and constitute an active branch of applied physics, they are used in a large ongoing research project such as ITER (International Thermonuclear Experimental Reactor) whose goal is to obtain a new source of energy through thermonuclear fusion. If the goals of this ambitious project are met, it would provide the energy needed by Earth for more than 1000 years [5,26].

To resume, the different properties of plasmas can be categorized in different ways as shown in the Figure 1.3 below.

---

[2] In plasma physics, Debye length, named after the chemist Peter Debye, is the length scale on which electrical charges (electrons) screen the electrostatic field in a plasma or other electrolyte. In other words, the Debye length is the distance above which significant charge separation can occur.

[3] The degree of ionization is an indicator of the behavior of particles in plasma. For example, in weakly ionized plasma, the number of neutral particles is much greater than the number of charged particles. As a result, charged particles more often collide with neutral particles than with particles of the same species and particle interactions due to Coulomb force can be neglected. The opposite can be said of strongly ionized plasma, where the interaction between charged particles due to Coulomb force is dominant.

[4] A fully ionized plasma has a degree of ionization equal to 1

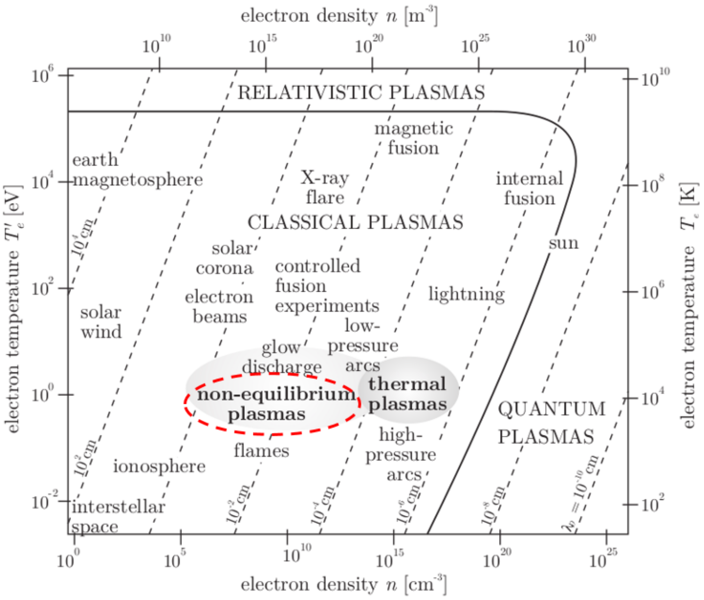

Figure 1.2: Sample of neutral plasmas found in nature and in Laboratories. Order of magnitude of their electronic temperature T_e and densities [23, 25].

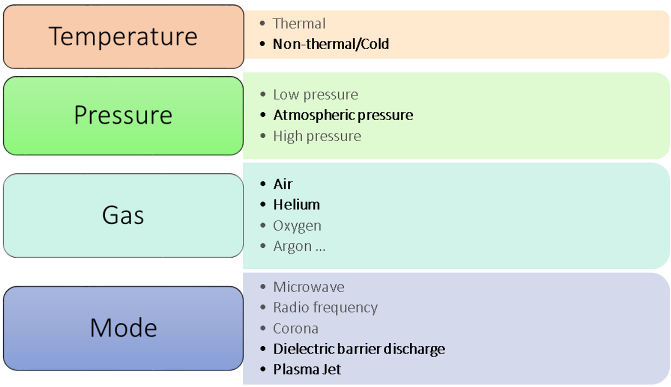

Temperature
- Thermal
- **Non-thermal/Cold**

Pressure
- Low pressure
- **Atmospheric pressure**
- High pressure

Gas
- **Air**
- **Helium**
- Oxygen
- Argon ...

Mode
- Microwave
- Radio frequency
- Corona
- **Dielectric barrier discharge**
- **Plasma Jet**

Figure 1.3: Relevant properties to perform the qualification/classification of plasmas.

The most relevant criterion is to divide them into two main categories regarding their temperatures (T_i is ions temperature, T_e is electron temperature, and T_g is gas temperature) : "hot or high temperature plasmas" and "cold or low temperature plasmas" such that :

- **Cold plasmas** : ($T_i \ll T_e \ll 10^5\,\text{K}$ and $T_i \approx T_g = 300\,\text{K}$ *e.g.* low-pressure glow discharge) The term cold plasma has been recently used as a convenient descriptor to distinguish the one-atmosphere, near room temperature plasma discharges from other plasmas, operating at hundreds or thousands degrees above ambient temperature. Cold plasmas are the most common because they are found everywhere. The majority of our atmosphere is made up of cold plasma. Excellent reviews of these plasma sources can be found in [23, 27, 28]. These are generally weakly ionized given their temperature (the electrons do not acquire enough kinetic energy to be torn from their nucleus). They are very chemically reactive and have a very high electrical conductivity, leading to their wide use in industry. Cold plasma is a novel non thermal cost-effective food processing technology, especially used in food decontamination (a nonthermal plasma (NTP) is specifically an antimicrobial treatment being investigated for application to fruits, vegetables and other foods with fragile surfaces) [29–31], and packaging [30, 32].

- **Hot plasmas** : ($T_i \approx T_e \geq 10^7$ K, *e.g.* fusion plasmas; $T_e \approx T_i \approx T_g \leq 2 \times 10^4$ K, *e.g.* arc plasmas at normal pressure)
  Plasmas with a high degree of ionization are known as hot plasmas. Hot plasmas are a bit more exotic than cold plasmas. In fact, we find them in very specific areas of our universe (stars, supernova nebulae, thermonuclear fusion, thermal arc torches and plasma jets emitted by black holes). For more information about hot plasmas you can refer [33–35].

Pointu *et al.* [36] distinguish plasmas by different criteria :

- their **state of ionization**, which can range from very weak (a few electrons) to fully ionized (there are only electrons and ions left),
- **collisions** between the particles composing them, with a separation between thermal plasmas and discharge plasmas,
- plasmas without **interactions** (or practically without collisions) where the pressures are very low (< 0.1 Pa),
- relativistic plasmas where the **speeds of particles** approach that of light,
- very **dense and fully ionized** plasmas, which behave like solids or liquids (charged submicron particles),
- plasmas falling under **quantum statistics** like that of Fermi-Dirac, for example an electron gas .

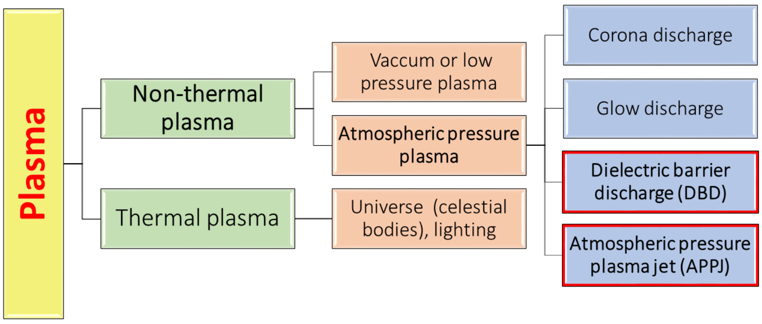

Figure 1.4: Types of plasma and their examples [6, 37].

Figure 1.4 illustrates the different types of plasmas and their examples. Examples of thermal plasma include electrical arcs, thermonuclear reaction-generated plasmas, etc., while low-pressure direct current (DC) and radio frequency (RF) discharges (silent discharges), discharges from fluorescent (neon) illuminating tubes, corona discharge, and dielectric barrier discharge (DBD), are those of nonthermal plasmas [38, 39]. **Thermal and non-thermal plasmas provide a wide range of applications that spans the field of chemistry, physics, life sciences, environmental issues, medical sciences and biomedical applications and related fields. Among all these plasmas, we will limit our discussion to the non-thermal atmospheric pressure plasmas since they have very promising biomedical applications, such as sterilization of medical devices and**

implants, and can be used for the treatment of viable tissues. These types of plasmas are capable of interacting with living matter without burning it and thus offer a set of possible applications, particularly in the fields of oncology, odontology and dermatology. This new field has aroused growing interest in recent years and two different types of cold plasma appear suitable : Indirect (Cold Atmospheric Pressure Plasmas Jet - APPJ) and Direct (Dielectric Barrier Discharge - DBD) plasma sources (discussed in section 1.2.3).

Nowadays, electric discharges in gases are arousing renewed interest because of their potential applications or already implemented in laboratories and in industries. These applications use all or part of the species present in the plasma, *i.e.* electrons, ions, reactive neutral species, which are the agents of a volume or surface physico-chemistry inexpensive in energy. The progresses made simultaneously in numerical modeling and in experimental characterization techniques, facilitate the choice of a discharge and the control of its phenomenology, according to the desired objective.

1.2.3 Plasma sources and applications

Each of the sources discussed in the following section has its advantages and drawbacks. We here define the two kinds of plasmas in DBD and CAPPJ.

Dielectric Barrier Discharges (DBD)

Dielectric barrier discharges are non-equilibrium low-temperature discharges and constitute simple devices to generate cold atmospheric plasmas [40], ionized gases or liquids [41, 42]. DBDs, also known as **silent discharges**[5], and it was in 1857 that Siemens used it for ozone generation, which is still one of its most important industrial applications and extensive investigations allowed for a good understanding and improvement of their operation.

Unlike conventional direct discharges where plasma is created through the gas between two electrodes, DBDs reactors typically consists of two electrodes, which are usually a few mm apart and have the particularity of having at least one electrode covered with a dielectric[6] material (such as glass, quartz or a ceramic material) [45] (Figure 1.5).

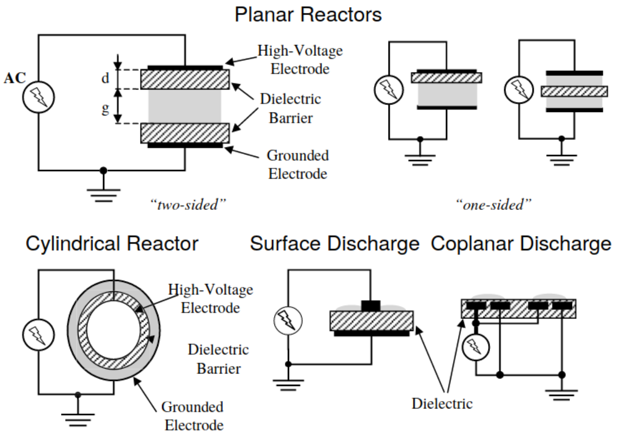

Figure 1.5: Typical electrode arrangements of dielectric barrier discharges proposed by Wagner et al. [46].

---

[5] the name of silent discharge was proposed in 1860 by Andrews and Tait [43]. The filamentary and transient nature of the discharge was revealed in 1932 by Buss in a coplanar DBD [44]

[6] the dielectric plays two complementary roles : it distributes the micro-discharges over its entire surface and it limits the quantity of charges for each micro-discharge, thus avoiding the transition to an arc regime.

Typical electrode arrangements of planar and cylindrical barrier discharges are shown in Figure 1.5. DBDs operate in a wide range of pressures [47, 48] in various gases [49–52]. The electrodes are driven by high AC voltages in the kV range (applied voltage ranges typically from 0.5 kV up to a few 100 kV) and at frequencies in the kHz. The plasma generated consists of a numerous small streamers, called micro-discharges. Due to the dielectric material, the discharge current is limited, giving cause to very short-lived (1-10 ns) micro-discharges that are distributed homogeneously across the electrode. The characteristics of the plasma strongly depend on the nature of the gas, the pressure, the inter electrode distance, the properties of the dielectric, etc..

Figure 1.6 shows an example of DBD configuration developed by Diener electronic called Pico plasma system (Pico plasma systems are primarily used in the many sectors like archaeology, automotive, sterilization, textile technology etc..).

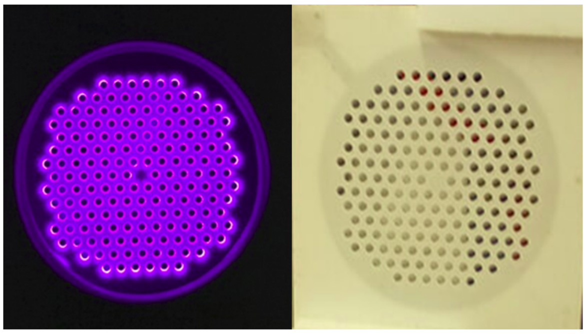

Figure 1.6: Photograph of a DBD configuration for the treatment of textile webs (diameter about 150 mm) in order to modify the surface of the fibers, in particular to make them hydrophilic and stain resistant.

The main advantage of DBDs over other plasma techniques is their ability to operate at pressures that do not require extensive vacuum equipment, making it less expensive and more time-effective. In addition, they adress a wider range of applications purposes concerned by ozone generation [53–55], treatment of exhaust gases [56, 57], ultraviolet or vacuum ultraviolet radiation generation [58–60], surface modification [61, 62], plasma jet production [63–65], sterilization and biomedical applications [66, 67] including wound healing and destruction of cancer cells and tumors after their successful early use in the mid-1990s to inactivate bacteria [40, 68]. All these applications make DBDs processing attractive for plenty of industrial applications due to their very low heat generation. Furthermore, the plasma-chemical synthesis of ozone from either pure oxygen or air has become one of the major industrial applications of DBDs [69]. In the same manner, DBDs can also modify the chemical composition of liquids for treatment applications like tap water depollution and more generally for plasma activated water treament [70]. Indeed, plasma-liquid interactions have recently drawn considerable attention in the field of water treatment : numerous studies have indeed shown the effectiveness of plasma DBD activation to decontaminate water, *e.g.*, removing pesticides [71], phenols [72] or pharmaceutical compounds [73, 74]. DBDs will be more discussed in chapter 4 of this manuscript.

Cold Atmospheric Pressure Plasma jets (CAPPJ)

In this paragraph some special attention will be given to a kind of set-up that has hugely gained in popularity for the last decade : the cold atmospheric pressure plasma jet (CAPPJ). CAPPJs, one of the objects studied during this thesis, are new sources of plasma, which have the particularity of allowing the creation of a plasma at ambient temperature and at atmospheric pressure.

DBDs are generally used, for example, to purify the air or to produce ozone, but they are also used in the form of a plasma jet at nonthermal atmospheric pressure. CAPPJs in literature refer to all types of plasma sources, but here only DBD plasma jets will be considered. **The main difference between a DBD plasma jet and a DBD is that the plasma is ignited in a tube with a volume which is small enough to spatially force the confinement of the charges, so that the electric field induced by these charges remains high enough for the plasma to grow and spread.**

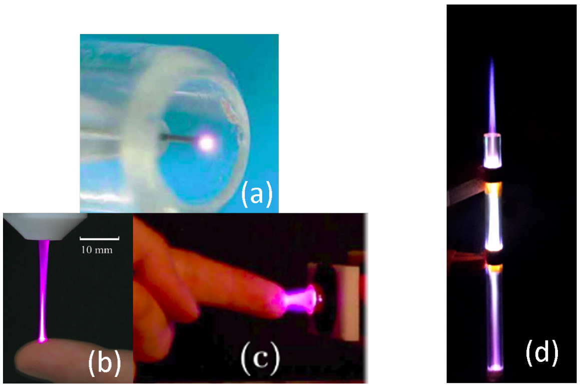

Figure 1.7: Photographs of different plasma jets (a), (b) and (c) collected from [75–77] respectively. Plasma jet developed in IMEP-La HC laboratory during this work (d).

Claire Douat [5] explained well in her thesis the history of plasma jets since the 19^{th} century. To sum up, she presented the different plasma jets over the years in Figure 1.7. The first plasma jet carried out in 1991 was made by Koinuma *et al.* [78], the discharge was a capacitive radiofrequency reactor powered by a gas (majority Helium). The addition of small amounts of gases, such as carbon tetrafluoride (CF_4), aimed at etching compounds in silicon and study its effect on plasma. Despite this discovery, it was not until the 2000s that atmospheric pressure plasma jets were revived the interest for plasma medicine [79, 80]. In 2002, Stoffels *et al.* [75] set up a new system to generate a non-thermal micro-plasma at atmospheric pressure. As shown in Figure 1.7.a, the plasma is confined around the central electrode and has a length of a few millimeters. They demonstrate that this plasma, initiated by RF excitation, is well suited for biomedical applications (*e.g.* cleaning of decayed matter in dental cavities prior to filling, high-precision removal of unwanted tissue/cells [75]). This plasma represents the beginnings of micro-jets. After Stoffels, Laroussi *et al.* and Forster *et al.* [77, 81] demonstrate that a pulsed high voltage source with a repetition rate of 1 to 25 kHz is capable of initiating a micro-jet of helium plasma (examples are shown in Figure 1.7.b and Figure 1.7.c). The latter is initiated in a discharge with a capillary dielectric barrier, creating a jet several centimeters long. Figure 1.7.d presents the plasma jet, developed in IMEP-LaHC laboratory, used in this thesis. Thanks to two copper electrodes, wrapped arround a quartz tube, covered (or not) with a dielectric material, a mixture of different gases is sent. High voltage is applied and ionized gas is sent through a tube, forming a plasma plume. The substrate is typically placed a few mm underneath the nozzle, in the so-called afterglow, where it is exposed to the reactive species of the plasma [82–84]. These jets can emit low temperature plasma plumes in the surrounding air. Because they can maintain temperatures below 40°C, they can come in touch with soft matter, including biological tissues, without causing thermal damage. The applied gas is generally a noble gas such as helium or argon and the ambient gas is generally air, nitrogen or oxygen (we use Helium flow in air in our case). In 2007 Laroussi *et al.*, wrote an interesting review on the topic of arc-free CAPPJs which covers all the essentials [79]. For more details, CAAPJs will be discussed and studied in Chapter 5.

1.2.4 Plasma diagnostics

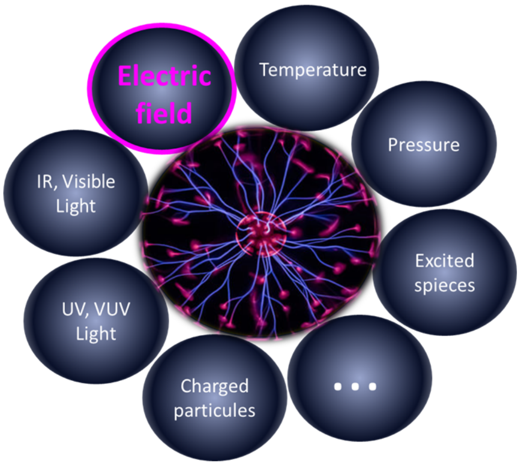

Figure 1.8: Physical quantities to be characterized for plasma analysis. Highlight on E-field, which is the topic of this work.

Plasma diagnostics are a pool of methods, instruments, and experimental techniques used to measure properties of a plasma, such as plasma compounds densities, distribution function over energy (temperature), their spatial profiles and dynamics, which enable to derive plasma parameters. **Among all the relevant characteristics of a plasma, its associated electric field (E-field) behavior is one of the critical parameter to be analyzed. Current and voltage driven by the plasma source are usually measured [84], but are definitely not sufficient for an exhaustive analysis.** Historically, charge density gives additional informations on the plasma and can be assessed thanks to Langmuir probes [85] or a plasma ion analyser. The non stationary magnetic field can be measured using a B-dot probe [86]. Concerning the E-field, numerical simulations [87, 88] are mainly performed. Actually, there is a lack of available tool allowing the actual measurement in the vicinity or within the plasma. For that purpose, in the following section 1.3 we discuss the different methods dedicated to the E-field measurement.

1.3 Electric field measurement methods

E-field is the driving force behind every plasma. Its importance for plasma characterization requires no overstating and the characterization of this field is a challenge, and sets of experimental data are still rare [1]. It is one of the most important parameters to know in plasma (such as glow discharges, DBD, RF and plasma jets, etc), since it is closely connected with others such as charge densities, fluxes of electrons and ions, and since it controls the distribution of energy within a plasma and nanosecond discharges. Furthermore, the E-field distribution is often used as input data for plasma modelling [89].

Essentially, the ability to measure the E-field is synonymous with an understanding of the plasma reactivity, and one of the greatest difficulties in the quantitative analysis of these discharges is the **lack of non-intrusive measurements of the transient E-field**, as well as of the electron density and temperature. It requires generally temporal (sub-ns) and spatial (sub-mm) resolutions, under moderate to ambient pressures. To improve the understanding of gas discharges phenomenas and their applications [90, 91], it is necessary to understand the spatial distributions of E-field in the plasma and their temporal evolutions. Unfortunately, predicting the E-field distribution by solving the "Poisson equation" for the electric potential is inaccurate due to the strong sensitivity of the space charge distribution to rates of ionization, recombination, ion molecule reactions, electron emission from electrodes, and transport coefficients of electrons and ions. This is why the quantitative insight into these processes requires E-field measurements using non-intrusive experimental technique [92].

There are few methods that can measure directly the E-field strength in DBDs and in plasma jets at atmospheric pressure, which are based on optical emission spectroscopy, the Stark effect and by four-wave mixing. State-of-the-art methods such as Stark shift measurements or **Stark polarization spectroscopy**, **laser-induced fluorescence dip Stark (LIF) spectroscopy** and **coherent four-wave mixing** might offer the most promise going forward. But in recent years, two other methods dedicated to the characterization of the electric field have appeared : i) an optical electric field measurement method (laser-based method) which relies on quantifying the optical **second harmonic generation induced by the electric field (E-FISH)** to be measured, ii) the **electro-optical method (EO)**, based on the pockels effect, which has shown significant potential.

1.3.1 Stark polarization spectroscopy

Over the last few decades, several techniques to measure E-field in plasmas using the Stark effect spectroscopy have been developed. In general, the **Stark effect** is the division and shift of spectral lines under the influence of an external E-field. It was discovered by the German physicist Johannes Stark[7] in 1913 (it is the E-field analogue of the Zeeman effect, where a spectral line is split into several components due to the presence of the magnetic field). The application of the Stark effect on hydrogen (and hydrogen-like atoms such as helium) can be found in literature [93–95] and the whole history has been treated in the PhD thesis from Hofmans [96]. Figure 1.9 represents a typical schematic of the Stark polarization spectroscopy.

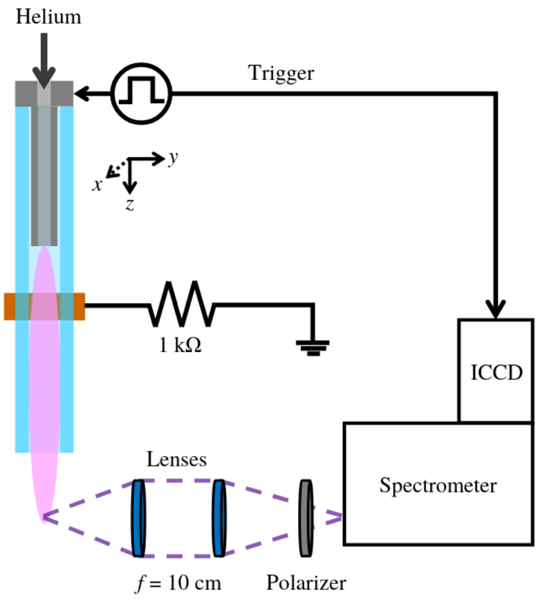

Figure 1.9: Schematic overview of the Stark polarization spectroscopy setup from Hofmans thesis [96].

The Stark effect is important because the E-field affects the electron charge distribution directly. It is due to the interactions of the emitter with charged particles (ions or electrons). More

---

[7] Johannes Stark won the 1919 Noble Prize of Physics for his discovery in 1913

precisely, the existence of an E-field, either of internal plasma origin or of an external E-field applied to the medium, leads to a degeneration of the atomic levels of the atoms and ions, and subsequently to a widening of the spectral lines. This can be described by the quasi-statistical theory of Holtsmark, in which the interaction potential varies as r^{-2} (linear Stark effect) for the hydrogen atom or hydrogenoid atoms, while for the other atoms the potential varies r^{-4} (quadratic Stark effect).

Laser-Induced Fluorescence-dip Stark spectroscopy (LIF-dip)

Furthermore, an interesting technique to directly measure E-field in plasmas is the DC Stark spectroscopy. This technique is based on measuring the shift and mixing of energy levels in atoms caused by the Stark effect. Czarnetzki *et al.* [97] introduced a new method for detecting **Stark effects based on laser-induced fluorescence spectroscopy (LIF-dip)**.

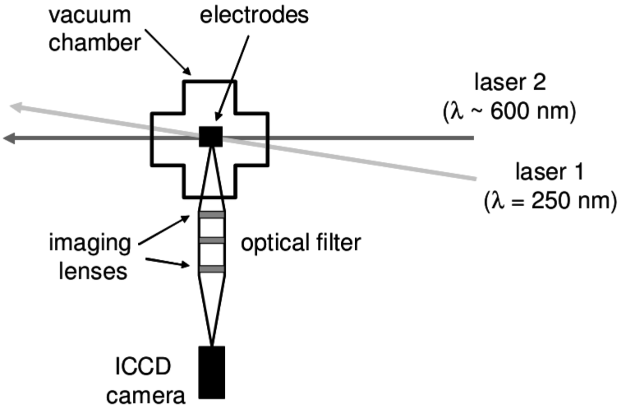

Figure 1.10: Schematic diagram of the experimental arrangement for LIF-dip Stark spectroscopy from Wagenaars et al. [89].

This technique can determine the concentrations, energies and kinetics of atoms, radicals and ions, and can also be used to measure fields that influence the movement of charged particles. Measurements can be performed spatially selectively within the plasma reactor, and non-invasively [98, 99]. After that, the LIF-dip technique has been applied to argon discharges [89]. An example for a schematic setup is given by Figure 1.10.

1.3.2 Four-Wave Mixing techniques (FWM)

Recent work has demonstrated the ability to measure the E-field using **nonlinear four wave mixing (FWM) techniques**, in particular, a technique which is very similar to coherent anti-Stokes Raman spectroscopy[8], a well-known diagnostic for measurement of gas temperatures, species concentrations, and vibrational distribution functions [100]. This basic technique was first described and disassembled by Gavrilenko *et al.* in 1992 [101] and is described in detail in Refs [102, 103].

According to Simeni *et al.* [92], the FWM method has many practical applications using various nonlinear media in the visible-to-infrared region of the electromagnetic spectrum (*e.g.*, dispersion compensation, cavity resonators, and image processing), viable nonlinear media for

---

[8] also called Coherent anti-Stokes Raman scattering spectroscopy (CARS), is a nonlinear Raman spectroscopy technique that uses two very strong collinear lasers to irradiate a sample. The frequency is usually kept constant, with the second laser tuned so that the frequency difference between the two lasers equals to the frequency of a Raman-active mode of interest

wavelengths longer than 10 μm have not been fully developed. Using four-wave mixing plasma diagnostics, important plasma parameters such as wave resonances, plasma susceptibility, electron temperature, plasma velocity, plasma density, magnetic field strength, etc., may be measured non intrusively by electromagnetic waves. The FWM beam intensity is proportional to the squared E-field integrated along the length of the discharge electrodes. Figure 1.11 shows a schematic of the FWM experimental made by Muller *et al.* [104].

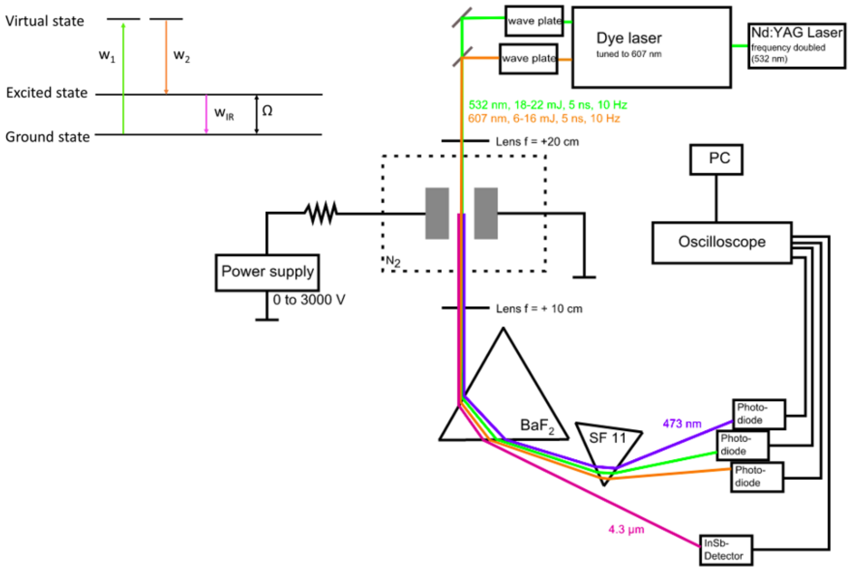

Figure 1.11: Schematic diagram of the experimental arrangement for electric field measurement by FWM [104] with the FWM principle.

1.3.3 Electric-Field Induced Second Harmonic generation (E-FISH) method

In the presence of an external E-field, the symmetry can be broken, allowing the molecules to radiate light at the second harmonic frequency normaly forbiden in centro-symetric media like gas. **Electric-field-induced second harmonic generation (E-FISH)**, a non-linear optical phenomenon, arises from the interaction between the E-field of an external bias and that of two incident photons. The technique was first discovered in the 1960s and 1970s, and has since been used largely to measure the hyperpolarizabilities of different species [105]. It has recently demonstrated significant potential as a method for making absolute E-field measurements in non-equilibrium plasmas and gas discharges. Research at the Laboratory of Plasma Physics (LPP[9]) has focused on both the application and development of the E-FISH method (see Figure 1.12). For more information about this technique we can refer to [91, 106, 107].

---

[9] The teams of the LPP work on laboratory and space plasmas, cold and hot plasmas website: https://www.lpp.polytechnique.fr/-A-propos-du-LPP-

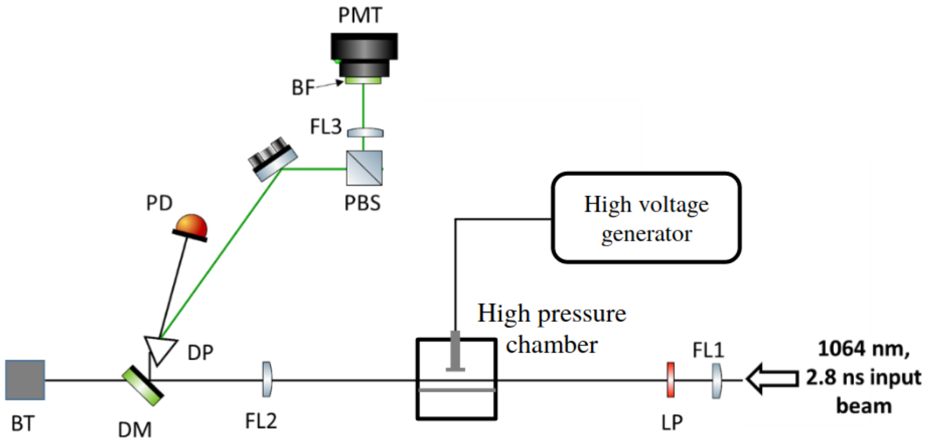

Figure 1.12: Schematic of the E-FISH optical setup from [91]. BT: beam trap; DM: dichroic mirror; DP: dispersive prism; FL: plano-convex spherical lens; HWP: half-wave plate; LP: long pass filter; PB: 532 nm polarizer; PD: photodiode; PMT: photomultiplier tube with attached iris and 532 nm band pass filter.

1.3.4 Electro-Optical method (EO)

The goal of this research was to develop and evaluate a diagnostic technique to perform the **real time analysis of the E-field vector associated to plasma discharges**. The technique is based on electric field measurement via the Pockels' effect and will be used for the measurement of vectorial electric field in DBDs and plasma jets and will be detailed later in this manuscript (Chapter 3).

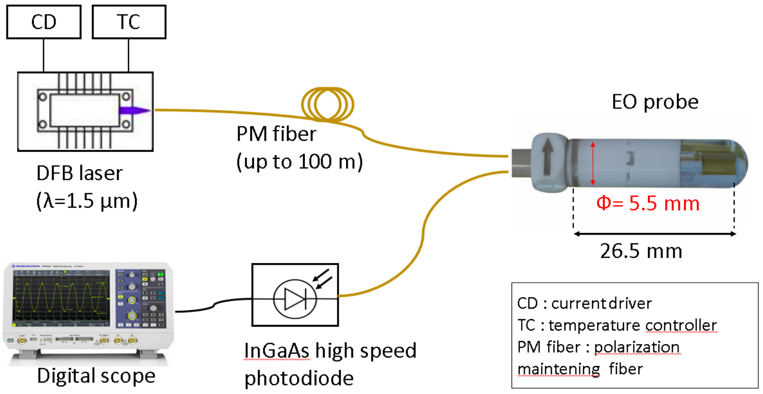

Figure 1.13: Schematic of an EO setup.

The use of this effect for high voltage measurement was considered in 1999 by [108] and [109]. Pigtailed EO sensors are naturally becoming a reliable and consistent mean of characterization for many applications, *e.g.* high power microwaves (HPM), electromagnetic interference (EMI), on-chip diagnostic, bio-electromagnetism (*e.g.* influence of mobile phones on the human body) [110, 111]. An example of a schematic of this EO technique exploiting a fibered sensor is represented in Figure 1.13.

1.3.5 Advantages and limitations of different techniques

In this section, we will discuss some advantages and limitations of all the techniques above-mentioned and summarized in Table 1.2.

For non-invasive E-field measurement, techniques that monitor the field-induced Stark shift, such as Stark spectroscopy and LIF-dip Stark spectroscopy, have been used with great success and allow the measurement of E-fields in neutral gases and low ionization plasmas. But the main limitation is the pressure of the gas of the discharge (the maximum pressure has been estimated to be around 10^4 Pa) due to effects such as the collision quenching of the intermediate level reduces the fluorescence intensity at higher pressure.

The FWM technique has been used for several years to measure discharge fields containing hydrogen and nitrogen. While being a useful measuring tool, it suffers from the drawback that it relies on molecular resonances and has therefore only been used in the gases above-mentioned. Additionally, due to phase matching requirements, a collinear geometry must be used, limiting the spatial resolution of the technique. The temporal resolution of these measurements is also limited by laser pulse duration and discharge time jitter [102].

E-FISH, which has lately been redeveloped and successfully employed as a diagnostic for E-field measurements in plasma, presents the key advantage to be applied in virtually any gas, without constraints on the gas composition [91]. The signal production is governed by the duration of the laser excitation, and in principle permits sub-ps temporal resolution with ultrashort laser pulses. But it also remains some disadvantages that rely on the high intensity of the laser (some experiments done in our laboratory verify the initiation of plasma by a femtosecond laser). Indeed, the measurement uncertainty of the absolute E-field and the Gouy phase-shift[10].

EO sensors have been the object of growing attention for more than four decades [112]. They present a frequency bandwidth spreading from 30 Hz up to several GHz, a dynamic range higher than 130 dB, a sensitivity much better than 1 V/m, a 1 dB compression point exceeding several 100 kV/m, and a spatial resolution lower than 1 mm^3. Those pigtailed EO sensors constitute handful tools suitable for many applications, especially for absolute and vectorial measurements of high E-fields in harsh environments [113–117]. But it also presents some limitations inherent to the sensor used. These limitations mainly concern the disturbance induced by the sensor in case of measurement within the plasma and the potenial presence of space charges onto the sensor itself.

---

[10] Along its propagation direction, a Gaussian beam acquires a phase shift which differs from that for a plane wave with the same optical frequency. This difference is called the Gouy phase shift and defined by: $\phi_G(z) = -\arctan\left(\frac{z-Z_0}{Z_R}\right)$, where Z_R is the Rayleigh length and Z_0 corresponds to the position of the focal point where the beam waist is the smaller

Characteristics	**Stark spectroscopy**	**FWM**	**E-FISH**	**EO**
Linear technique	✗	✗	✗	✓
Non-linear optics	✗	✓	✓	✓
ICCD camera	✓	✓	✓	✗
Gas constraint	Low pressure (max pressure $\approx 10^4$ Pa)	Hydrogen & Nitrogen	No	No
Laser	Pulses (ps, fs)	Pulses (ps, fs)	Pulses (ps, fs)	CW
Polarimetric & vectorial measurement	✗	✗	✗	✓
Remarks	-N/A for higher pressures	-Temporal & spatial resolution limited -Gas constraint	-The intense laser disturbs the plasma -The measurement uncertainty -Gouy phase-shift	-"Block" the plasma if placed within -Eventual space charges

Table 1.2: Table of comparison between the different techniques for E-field measurement.

2

Plasma induced by femtosecond laser as THz emitter

Sommaire

Electromagnetic (EM) waves are one of the most powerful tools for studying the world around us. Among the various domains of the electromagnetic spectrum, the visible domain corresponds to a small window through which we see the world every day (spectral interval between 7.10^{14} Hz and 4.10^{14} Hz). On one side of this frequency range are the ultraviolet (UV) rays, responsible for our summer tanned complexion, and on the other side is the infrared (IR) domain discovered by William Herschel in 1800. In recent years, the scientific community has paid increasing attention to EM waves whose frequencies are in the terahertz range. **This spectral range located between 100 GHz and 10 THz, corresponds to the far infrared of opticians or the sub-millimeter range of electronics**. In this chapter, we are interested in studying the **terahertz "THz" domain**. Section 2.1 is devoted to the presentation of THz sources and applications related to the THz range while section 2.2 presents their different method of generation and detection using femtosecond laser pulses.

2.1 Generalities and applications of THz radiations

Among the different wavelength ranges of the electromagnetic spectrum, the scientific community studies very intensely the waves of TeraHertz frequencies (THz). It defines the area of the spectrum of electromagnetic waves whose frequencies spread from 100 GHz to 10 THz, which corresponds to wavelengths between 30 μm and 3 mm [118]. The electromagnetic spectrum is represented as a function of frequency and wavelength in Figure 2.1.

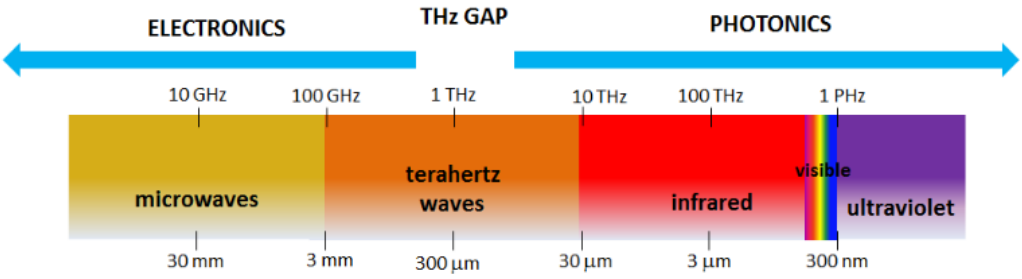

Figure 2.1: Diagram of the electromagnetic radiation spectrum, showing the location of terahertz (THz) radiation [119].

For about twenty years, the THz frequency range has become more easily accessible with the development of ultra-fast lasers capable of generating pulses lasting few tens of femtoseconds (fs, 10^{-15}s). Previously, these THz frequencies were only accessible by synchrotrons, free electron lasers, and molecular gas lasers [120].

THz radiation, usually abbreviated as THz or even T-ray or far-infrared radiation, thus bridges the technological gap that use to lie at the boundary between the electronics and optics domains and it remains one of the least explored spectral regions despite its predicted high potential to probe condensed and diluted matters [119, 121]. It has been for long time considered as a rather poorly explored region.

Waves in the THz domain have period between 0.1 and 10 ps. THz photon energy is between 0.42 and 41.5 meV, corresponding to a temperature between 4.8 and 478 K [118, 122].
As shown in Figure 2.1, the so-called "THz gap" corresponds in the electromagnetic spectrum to the frequency range in between the microwaves and far infrared (IR) waves and it benefits from the techniques of these two neighboring domains (IR & microwave).

Researchers and engineers dream of using terahertz (THz) waves, in many applications interviewed in fields as varied as image processing, astronomy, biology, and many other fields

[123–125] among which security and defense play a preponderant part. With the advent of THz time-domain spectroscopy (THz-TDS), terahertz radiation is nowadays fully attractive thanks to its many applications in a large number of scientific domains. For example, we shall highlight the following ones in Figure 2.2.

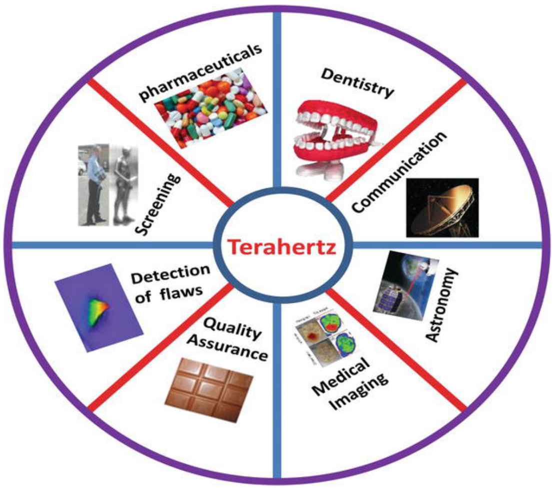

Figure 2.2: The wide application range of THz [126].

In the security domain, THz is used in new imaging systems (see Figure 2.3).

Figure 2.3: Surveillance of the Shanghai metro using a terahertz camera. (Photo is taken from [127])

Since THz waves pass through clothings but are reflected by metal and absorbed by water molecules, they could be used to detect concealed weapons (these body scanners already exist in some airports.They operate at few hundreds of gigahertz (GHz) but by switching to terahertz, we could make them more precise). *" Likewise, this radiation could secure the parcel distribution chain by making it possible to search for dangerous objects in the packages without having to open them. Several demonstrations have been successfully carried out around the world, including some in France, but postal sorting rates still make it difficult to set up such systems with current imaging means "* (from Le journal CNRS [127]).

Another example in the medical sector : the medical THz imaging. Unlike X-rays, THz radiation is not ionizing and it can pass through several millimeters of tissue presenting rather low hydration. Figure 2.4 shows the THz image of brain cancer, it can be seen that the results of terahertz imaging directly reflect the severity of brain cancer.

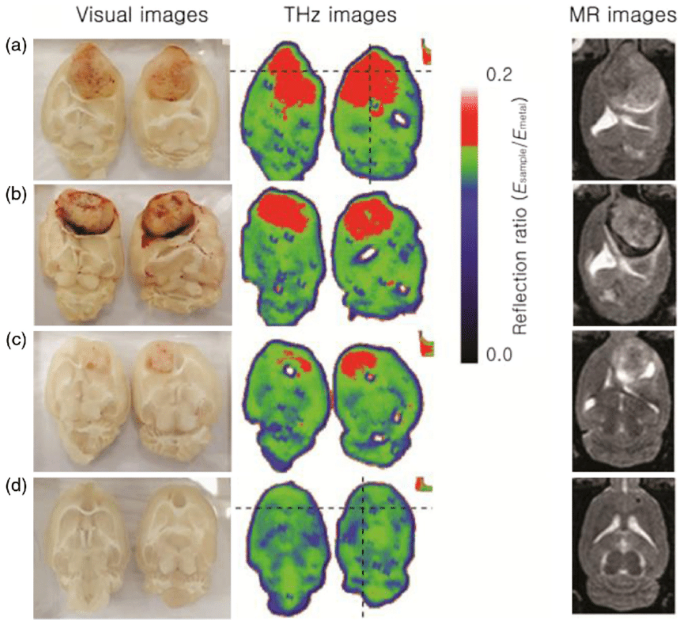

Figure 2.4: THz and MRI images of brains (a)-(c) with and (d) without tumors. Note that THz imaging is highly adept at locating both presence and size of tumors (Photo is taken from [128]).

2.2 Generation and detection of THz radiations

For a long time, THz waves remained somewhat neglected by scientists. And this, for lack of sufficiently efficient sources and detectors. Historically, it was the astrophysicists who were first interested in this type of waves because they are predominant in the universe. Following the awareness of the wide field of applications offered by these waves, we have witnessed for twenty years the appearance of many techniques for generating and detecting THz waves, most of which are based on optical methods. This section is divided into two parts, in we will present the techniques of generation of THz waves while the second presents the most used detection techniques.

2.2.1 THz generation techniques

Taking advantage of the two neighboring domains (IR and microwave), classical THz sources are extrapolated from microwave or optical sources. **The reasons why the scientific community is intensifying research in the development of generation techniques, detection techniques and of course in THz applications, is that THz waves have unique characteristics for probing matter since they can penetrate non metals materials such as plastics, paper, wood, gases, textiles and organic materials.** These materials are transparent to THz waves since they are devoid of free charges. On the other hand, these low energy waves are said to be non-ionizing (unlike X-rays) and do not damage the samples. Finally, many molecules have distinct fingerprints in the THz spectrum. Indeed, many molecules (water, DNA, drugs, TNT..) absorb THz waves because the rotation and vibration energies of these large molecules correspond to the energy of a THz photon [129, 130]. The key performance characteristics of the THz sources was detailed by Coutaz *et al.* book [118]. Today, we now count numerous techniques for THz generation, R.A. Lewis list six main types of terahertz sources [131]. These include thermal [132], solidstate electronic [133], sources pumped by lasers [134], vacuum electronic [135], lasers [136], and mechanical-excitation types of terahertz radiation sources [137].

In this section, we will focus on reviewing the principles and the evolution of intense **THz**

sources based on photoconductive antennas (PCAs) emitter, Optical rectification (OR), and laser induced breakdown in air. All these techniques involve femtosecond (fs) laser and are available in our laboratory. They are used in THz time domaine setup (TDS).

Photoconductive antennas (PCAs)

Photoconductive antennas (PCAs) have been widely used for the generation (and detection) of broadband THz waves, and are most efficient at low power. They were first accomplished in the late 1980s by the research groups of THz pioneers David Auston [138, 139] and Daniel Grischkowsky [140, 141].

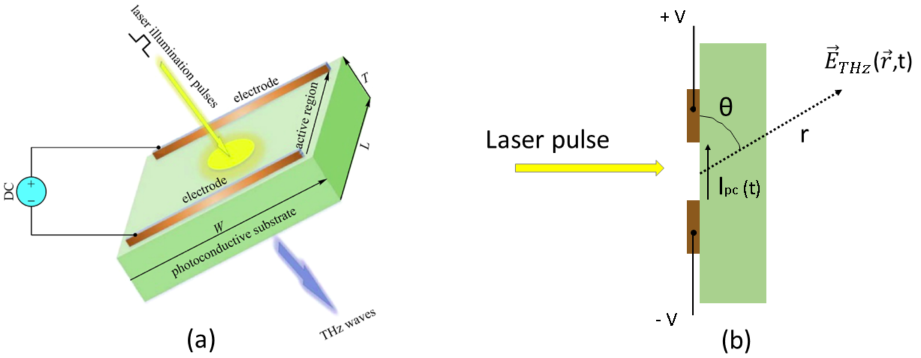

Figure 2.5: (a) Schematic view of a typical photoconductive emitter. (photo is taken from [142, 143]) (b)The side view of PCA with the radiated THz electric field.

These devices equipping many THz imaging and spectroscopy systems, have shown performances that meet requirements for various promising applications in industries and research fields. A simplified scheme is shown in Figure 2.5. THz PCA consists of two metal electrodes (usually gold or aluminium) deposited on a wafer of a semiconductor like Gallium Arsenide (GaAs) or Indium Gallium Arsenide (InGaAs) grown by molecular beam epitaxy (MBE) [144] with a space between these two electrodes (gap). To generate THz pulses, a DC bias voltage (of several kV/cm) is applied across the electrodes. Under illumination with ultrashort laser pulses (a femtosecond laser pulse) hitting this wafer, electron-hole pairs are generated (if the photon energy of the laser pulse is higher than the band gap of the semiconductor). The free charge carriers are immediately accelerated by the bias field (like shown in Figure 2.5.b) and the resulting fast change in polarization drives the emission of pulses in the order of one picosecond and with frequencies in the THz regime.

A schematic of a typical THz generation setup by photoconductive antenna is presented in Figure 2.6. The THz electric field, $\overrightarrow{E}_{THz}$, is dependent to the photocurrent I_{PC}(t) generated between the metal. It is vectorially described at a distance r and time t by the following equation :

$$\overrightarrow{E}_{THz}(t) = \frac{\mu_0 \omega_0}{4\pi} \frac{sin\,\theta}{r} \frac{\partial^2 p(t_r)}{\partial t_r^2} \hat{\theta}, \tag{2.1}$$

where μ_0 is the permeability of the free space, ω_0 is the spot size of the laser beam, θ is the angle from the direction of the dipole and $p(t_r)$ is the dipole moment of the source at the retarded time ($t_r = t - \frac{r}{c}$, c is the speed of light), which was induced by the photocurrent in the PC gap.

In the far field region (r is much bigger than the wavelength of THz field), the radiated THz is proportional to the first derivative of the photocurrent :

$$\overrightarrow{E}_{THz}(t) \propto \frac{\partial I_{PC}}{\partial t}. \tag{2.2}$$

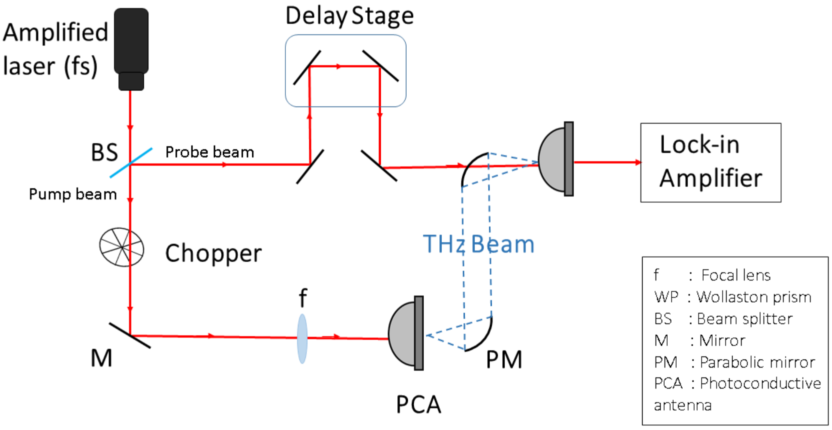

Figure 2.6: Schematic view of a typical THz generation setup by photoconductive antenna.

Optical rectification (OR)

In the recent years, nonlinear optical phenomena such as optical rectification (OR), and the linear electro-optic effect (Pockels effect) have become attractive options for broadband generation and detection of THz radiation [145, 146] with a first experiment reported in 1962 by Bass *et al.* [147] performed with potassium dihydrogen phosphate (KDP) and potassium dideuterium phosphate (KD_dP) as non linear crystals.

Several laser-based THz generation techniques are available, one of the most common being optical rectification, which is mentioned in this section. This secondorder nonlinear optical process is a special case of difference-frequency generation (DFG). The generation of THz by OR with a femtosecond laser source doesn't present any major difficulty today. However, to achieve an efficient generation process, the choice of the nonlinear crystal remains limited. They must both exhibit strong nonlinearity and meet the criteria of transparency and phase matching for extreme wavelengths. Among the solid materials that can be used (GaAs, GaSe, ZnTe, DAST, etc.), we will see that the "ZnTe" semiconductor crystal best meets these conditions.

Whenever an external electric field (E-field) is applied to matter, it induces or reorients dipole moments of atoms or molecules of the matter and deforms the electronic orbitals leading to a nonzero average dipole moment per unit volume or polarization of the medium $\overrightarrow{P}$. If the applied electric field is not large, the polarization is proportional to the field strength, *i.e*,

$$\boxed{\overrightarrow{P}(t) = \varepsilon_0 \overleftrightarrow{\chi}^{(1)} . \overrightarrow{E}}, \tag{2.3}$$

where $\overleftrightarrow{\chi}^{(1)}$ is the dielectric susceptibility of linear optics and ε_0 ($\varepsilon_0 \approx \left(36\pi 10^9\right)^{-1}$ F/m) is the vacuum permittivity.

If the electric field becomes intense, the simple linear relation 2.3 no longer holds. The displacement of the electronic cloud is no longer proportional to E and anharmonic components begin to appear. It is these components that explain nonlinear optics [148, 149]. We express this vector as follows :

$$\begin{aligned}\overrightarrow{P}(t) &= \varepsilon_0 \big(\underbrace{\overleftrightarrow{\chi}^{(1)} . \overrightarrow{E}_{\omega_1}}_{1} + \underbrace{\overleftrightarrow{\chi}^{(2)} . \overrightarrow{E}_{\omega_1} . \overrightarrow{E}_{\omega_2}}_{2} + \underbrace{\overleftrightarrow{\chi}^{(3)} . \overrightarrow{E}_{\omega_1} . \overrightarrow{E}_{\omega_2} . \overrightarrow{E}_{\omega_3}}_{3} + \ldots\big) \\ &= \varepsilon_0 \sum_n \left(\overleftrightarrow{\chi}^{(n)} . \prod_{\omega_i} \overrightarrow{E}_{\omega_i}\right),\end{aligned} \tag{2.4}$$

where $\overrightarrow{E}$ is the electric field that $\overrightarrow{E} = \overrightarrow{E_0}(\overrightarrow{r}).cos(\omega t)$ with ω the angular frequency of the incoming E-field and $\overleftrightarrow{\chi}^{(n)}$ is the n-th order nonlinear dielectric susceptibility.
To resume :
Term 1 describes the linear optics such as how lenses work.
Term 2 describes second-order effects, *e.g.* second-harmonic generation (SHG), linear electro-optic effect, etc..
Term 3 describes third-order effects, *e.g.* Kerr effect, four-wave mixing, etc..

Let us consider the circumstance for a second order nonlinear medium, which is excited by two optical fields oscillating with angular frequencies at ω_1 and ω_2 namely $\overrightarrow{E}_1(t) = \overrightarrow{E}_{\omega_1}.cos(\omega_1 t)$ and $\overrightarrow{E}_2(t) = \overrightarrow{E}_{\omega_2}.cos(\omega_2 t)$. It is important to remind that the second order polarization can only occur in a non-centrosymmetric crystals otherwise $\overleftrightarrow{\chi}^{(2)} = 0$. So the second order nonlinear polarization, illustrated in Figure 2.7, is in a form of :

$$\begin{aligned}\overrightarrow{P}^{(2)}(t) &= \frac{\varepsilon_0}{2}\overleftrightarrow{\chi}^{(2)}(\omega_1+\omega_2,\omega_1,\omega_2).\overrightarrow{E}_{\omega_1}.\overrightarrow{E}_{\omega_2}.cos(\omega_1+\omega_2)t \\ &+ \frac{\varepsilon_0}{2}\overleftrightarrow{\chi}^{(2)}(\omega_1-\omega_2,\omega_1,-\omega_2).\overrightarrow{E}_{\omega_1}.\overrightarrow{E}_{\omega_2}.cos(\omega_1-\omega_2)t \\ &= \overrightarrow{P}^{(2)}_{\omega_1+\omega_2} + \overrightarrow{P}^{(2)}_{\omega_1-\omega_2} \\ &= \overrightarrow{P}^{(2)}_{(SHG)} + \overrightarrow{P}^{(2)}_{(OR)}.\end{aligned} \tag{2.5}$$

As a result (from equation 2.5) the second order polarization is composed of two terms : $\overrightarrow{P}^{(2)}_{\omega_1+\omega_2}$ for the summation of the frequencies and is called **Second Harmonic Generation (SHG)** and $\overrightarrow{P}^{(2)}_{\omega_1-\omega_2}$ for the difference of the frequencies what is called **Optical Rectification (OR)**. Scheme of Figure 2.7 resumed this phenomena.

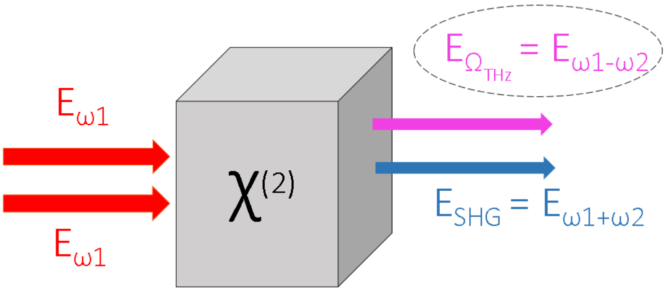

Figure 2.7: Schematic of optical rectification for terahertz generation.

Here, an ultra-short and intense laser pulse passes through a nonlinear crystal (zinc telluride ZnTe, for instance). Based on DFG process in between the frequency components of the laser pulse over the length of the non linear crystal, an electromagnetic burst is generated (see Figure 2.8) whose spectral bandwidth is linked to the optical pulse duration : the shorter the optical pulse, the shorter the THz pulse, and the wider the THz spectral bandwidth.

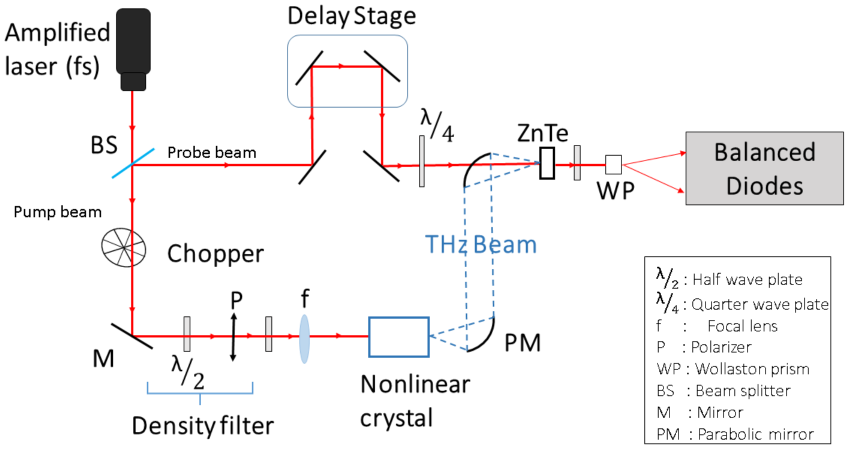

Figure 2.8: Typical setup of the optical rectification technique for THz generation.

ZnTe crystal

Zinc telluride is a binary chemical compound with the formula ZnTe. It is a zinc-blende II-VI semiconductor crystal. Its crystal lattice, like that of diamond, is of the blende type.

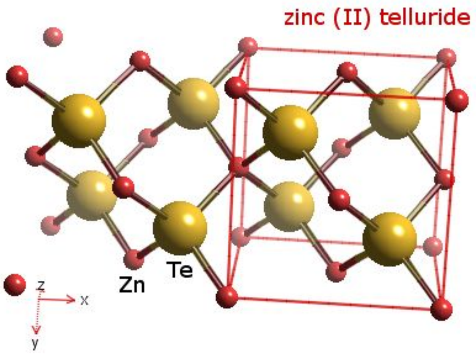

Figure 2.9: The ZnTe zinc blende structure [150].

ZnTe is a very good candidate for the THz generation by OR of laser pulses at 800 nm. Vidal explained in his thesis the importance of ZnTe in the THz generation [151].

- ZnTe is **transparent** at this wavelength, the energy difference between the valence band and the conduction band being $E_g = 2.2$ eV, which corresponds to a radiation of wavelength $\lambda = 564$ nm.

- This crystal has a **strong second order nonlinear susceptibility**. Its tensor consists of 27 elements, whose only non-zero element is the coefficient $\chi^{(2)}_{ijk} = 2d_{14}$ with $i \neq j \neq k$.

- ZnTe has a **very low absorption in the 0-5 THz range**. Stationary spectroscopy experiments have shown that the absorption of THz radiation due to the presence of phonons around 1.6 THz and 3.7 THz is negligible. However, the latter becomes important around 5.3 THz due to the presence of an optical transverse phonon [152, 153].

Generation of THz radiation due to air breakdown

As mentioned earlier, THz pulses can be generated by laser excitation of a photoconductive antenna or semiconductor surfaces, while one of the most intriguing techniques is plasma THz generation. In particular, the use of an air/gas plasma for THz generation is advantageous because, unlike nonlinear crystals and other bulk materials, gases have no damage thresholds and are continuously renewable; therefore, they can be pumped at extremely high intensities. Note that phase matching is less critical since diluted medium are less dispersives than bulk crystal.

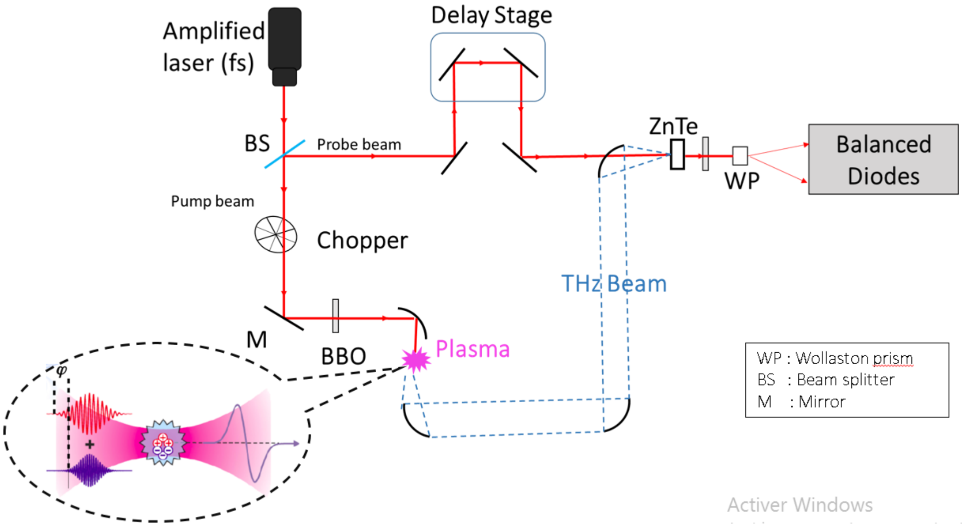

Figure 2.10: Typical setup for generation of THz radiation by breakdown in air.

It was in 1990 that a strong radiation in the THz frequency range was predicted resulting from the electric field created by the free ions present in the plasma. This effect was subsequently observed in an experiment by Hamster *et al.* [154–156]. In Hamsters experiment, an intense laser was focused on high-pressure air to produce a plasma. Few years later, the researchers worked on increasing the intensity of the THz radiation, for this they used the Beta Barium Borate (BBO) crystal. The BBO crystal produces the second harmonic field when the fundamental laser beam is transmitted through it. Based on the four-wave mixing (FWM) theory (third order non-linear effect), this second harmonic field will interact with the fundamental laser field at the focal point where the ionized air forms a plasma and the THz pulse is generated. The THz generated depends on the fundamental and second harmonic intensities I_ω and $I_{2\omega}$, respectively, together with the relative phase shift φ between these two pulses (see left scheme in Figure 2.10) :

$$|E_{THz}| \propto I_\omega \sqrt{I_{2\omega}} \cos(\varphi) \tag{2.6}$$

2.2.2 THz radiations Detectors

This section will provide an overview of THz waves detection, the newly developed technology for THz pulse detection in recent years will be described in this section. In THz domain, we have two kinds of detectors : Coherent and Incoherent detectors. For coherent detectors, both amplitude and phase of the THz signal are measured. **The most common techniques are introduced in this section, which are photoconductive antennas (section 2.2.2), electro-optic method (section**

2.2.2), and air-biased coherent detection (section 2.14). While the incoherent detectors *i.e.*, which measure the energy of the radiation and do not give us direct access to its phase consist of two types : Bolometers, and intrinsic and extrinsic photoconductors (for more information on the latter, Coutaz *et al.* explain them in their book [118]).

Photoconductive antennas (PCAs)

As mentioned before (in section 2.2.1), PCAs can be used for generation as well as for detection. Here, no bias voltage is applied. The free charge carriers, generated by incident laser pulses, are accelerated by the electric field of the THz radiation to be measured, and the current I_d between the two bias electrodes, given by equation (2.7), allows to measure the electric field strength of the THz field via a current meter [144, 157, 158].

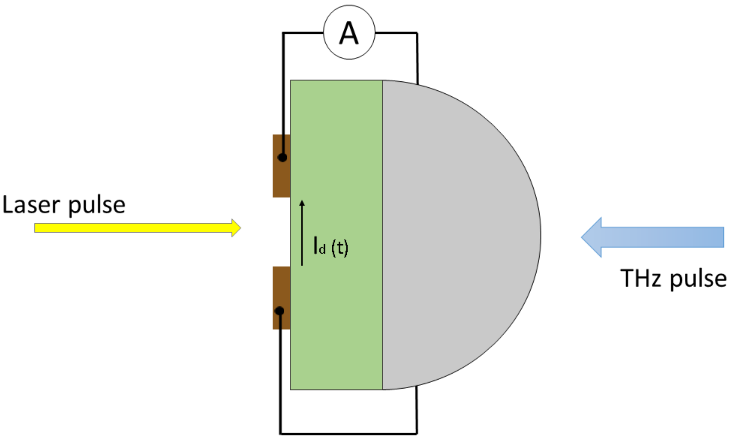

Figure 2.11: The side view of a photoconductive antenna detector. The laser and THz pulse pass through the detector.

Since the same fs laser is used to generate and to detect THz signal, the current is recorded in the time domain by varying the delay between the opticl probe beam and the THz pulse, to obtain THz waveform [159]. The recorded current is quite weak (sub-nA), hence the need to use a current lock-in amplifier. The detected electric current I_d at a time t is given by the following equation [160] :

$$I_d\,(t) = E_{THz} \times \sigma_s(t) = \int E_{THz}(t')\,\sigma_s(t-t')\,dt', \tag{2.7}$$

where E_{THz} is the THz electric field, t' is the delay between the probe and THz pulses, and the surface conductivity is σ_s[1].

Electro-optical method (EO)

It was in 1984 that the first detection of THz radiation by electro-optic sampling was demonstrated by Auston *et al.* [161]. It is based on the well-known Pockels effect. This part is devoted to the description of the principle of detection of THz pulses by electro-optic effect (EO) in the

---

[1] $\sigma_s(t) = e\mu_e n'(t)$, where e is the electron charge, μ_e is the constant electron mobility and $n'(t)$ is the time-dependent electron charge density.

ZnTe crystal. We will present the experimental technique for measuring the EO signal (chapter 3 described the electro-optic principle).

EO effect is a nonlinear phenomenon of second order, which reflects the influence of a low frequency E-field (generally THz frequencies) on the dielectric properties of a crystal. The principle of the detection method based on this effect is as follows : the presence of a THz wave in an EO crystal causes the appearance of an induced birefringence[2], which causes a rotation of the polarization of a probe beam (wavelength of 800 nm in our case) crossing the crystal, the rotation being proportional to the THz field. The measurement of this rotation of polarization in time determines the amplitude and the phase of the E-field associated to the THz pulse [151]. For efficient detection, it is necessary to use a crystal having a high electro-optic coefficient. To compare the different crystals, Q. Wu and X. C. Zhang [160] introduced a coefficient of merit η defined as follows :

$$\eta = \frac{2n_s^3 r_{ij}}{\sqrt{1+\varepsilon}}, \tag{2.8}$$

where n_s is the refractive index seen by the probe beam, r_{ij} is the electro-optic coefficient involved and ε represents the permittivity of the crystal in the THz domain. Figure 2.12 shows the characteristics of the main crystals that can be used for electro-optic detection.

Cristal	r_{ij} (pm/V)	n_s	ε	η (pm/V)	DVG (ps/mm)
ZnTe	$r_{41} = 4.04$ @ 633 nm	2.85 @ 800 nm	10.1	51.7	1.1
CdTe	$r_{41} = 4.5$ @ 1 μm	2.84 @ 800 nm	9.4	50.9	0.75
DAST	$r_{11} = 160$ @ 820 nm	$n_o = 2.46$ $n_e = 1.70$ @ 820 nm	8 2.9	max 633	1.22
LiTaO3	$r_{33} = 30.5$ $r_{13} = 8.4$ @ 633 nm	$n_o = 2.176$ $n_e = 2.180$ @ 633 nm	$\varepsilon_{1,2} = 41$ $\varepsilon_3 = 43$	max 87.2	14.1
LiNbO3	$r_{33} = 30.9$ $r_{51} = 32.6$ @ 633 nm	$n_o = 2.29$ $n_e = 2.20$ @ 633 nm	$\varepsilon_{1,2} = 43$ $\varepsilon_3 = 28$	max 110	14.2

Figure 2.12: Characteristics of the main electro-optic crystals that can be used for EO detection [162]. η is the coefficient of merit defined by Q. Wu and X. C. Zhang, the group speed mismatch between the optical pulses and THz wave is denoted by DVG. (Table is taken from [151])

To summarize, the EO crystal used must meet the following conditions :
- be transparent to the wavelength of the probe used (here 800 nm);
- be transparent in the THz domain;
- have a high coefficient of merit η;
- have a weak group velocity mismatch, noted DVG, between the probe (optical) and THz pulses.

The most common scheme for electro-optic sampling detection of a THz signal is illustrated in Figure 2.13. Since the ZnTe crystal is cubic, it does not change the initial state of polarization of the probe beam in the absence of THz field, which is linearly polarized. This probe beam has become circularly polarized by a quarter wave plate ($\lambda/4$). A Wollaston prism (WS) divides the circular polarized beam to two orthogonal linearly polarized beams (x and y axes). These

---

[2] Birefringence is a property that certain transparent materials have with respect to light. Their main effect is to divide in two a ray of light which penetrates them. Birefringence, also called double refraction, is explained by the existence of two different refractive indices depending on the polarization of the light. These two indices are called ordinary index n_0 and extraordinary index denoted n_e. The birefringence is the dimensionless value : $\Delta n = n_e - n_0$; knowing that n_0 is the refractive index of the polarization perpendicular to the anisotropy axis of the material, while n_e is the refractive index of the polarization parallel to the anisotropy axis.

two pulses are incident on a balanced detector and we can measure the E-field of THz using the difference of intensity between two pulses $\Delta I = I_y - I_x$. The I_x and I_y components in this condition are the same, so the difference in the optical beam intensities is almost zero and there is no signal detected by the balanced photodiodes. (ΔI is measured by a current preamplifier and a lock-in amplifier).

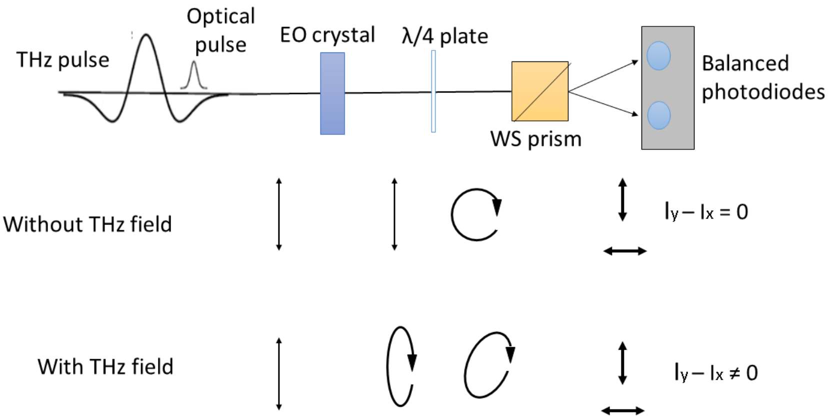

Figure 2.13: Schematic of electro-optic sampling by modulation of the optical polarization state.

On the other hand, the presence of a THz field in the crystal causes the appearance of an induced birefringence, which causes a rotation of polarization. The polarization of the transmitted optical beam becomes elliptical since the two components of the optical field encounter two different phase because of the crystal ellipticity (as seen in Figure 2.13). The corresponding phase retardation ($\Delta\phi$) caused by the impinging THz field is measured for different time delays between the THz field and the optical beam. $\Delta\phi$ is proportional to the THz field :

$$\Delta\phi = \frac{\omega n_0^3 L r_{ij}}{c} E_{THz}, \tag{2.9}$$

where n_0 is the refractive index of the EO crystal at the frequency of the optical beam, L is the thickness of the EO crystal, r_{ij} is one unit EO coefficient in standard crystallographic coordinate system, which varies for different crystal classes, ω and c are the angular frequency and the speed of light for the optical beam, respectively [163]. The balanced photodiodes measure intensities of x and y components :

$$I_x = \frac{I_0}{2}(1 - sin\Delta\phi) \approx \frac{I_0}{2}(1 - \Delta\phi)$$

$$I_y = \frac{I_0}{2}(1 + sin\Delta\phi) \approx \frac{I_0}{2}(1 + \Delta\phi),$$

where I_0 is the intensity of the optical probe.

However, the signal of the balanced photodiodes is directly proportional to the amplitude of THz field as follows :

$$\Delta I = I_y - I_x = \frac{I_0\,\omega n_0^3 L r_{ij}}{c} E_{THz}. \tag{2.10}$$

For more detailed see section 3.1.3.

Air-Biased Coherent Detection (ABCD)

The third method used as an ultra-broadband THz detection scheme is called air-biased coherent detection (ABCD), first introduced and developped by Karpowicz *et al.* [164]. Unlike asymmetric materials used in electro-optical sampling, ABCD uses gases as a centro-symetric nonlinear media and exploites therefore the third-order optical non linearities (Kerr effect). An amplitude-modulated bias field is necessary to overlap the THz field. The THz field amplitude is measured using heterodyne detection [165]. An example of an ABCD detection geometry is shown in Figure 2.14.

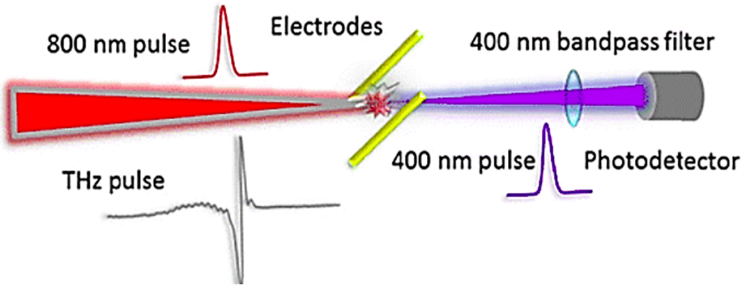

Figure 2.14: THz detection with air-biased coherent detection (ABCD) method (photo is taken from [166]).

This detection of THz radiation by a plasma being complex to set up, and has many drawbacks, such as limited laser power, the presence of resonances or photonic reflections. We chose not to use it within the framework of this thesis work, preferring a detection based on EO crystals taking advantage of the knowledge acquired from our laboratory (this technique is already detailed in section 2.2.2). For more information about ABCD technique we can consult these Refs. [165, 167, 168].

3

Electro-optics techniques from quasi DC to THz range

Sommaire

In this chapter we present the linear and nonlinear optical phenomena, in particular for isotropic crystals. Section 3.1 shows the different contributions of the electro-optic effects, their origins and their behavior. This will provide the knowledge necessary for the interpretation of the experimental results and the theoretical calculations. Then section 3.2 is devoted to the real time EO measurement at low frequency (below 100 GHz), while section 3.3 presents the EO measurement at higher frequency.

3.1 Electro-optics in isotropic crystals (vectorial calculation)

3.1.1 Electro-optic effect

The EO effect results from the coupling between an **electric field** and an **optical field**. In other words, it describes the variation of the optical properties of a medium under the effect of an applied electric field. At the atomic level, this E-field applied to certain crystals causes a redistribution of the binding charges and possibly a slight deformation of the crystal lattice. In general, these modifications are not isotropic. In other words, the modifications depends on the orientation of the E-field relatively to the crystal axis. This effect encompasses distinct effects, such as changes in refractive index (electro-refraction), changes in absorption (electro-absorption), and changes in reflection (electro-reflection). The electro-refraction effect consists of a change in the refractive index of the material by the application of an E-field. This change can be linear or non-linear :

- The **linear effect** (case of non-centrosymmetric[1] medium) or "Pockels effect", independently observed by Rôntgenet Kundt in 1883 in quartz and tourmaline. However, they attributed it to a deformation due to the electric field, which induces a variation of refractive index by photo-elastic effect. Pockels, in 1894 demonstrated that the field acts directly on the refractive index (referring to the second term of equation 2.4).

- The **quadratic effect** (case of centrosymmetric medium) or "Kerr effect" observed in 1875 in liquids and glasses, which are isotropic under normal conditions, and become birefringent when an electric field is applied. They then resemble unified crystals whose optical axis is parallel to the direction of the electric field. This effect is independent of the direction of the electric field and no condition of symmetry is imposed on the medium (effect described by a tensor of order four) [169].

The discovery of the laser made it possible to advance considerably the study of these effects, and gave them a large number of applications in the field of optical telecommunications to modulate the intensity or the phase of a light beam, and in optical signal processing.

3.1.2 Isotropic crystal

Isotropic and anisotropic are two important terms widely used to explain the atomic orientation, structure, and morphology of materials in material science and crystallography. In certain materials like crystals, the physical and mechanical properties often differ with crystal orientation. Based on the orientation of atoms, materials are broadly divided into two classes namely : **isotropic** materials and **anisotropic** materials. When the properties of a material vary with different crystal orientations, the material is said to be anisotropic (such as wood and composites). Alternately, when the properties of a material are the same in all directions, the material is said to be isotropic (such as cubic crystals and amorphous material). Yariv's book [170] is an important reference in optics. Table 3.1 is a summary of a direct comparison of isotropic and anisotropic crystals.

---

[1] non-centrosymmetric crystals do not have an inversion center.

CHARACTERISTICS	**ANISOTROPIC**	**ISOTROPIC**
Crystal example	**LiNbO$_3$**	**ZnTe**
Crystal structure	Trigonal	Zincblende
Group point	3m	$\bar{4}$3m
Speed of Light	Different, depending on the direction	Equal, regardless of the direction
Influence of the crystal on polarization state ($\vec{E}=0$)	Modified if not linear along eigen axis	Not modified
Influence of the temperature on polarization state	$\frac{\partial n_i}{\partial T} - \frac{\partial n_j}{\partial T}$	No influence, $\frac{\partial n_x}{\partial T} = \frac{\partial n_y}{\partial T} = \frac{\partial n_z}{\partial T}$
Measurement of $\vec{E}$	$E_x \; or \; E_y \; or \; E_z$	$E_i + \theta_i$, if orientation well chosen (i.e <1 1 1> axis for $\bar{4}$3m crystals)
Associated EO tensor	$\begin{pmatrix} 0 & -r_{22} & r_{13} \\ 0 & r_{22} & r_{13} \\ 0 & 0 & r_{33} \\ 0 & r_{51} & 0 \\ r_{51} & 0 & 0 \\ -r_{22} & 0 & 0 \end{pmatrix}$	$\begin{pmatrix} 0 & 0 & 0 \\ 0 & 0 & 0 \\ 0 & 0 & 0 \\ r_{41} & 0 & 0 \\ 0 & r_{41} & 0 \\ 0 & 0 & r_{41} \end{pmatrix}$
Typical r$_{ij}$ @ 633 nm (pm/V)	r_{33}=30.9	r_{41}= 4.04
Other typical examples	KTP, LiTaO$_3$..	BSO, CdTe..
Applications in linear optics	Polarizers, optical waveplates, wedges,...	Prism, windows, lenses,...

Table 3.1: Comparison between isotropic and anisotropic crystals.

The main difference between anisotropic and isotropic crystals can be seen on the three-dimensional (3D) representations of the Figure 3.1.

The refractive indices are modified by the E-field in both cases. However, the orientation of the proper dielectric axes remains unchanged (first order) only in the case of anisotropic crystals. In the following paragraphs, we will explain the principle of the measurement of the E-field $\vec{E}_\Omega$ by the variation of the refractive indices of an isotropic crystal. Within the framework of this thesis, we have chosen BSO crystal for the development of the EO probes and the ZnTe for the THz generation and detection.

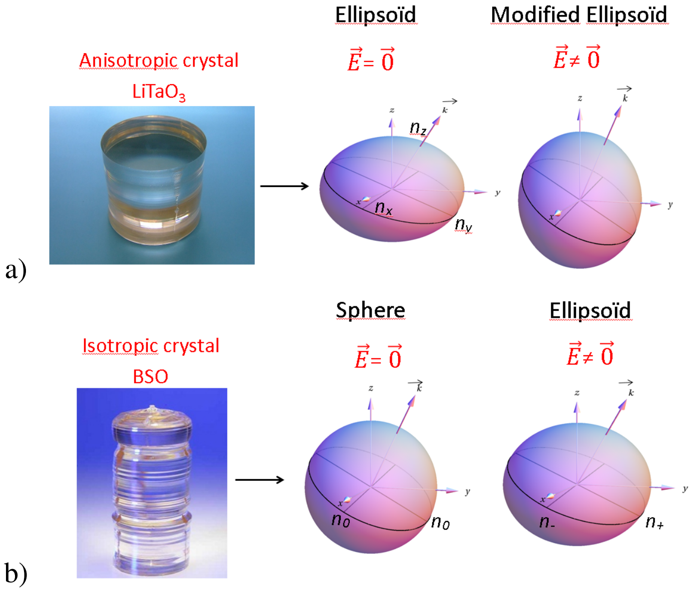

Figure 3.1: Ellipsoid of refractive indices in the case of a) anisotropic and b) isotropic crystals.

3.1.3 Theoretical calculation

The electro-optic technique described here, allows the vector measurement of the E-field in terms of phase, amplitude, and direction, by using the convenient formalism of index ellipsoid introduced by [170].

The index ellipsoid, which represents the dielectric characteristics of the crystal (see Figure 3.2), is written as follows :

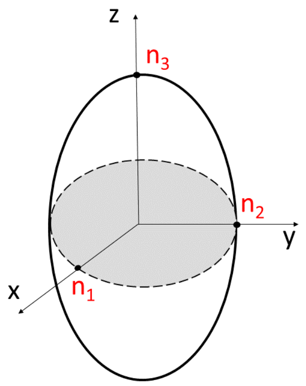

Figure 3.2: The index ellipsoid. The coordinates (x, y, z) refer to the eigen dielectric axes of the crystal and (n_x, n_y, n_z) are its principal refractive indices.

$$\boxed{Ax^2+By^2+Cz^2+Dyz+Ezx+Fxy=1},$$

x, y and z defining the eigen dielectric axes of the EO crystal.

→ **In absence of an E-field**, the coefficient of the ellipsoid are :

$$A=\frac{1}{n_1^2} \quad ; \quad B=\frac{1}{n_2^2} \quad ; \quad C=\frac{1}{n_3^2} \quad ; \quad D=\frac{1}{n_4^2}=0 \quad ; \quad E=\frac{1}{n_5^2}=0 \quad ; \quad F=\frac{1}{n_6^2}=0\,.$$

So the refractive index ellipsoid, is of the following form :

$$\frac{x^2}{n_1^2}+\frac{y^2}{n_2^2}+\frac{z^2}{n_3^2}=1.$$

→ **Under the influence of an E-field** ($\overrightarrow{E}_\Omega=\{E_x,E_y,E_z\}$ [171]), the index ellipsoid is then distorted and its equation writes :

$$\boxed{\left(\frac{x}{n_1}\right)^2+\left(\frac{y}{n_2}\right)^2+\left(\frac{z}{n_3}\right)^2+2\left(\frac{1}{n_4}\right)^2yz+2\left(\frac{1}{n_5}\right)^2xz+2\left(\frac{1}{n_6}\right)^2xy=1}, \tag{3.1}$$

and the E-field induced variation of n_i being defined by :

$$\boxed{\Delta\left(\frac{1}{n_i}\right)^2=\sum_j r_{ij}E_j}, \tag{3.2}$$

where r_{ij} are the EO coefficients of the tensor associated to the crystal, i corresponding to the coefficients of the ellipsoid and j the component of the electric field vector.

The tensor of a crystal is a matrix (6×3) representing the direct link between the components of the electric field $\{E_x,E_y,E_z\}$ and the linear disturbance of the coefficients due to the electric field $\overrightarrow{E}_\Omega$. This tensor, presented just below in matrix (3.3), has 18 coefficients, 6 corresponding to the coefficients of the ellipsoid by 3 corresponding to the three components of the E-field vector. The values of the tensor depend on the point group of the crytsal [149, 170].

$$\begin{pmatrix} r_{11} & r_{12} & r_{13}\\ r_{21} & r_{22} & r_{23}\\ r_{31} & r_{32} & r_{33}\\ r_{41} & r_{42} & r_{43}\\ r_{51} & r_{52} & r_{53}\\ r_{61} & r_{62} & r_{63} \end{pmatrix}. \tag{3.3}$$

Take the case of a **cubic crystal** (for example BSO that used in the EO sensor or ZnTe in the detection of THz in this thesis work), $n_1=n_2=n_3=n_0$, and the non null EO coefficient $r_{41}\,(=r_{52}=r_{63})$, is leading to the following EO tensor :

$$\begin{pmatrix} 0 & 0 & 0\\ 0 & 0 & 0\\ 0 & 0 & 0\\ r_{41} & 0 & 0\\ 0 & r_{41} & 0\\ 0 & 0 & r_{41} \end{pmatrix}. \tag{3.4}$$

Thus, the ellipsoid (3.1) writes :

$$\left(\frac{x}{n_0}\right)^2+\left(\frac{y}{n_0}\right)^2+\left(\frac{z}{n_0}\right)^2+2r_{41}E_xyz+2r_{41}E_yxz+2r_{41}E_zxy=1. \tag{3.5}$$

Orientation of the electro-optical crystal for vector measurement of the E-field

Gaborit *et al.* have detailed this important vector calculation of the birefringence induced by the E-field in this Ref [172]. In this section, I want to try to repeat some steps in order to have the general calculation and apply it to different particular cases (different crystal cut).

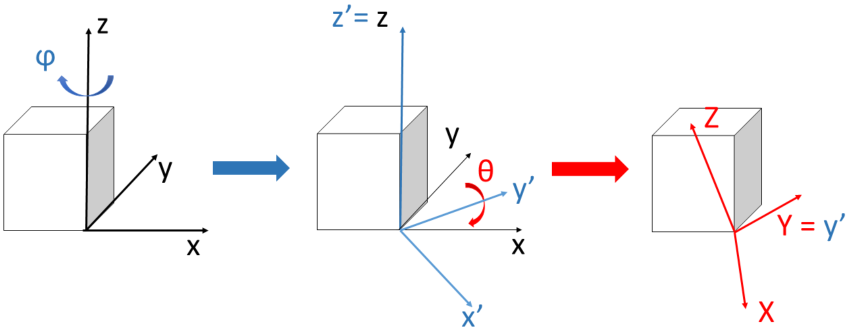

Figure 3.3: Schematic representation of the change of reference from that specific to the crystal (x, y, z) to (X, Y, Z), carried by the optical wave (wave vector being aligned along Z).

To access all the possible orientations relating to the crystal, it is necessary to make a change of reference in order to have the optical wave vector conveyed by a Z axis (see Figure 3.3). This change of reference is ensured by two successive rotations around the spherical angles φ and θ of the initial axis z (Figure 3.3). The matrices of rotations associated with this change of reference are the following ones :

$$R_y(\theta) = \begin{pmatrix} \cos(\theta) & 0 & -\sin(\theta) \\ 0 & 1 & 0 \\ \sin(\theta) & 0 & \cos(\theta) \end{pmatrix}, \qquad R_z(\varphi) = \begin{pmatrix} \cos(\varphi) & \sin(\varphi) & 0 \\ -\sin(\varphi) & \cos(\varphi) & 0 \\ 0 & 0 & 1 \end{pmatrix}.$$

The new matrix of the ellipsoid with the change of orientation, corresponds to that seen by the optical wave, it is written :

$$\boxed{\text{Ellipsoid} = R_y(\theta) \,.\, R_z(\varphi) \,.\, \text{Ellipsoid} \,.\, R_z(-\varphi) \,.\, R_y(-\theta)}. \tag{3.6}$$

The nonlinear index ellipsoid, seen by the optical wave, corresponds to the intersection matrix between the ellipsoid and the wave plan. This ellipsoid carries the transverse proper indices to which the optical wave will be sensitive. It is written :

$$\text{Matrix}_{\text{Ellipse}} = \begin{pmatrix} a & b \\ c & d \end{pmatrix} \tag{3.7}$$

$$\text{with,}\quad \begin{cases} a = r_{41}\,\left(E_z\cos^2(\theta)\,\sin(2\varphi) - \sin(2\theta)\,\left(E_y\cos(\varphi) + E_x\sin(\varphi)\right)\right) + \dfrac{1}{n^2}, \\[2ex] b = r_{41}\,\left(E_z\cos(\theta)\,\cos(2\varphi) - \sin(\theta)\,\left(E_x\cos(\varphi) - E_y\sin(\varphi)\right)\right), \\[2ex] c = r_{41}\,\left(E_z\cos(\theta)\,\cos(2\varphi) - \sin(\theta)\,\left(E_x\cos(\varphi) - E_y\sin(\varphi)\right)\right), \\[2ex] d = \dfrac{1}{n^2} - E_z r_{41}\,\sin(2\varphi). \end{cases}$$

In this work, the polarization state modulation of a laser beam probing the crystal is used to study the index change due to the presence of a field. This index variation induced by an E-field $\overrightarrow{E}_\Omega$, is written :

$$\boxed{\delta n_\pm(\overrightarrow{E}_\Omega) = n_\pm(\overrightarrow{E}_\Omega) - n_\pm(\overrightarrow{0})}, \tag{3.8}$$

where n_+ and n_- are the eigen refractive indices.
The calculation of this index variation is done for different values of θ and φ. Indeed, this index variation will be decisive in the sensitivity and vector selectivity of the sensor incorporating the crystal.

3.1.4 Several crystal cut

The following exhaustive analysis is summarized in Figure 3.4 for three directions of interest (i.e. $< 100 >$, $< 111 >$ and $< 110 >$) classically used as cutting orientations. Note that the axis corresponding of these orientations is perpendicular to these green plane (red arrows).

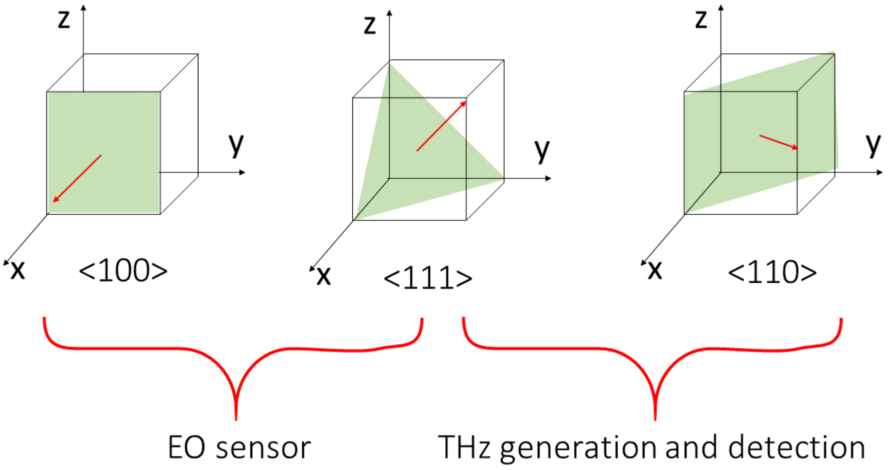

Figure 3.4: Schematic of a cubic crystal correspond to $< 100 >$, $< 111 >$ and $< 110 >$ orientation, respectively.

Case of $< 100 >$ crystal cut

We therefore consider an optical plane wave probing the crystal along the $< 100 >$ direction. In this case, the nonlinear index ellipsoid can be deduced after two successive spherical rotations of the ellipsoid. The particular values $\varphi = 0$ and $\theta = \frac{\pi}{2}$, the optical beam propagation along x axis, this leads to the following matrix form of the index ellipsoid :

$$M_{<100>} = \begin{pmatrix} \frac{1}{n_0^2} & -E_x r_{41} \\ -E_x r_{41} & \frac{1}{n_0^2} \end{pmatrix},$$

E_x is the E-field component along the x axis of the crystal. In this configuration, we notice that the modification of the indices is zero for an E-field in the XY-plan. It is maximum for a field along the Z axis. This optical arrangement will allow the development of a so-called **longitudinal sensor**, *i.e.* its axis of sensitivity will be collinear with the optical wavevector (Figure 3.5).

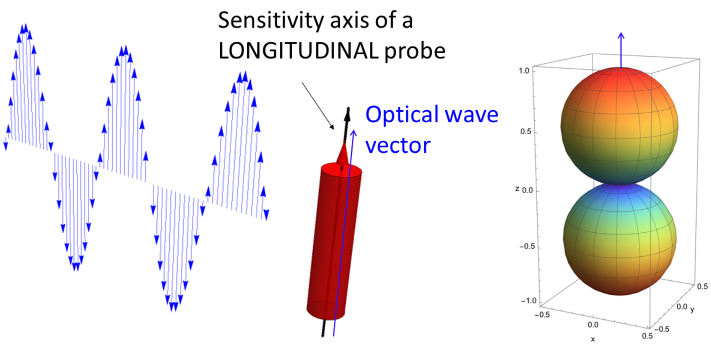

(a) (b)

Figure 3.5: (a) Schematic representation of a longitudinal EO sensor using a probe beam laser along the <100> axis of the crystal. (b) Representation of the vector sensitivity for this configuration.

The eigenvalues associated to this matrix are :

$$V_1 = \frac{1}{n_0^2} - E_x r_{41} \qquad \text{and} \qquad V_2 = \frac{1}{n_0^2} + E_x r_{41},$$

then,

$$n_1 = \sqrt{\frac{1}{V_1}} \qquad \text{and} \qquad n_2 = \sqrt{\frac{1}{V_2}}. \tag{3.9}$$

Taking into account the very low value of the coefficient r_{41}, it is possible to carry out a Taylors series expansions of equations 3.9. The refractive indices can then be written :

$$n_1 = n_0 + \frac{1}{2} E_x n_0^3 r_{41} \qquad \text{and} \qquad n_2 = n_0 - \frac{1}{2} E_x n_0^3 r_{41},$$

and by applying equation (3.8), the relative variation of index δn induced by an applied E-field :

$$\delta n = (n_1(E_x) - n_1(0)) - (n_2(E_x) - n_2(0)) = E_x n_0^3 r_{41},$$

that we will write as follows :

$$\boxed{\delta n = ||E_{||}|| n_0^3 r_{41}},$$

with $||E_{||}||$ is the modulus of the longitudinal component of the E-field, i.e the field co-linear to the optical wave vector.

Case of $< 111 >$ crystal cut

We therefore consider an optical plane wave probing the crystal along the $< 111 >$ direction. In this case, the particular values $\varphi = \frac{\pi}{4}$ and $\theta = \arccos(\frac{1}{\sqrt{3}})$ for the probing optical wave vector (Z axis) lead to the following matrix form of the index ellipsoid:

$$M_{<111>} = \begin{pmatrix} \frac{1}{n_0^2} + \frac{1}{3} r_{41}(-2(E_x+E_y)+E_z) & \frac{1}{\sqrt{3}} r_{41}(-E_x+E_y) \\ \\ \frac{1}{\sqrt{3}} r_{41}(-E_x+E_y) & \frac{1}{n_0^2} - r_{41} E_z \end{pmatrix}.$$

The analytical form of this ellipsoid includes the three components of the E-field vector. To decorrelate the influence of its orientation and its modulus, we define E as a function of its magnitude E_f and the spherical angles Ω and γ. The Cartesian coordinates of the E-field are expressed as a function of the spherical coordinates: $(E_x, E_y, E_z) = (E_f \sin(\Omega)\cos(\gamma), E_f \sin(\Omega)\sin(\gamma), E_f \cos(\Omega))$. After rotation, to position itself along the $< 111 >$ axis, its coordinates are expressed as follows:

$$\begin{cases} E_x = E_f \left(-\frac{\sin(\gamma)\sin(\Omega)}{\sqrt{2}} + \frac{\cos(\gamma)\sin(\Omega)}{\sqrt{6}} + \frac{\cos(\Omega)}{\sqrt{3}} \right), \\ E_y = E_f \left(\frac{\sin(\gamma)\sin(\Omega)}{\sqrt{2}} + \frac{\cos(\gamma)\sin(\Omega)}{\sqrt{6}} + \frac{\cos(\Omega)}{\sqrt{3}} \right), \\ E_z = E_f \frac{\left(\cos(\Omega) - \sqrt{2}\cos(\gamma)\sin(\Omega)\right)}{\sqrt{3}}. \end{cases}$$

The matrix of the ellipse $M_{<111>}$ can then be written:

$$M_{<111>} = \begin{pmatrix} \frac{1}{n^2} - \frac{E_f r_{41}\left(\cos(\Omega) + \sqrt{2}\cos(\gamma)\sin(\Omega)\right)}{\sqrt{3}} & \sqrt{\frac{2}{3}} E_f r_{41} \sin(\gamma)\sin(\Omega) \\ \\ \sqrt{\frac{2}{3}} E_f r_{41} \sin(\gamma)\sin(\Omega) & \frac{1}{n^2} + \frac{E_f r_{41}\left(\sqrt{2}\cos(\gamma)\sin(\Omega) - \cos(\Omega)\right)}{\sqrt{3}} \end{pmatrix}.$$

The eigenvalues associated to this matrix are:

$$V_1 = \frac{1}{6} n_0 \left(6 + \sqrt{3} E_f n_0^2 r_{41} \cos(\Omega) + \sqrt{6} E_f n_0^2 \sqrt{r_{41}^2 \sin^2(\Omega)} \right),$$

$$V_2 = \frac{1}{6} n_0 \left(6 + \sqrt{3} E_f n_0^2 r_{41} \cos(\Omega) - \sqrt{6} E_f n_0^2 \sqrt{r_{41}^2 \sin^2(\Omega)} \right).$$

The refractive indices associated are:

$$n_1 = n_0 + \frac{E_f n_0^3 r_{41}(\cos(\Omega) + \sqrt{2}\sin(\Omega))}{2\sqrt{3}} \quad \text{and} \quad n_2 = n_0 + \frac{E_f n_0^3 r_{41}(\cos(\Omega) - \sqrt{2}\sin(\Omega))}{2\sqrt{3}},$$

and by applying equation (3.8), the relative variation of index δn induced by an applied E-field:

$$\delta n = \Delta_{n_1} - \Delta_{n_2} = (\, n_1(E_f) - n_1(0)\,) - (\, n_2(E_f) - n_2(0)\,) = \sqrt{\frac{2}{3}}\, E_f\, n_0^3\, r_{41}\, \sin\Omega,$$

that we will write as follows for any γ values :

$$\boxed{\delta n = \sqrt{\frac{2}{3}}\, ||E_\perp||\, n_0^3\, r_{41}},$$

with $||E_\perp|| = E_f \sin\Omega$ is the modulus of the transverse component of the E-field. Let us notice that δn does not depend on γ, so on orientation of the field.

In this configuration, we notice that the modification of the indices is zero for an E-field along the Z axis. It is maximum for a field in the XY-plan. This optical arrangement will allow the development of a so-called **transverse sensor**, *i.e.* its axis of sensitivity will be perpendicular to the optical wave (Figure 3.6). The sensitivity vector axis will ultimately be determined by the orientation of the optical polarization state within the crystal.

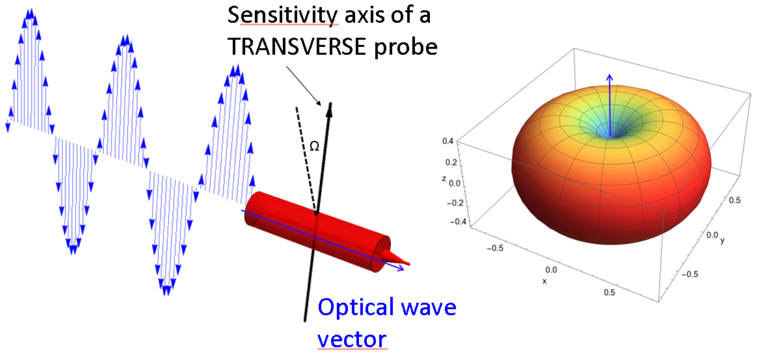

(a) (b)

Figure 3.6: a) Schematic representation of a transverse sensor using a probe beam laser along the <111> axis of the crystal. (b) Representation of the vector sensitivity for this configuration.

Case of $< 110 >$ crystal cut

We therefore consider an optical plane wave probing the crystal along the $< 110 >$ direction. In this case, the particular values $\varphi = \frac{\pi}{4}$ and $\theta = \frac{\pi}{2}$ for the probing optical wave vector lead to the following matrix form of the index ellipsoid :

$$M_{<110>} = \begin{pmatrix} \dfrac{1}{n_0^2} & \dfrac{(E_y - E_x)\, r_{41}}{\sqrt{2}} \\[2em] \dfrac{(E_y - E_x)\, r_{41}}{\sqrt{2}} & \dfrac{1}{n_0^2} - r_{41} E_z \end{pmatrix}.$$

After rotation, to position itself along the $< 110 >$ axis, its coordinates are expressed as follows :

$$\begin{cases} E_x = -\dfrac{E_f\,(\sin(\gamma)\,\sin(\Omega)+\cos(\Omega))}{\sqrt{2}}, \\ \\ E_y = \dfrac{E_f\,(\sin(\gamma)\,\sin(\Omega)-\cos(\Omega))}{\sqrt{2}}, \\ \\ E_z = E_f\,\cos(\gamma)\,\sin(\Omega). \end{cases}$$

The matrix of the ellipse $M_{<110>}$ can then be written :

$$M_{<110>} = \begin{pmatrix} \dfrac{1}{n^2} & E_f\,r_{41}\,\sin(\gamma)\,\sin(\Omega) \\ \\ E_f\,r_{41}\,\sin(\gamma)\,\sin(\Omega) & \dfrac{1}{n^2} - E_f\,r_{41}\,\cos(\gamma)\,\sin(\Omega) \end{pmatrix}.$$

The eigenvalues associated to this matrix are :

$$V_1 = \frac{1}{n_0^2} - \frac{1}{4}E_f\,r_{41}\left(\sqrt{2}\sqrt{(5-3\cos(2\gamma))\sin^2(\Omega)} + 2\cos(\gamma)\sin(\Omega)\right),$$

$$V_2 = \frac{1}{4}\left(\sqrt{2}E_f\,r_{41}\sqrt{(5-3\cos(2\gamma))\sin^2(\Omega)} - 2E_f\,r_{41}\,\cos(\gamma)\sin(\Omega) + \frac{4}{n^2}\right).$$

The refractive indices associated are :

$$n_1 = -\frac{2n_0}{\sqrt{-\sqrt{2}E_f\,n_0^2 r_{41}\sqrt{(5-3\cos(2\gamma))\,\sin^2(\Omega)} - 2E_f\,n_0^2 r_{41}\,\cos(\gamma)\,\sin(\Omega) + 4}},$$

$$n_2 = -\frac{2n_0}{\sqrt{\sqrt{2}E_f\,n_0^2 r_{41}\sqrt{(5-3\cos(2\gamma))\,\sin^2(\Omega)} - 2E_f\,n_0^2 r_{41}\,\cos(\gamma)\,\sin(\Omega) + 4}},$$

and by applying equation (3.8), the relative variation of index δn induced by an applied E-field :

$$\delta n = \Delta_{n_1} - \Delta_{n_2} = \frac{E_f\,n_0^3 r_{41}\sqrt{(5-3\cos(2\gamma))\,\sin^2(\Omega)}}{2\sqrt{2}}$$

$$= \frac{||E_\perp||\,n_0^3 r_{41}\sqrt{5-3\cos(2\gamma)}}{2\sqrt{2}},$$

δn depends here on γ, thus on the transverse orientation of the field. That we will write for $\gamma = \frac{\pi}{2}$ as follows :

$$\boxed{\delta n = ||E_\perp||\,n_0^3 r_{41}},$$

with $||E_\perp|| = E_f\,\sin(\Omega)$ is the modulus of the transverse component of the E-field.

To conclude, two configurations, $< 111 >$ and $< 110 >$ permit to measure the transverse components. $< 111 >$, is used in the development of kapteos (transverse) probes because of its independence from the orientation of the field. While in configuration $< 110 >$ is preferable in the detection of THz since we gain signal and we can play on the orientation of the field by varying the wave plates or the crystal orientation.

3.2 Real time electro-optic measurement techniques at "low" frequency (< 100 GHz)

The EO sampling by Pockels effect is really exploited since the 1980s (see Figure 3.7). But this new technique has nevertheless remained confined to research laboratories due to a two major reasons compared to conventional techniques : a real difficulty of implementation linked to the need to route a laser beam into the EO crystal acting as a sensor and the influence of temperature on the performance of the electro-optic transducer and on the remote optical fiber.

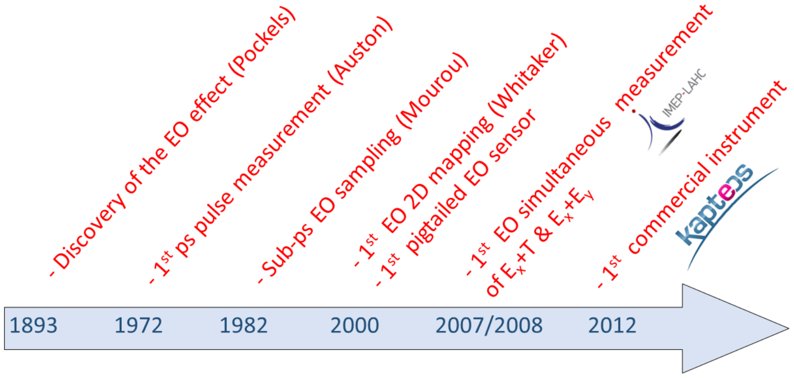

Figure 3.7: History of the exploitation of the electro-optic effect from 1893 until today.

However, this situation rapidly evolved with the appearance of the first EO fiber optic sensors at the beginning of the year 2000s [173]. It was at this time that the IMEP-LaHC laboratory launched an activity centered on the development of EO sensors through a call for tenders from the Délégation Générale de l'Armement. The history of these advances is summarized in Figure 3.7.
Two companies commercially offer optical solutions for measuring the E-field suitable at high voltage : Srico [174] and Kapteos [175]. A photograph of a Kapteos sensor is given in Figure 3.8.a.

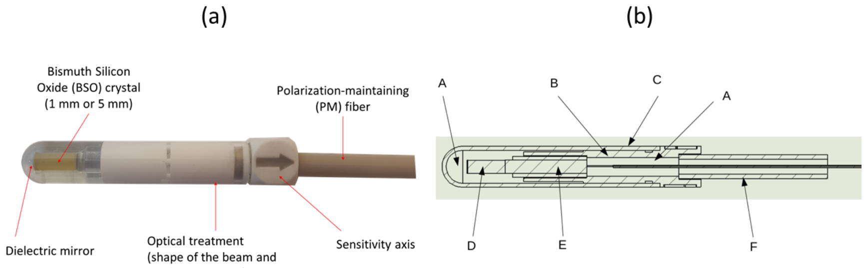

Materials	A	B	C	D	E	F
Permittivities	2.8	9	3.9	45	3.9	3.2

Figure 3.8: (a) Photograph showing the last generation of Kapteos pigtailed probe involving the transducer itself, which is an EO crystal (BSO). The sensitivity axis, which corresponds to the field component is given by the arrow. (b) Diagram showing the permittivity of the different elements making up the probe (see Appendix A).

The Kapteos company has acquired substantial experience in EO measurement since the 2010s. Real-time compensation of thermal effects was demonstrated in 2007 and then temperature insensitive measurements were proven [110, 115, 176, 177]. The first results obtained were then very encouraging. It is therefore this optical technology that is chosen and used in the part II of the work presented in this manuscript. Optical sensors offer better bandwidth, better spatial resolution and no disturbance, among other things, compared to antennas.

Kapteos EO sensor [175] (see Figure 3.8) consists of a pigtailed optical arrangement allowing a non invasive and accurate remote measurement up to more than 100 meters over an ultra-wide band in almost any location and environment (air, liquids, gases) under harsh conditions whatever the temperature. Courjal *et al.* [112] present in their interesting review recent developments over the last 10 years on invasive E-field sensors, with a highlight on the specificities of each photonic architecture. They implement the wide variety of measuring devices, among which the EO probes are distinguished by their high bandwidth potential up to THz, their minimal invasiveness and their capacity for vectorial measurements.
Data-sheet of the EO probe can be found in Appendix.

Electro-optical crystal selection criteria

The EO crystal chosen for the field measurement must allow a non-disturbing measurement and must be non-absorbent, that is to say have an extended transparency range around the wavelength. The electro-optic coefficients must be high to have a large index variation with the E-field. The crystal must also be isotropic. Indeed, this type of crystal has two advantages :
- the simultaneous measurement of two components of the E-field vector is accessible,
- the polarization of an optical wave passing through this type of crystal remains unchanged regardless of the surrounding temperature, unlike anisotropic crystals [171, 178].

Several interesting studies have made it possible to determine the most suitable crystal for our applications. Following an experimental campaign dedicated to the characterization of electro-optic crystals, **Bismuth Silicon Oxyde BSO** was identified as the best for the realization of vectorial EO probes. Beyond its intrinsic performance linked to its EO properties and its relative permittivity, this type of crystal has fewer charged inclusions compared to crystals of the ZnTe family. These space charge zones mask the field and thus limit the measurement bandwidth, in particular at low frequencies [149, 179].

Certain characteristics of the BSO are recalled in Table 3.2 resumed from [149] :

An example of an experimental setup of a real time EO measurement is schematized in Figure 3.9. The EO probe is separated by a 5 meters long polarization-maintaining (PM) fiber from the Kapteos eoSense converter (also called Optoelectronic unit). It involves firstly the DFB (distributed feedback) Laser feeding the probe. This laser provides a low noise CW optical wave at a vacuum wavelength of 1.5 μm. For the detection, a photodiode performs the linear conversion between the optical modulation induced by the field and the useful electrical signal recordable on the digital oscilloscope. This opto-electronic unit delivers finally an analog voltage proportional to the E-field component over a bandwidth spreading from 30 Hz to 30 MHz, with the upper frequency cut-off only limited by the photodiode. The optoelectronic converter measures also in real time the mean optical power in order to compensate any parasitic losses (eventually induced by temperature drift, curvature radius of the optical fibers, mechanical stress on the optical arrangement,...). The signal is recorded using a digital oscilloscope with a sampling rate of 1 GHz.

General properties	- The melting point is high (1163 K) - BSO is insoluble in water - Its density is 9.5 g/cm^3
Dielectric properties	- At low frequencies, the permittivity is 50-60 - At high frequencies, the permittivity is 40-45
Optical properties	- BSO is an isotropic crystal : $n_x = n_y = n_z = n_0 = 2.46$ @ 1.55 μm - Its transparency range extends from 0.4 to 6 μ.
Remarks	- BSO growth is under control - The BSO is available in different cuts (<111>, <110>, <100>) [180]

Table 3.2: Characteristics of the BSO. (The low frequencies correspond to the frequencies below the piezoelectric resonances, the high ones, above).

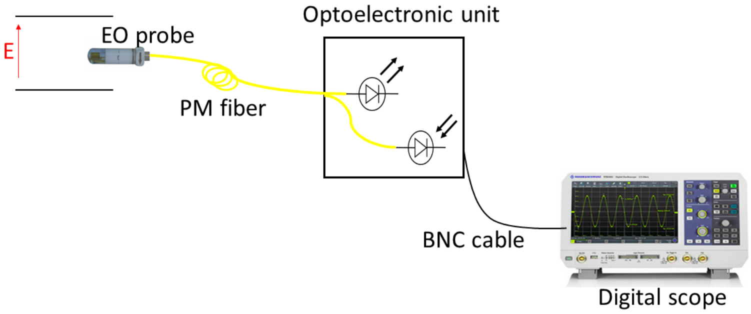

Figure 3.9: Real time EO setup.

3.3 Equivalent time electro-optic measurement techniques at "high" frequency (THz)

There is currently no electronic device with an instantaneous bandwidth much greater than 100 GHz, therefore capable of directly measuring sub-ps electrical signals. However, it is possible to characterize these ultra short signals with a "slow" measurement system using the equivalent time sampling technique.

Equivalent-time sampling makes it possible to characterize very fast signals using measurement systems whose bandwidth is much lower than that of the signal being measured. The signal must be measured at a certain time by an optical pulse via a fast physical phenomenon involving a light/E-field interaction. If this signal is periodic, this measurement can be repeated over all the periods, samples of the signal being taken at different times (see Figure 3.10).

The signal can then be rebuilt from this series of point measurements. This is only possible if the signal to be measured is perfectly periodic and if it can be synchronized with the signal used for the measurement [114]. This synchronization is easily obtained when these signals are both optically generated from a single pulsed optical beam, which is separated by a semi-reflecting plate into pump and probe beams. The pulses of the first beam generate the signal (pump beam) and those of the second beam measure the generated signal (probe beam). By delaying the optical measurement

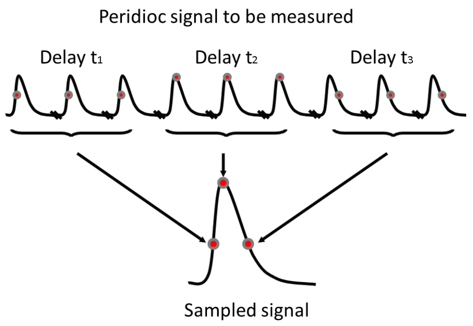

Figure 3.10: Equivalent time sampling principle.

pulse relatively to the electrical signal to be sampled, it is therefore possible to measure the cross-correlation trace of the electrical signal with the shape of the time window of the measurement. To obtain a good temporal resolution, the signal to be measured is supposed not varying too much during the duration of a measurement point. It is therefore imperative that this time window be very short compared to the variations of the signal to be measured. Only periodic signals can be sampled in this way. In our case, the time delay is obtained using an optical delay line whose spatial increment determines the time step. The measurements are therefore carried out not in real time, but in equivalent time, the correspondence of which is deduced from the spatial increment of the optical delay line [114].

This technique has been used in all of the work presented in part III and the schematic setup is shown in Figure 3.11.

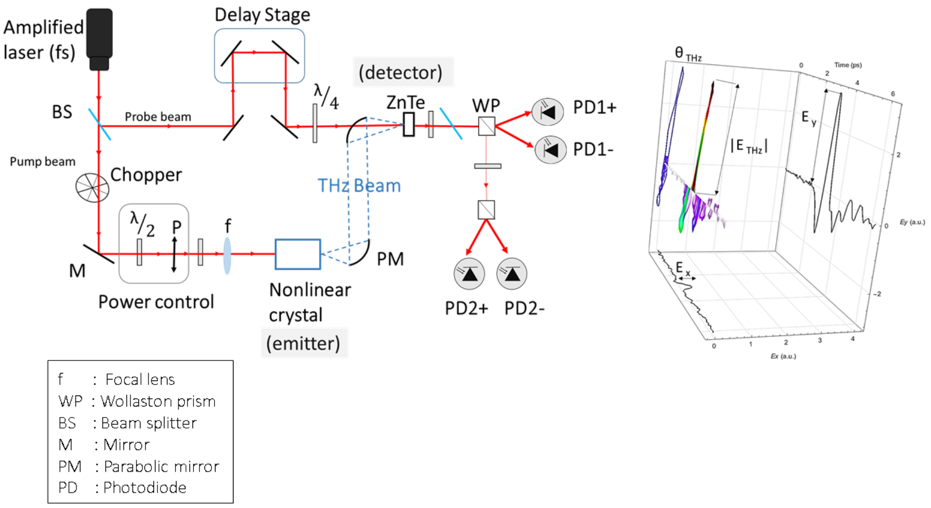

Figure 3.11: Scheme of THz pulse emission and detection in time-domain systems (TDS) setup. On the right an example of the E-field of the THz radiation as a function of time, measured by the polarization-sensitive electro-optical detection represented in the proper reference of the EO crystal (ZnTe <111>).

The nonlinear crystal has been illuminated under normal incidence by the beam of an amplified femtosecond laser chain (Coherent Libra He+) that delivers pulses of 45 fs duration, 5 mJ of energy at 800 nm, and at a 1 kHz repetition rate (laser available in our laboratory). The pump laser beam is modulated at 160 Hz a mechanical chopper, which triggers the detection lock-in amplifier. A half wave plate ($\lambda/2$) is used to define the angle of the impinging polarization state. A wave plate rotation of ψ leads to a rotation of $2\,\psi$ of the linear polarization state. The detection has been performed and recorded thanks to an EO setup : the use of a quarter wave plate($\lambda/4$) generates circular polarization in the probe beam. Thus, the THz signal induces a birefringence in a 1 mm thick $< 111 >$ ZnTe crystal, which modifies the probe polarization state to elliptical. This birefringence is read with a Wollaston prism and two balanced photodiodes. Therefore, the rotation of the ZnTe crystal is not required for optimizing the detection. A half wave plate permits to select initially the referential orientation of the balanced detection. The obtained differential signal is directly proportional to one component of the THz field vector.

Part II

Vectorial and real time characterization of plasmas by EO method

4

Filamentary discharges: Vectorial characterization of the electric field induced by dielectric barrier discharges

Sommaire

As reported in chapter 1, there has been an impressive interest in the characterization of discharges and plasma. Among all their relevant characteristics, its behavior in an E-field is a subject of major interest and one of the critical parameters to be analyzed. And as mentioned in Section 1.2.3, DBDs are non-equilibrium low-temperature discharges and constitute simple devices to generate cold atmospheric plasmas [40], partially ionized gases [41, 42]. They operate in a wide range of pressures [47, 48] in various gases [49, 50, 52, 181]. DBDs, also known as silent discharges, are characterized by the presence of at least one dielectric barrier in the discharge gap separating the electrodes [45].

In this work, the E-field is investigated in the close vicinity of a filamentary plasma produced with a DBD configuration. We focus on the spatio-temporel characteristics of the E-field. The interaction of plasma and liquid (particularly aqueous solutions) is if high interest for biomedical and biological applications where water molecules are playing a key role in the production of reactive oxygen species as well as ions and water clusters. The results will support non-equilibrium kinetic modeling of atmospheric pressure plasma involving liquids since the electron energy distribution function is directly correlated to the E-field in space and time.

Section 4.1 is dedicated to measurement configuration and experimental set-up. We demonstrate the ability of the EO transducers to provide a complete vectorial analysis of the E-field induced by the high voltage source that initiates the ionization process, on the one hand, and by the plasma itself, on the other hand. Then we are interested in studying and analyzing the E-field that surrounds the DBDs, regarding their importance and their wide variety of applications (Section 4.2). The analysis leads to the accurate determination of the breakdown voltage and the associated E-field in the vicinity of the discharge. The I (V) curve is generally measured [84], but is not sufficient for an exhaustive analysis. The real-time measurement of longitudinal and radial components of the E-field allows to extract its polarization state. Moreover, the transition from capacitive to resistive behavior is demonstrated at the breakdown field. The disturbance induced by the probe on the field to be measured is also investigated in Section 4.3. Existing measurement and evaluation strategies, together with additional new approaches have been applied and are discussed in this chapter.

4.1 Experimental setup

The experimental bench used is presented in Figure 4.1.

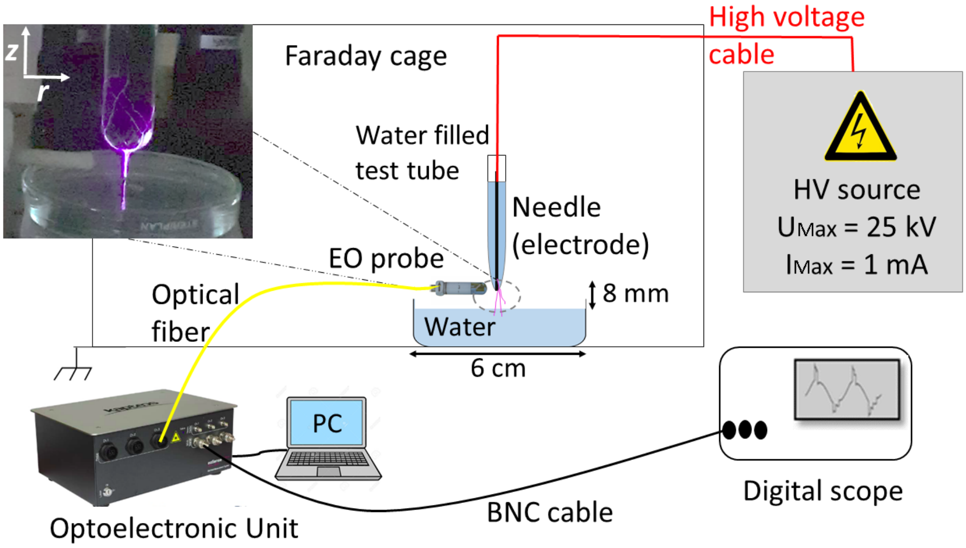

Figure 4.1: Schematic of the experimental setup constituted of an AC high voltage source, an electro-optic probe and an opto-electronic unit from Kapteos company, a digital oscilloscope, and a DBDs reactor made of electrodes immersed in water.

An AC voltage is imposed by a high voltage source to a metallic needle immersed in a test tube (diameter 1.2 cm, length 14 cm) filled with tap water, while a Petri dish (diameter 6 cm) filled with tap water is superimposed to the grounded electrode. The voltage function generator delivers a sector-synchronized AC voltage (50 Hz) whose magnitude is adjustable between 1 kVrms and 25 kVrms. These electrodes surrounded by dielectric barriers separated each other by 8 mm, constitute the DBD reactor. The E-field generated by the above described DBD reactor is then measured by using either one longitudinal EO probe, or by a pair of crossed EO probes. Note that since EO probes are polarization-sensitive along one perfectly known axis, this latter configuration (2 crossed EO probes) permits a polarimetric measurement of the E-field as described in Section 4.2. In the present case, the probes are deported by a 5 meters long polarization-maintaining (PM) fiber from the *Kapteos* eoSense converter [182]. This opto-electronic unit delivers an analog voltage proportional to the E-field component over a bandwidth spreading from 30 Hz to 30 MHz. The signal is recorded using a digital oscilloscope with a sampling rate of 1 GHz.

4.2 Experimental results: transient measurement and analysis of the field surrounding the DBD

4.2.1 Voltage threshold & simulation analysis of the DBD configuration

The front of the ionization waves generated in the DBD reactor relies intrinsically on the creation of an intense E-Field peak from which one can precisely determine the voltage threshold above which discharges occur in the reactor. In this measurement campaign, the transient evolution of the radial component E_r is measured with an EO probe placed between the electrodes (needle and dish). Figure 4.2 represents two recorded signals when the DBD reactor is powered with 16 kVrms and 18 kVrms (just below and above the threshold voltage).

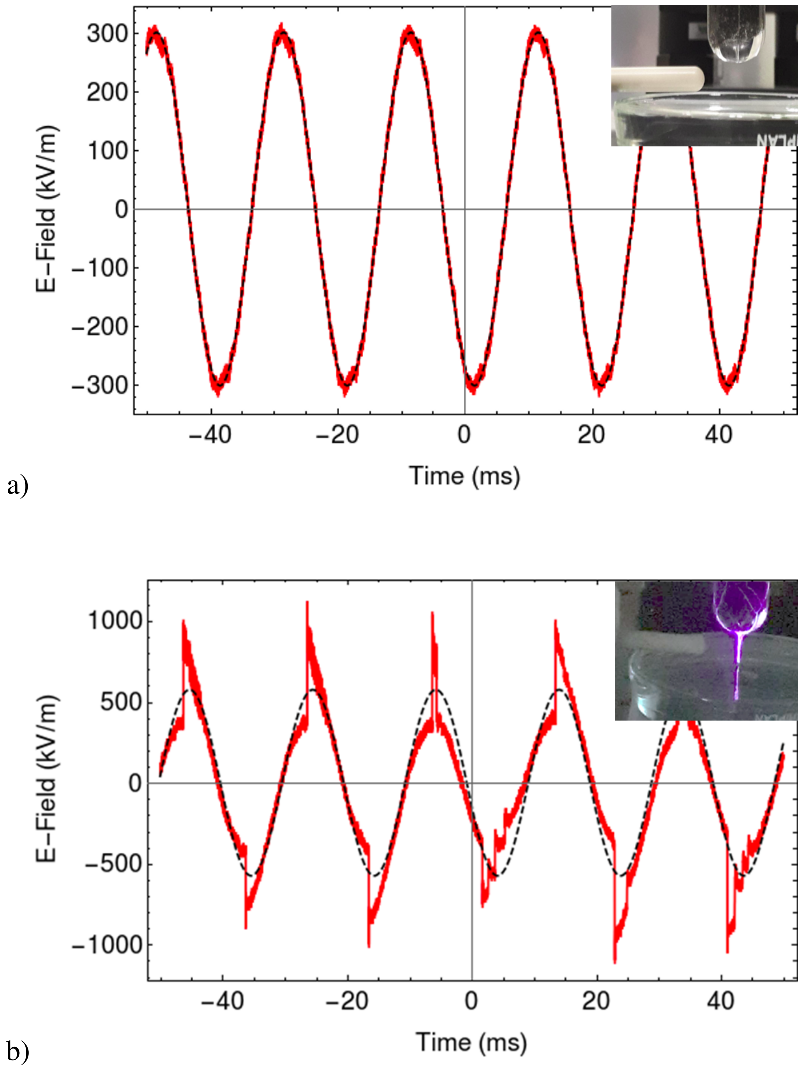

Figure 4.2: Temporal evolution of the radial E-field a) Result for a feeding voltage of 16 kVrms and b) Result for a feeding voltage of 18 kVrms. The E-Field magnitude is shown with a continous red line curve. The sine fit curve is represented by a black dash line.

Before threshold, the radial field is a sinusoidal signal such that voltage and field are proportional each other with a maximum field strength of the order of a few 100 kV/m. **Above threshold, a dramatic increase of the field** is observed and the temporal profile becomes no more linear with the applied voltage. The field reaches a value of the order of 1 MV/m.

Figure 4.3 presents peak values of measured E-field versus the applied voltage with 1 kVrms increment, from 1 kVrms to 25 kVrms. Up to 16 kVrms the measured component behaves linearly with the applied voltage as expected in the absence of DBD. It has been extracted versus the applied voltage, incrementally set from 1 to 25 kV. As shown by Figure 4.3, up to 16 kV the measured component behaves linearly with the bias voltage as predicted by electro-static simulations (Figure 4.5).

Above 16 kVrms, corresponding to a field greater than 1 MV/m in between the electrodes, the peak value dramatically increases, being the signature of discharge-induced radial component (see blue curve of Figure 4.3 and photo on the top left of Figure 4.1). Black dots in Figure 4.3 represent the magnitude of the radial field at 50 Hz at different voltage values. These latter ones exhibit also a non-linearity. This graph is divided into 2 parts: from 0 kVrms to 16 kVrms, where the field increases linearly and gradually to reach a value of 300 kV/m and suddenly above 16 kVrms there is a jump to reach a value twice larger than before (600 kV/m) and remains approximately constant beyond this voltage value.

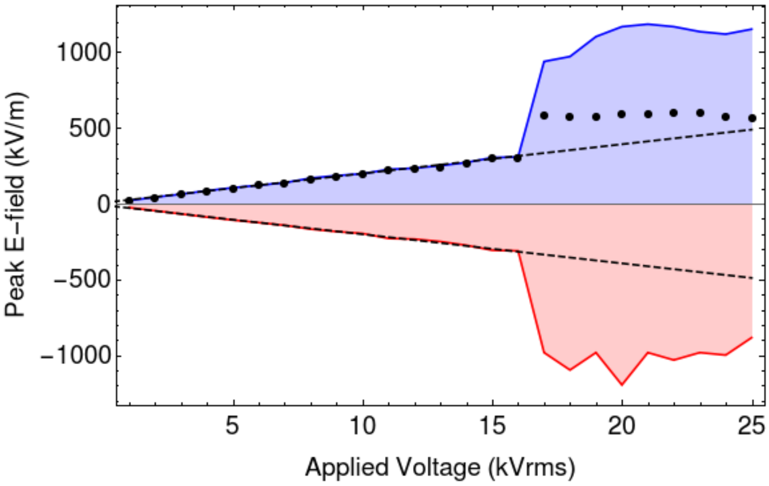

Figure 4.3: Peak E-field induced as a function of the applied voltage. In blue: positive peak values, in red: negative peak values, dashed lines linked to the fitting curves of the linear zone before threshold. Black dots represent the amplitude of the radial electric field at 50 Hz as a function of the applied voltage (Amplitude of the sine curve).

After the threshold, the amplitude of the 50 Hz signal remains almost constant (see black dots of Figure 4.3). This means that the appearance of the filamentary discharges, for a given threshold value, limits the increasing of nominal field with the increasing voltage. As the 50 Hz field strength response is quite flat between 17 kV and 25 kV, this means that the DBDs appears with a quite good reproducibility, at the same breakdown voltage or breakdown field. Considering the geometry of the DBD reactor, and regarding previous results, a voltage threshold of 17 kVrms separates what we call in the following sections, the "low voltage" (no discharge) and the "high voltage" (with discharge) regimes as evidenced in Figure 4.3.

Below the threshold, the measured E-field is a 50 Hz sine wave signal proportional to the applied voltage, while above the voltage threshold, spikes appear in the sine wave leading to harmonic distortion. **The harmonic analysis, using numerical Fast Fourier Transform, is also proposed as a quantitative signature of the development of the ionization wave accross the gap of the DBD reactor.**

This discharge-induced behavior is clearly shown in Figure 4.4, which exhibits the harmonic distortion in function of the applied voltage. The total harmonic distortion (THD) is here defined up to the 9th harmonics of the signal and calculated through the following equation :

$$THD_9 = \frac{\sqrt{\sum_{i=2}^{9} V_i^2}}{V_{50\,\mathrm{Hz}}}, \tag{4.1}$$

where V_i corresponds to the magnitude of the ith harmonic of the distorted 50 Hz sine wave.

This measurement concerns the analysis of transient signals and discharges initiated by the needle. This analysis can be carried out thanks to the flat response of the EO system over the frequency bandwidth of interest.

The signal spectrum is then strongly modified with a significant enhancement of spectral components exceeding the fundamental frequency of 50 Hz, induced by the discharge. Indeed, the

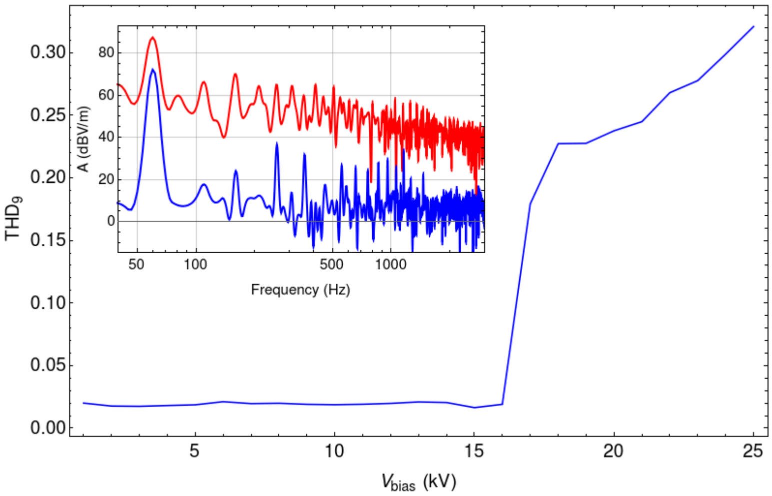

Figure 4.4: Total harmonic distortion in function of the applied voltage.The inset shows the spectral distribution of temporal waveforms for applied voltage of 5 kV (blue curve) and 20 kV (red curve).

calculation shows a THD of about 2% below the threshold, which corresponds to the THD of the high voltage source. This THD exceeds more than 22% over the threshold and reaches even 32% for an applied voltage of 25 kVrms.

The above-described behavior can be predicted by an electrostatic simulation as long as we stay in the low voltage regime (in the absence of discharge). The DBD reactor, described in section 4.1 has been simulated with the finite element method (using QuickField software) and meshed with more than 300000 nodes. The result is presented in Figure 4.5.

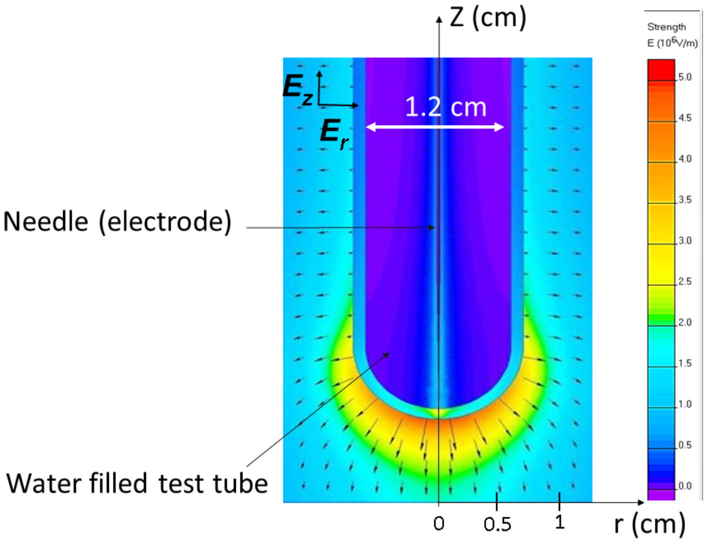

Figure 4.5: 2D axisymmetric simulation. Spatial distribution of the electric field with the structure under test at 17 kVrms. The vertical axis is the temporal evolution of the field.

The dielectric permittivity and geometry of all constituting elements are considered in this virtual reactor (metallic needle and ground plate, glass tube, Petri dish, air and water). Under the conditions corresponding to the experimental parameters of Figure 4.1, the model predicts an appearance of the plasma when the electric field value is greater than the breakdown value in the air (3 MV/m [183]). The measured threshold of DBD appearance at 16.5 kVrms is in agreement with the numerical expectations shown in Figure 4.5, with an expected threshold of 17 kVrms.

Figure 4.6 exhibits the I(V) curve of the whole system (high voltage source + discharge reactor). It exhibits a resistance-like behavior (linear I(V) curve) from 0 to 25 kVrms. The resistance value is inversely proportional to the slope of the linear fitting curve (red lines in Figure 4.6) and equal to 43 MΩ. The system is obviously not an open circuit but the remaining current, known as leakage current is explained by non ideal lumped electrical elements that constitute the high voltage source.

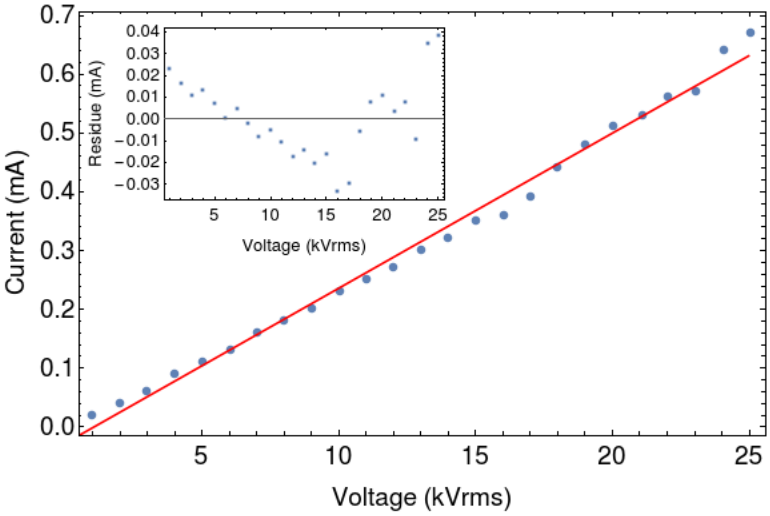

Figure 4.6: Linearity of the current versus the applied voltage. Blue curve correspond to the experimental value, red one is the fitting curve. The inset shows the residue of the difference between fit and measurements, exhibting a standard deviation of 0.017.

Despite the presence of discharge channel at high voltage regime (> 16 kV), the slope of the i-v curve remains unchanged, meaning that do not provide any current : it is a dielectric barrier discharge.

4.2.2 1D mapping of the radial field

Temporal evolution of the radial electric field around the discharge is measured for different positions of the probe. Measurements have been performed every 5 mm from 0 cm (within the discharge) to 10 cm away (cf Figure 4.5) along the r axis, where the probe is placed between the 2 electrodes. Applied voltage has been set to 23 kVrms in order to generate discharge in between the electrodes of the DBD reactor. The raw measurement is presented in Figure 4.7, with a representation of the temporal traces for each position of the probe.

Two different zones can be clearly observed. From 0 cm to 2 cm, this is the area associated to the intense electric field, with a typical signature of the ionization waves (see red and purple zone in Figure 4.7). After 2 cm, for remote distance from the discharge, only contributions of the Laplacian field (radial field induced by the needle) are seen.

A further analysis is proposed in Figure 4.8. It shows the spatial distribution of the radial component and their maximum. Experimental results are represented and compared with analytical calculations and numerical simulations.

Note that the theoretical equation is given by calculation of the spatial derivative of the potential between a point-plane configuration (in two dimensions), based on the electrostatic equations. E(r,z) writes :

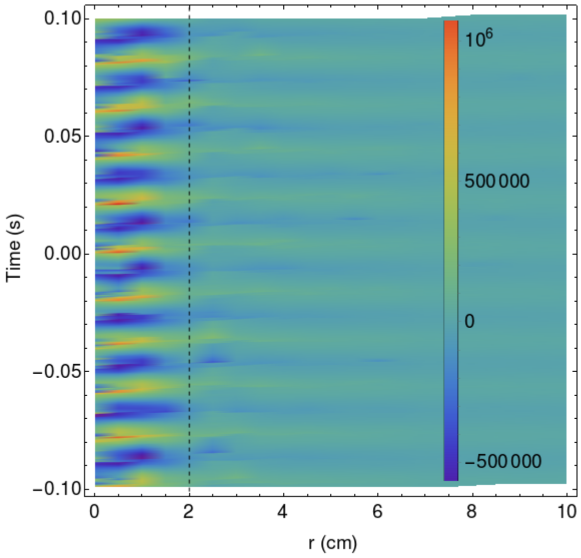

Figure 4.7: 1D mapping of the radial component of the field at 23 kVrms.

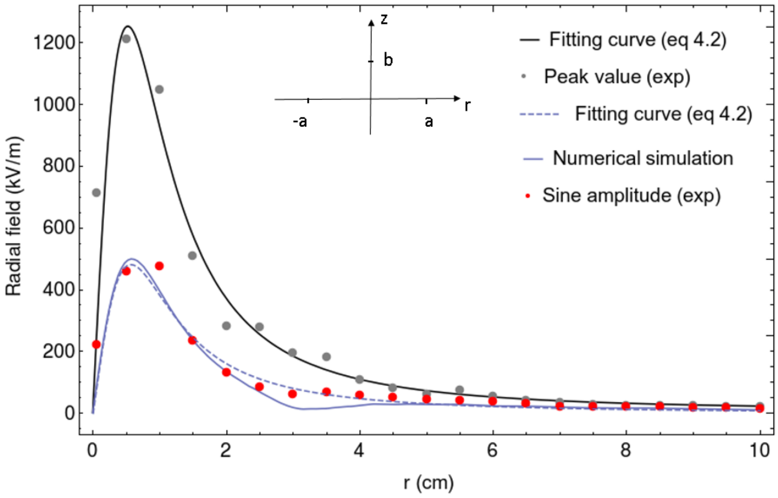

Figure 4.8: Spatial distribution of the radial component of the field. Data obtained at 23 kVrms and each 5 mm.

$$E(r,z) = \frac{2r}{(r^2+(z-b)^2)^{3/2}} + \frac{\frac{r-a}{\sqrt{(r-a)^2+z^2}}+1}{\sqrt{(r-a)^2+z^2}+r-a} - \frac{\frac{r+a}{\sqrt{(r+a)^2+z^2}}+1}{\sqrt{(r+a)^2+z^2}+r+a}, \quad (4.2)$$

a is the radius of the plane, as indicated in the inset of Figure 4.8 and b is about 8 mm, it corresponds to the point-plane distance as shown in Figure 4.1. When a tends to infinity it gives:

$$E(r,z) = \frac{2r}{\left(r^2+(z-b)^2\right)^{3/2}}. \quad (4.3)$$

In Figure 4.8, zero corresponds to the position of the DBD which shows no radial field (the field is here vertical). Then we move the probe, each 0.5 cm, from the DBD, and the electric field reaches a value of 500 kV/m at 1 cm away from the discharge. And by moving further and further away from the discharge, the field gradually decreases and vanishes as expected. A good agreement between experiment, theory and simulation, for field distribution and absolute values, is observed.

4.2.3 Additional experiment campaigns involving two EO probes

Contribution of needle and DBDs to the field

The goal of the below-described measurement campaign is to identify the E-field from the filamentary discharge with the Laplacian field from the needle electrode, on the one hand, within the electrodes gap, on the other hand. This would lead to measure the E-field contribution of discharge generated by the DBD reactor configuration.

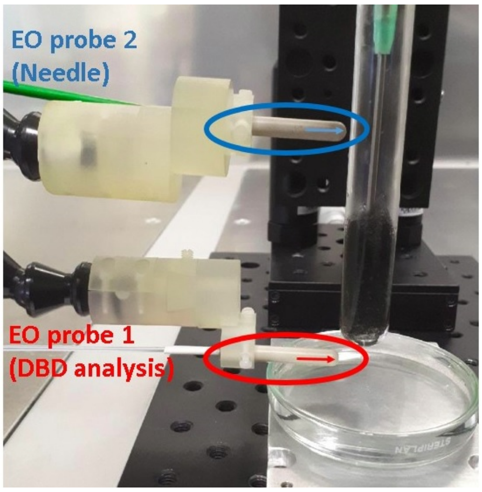

Figure 4.9: Representive photograph showing the two EO probes with their sensibility axis.(colored arrows indicated on the probe packaging).

For that purpose two separated longitudinal EO probes (*i.e.* sensitive to the E-field component aligned with the probe axis), were positioned such as they both give access independently to the radial component of the radiated E-field (see Figure 4.9).

In such configuration (see Figure 4.9), probe 2 provides the applied AC voltage, while probe 1 leads simultaneously to the knowledge of the E-field in between the electrodes. Such experimental configuration has led to the signals presented by Figure 4.10.a (in absence of discharges) and 4.10.b (with discharges). According to Figures 4.10, the signals delivered simultaneously by the two EO probes, both calibrated to get the absolute value of the E-field, depend on the magnitude of AC voltages applied to the DBD reactor. For relatively low voltage (Figure 4.10.a) the signal measured within the electrodes gap (blue curve) has a lower amplitude than the one radiated from the needle (red curve). Indeed, taking into account the E-field lines and strength shown by the simulation (see Figure 4.5), it is obvious that the radial components measured by both probes, is smaller in between the electrodes gap than laterally close to the needle. This is no longer true when high voltage is applied to the DBD reactor as shown by Figure 4.10.b, meaning that the discharge filament propagating across the gap increasing virtually the needle length. The outcome of the electrostatic simulation of a filamentary conductive channel is in agreement with the results presented in Section 4.2.2.

In addition, to the discharge induced disturbances above described, one notices that the radial components simultaneously measured by the two EO probes are in phase in high voltage regime while they are in quadrature at a lower voltage (below voltage threshold). This is explained by considering the electrical equivalent circuit of the discharge reactor. Indeed, **without discharge, the reactor is mainly a capacitor presenting a pure imaginary impedance. In turns, this**

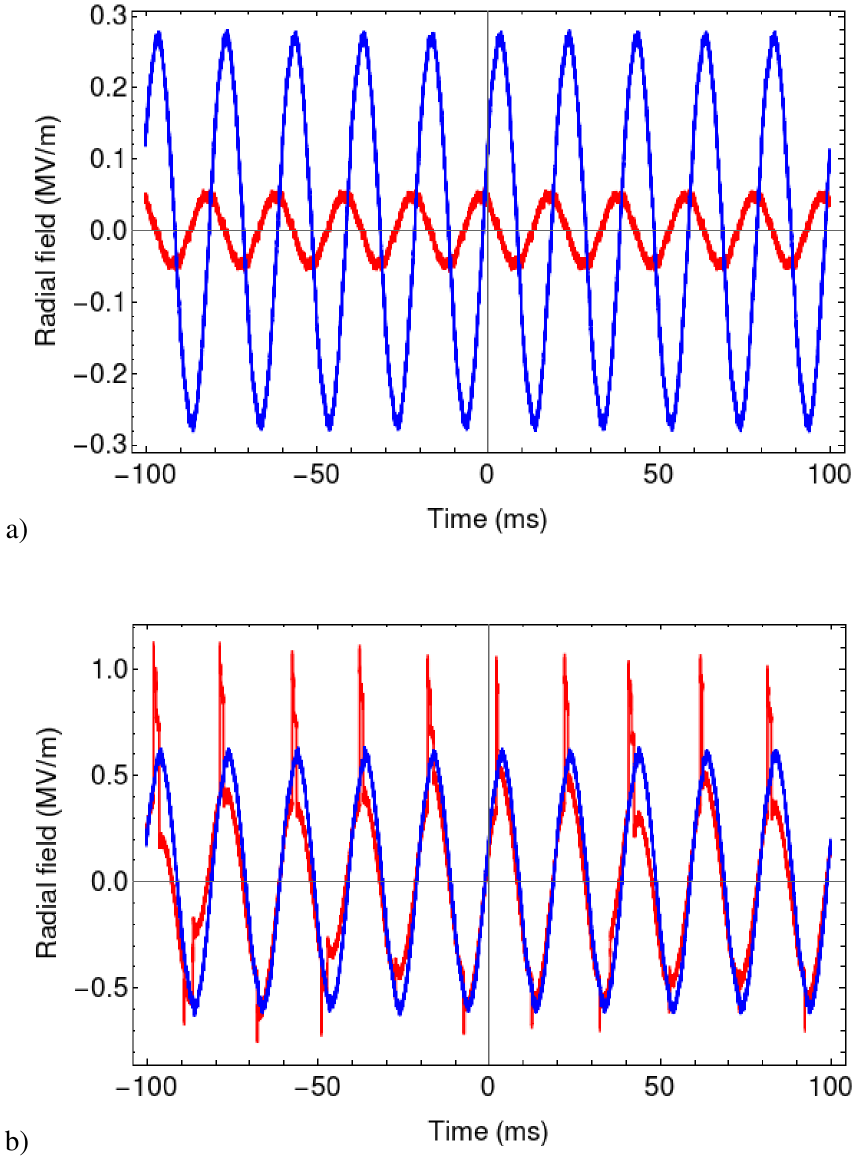

Figure 4.10: Temporal evolution of the radial field. Red and blue curves correspond to probe 1 (closed to DBD location) and probe 2 (higher position, closed to the top of the needle), respectively. a) Result for a feeding voltage of 11 kVrms. b) Result for a feeding voltage of 22 kVrms.

capacitive reactor at low voltage introduces a $\frac{\pi}{2}$ phase shift in between the applied voltage measured by the EO probe 2 (blue curve), and the E-field measured by probe 1 (red curve). In high voltage regime it is different (see Figure 4.10). When the applied voltage is high enough to initiate a breakdown, a conducting channel is set from one electrode to the other. **This channel is electrically equivalent to a conducting wire whose resistance depends on the characteristics of the DBD reactor (type of barriers/target, dielectric properties and shape of the inter electrodes media...)**. The reactor turns mainly into a resistive equivalent circuit presenting a real impedance: almost no phase shift is seen between red and blue curves of Figure 4.10.b.

Consequently, as the E-field radiated by a wire-equivalent discharge aligned from the needle tip to the ground is mainly radial, the peak observed in Figure 4.10.b originate from the discharge. This support the hypothesis made in section 4.2.3.

Polarimetric analysis of the field

Due to excellent rejection of orthogonal E-field components to the sensitivity axis of the one probes, a real-time polarimetric analysis can therefore be performed. **The synchronized acquisition of the radial and longitudinal components, (E_r and E_z like shown in Figure 4.11), gives access to the E-field vector and its temporal evolution leads in turn to its polarization state**. The inset of Figure 4.11 gives a photography of the two probes.

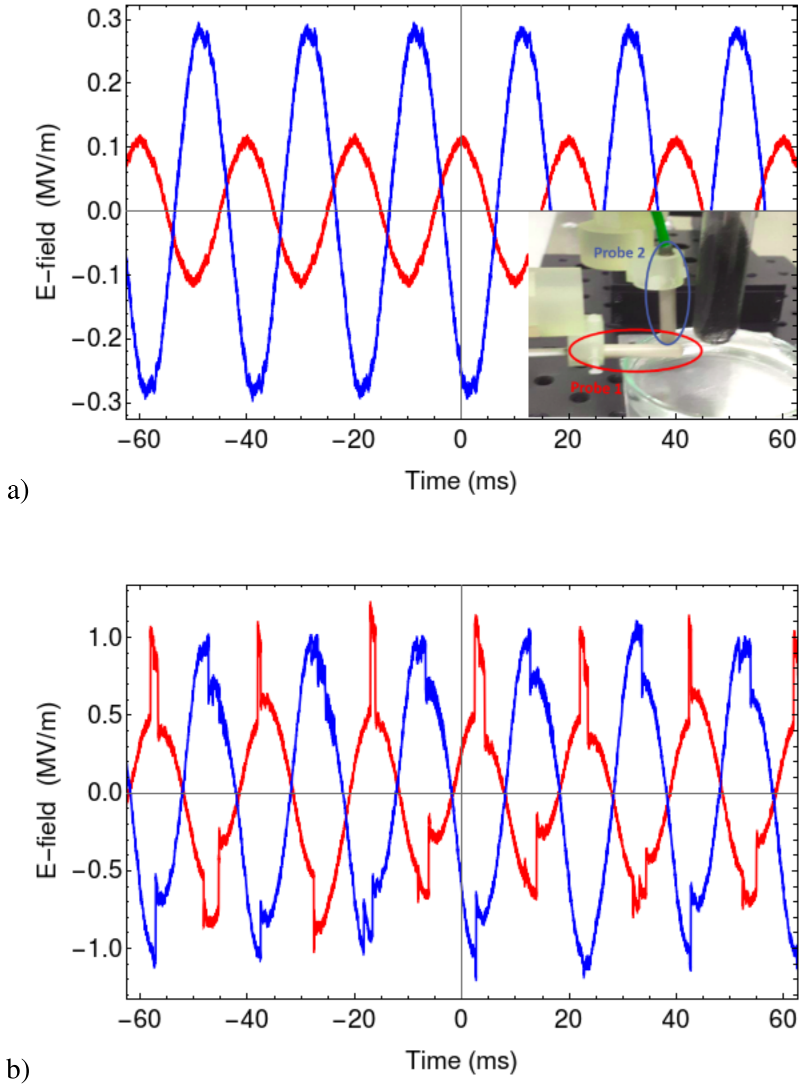

Figure 4.11: Temporal evolution of the two components of the field. Red and blue curves correspond to E_r and E_z, respectively. a) Result for a feeding voltage of 10 kVrms. b) Result for a feeding voltage of 23 kVrms.

Figure 4.11 gives some examples of temporal measurements required to obtain the polarization state of the field in between the needle and the ground plane. Two applied voltage, below and above the threshold, are investigated. Under 16 kVrms, a phase shift of $\sim \pi$ is observed between E_r and E_z. Probe 1, with its sensitivity axis along E_r is located just below probe 2 (in the capacitance area, just below the bottom of the electrode under voltage). This position is clearly chosen to improve the detection of DBDs, which dramatically influence E_r. When the applied voltage (here 23 kVrms) exceeds the threshold, one can notice that the appearance of DBDs induces a phase shift between E_r and E_z (output signal and probe direction are correlated). Once again, concerning the E_r component, a voltage multiplied by a factor of two leads to field values multiplied by 5, due to the contribution of DBDs induced charges.

Another representation is proposed in Figure 4.12 for the synchronized two-component measurement.

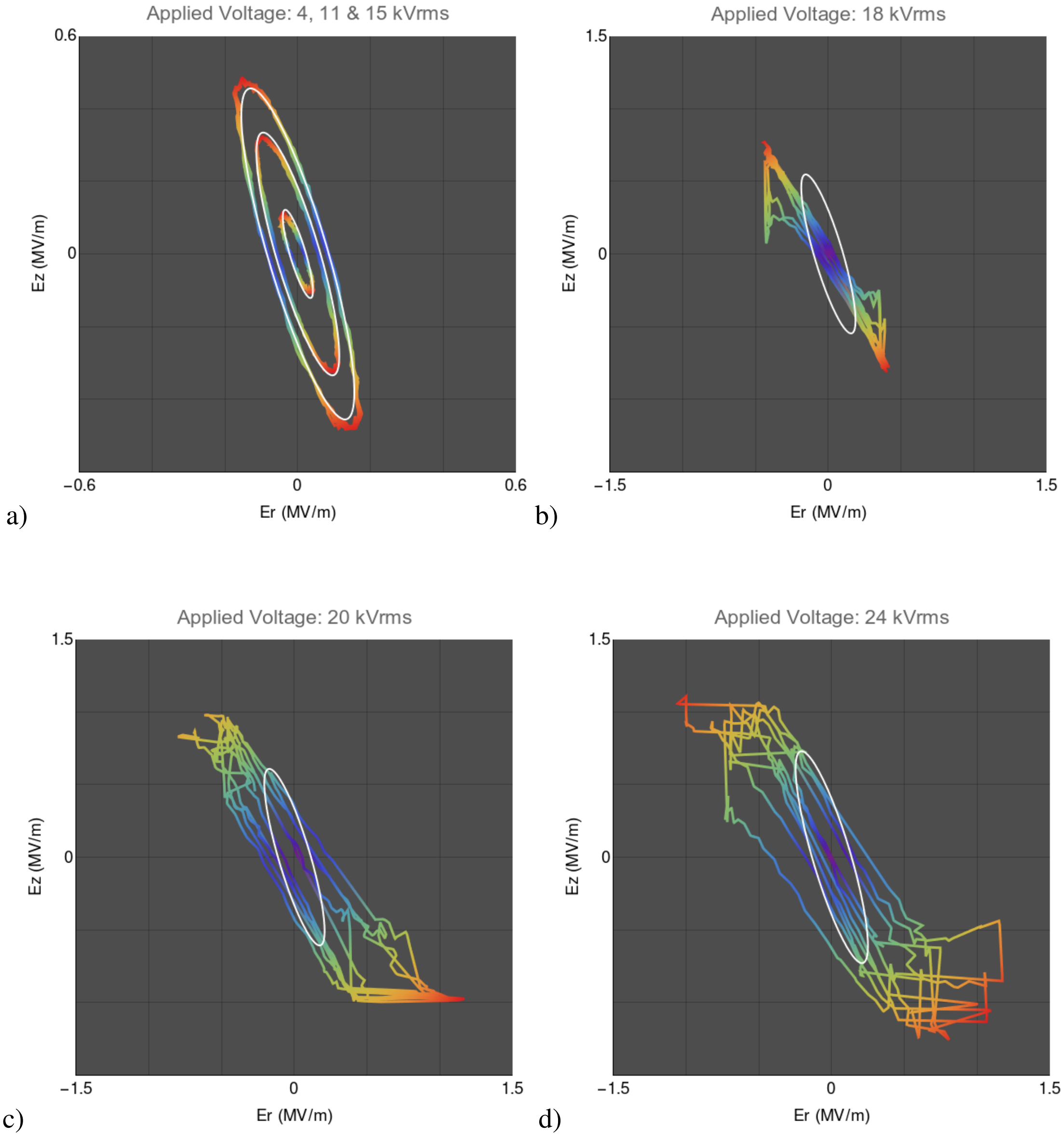

Figure 4.12: Polarimetric trace of the E-field vector calculated from the measurements of temporal E_r and E_z for an applied voltage of a) 4, 11 and 15 kVrms, b) 18 kVrms, c) 20 kVrms and d) 24 kVrms and their fitting ellipses (in white).

Figure 4.12.a corresponds to configurations with too low voltages for DBD generation. Due to the phase shift between the two eigen components of the field, the polarimetric Figures describe ellipses. This elliptical shape of the field pattern is mainly vertical due to the location of the measurement (in between the two electrodes). Three different voltages are here considered and the associated obtained ellipses are proportional to each other. Their ellipticity remains the same and their size are linearly linked to the feeding voltage. After the threshold, we can notice a dramatic difference between the signature with and without DBD. Once the breakdown has occurred, there is no ellipsoidal behavior, the shape is defined by several almost straight lines (see blue and green zone of Figure 4.12.b, 4.12.c and 4.12.d). This illustrates a proportional link between E_r and E_z,

with linear coefficients depending slightly on the considered period of the temporal waveform. The slope $|E_z/E_r|$ ranges from 0.9 to 1.6. Nevertheless, a comparison between the 3 polarization states above 17 kVrms clearly shows that the higher the voltage is, the wider is the space between the straight lines. This can be explained by the fact that for a high value of applied voltage, the instantaneous required field strength for the generation of ionization wave differs dramatically from one period to another. Moreover, the higher the voltage is, the higher is the dispersion for the discharge location in the $\{E_r, E_z\}$ space (see orange and red zone of Figure 4.12.b, 4.12.c and 4.12.d). Finally, white ellipses (linearly scaled from measurement without DBD at 14 kVrms) have been superimposed to the actual polarimetric measurement to easily identify the qualitative and quantitative influence of the DBDs themselves on the field pattern and defined by :

$$E_r = A_{14} \cos(\omega t) \qquad \text{and} \qquad E_z = B_{14} \cos(\omega t + \phi),$$

where A_{14} and B_{14} are the relative components for the ellipse at 14 kVrms.

For lower values of the field strength (Figure 4.12.a), E_r increases linearly together with E_z. The slope $|E_r/E_z|$ ranges from 0.62 to 1.16. The different color from blue to red presents the low to the high value of the E-field. One notices a significant difference between the signature with and without discharge.

4.3 Influence of the probe on the DBD behavior

The latest results concern the analysis of the **probe's ability to measure the E-field**. This measurement has been achieved once again by using two EO probes.

First, the 2 probes located near the DBD (between the tube and the Petri dish) but separated with an angle of 90° like shown in the inset of Figure 4.13.

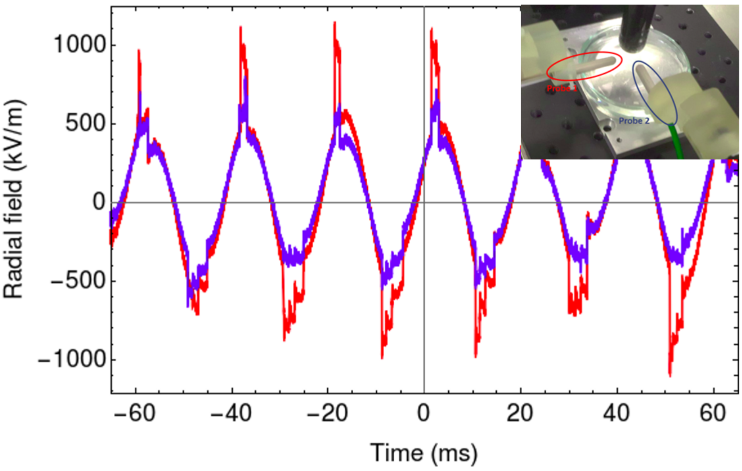

Figure 4.13: Temporal evolution of the radial field using 2 EO probes placed in the same radial distance with different orientation, closed to the DBD, like shown in the photograph inset. The feeding voltage is 25 kV.

Figure 4.13 shows us the temporal traces of the radial component E_r in two different radial positions (see inset of Figure 4.13). In Figure 4.13, the two signals are quiet similar (we have about the same sine amplitude and same phase). Taking into account the geometry of the filamentary discharge, this explains the difference in amplitude. **We can therefore conclude that regardless**

of the orientation of the sensor, at a given position the same radial field can be measured.

Furthermore, we have performed the measurement of the radial component with one single probe (probe 1). Then, we have mounted a second longitudinal probe onto the fist one (probe 2) like shown in the inset of Figure 4.14. We have perform the acquisition of the signal from the two probes (in red and in blue). The result is given in Figure 4.14.

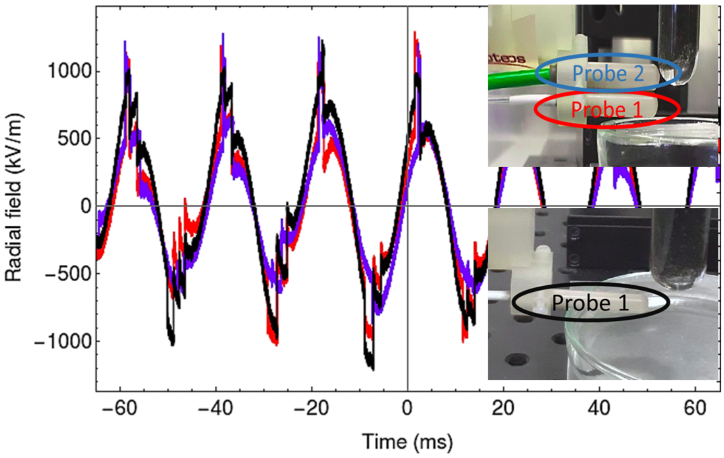

Figure 4.14: Temporal evolution of the radial field using 2 EO probes placed on the same holder. The feeding voltage is 25 kVrms.

The Figure 4.14 shows the three temporal traces measured by probe 1 and probe 2. As can be seen on the previous graph, the red and black curves (corresponding to probe 1 with and without probe 2 respectively) are quite similar, which means that the presence of one probe glued on top of the other (here probe 2 (blue curve)) does not significantly influence the measuring probe (probe 1). The blue signal measured by probe 2 is a little different with weaker negative discharges, but the measurement is made at another place above probe 1 and this is quite normal (we do not have the same position). **We can therefore conclude that one probe has no impact on the second.**

4.4 Conclusion

In this chapter, we have used EO probes to perform a comprehensive analysis of the E-field induced by a filamentary discharge in a DBD configuration. The measured threshold for discharge breakdown generation is determined and it is in good agreement with the electrostatic simulation. A quantitative assessment of nonlinear behavior between the field and the applied voltage is demonstrated. Moreover, the real-time evolution of the two eigen field vector components induced by the high voltage source and the ionization waves propagating within the electrodes gap of the DBD reactors has been carried out. A specific polarimetric signature of filamentary discharge is here identified.

5

Vectorial analysis of the electric field induced by a cold atmospheric pressure plasma jet

Sommaire

Atmospheric-pressure plasmas jets have recently become a topical field of research due to their diverse and their many advantages of their uses in the field of plasma medicine [184–187], sterilization [188–190], biomedical [68, 191–193], agriculture [194–196] and industrial [11, 197, 198], the cold atmospheric pressure plasma jet (CAPPJ), also called non-thermal plasmas (NTP), attracted significant attention. Different jet configurations and feedings bring different plasma characteristics [199] such as DBD (ring-ring) [200], DBD with single charged ring [201], coaxial [202], pin-to-plane [203, 204] and different driving voltage profiles such as sine (10-200 kHz range) [200, 201, 205], RF [205], repetitively pulsed [179, 202, 204], self-pulsing DC [203]. The CAPJs are usually generated with a capacitive coupled dielectric barrier discharge (DBD) and in many different noble gas, usually helium or argon, flowing into a dielectric tube [199, 206–210], while the electrodes are supplied by AC or pulse high-voltage. Indeed, at atmospheric pressure, these CAPPJs generate plasma plumes which propagate over a few centimeters in a free atmosphere where they can be used for direct treatment regardless of the size of the objects to be treated in particular in biological sectors, which is harmless to humans due to its low voltage and can be used clinically [211]. One of the prerequisites for biomedical applications, based on the direct interaction of plasma with living tissues or cells [212–214] is that the diagnosis of the E-field delivered by the plasma jets has so far been quite limited. Therefore, knowledge of the main plasma parameters is of utmost importance for the understanding and control of these devices. Another major challenge is to electrically characterize CAPPJ with respect to applied voltage and frequency to understand the dynamic behavior of discharge [215] to achieve high temporal and spatial resolution. It has been shown that atmospheric-pressure plasma jet discharge could be divided into three parts: (1) inter-electrode gap discharge - usually dielectric barrier discharge; (2) discharge in the dielectric tube; and (3) discharge into the jet plume [208, 214]. Electric field measurements in this type of discharge are infrequent due to the associated experimental difficulties. Nevertheless, the amplitude of the electric field is of paramount importance for experimental and theoretical work on plasma jets and their applications. It has been shown that the electric field may be responsible for various effects observed in experiments on biological samples.

In plasma physics, in low ionization transient discharges, such as plasma jets, the electric field is the driver of the discharge and its amplitude is the central component which determines its behavior and its charge production, hence the need of its measurement, for the community plasma, whatever the experimental conditions and the measurement medium.

This chapter focuses is on the spatially and temporally resolved measurements of the E-field associated to a plasma working under atmospheric pressure condition inside long insulating quartz tube through an electro-optical method. The EO transducer provides a detailed characterization the E-field vectorial behavior induced by the high voltage source that initiates the ionization process, on the one hand, and by the plasma itself, on the other hand. Interest in the characterization of E-field in plasma jets has recently increased [216–218] due to the potential role of E-field in biological mechanisms [219] and the impact of the action E-fields on cells [220].

Sylvain Iseni has already studied in his very interesting paper [221] the evolution of the electric field with the EO technique. This technique takes advantages to measure the vector E-field. Cold atmospheric pressure plasma jet (CAPPJ) has been generated by a high-voltage power supply (amplitude of 6 kV) at a fixed frequency of 18 kHz.

This chapter is divided into three sections : Section 5.1 presented the development and experimental setup, including the EO measurement bench and the APPJ device, while Section 5.4 presents also the calibration of the EO probe, required for the absolute measurement of the E-field vector components. Moreover, Section 5.3 provides additional results linked to the disturbance induced by the probe itself on the field to be measured. The ionization wave propagation and the polarimetric pattern are analyzed and discussed.

5.1 Experimental setup

The experimental apparatus is depicted in Figure 5.1. The cold helium atmospheric pressure plasma jet (He-APPJ) is generated in a dielectric barrier discharges (DBD) configuration.

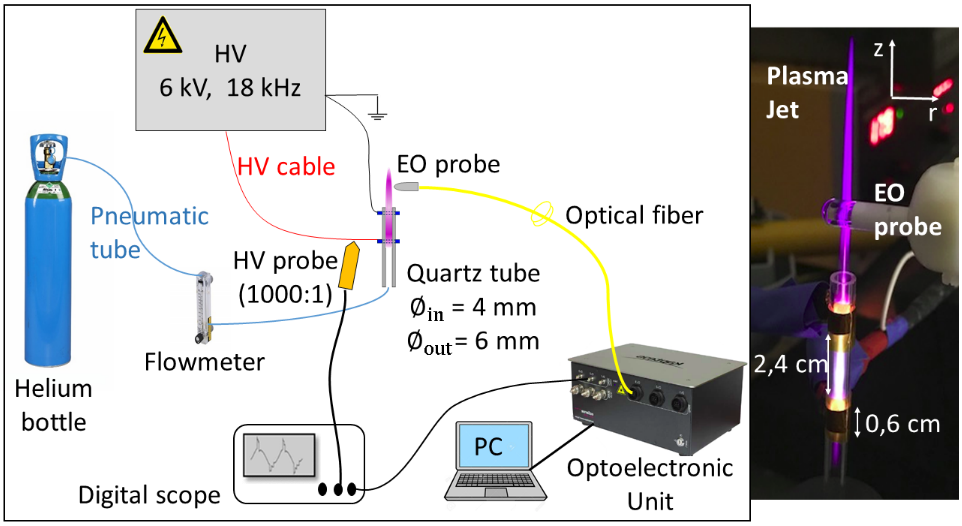

Figure 5.1: Schematic of the experimental setup: On the left side, the whole experiment setup. On the right side, photograph of the APPJ configuration, with the EO probe used for the E-field measurement.

As shown on the left side of Figure 5.1, a gas bottle, delivering a helium gas (Alphagaz 1, Air Liquide) is connected to a flow meter. The flow rate of about 2 L/min, leads the mean gas flow velocity, within the tube of about 2.65 m/s. The gas flows into a quartz tube of 4 mm diameter on which two ring-copper electrodes of 0.6 mm are separated by a distance of 24 mm. The grounded electrode is 35 μm thick is wrapped around the outer tube surface. The powered electrode is supplied by sinusoidal high voltage (amplitude of 6 kV at a fixed frequency of 18 kHz. For the electrical measurements, a TESTEC (TT-HVP 15HF) high voltage probe was connected to the bottom wrapped electrode. The attenuation ratio of the voltage probe is 1000:1. The electric field measurements are carried out with an electro-optic sensor (eoProbe) commercialized by KAPTEOS company (detailed in [111, 222, 223]). The probes are separated by a 5 m long polarization-maintaining (PM) fiber from the KAPTEOS eoSense converter. This opto-electronic unit delivers an analog voltage proportional to the E-field component over a bandwidth spreading from 30 Hz to 30 MHz. The useful temporal waveforms of the voltage and the field are recorded with a fast digital oscilloscope with an instantaneous bandwidth of 70 MHz (and a sampling rate of 1 GHz). All the acquired waveform are triggered using the voltage signal.

5.2 Specific calibration of the EO probe

In order to perform an absolute measurement of the E-field strength, the EO setup requires to be calibrated using an electric field applicators that is called "eoCaL". eoCal can calibrate any EO probe in any medium (air, gas or liquid) up to 10 GHz for measurements in air. They have been specially designed for EO probe and ensure the correct configuration of the eoSense system with regard to the measurement conditions that are yours. We can check the data sheet in appendix B.

For calibration, the probe is placed in between two parallel electrodes (see Figure 5.2, separated by 40 mm and fed by a synthesized voltage waveform. This to properly generate an homo-

geneous field vector. The standard deviation of the field strength distribution in the probe location has been measured and is weaker than 0.2 dB. The frequency bandwidth of this field applicator reaches more than 20 MHz.
Figure 5.2 resumed the setup done in the laboratory. This specified calibration is done in order to determine the Antenna Factor (AF) of the probe.

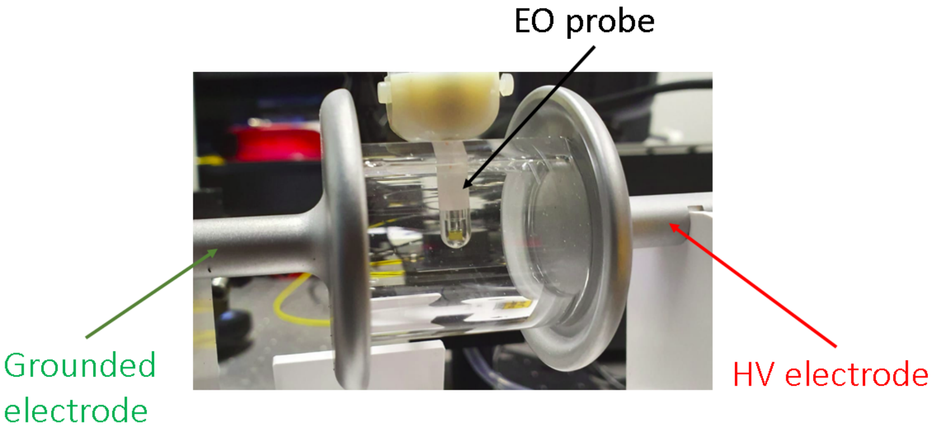

Figure 5.2: Specific calibration of the EO probe using a Kapteos eoCal for determining the antenna factor (AF).

It is important to remember the link between the signal obtained and the value of the E-field. This relationship is the AF given by the eoSense instrument and is determined by a calibration of the probe used. This AF can be expressed in m^{-1} (AF_{lin}) or in dB.m^{-1} (AF_{dB}). The antenna factor is determined by prior calibration : a known field is applied (E_{app}) with a GBF on the eoCal. The links between field strength, antenna factor and electro-optic signal (S_{eo} in volt) are specified by equations (5.1) and (5.2) (for more information we can consult Appendix A and this Ref. [115]).

$$\begin{gathered} E_{app} = AF_{lin} \times S_{eo}\,, \\ AF_{lin} = \frac{E_{app}}{S_{eo}} = \frac{\frac{V_{pp}}{d}}{S_{eo}}\,, \end{gathered} \tag{5.1}$$

where,

$$AF_{dB} = 20\log\left(AF_{lin}\right) = 20\ \log\left(\frac{E_{app}}{S_{eo}}\right). \tag{5.2}$$

The theoretical and experimental responses of the system with respect of the field magnitude are given in Figure 5.3.
The linearity curve is obtained by varying the magnitude of the E-field, either using a frequency synthesizer in the frequency domain (blue signals on Figure 5.3) or using the high voltage source in the time domain (red signals on Figure 5.3). The output signal of the EO setup is measured either with a spectrum analyzer or with the digital scope. The EO response with respect to the field strength exhibits a dynamics greater than 120 dB (limited to about 80 dB in the time domain due to the increase of the noise). A very good agreement is observed between experimental data and expected fitting curve.
Moreover, even if further measurements will all be performed in the time domain for quite high

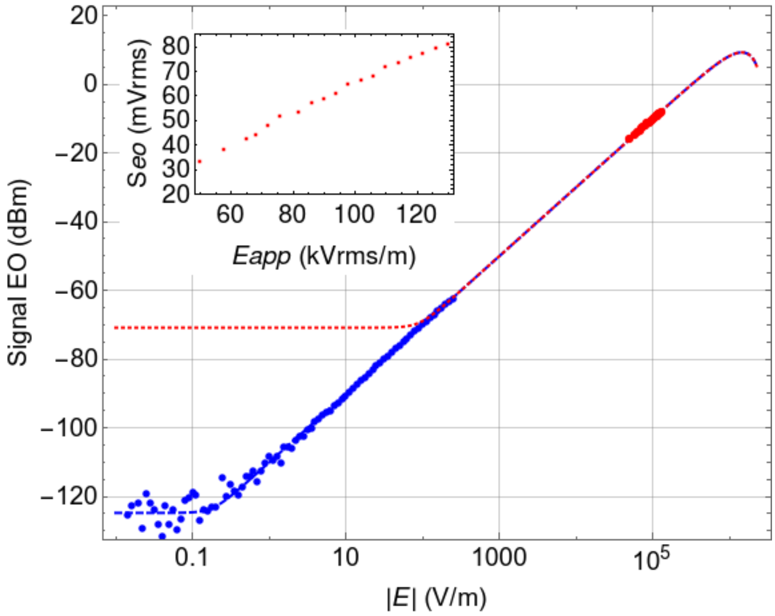

Figure 5.3: Theoretical and experimental responses of the EO probe used, as a function of the E-field magnitude. The blue dashed curve is the fitting curve corresponding to a characterization in the frequency domain, with a noise floor obtained in a resolution bandwidth of 3 Hz. Blue dots correspond to the experimental data. The red dotted curve is the fitting curve corresponding to a characterization in the time domain, with the lowest noise of the oscilloscope (measured with an averaging of 64 samples). Red dots are associated to the experimental data. The inset represents the raw EO signal as function of the applied voltage in the time domain using the high voltage source.

field strength, the measurement in the frequency domain allows to extract a minimum detectable field much lower than 1 V/m.

Finally, as mentioned before this experimental result permits determining experimentally the scaling factor between the output signal of the setup and the actual field strength (this factor is called antenna factor AF). For a RX antenna it is calculated as the ratio $AF = \frac{|E_i|}{V_{out}}$, with $|E_i|$ the modulus of the measured field component and V_{out} the output useful signal. The numerical value of the antenna factor is here $AF = 1.65$ (kV/m) mV or 124 dB/m^{-1} in the logarithmic scale.

The equation used to fit the link between the E-field and the output signal P_{EO} reads [115],

$$P_{EO} = 10\log_{10}\sqrt{P_{Noise}^2 + P_{Mod}^2}, \tag{5.3}$$

with P_{Mod}, the electrical power directly associated to the electro-optic modulation and optoelectronic conversion, and P_{Noise}, the noise level of the system measured either on the spectrum analyzer or on the oscilloscope.The form of the equation explains the curvature of the fitting curves in the vicinity of the noise floor (bottom of the curves). P_{Mod} can be written as a function of R, the resistive load of the photodiode,η its responsivity and the actual modulation of the optical power P_{modopt} :

$$P_{Mod} = R \times \left(\eta\, P_{modopt}\right)^2. \tag{5.4}$$

The whole optical response, giving P_{modopt}, is expressed as follows :

$$P_{modopt} = P_{optmean}\left(0.5 - \cos^2\left(\alpha E + \frac{\pi}{4}\right)\right), \tag{5.5}$$

with $P_{optmean}$ the mean optical power, and α the linear coefficient between the E-field to be measured and the optical modulation. This later coefficient alpha is linear with the length of the crystal and with its involved electro-optic coefficients. The form of P_{modopt} includes a cosine function illustrating the saturation of the signal for intense field strength (see top of curves in Figure 5.3).

5.3 Experimental results and discussions

For all the experimental results presented in this paper, the operating gas was helium and the applied peak voltage and pulse frequency were $V = 6$ kV peak-to-peak at $f = 18$ kHz, respectively.

5.3.1 Spatial evolution of the Laplacian field along the tube & Electrostatic simulation

The goal of the measurement campaign is to give an exhaustive spatio-temporal characterization of the field and this experimental study begins with the analysis of the field distribution in the vicinity of the tube along the *Z-axis*. There is here no gas flow. The results are presented in Figures 5.4 and 5.5, for numerical simulations and for the comparison with the measured data, respectively. Using finite element method (FEM), a 2D numerical simulation has been performed to provide a preliminary analysis of the spatial distribution of the field induced by the electrodes configuration set with a AC voltage potential. The geometry is meshed with more than 200000 nodes. The relative permittivity $\varepsilon_r = \varepsilon/\varepsilon_0$ for all elements are considered like quartz and air. Under the conditions corresponding to the experimental parameters, the model predicts the appearance of the Laplacian field with the order of 100 kV/m in the vicinity of the charged electrode.

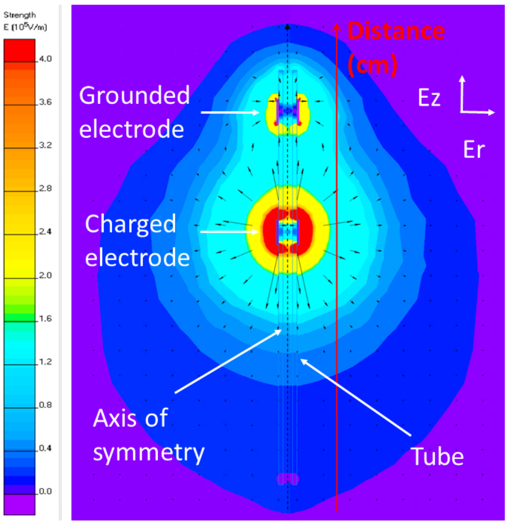

Figure 5.4: 2D axisymmetric simulation. Spatial distribution of the electric field with the structure under test at 6 kV (FEM simulation). The spatial distribution is then analyzed along the vertical red line.

The comparison between the simulations and the experimental data is presented in Figure 5.5.

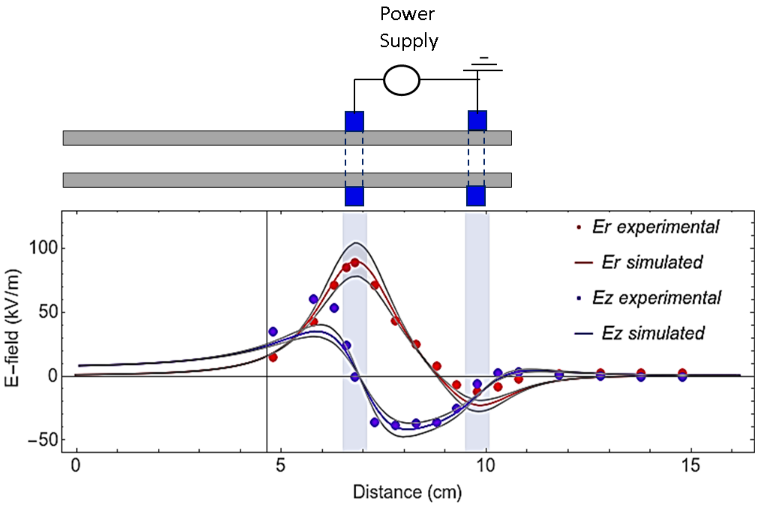

Figure 5.5: Spatial distribution of E_r and E_z in the vicinity of the tube . The position of the electrodes are indicated in light blue. Red dots and associated curve correspond the measured and simulated value of E_r, respectively. Blue dots and associated curve correspond the measured and simulated value of E_z, respectively. Surrounding black line give the uncertainty to to eventual error in the probe positioning (maximum 1 mm for the distance between the probe and the tube).

In order to analyze this distribution, let's follow for example the radial component (red curve). The graphic is divided into three parts. From 6.5 cm (zone just before the charged electrode), the field increases linearly and gradually to reach his maximum in a value more than 80 kV/m in the vicinity of the charged electrode. After this electrode, the field decreases linearly between the two electrodes to reach another local negative maximum in the vicinity of the grounded electrode. Then, it vanishes and remains approximately zero after this value (in between the grounded electrode and the rest of the setup). A good agreement between experiment and simulation for field distribution is observed.

5.3.2 Electric field measurements: Mapping of radial and longitudinal E-field components associated to the APPJ

The radial component E_r of the E-field vector is here firstly recorded by the transverse probe for each position scanned by a Cartesian robot in the symmetry plane of the plasma jet. Then, by rotating the probe with an angle of $\frac{\pi}{2}$ around it symmetry axis, the mapping of the longitudinal E-field component E_z is carried out. The interference induced by the probe on the E-field distribution being weak but not null (especially when probe is in the plasma jet), this experimental configuration with a single probe at same positions for measuring both radial and longitudinal E-field components minimizes therefore potential artifacts. It constitutes the best configuration, especially because the signal to be characterized is repetitive. As an example, the raw temporal traces of E_r and E_z, in presence of plasma, are given in Figure 5.6.

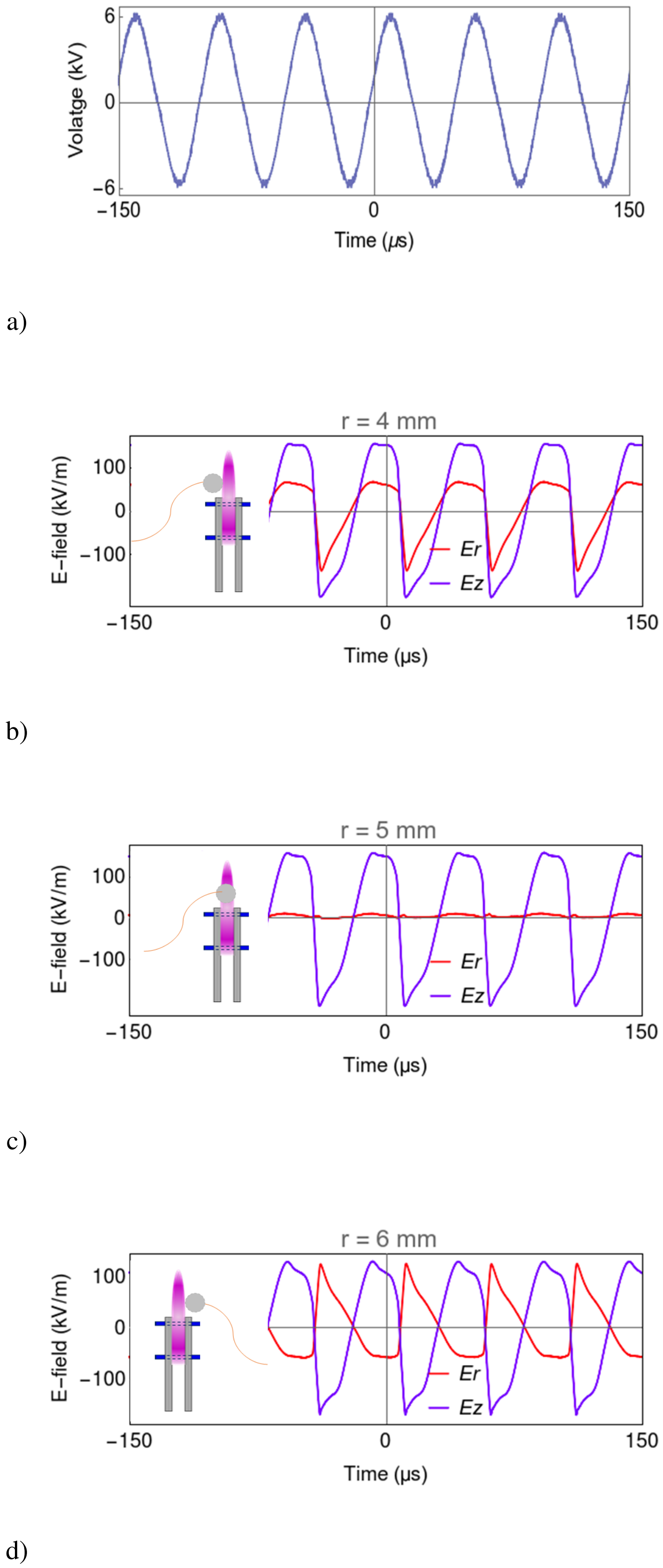

Figure 5.6: a) Temporal evolution of the applied voltage at 18 kHz. Temporal evolution of the field components E_r and E_z, 8 mm above the quartz tube, in 3 radial locations a) in the top right of the tube, b) within the jet and c) in the top left of the tube.

In this measurement campaign, the transient evolution of the radial component E_r and the longitudinal component E_z is measured with an EO probe placed above the tube nozzle. Temporel evolution of the applied voltage is presented in Figure 5.6.a). Lateral profiles of the E-field of the plasma jet are recorded at three characteristic positions : in the top right of the tube (Figure 5.6.b), in the middle of the jet (Figure 5.6.c), i.e., eight millimeters from the exit of the glass tube and top left of the tube (Figure 5.6.d).

For the positions around the jet (at ± 1mm) (see Figure 5.6.b and Figure 5.6.d), the measured radial signal (red curve) has a much stronger amplitude than the one presented within the jet (Figure 5.6.c)). In this latter position, the field is mainly vertical (of the order of 100 kV/m), the radial field is weak and almost null. The time profile for these positions does not become linear with the applied voltage (see Figure 5.6.a). Moreover, we notice the expected symmetric of E_r (inversed signal) between positions r = 4 mm and r = 6mm. In these two cases, the radial field reaches a value of about 120 kV/m. For the longitudinal component, E_z, it has almost the same amplitude whatever the radial position of the EO probe.

5.3.3 Spatio temporal evolution of both components of the field

Temporal trace of E_r or E_z one recorded for several positions of the probe above the quartz tube. The spatial steps of the mapping is 0.5 mm (for x-axis). A post-treatment with Mathematica software is here used to get the electric field lines from both E_r and E_z maps. From there it is straightforward to make a video of the temporal evolution of both E-field strength and E-field lines in and around the plasma jet over one period of the signal.

Figures 5.7, 5.8 and 5.9 present the spatio-temporal evolution of the longitudinal vector components of the field at different specific times.
At t = -2 μs and for a voltage lower than 6 kV, we can clearly see the evolution of the ionization front from the longitudinal field vectors. The field is at its maximum in the order of more than 200 kV/m. We could determine the center of the jet (where the field is mostly vertical) which appears for a position r = 5 mm. It is clearly stronger in the middle of the jet than at the ends. Then, the voltage increases until 6 kV which is the maximum voltage applied to initiate the jet. At t = 7 μs, we start to see variations in the direction of the field. We can visibly notice the fall of the field and its total inversion to reach a local maximum (blue zone) of about 400 kV/m at t = 10 μs. After that, the voltage starts to decrease to zero (at t = 23 μs). For this zero voltage, the Laplacian field is zero, we can note that the remaining total field is induced by the plasma. The plasma field is always present, there is no voltage that cancels the total field. Beyond this time, the voltage increases again until - 6 kV (at t = 35 μs) and the field reverses and increases again to reach its maximum (red zone) and so on.

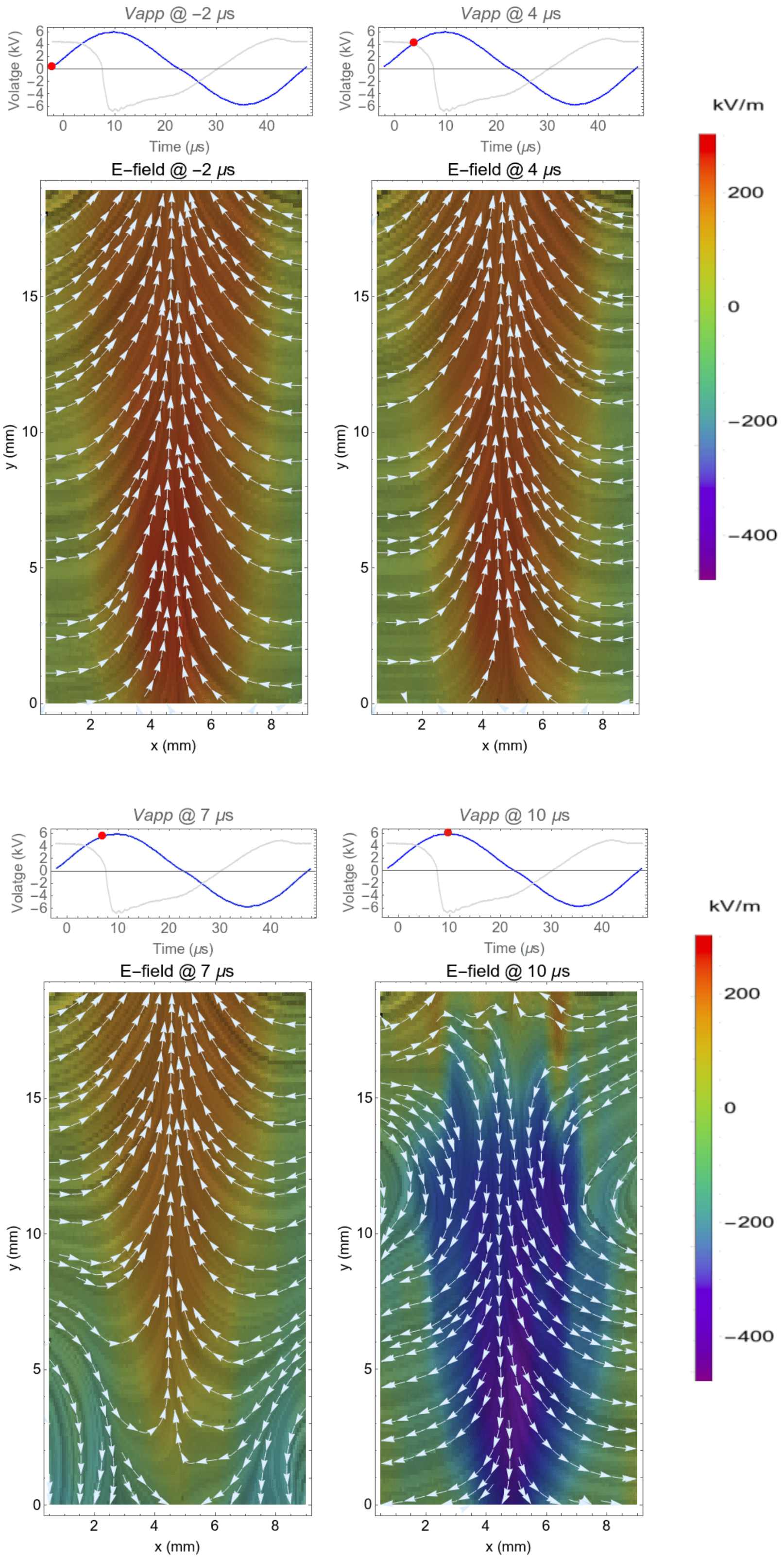

Figure 5.7: Spatio-temporal evolution of the longitudinal vector components E_z. Top graphics shows the temporal evolution of the applied voltage (gray curve) and an image of the longitudinal field in the vicinity of the quartz tube aperture. Red dot indicates the time stamp of the 2D mappings.

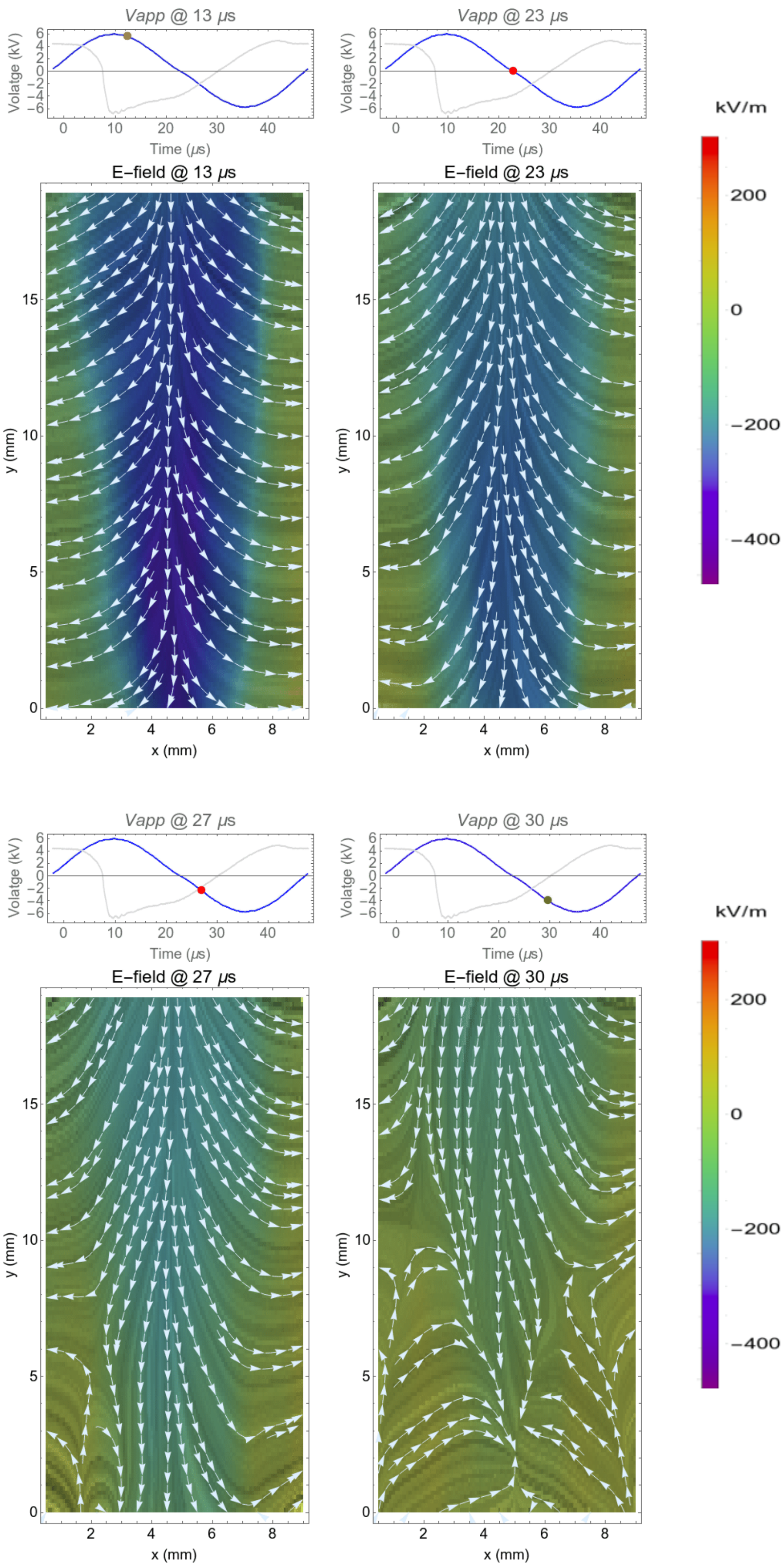

Figure 5.8: Spatio-temporal evolution of the longitudinal vector components E_z. Top graphics shows the temporal evolution of the applied voltage (gray curve) and an image of the longitudinal field in the vicinity of the quartz tube aperture. Red dot indicates the time stamp of the 2D mappings.

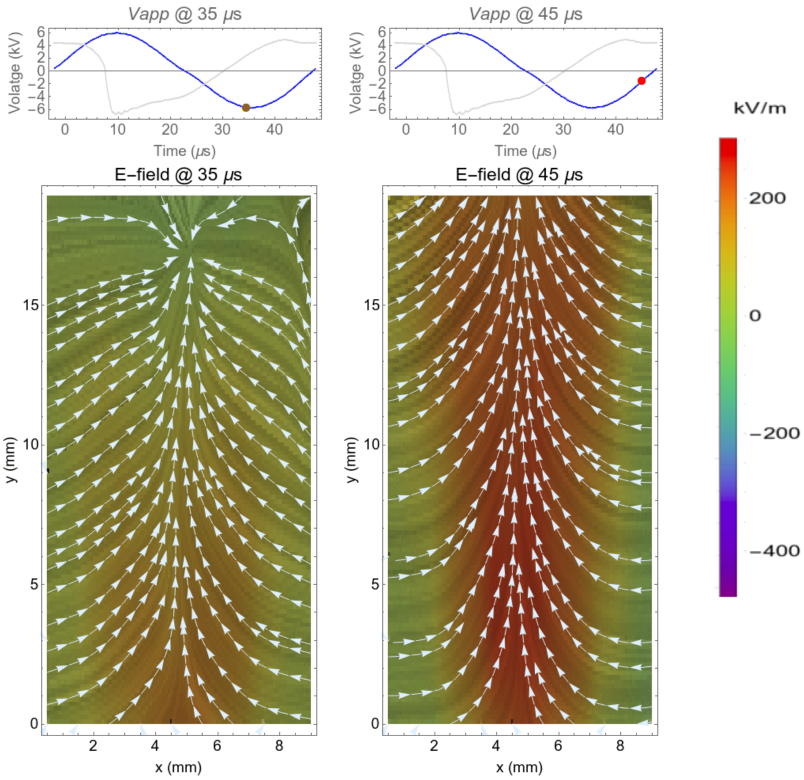

Figure 5.9: Spatio-temporal evolution of the longitudinal vector components E_z. Top graphics shows the temporal evolution of the applied voltage (gray curve) and an image of the longitudinal field in the vicinity of the quartz tube aperture. Red dot indicates the time stamp of the 2D mappings.

5.3.4 Polarimetric mapping of the E-field

Temporal evolution of the radial and longitudinal components E_r and E_z of the E-field around the discharge are measured in different positions of the probe and thanks to these temporal waveform a real-time polarimetric analysis can therefore be performed. The synchronized acquisition of the radial and longitudinal components, (E_r and E_z like shown in Figure 5.10), gives access to the E-field vector and its temporal evolution leads in turn to its polarization state. In Figure 5.10, the measurements have been performed every 1 mm from 0 cm to 1 cm along the r axis and at different heights, every 4 mm, and from 0 cm to 4 cm along the z axis.

Considering the geometry of the plasma jet, and regarding previous results, this graph can be divided into 2 symmetrical parts centered at r = 5mm (corresponding position of the center of the jet within ± 1 mm, like shown in the purple region of Figure 5.10). A parametric plots of E_z as a function of E_r allows getting the polarimetric behavior of the field, for different positions of the EO sensor.

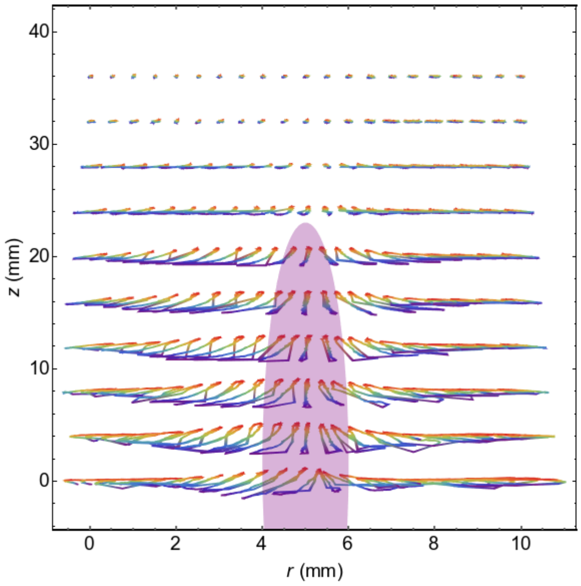

Figure 5.10: Ellipsoidal mapping obtained by a 2D mapping of the two eigen field components $\{E_r, E_z\}$ *with the exact position of the plasma plume (purple region).*

5.3.5 Determination of ionization wave front velocity

After applying voltage, an ionization wave was initiated from the charged electrode and, propagated through the helium channel inside the quartz tube, out of the tube into the ambient air. Normally, researchers used an intensified charge-coupled device (ICCD) camera to capture images of the discharge to investigate the interaction of the jets and then to calculate the ionization wave front velocity [224, 225].
In our case, to determine the ionization wave front velocity (IWFV), an original method was used. For that purpose a detailed mapping of the field along the jet is done.
Figure 5.11 presents the front waves within the jet for the longitudinal component.

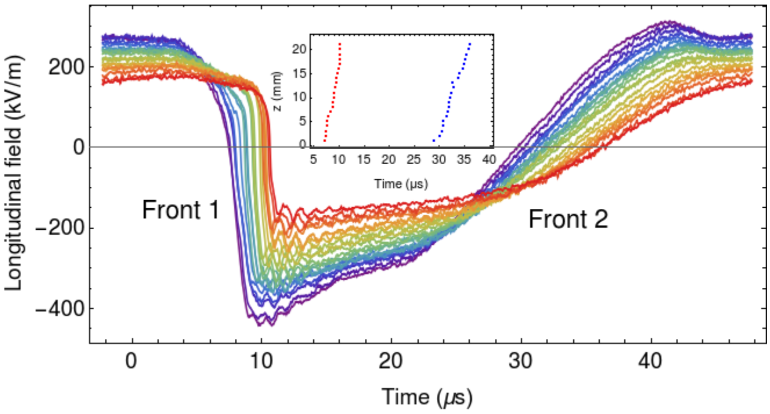

Figure 5.11: Temporal trace of the different front wave of the longitudinal component of the field, within the jet. Insets show the distance vs time of the 1 front and front 2 in red and blue respectively in aim to determine the velocity.

From the waves front (shown in Figure 5.11), we search where the vertical field change its direction, than we could know the time needed. In our case its corresponds to $E_z = 0$, its clearly appeared around $t = 10$ μs and $t = 30$ μs. The different heights z (from 0 to 2 cm) with their

exact time are represented in the insets of Figure 5.11). This illustrates a proportional relationship between z and t, with linear coefficients. The slope $|\frac{z}{t}|$ of front 1 corresponds to the IWFV and its about 5.5 km/s and it is totally in agreement with what Parkach *et al* demontrate in his recent paper [226].
Furthermore, a detailed mapping was also done for the radial component around the jet was leading to the same velocity.

For information, the velocity of the helium gas leaving the bottle (within the tube) is calculated from the flow rate and expressed by $v = \frac{Q_v}{S} = 2.65\,m/s$. v corresponds to the fluid velocity (in m/s), Q_v is the helium flow rate (in our case 2L/min) and S is the cross-sectional area ($S = \pi \times r^2$ with $r = 2$ mm).

5.3.6 Influence of an organic target on the field behavior

The use of cold plasma jets for biomedical treatment constitutes a very general subject and involves an interaction between the jet and the target to be treated [227]. For in vivo treatments, the plasma interacts with more or less conductive living tissues. The conductive target in front of the jet has been shown to have a drastic influence on the properties of the plasma plume. The effect of the contact of a conductive target on the plasma plume behavior is here studied for an organic target, which is in our case a green tree leaf, and compared to the free jet configuration. Pouvesle et al, give an attention of the measurement of E-field in presence of a conductive target in [99, 227]. Norberg et al. showed in [228] that strong differences appear in the properties of the plasma when it gets in contact with a dielectric or conductive target. The conductivity appears as a common factor between different environments (living tissue, metals, salt water, etc.).
An organic target will be considered here to study the discharge modifications in the presence of a conductive target in front of the jet. Figure 5.12 represents the temporal evolution of the longitudinal component E_z of the E-field in the presence of this target.

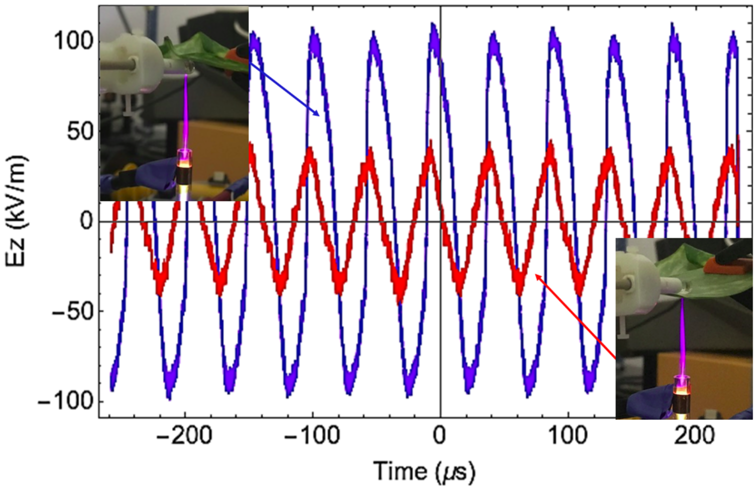

Figure 5.12: Temporal trace of the longitudinal field in the presence of a green tree leaf.

We are interested in the analysis of the longitudinal component because the field is mainly vertical in the plasma plume (as shown in Figure 5.13). Radial component is also analyzed but there is no significant signature noted due to the presence of the leaf ($\Delta V = 0$, $E_r = \frac{\Delta V}{d} = 0$). According to Figure 5.12, and under the same experimental conditions (voltage, gas flux and probe position) when the probe is located above the target (right photo of Figure 5.12), the signal (in red) has an amplitude lower than that measured below the target (blue curve). This means that the target is preventing the field from expanding. In addition, a phase shift $\pi/2$ between the 2 measurements (above and below target). This is explained by considering the equivalent electrical circuit. In fact, without a target, the jet is mainly a conductive wire, the resistance of which depends on the characteristics of the DBD reactor (type of barriers / target, dielectric properties and shape of the inter-electrode support, etc.). When the target is mounted, a capacitor with pure impedance is added. This is equivalent to an RC circuit which checks the phase shift of $\pi/2$ between the blue and red curves

Furthermore, Figure 5.13 represents the temporal trace of the E-field vector calculated from the measurements of E_r and E_z, in the presence or absence of the target (tree leaf).
Here, a parametric plots of E_z as a function of E_r allows getting the polarimetric behavior of the field, for different positions of the probe. Without target, due to the phase shift between the two eigen components of the field, the polarimetric Figures describe ellipses. This elliptical shape of the field pattern is mainly vertical (phase shift of $\pi/2$) due to the location of the measurement (just below of the target). In the presence of the target, we can notice a dramatic difference between the signature with and without target. Radial field is blocked by the tree leaf.

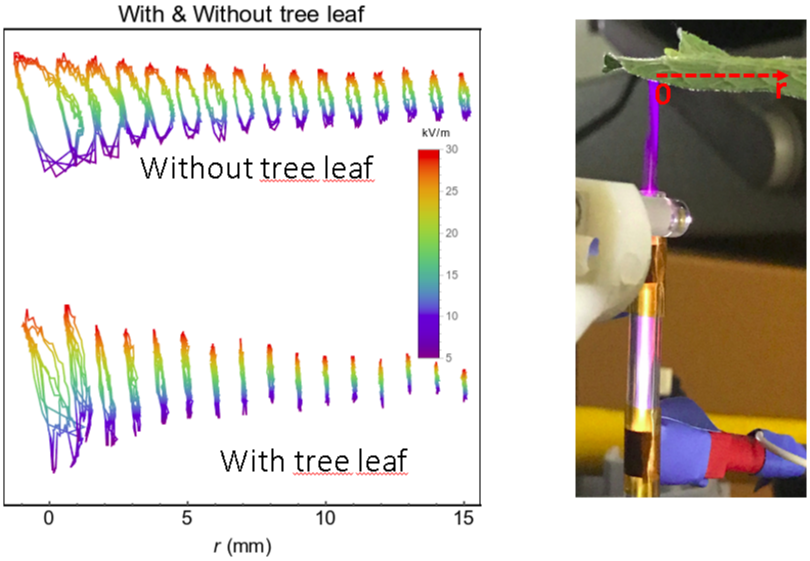

Figure 5.13: Temporal trace of the E-field vector calculated from the measurements of E_r and E_z, with and without target, for different positions of the probe along r axis.

5.4 Perturbation of the field induced by the EO probe

The latest measurement concern the analysis of the probe ability to measure the E-field. This measurement has been achieved once again by using two EO probes and after calibration. First, the 2 probes located near the plasma plume, it consists in putting the probes glued one on the other, on the same support, like shown in the inset of Figure 5.14.

If we check the evolution of the field, Figure 5.14, before and after disturbance (blue and gray curves) we can notice that signals are almost identical in terms of magnitude and phase this verifies that the probes are well calibrated and measure the same E-field. Moreover, the most important result is to show the influence of one probe on the other and therefore the induced disturbance. For this we represent the temporal evolution of the field measured by the same probe in the presence (red curve) and in the absence (blue or gray curves) of the disturbing probe. We can conclude that the presence of the disturbing probe does not disturb the field measured by the first probe, we have

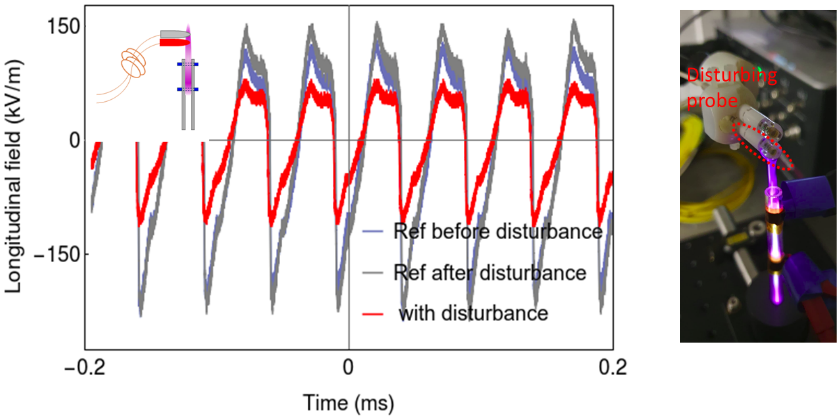

Figure 5.14: Temporal evolution of the longitudinal component of the E-field. Inset photo indicating the position of the disturbing probe (in red). On the left-hand side photo of the two sensors.

approximately the same E-field but it is just a decrease in amplitude and it is totally normal. The probes are therefore effectively non-invasive.

Another measurement was made by placing the disturbing probe just on the measurement probe (as indicated in the inset of Figure 5.15.

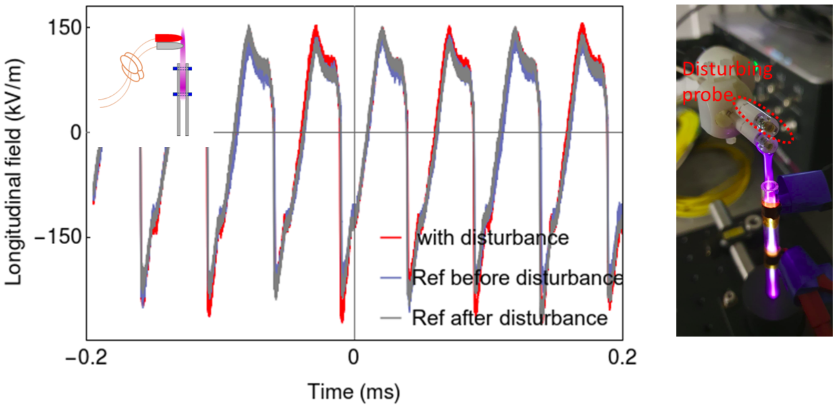

Figure 5.15: Temporal evolution of the longitudinal component of the E-field. Inset photo indicating the position of the disturbing probe (in red).On the left-hand side photo of the two sensors.

If we examine the vertical field behavior, we see that there is no difference in amplitude and phase in the presence or absence of the disturbing probe (curves red, gray and blue are the same).

5.5 Conclusion

In this chapter, we have studied the temporal evolution and the polarimetric signature of the E-field via an electro-optical probe in different environments with and without plasma for a cold atmospheric helium plasma jet. We then demonstrated the ability of the EO probe to measure the E-field in this complex environment in any position. A quantitative assessment of nonlinear behavior between the field and the applied voltage is also demonstrated. Very interesting measurements have been carried out in order to determine the ionization wave front speed by a new and original method. We were able to know the velocity of the ionization wave in different positions by measuring the field. Furthermore, a study in the presence of the target was carried out. We can notice a dramatic difference between the signature with and without target. Radial field is blocked by the tree leaf. Finally, the disturbance due to the probe itself is analyzed.

Part III

Non-linear optics for THz generation (different aspects involving optics and plasmas)

6

Impact of gases and plasmas on THz generation

Sommaire

Time - resolved spectroscopy setups historically used in the THz range take advantage of nonlinear effects in EO crystals or the photoconductive effect in semiconductors to generate and detect THz using laser pulses. Such solid-state emitters are still limited to generate intense and broadband THz pulses (photoconductive antennas based on semiconductors have limited bandwidths due to photo-carrier lifetime, while EO crystals absorb a part of the generated THz leading to dips in the available THz spectrum). The use of diluted media such as gases could therefore lead to a greater bandwidth. The first solution was proposed by Dai *et al.* [229] who used plasma as a centro-symmetric nonlinear support for the generation and detection of broadband THz. This technique offers the possibility of obtaining THz waves of one to two orders of magnitude more powerful than conventional methods. It also gives the possibility of obtaining a very wide band spectrum, from 0.1 THz to several tens of THz [230]. To generate such a broadband THz radiation, a high power femtosecond laser pulse delivered by an amplified laser chain, is focused in the air until breakdown : a plasma is generated. The charged particles produced by this ionization process yield to an overall dipole moment, which is accelerated by the ponderomotive force induced by the strong spatial gradient of the optical field itself: An electromagnetic burst whose spectrum spreads in the THz range, is radiated from the photogenerated plasma. This generation process has been first observed and described by Hamster *et al.* in 1993 [155] but was not really used since the optical-to-THz conversion rate was redibly inefficient. Few years later, Cook *et al.* [231] have proposed to improve the conversion efficiency by temporally and spatially overlapping the fundamental optical pulse and its second harmonic. In such configuration both pulses interact each other in the photogenerated plasma to efficiently generate THz bursts through the third-order non-linear response of the plasma. Nevertheless, the non-linear four-wave-mixing (FWM) process involved here is not enough to fully explain the THz generation. Indeed, as FWM can also occur in non ionized gas, THz could probably be generated even if the optical power is not enough to reach air breakdown, which does not meet the experimental observations. To overcome this latter, Kim *et al.* claimed in 2007 [232] that the THz is efficiently radiated from the charged particles accelerated by the intense optical field asymmetry that originates from the overlapping of the fundamental and second harmonic pulses.

Regardless the model used to describe the THz generation from plasma, the physical processes involved require the use of an expensive and fluctuating amplified laser chain, making the broadband and intense THz generation neither cost-effective, nor reliable. This is what motivated us to develop THz plasma sources based on classical femtosecond lasers. As the peak intensity of such laser is not enough to ionized gases, even when the beam is strongly focalized, a simple idea is to bring charged particles from external plasma source.

Therefore, in this chapter we aim at studying the interactions between an external plasma jet (detailed in chapter 5) and a photo-generated plasma. The plasma jet is the best solution to obtain a plasma source allowing to have a stable and uniform charge density without the appearance of total discharge necessary for our studies. Photo-generated plasma or plasma generated by air breakdown is carried out in collaboration with Bastien Muller a doctoral student from our laboratory whose thesis concerns the generation of THz waves by photo-generated plasma (Figure 2.10 is a photo of the setup developed in IMEP-LAHC laboratory). The main objective is to see if the addition of charge carrier via a plasma jet can promote THz radiation from the plasma filament. Indeed, to have a THz radiation, the formation of a plasma filament is a necessary condition, this is explained in section 2.2.1. The photo-generated plasma can be formed at lower optical energy if charge carriers are already present and thus allow THz radiation at low optical power. This would mean no longer using a laser system as complex, expensive and potentially dangerous as an amplified femtosecond laser.

The studies focus on these questions : **is it possible to control the THz generation using this plasma jet in term of amplitude or polarization ? Are there interactions between these two**

plasmas, making it possible to increase the yield of THz radiation generation by the addition of ionized species via the plasma jet ?

In parallel, studies will be carried out on the polarization state modulation of the THz radiation induced by the presence of the plasma jet. This latter could make it possible either to control the THz generation, or to measure/scan the E-field of the jet via the behavior of the measured THz radiation. This study requires a polarization sensitive detection capable of measuring simultaneously the transverse components of the THz field. This innovative detection setup which permits to perform polarimetric analysis of THz pulses has been developed and is described and detailed in section 3.3. Since polarization state is extracted from only one measurement, it limits the acquisition time, avoiding the systematic errors induced by the need to carry out several consecutive measurements to determine the polarization of the THz pulse, as it is classically done.

6.1 Experimental setup and THz pulse

The optical bench used is schematised in Figure 6.1.

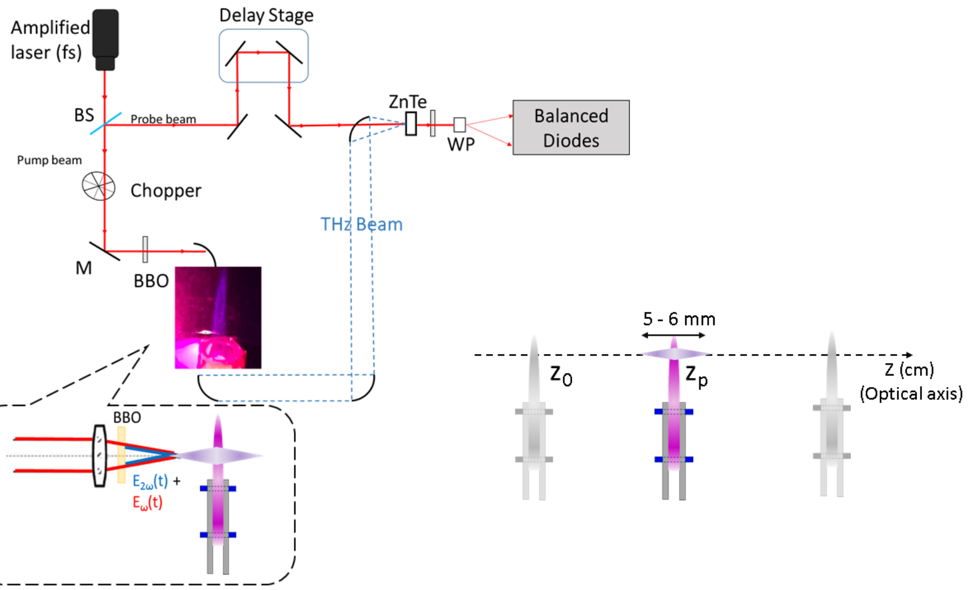

Figure 6.1: Experimental setup based on two-colors air-breakdown terahertz generation. Figure showing the interaction between the optical plasma and the Plasma jet/He which can move along the optical axis (z-axis).

This setup is based on an amplified laser, COHERENT Libra He+, delivering an ultrashort optical pulse (pulse duration = 45 fs) centered at 800 nm with an energy of 5 mJ per pulse and clocked at 1 kHz. It makes it possible to generate and detect ultra-short THz pulses (sub-picosecond). The laser beam is divided into two, using a splitter plate: a first beam, called the pump, allows the generation of THz radiation and a second beam, called the probe, is dedicated to the detection of THz radiation. The optical power of the pump beam can vary continuously from hundred mW to 3.2 W by using a half-wave/polarizer system. The beam is focused by a lens or a parabolic mirror in a nonlinear crystal dedicated to the generation of the second harmonic, of 2 ω pulsation. Then, the focused pump beam is sufficiently intense (greater than 1.7×10^{14} W.cm^{-2}) to ionize the air molecules and thus form an optical plasma (filament plasma). The plasma jet, which is oriented vertically toward the ceiling, is mounted on an XYZ translation stage allowing it to be precisely positioned in an area around the optical plasma. Plasma is used as a non-linear medium in which the pulses ω and 2 ω interact to generate THz radiation. The THz radiation generated is then shaped and focalized to the detection system by parabolic mirrors.

Figure 6.2 presents an example of a THz waveform delivered by the experimental bench above, and its associated spectrum.

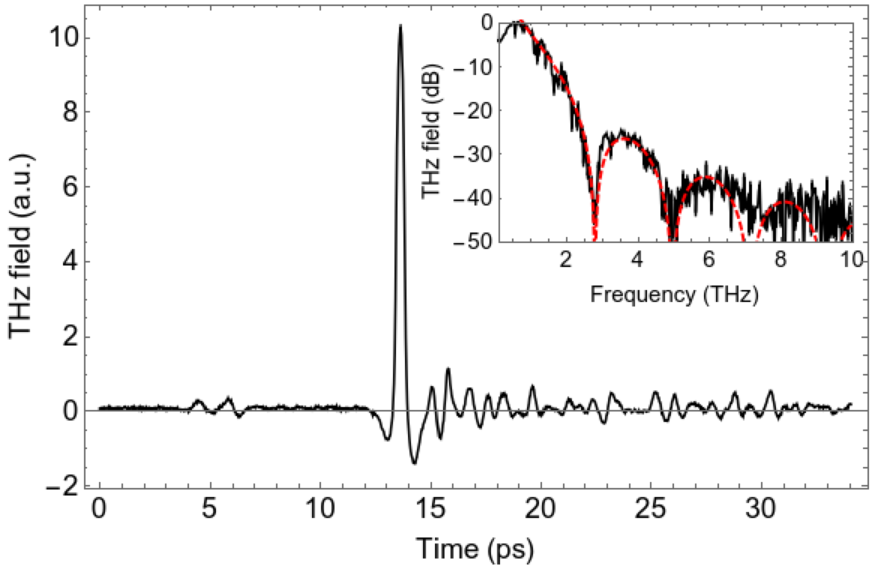

Figure 6.2: Terahertz waveform generated by the experimental setup, and coherently detected using electro-optic detection, and its associated intensity spectrum (inset). The dashed red curve is a theoretical fit including phase mismatch between THz field and optical field in the ZnTe crystal.

6.2 Experimental measurements and results

As described previously in this chapter, the objective of our studies is to understand the interactions between an external plasma and the optical filament, and this through the polarimetric analysis of the THz field generated by breakdown in the air. We are entitled to think that the presence of a plasma jet on the optical path of the pump (located between the BBO and the filament, or even downstream of this latter), induces modifications of the THz pulse generated by air breakdown. The physical phenomena involved in these interactions can potentially modify the spectral composition of the THz pulse but also modulate its polarization state, which is the reason why we have adapted the EO detection system to be sensitive to the transverse components of the THz field (see figureaborit *et al.* in 2015 [172].

Before understanding the interactions between plasma jet and the optical filament, and their influence on the radiated THz signal, we first wanted to ensure that the induced modulations are indeed linked to the plasma jet. To do this, we successively measured the transverse components of :

- a **reference signal**, obtained in absence of plasma jet (helium flow off and high voltage generator off),
- with **high voltage** close to the filament (helium flow turned off),
- with **helium flow** blown on the filament (high voltage generator off),
- with **plasma jet** launched in the filament (both helium flow and high voltage on).

Figure 6.3 presents the polarization state of the THz E-field extracted from these 4 configurations and their associated spectrum. Taking into account the fluctuation of the plasma based THz generation system, Figure 6.3 shows noticeably when comparing black (reference) and red curves, that the high voltage applied to the electrodes dedicated to the generation of the plasma jet impacts neither the spectrum, nor the polarization state of the THz pulse. This is explained by the fact that the optical field is at least 6 orders of magnitude more intense than the one imposed by the high voltage applied to the electrodes when compared in the filament. As the THz pulses are generated from the filament, this result confirms that the generation process is driven in first approximation by the optical characteristics of the fundamental and harmonic pulses (temporal and spatial overlapping, the pulse duration, optical intensity...), regardless the external E-field.

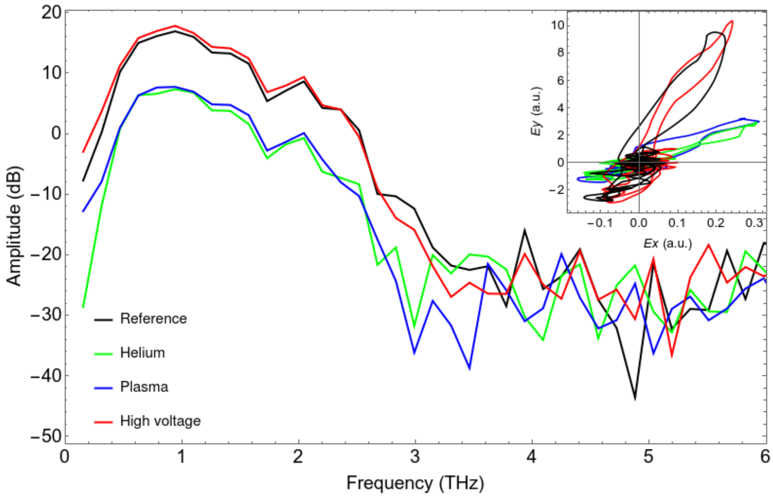

Figure 6.3: Terahertz spectra of the THz pulses generated by the experimental setup in absence of plasma jet (black curve), with only high voltage (red curve), with only helium flow (green curve), and with plasma jet (blue curve). Inset exhibits the polarization states of each THz pulses abovementioned on the transverse XY plane (THz pulse propagating in the z direction).

On the other hand, by comparing blue and green curves in Figure 6.3, one notices plasma does not make difference in the generated THz E-field: only He gas induces both magnitude and polarization state modulations in comparison to the reference(black curve). This is further confirmed by figure 6.4, which shows the evolution of the amplitudes of each transverse components of the THz signal (normalized by those obtained from the reference) as a function of the position z_0 of the nozzle that blows the He, along the optical axis (z-axis).

Once again this is coherently explained since the ionization rate of He in the plasma jet, which is a cold plasma, is far below 1% [233–236]. Therefore, adding plasma jet within the filament is almost like blowing only He gas. This is even truer when we know that the charge density supplied by the plasma jet (about 10^{13} cm^{-3}) is at least 4 orders of magnitude lower than the existing charge density within the filament [237, 238]. It is also interesting to notice that all the spectral components of the THz pulse are equally impacted by the replacement of air by He gas in the filament (the overall shapes of the black and blue spectra are identical).

Of course these observations would have been no longer true if considering a hot external plasma bringing a charge density close to the filament's one. It would have been undoubtedly interesting to study THz generation assisted by that kind of hot external plasma, but the lack of technical means and especially of expertises in this type of plasma, dissuaded us from it.

According to the above observations, from now on we only consider interactions with the helium gas even if use plasma jet for sake of clarity since it visible.

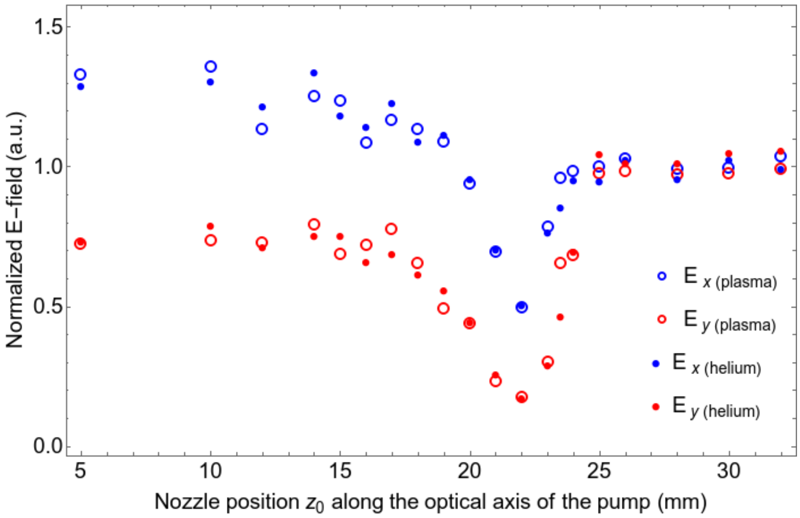

Figure 6.4: Normalized amplitudes of the E_x^{THz} *(blue) and* E_y^{THz} *(red) components of the THz pulses as a function of the* z_0 *position of the helium nozzle, extracted from measurements with gaseous helium flow (blue dots), and with plasma jet (red circles). Region between 18 and 24 mm corresponds to the optical plasma.*

6.2.1 Influence of plasma jet length on the orientation of the THz pulse

The EO detection system used, allowed the simultaneous measurement of both transverse components of the THz field. Figure 6.5 shows that the THz pulse is independent on the length of the jet.

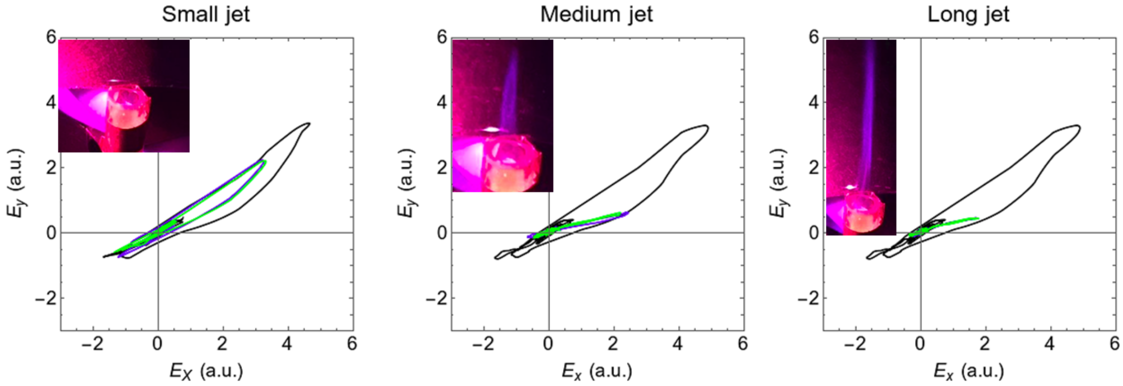

Figure 6.5: Polarization state projection on E_x *and* E_y *of THz radiation with He flow in green, with plasma jet in blue and without any of them in black (reference measurement), as a function of the plasma jet length.*

6.2.2 Influence of helium gas on the modulus and orientation of the THz pulse

The polarization state (ellipticity ζ, orientation θ) and the amplitude $|E_{THz}|$ of the pulse are then known :

$$|E_{THz}| = \sqrt{E_x^2 + E_y^2}, \tag{6.1}$$

$$\theta = \arctan\left(\frac{E_{0y}\cos(\phi_0 + \Delta\varphi/2)}{E_{0x}\cos(\phi_0 - \Delta\varphi/2)}\right), \tag{6.2}$$

$$\zeta = \sqrt{\frac{\cos(2\phi_0) - \cos(\Delta\varphi)}{\cos(2\phi_0) + \cos(\Delta\varphi)}}, \tag{6.3}$$

where $2\phi_0 = \arctan\left(\tan(\Delta\varphi)\left(\frac{E_{0x}^2 - E_{0y}^2}{E_{0x}^2 + E_{0y}^2}\right)\right)$ and $\Delta\varphi$ the relative phase shift between the components of the field.

As an example, Figure 6.6 shows a three-dimensional view (x, y, t) of a THz pulse generated by a breakdown in air. It has been reconstructed from the transverse components of the field (see lateral projections), obtained from a single measurement using the extraction process described above. The projection of the THz pulse onto the plane transverse to the time axis (wave plane) clearly shows the polarization state of the generated THz pulse.

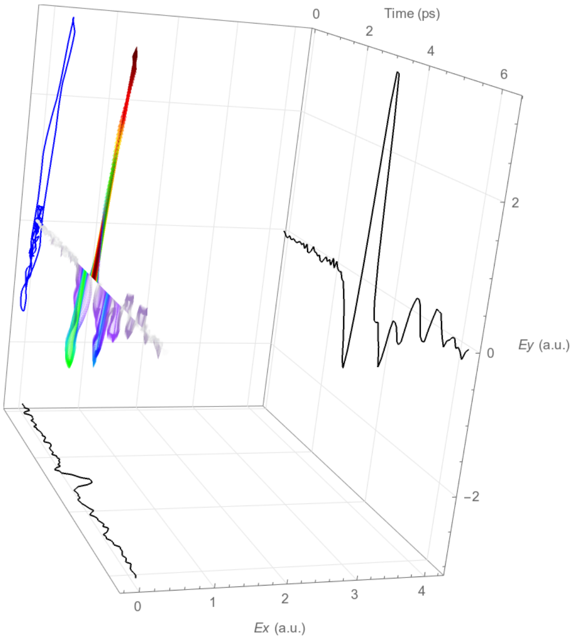

Figure 6.6: Electric field of the THz radiation (in the absence of jet plasma) as a function of time, measured by the polarization-sensitive electro-optical detection detailed and represented in the proper reference of the EO crystal (ZnTe <111>).

Figure 6.7.a shows the evolution of the modulus of the THz field induced by the presence of the helium gas located at different z_0 positions. The modulus is normalized with respect to the

reference signal (in the absence of He) and calculated from the E_x^{THz} and E_y^{THz} components according to equation (6.1).

While Figure 6.7.b presents the orientation variation of the THz pulse induced by the He flow as a function of its position along the pump optical axis. These variations are obtained by comparing the polarization orientation, θ, with and without (reference) He flow, calculated from equation (6.2).

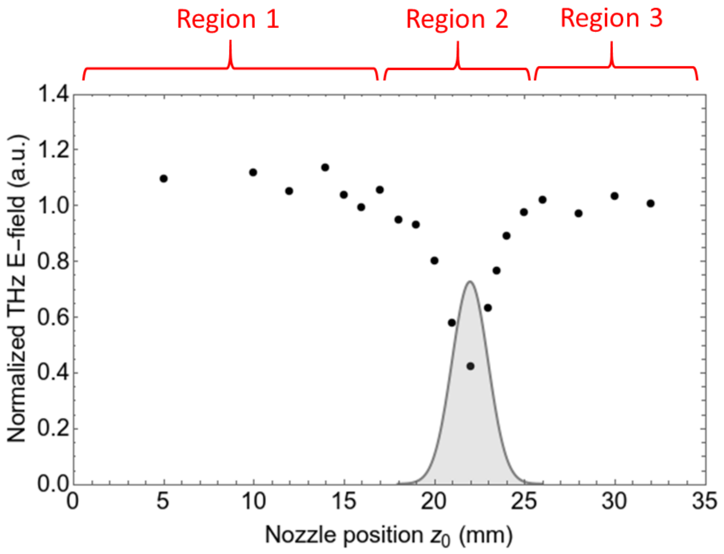

a)

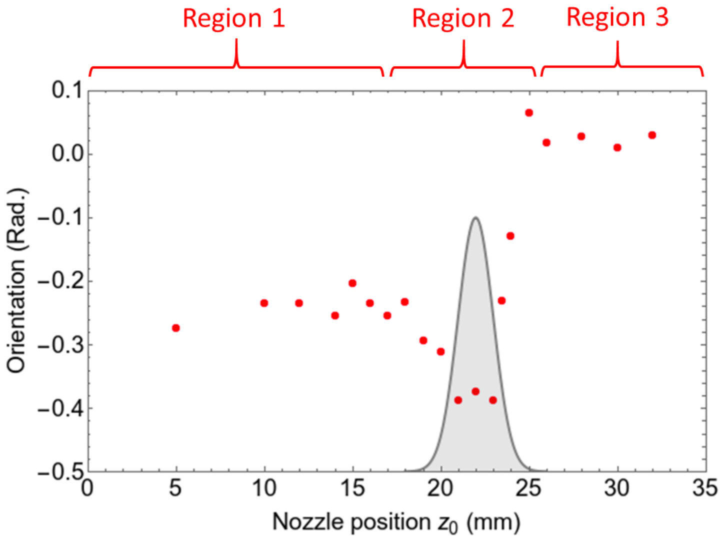

b)

Figure 6.7: a) Normalized modulus of the THz field as a function of the z_0 position of the helium nozzle (circles), and profile of the linear distribution of THz sources within the filament (solid line), which has been experimentally extracted from the z-scan experiment detailed in paragraph 6.3. b) Rotation of the THz pulse induced by the helium flux versus its position (red dots).

Three distinct regions can clearly be observed due to the presence of the Helium flow in Figure 6.7. These regions are defined with respect to the position of the optical filament inside which the THz sources are linearly distributed following a gaussian curve. The linear density of the THz sources along the filament is extracted from an experimental method called "$z-scan$" detailed in paragraph 6.3, and is represented by the solid line curve in Figure 6.7.

Region 1

Observations : When the helium flow is located before the optical plasma (0 mm $\leq z \leq$ 18 mm), the THz field is increased by more than 10% and the orientation is rotated by -0.2 rad, regardless the position z_0 of the He flow).

Analysis : By blowing a He flow at the pump beam, part of the air is replaced by He, generating a local modification of the refractive indices seen by the pump pulse (800 nm) and its second harmonic (400 nm). More specifically, the variation of the chromatic dispersion induced by the presence of He, generates a modification of the temporal overlap of the two pulses which governs in part the efficiency of the THz generation process by breakdown in the air [229]. Also in agreement with this reference, the THz pulse polarization undergoes a rotation equal to the relative phase shift between the two pulses. In conclusion, the presence of helium before the plasma filament generates a modification of the chromatic dispersion which results in a modification of the conversion efficiency and a rotation of the THz polarization whose values are independent of the position of the He flow.

Region 2

Observations : At the plasma filament (18 mm $\leq z \leq$ 24 mm), the generation efficiency as well as the rotation of the THz polarization evolve continuously with the position of the helium flow.

Analysis : As already shown for region 1, the THz sources located after the He flow are affected by the dispersion modification. By moving closer and closer the He flow along the filament, less and less THz sources are impacted until reaching region 3, where the temporal overlap between the optical pulses is no longer modified by the presence of He. This simple description would result, among other things, in an adiabatic transition of the THz generation efficiency between the three regions, which does not correspond to the observed behavior (see Figure 6.7.a). The modification of the dispersion is thus not the only effect induced by the presence of He.

To this, we must also consider the impact of the He on the characteristics of the optical filament, which is the nonlinear medium in which the THz radiation is generated by four wave mixing process. Indeed, the phenomenon of filamentation in gases arises from the competition between the phenomena of diffraction and the effects of nonlinear optics (Kerr lens) which tend to converge the optical beam until reaching optical intensities large enough to ionize the gases present at the focal point. The "breakdown" thus obtained, defocuses the optical beam which, by diverging, allows the nonlinear effects to become preponderant again to make the optical beam converging again. This succession of focusing/defocusing processes of the optical beam is at the origin of the formation of the optical filament (photo-induced plasma) whose geometry depends, among other things, on the molecular composition of the propagation medium. In addition to its geometrical shape, the carrier density within the filament also varies with the composition and pressure of the ionized gas. In our study, the He is injected at atmospheric pressure and therefore only the nature of the gas plays a role on this carrier density whose value governs the optical-to-THz conversion efficiency [239–241]. By replacing locally air by helium, which is more difficult to ionize (higher ionization energy), we reduce the density of photo-created carriers and thus the optical-to-THz conversion efficiency: the amplitude of the THz pulse drops abruptly to a minimum when the He flux overlaps the filament at best, before rising just as abruptly to its nominal value when reaching region 3.

If the cumulative effects of the linear dispersion and the gas composition of the filament described above are sufficient to explain phenomenologically the Figure 6.7.a, it is not so concerning the polarization orientation (see Figure 6.7.b). Indeed, according to Daï *et al.* [229], the orientation of the polarization depends only on the relative phase shift between the two pump pulses (fundamental and second harmonic), and is thus not related to the ionization energy of the gas. We should therefore find an adiabatic transition of the polarization rotation between the 3 probed regions, even considering the gas composition of the filament. This is not the case, indicating the presence of a complementary phenomenon that must be taken into account. This phenomenon is explained by a variation of the relative phase shift of the two pump pulses, which depends on the position of the He flow in the filament. Everything indicates therefore that the desired effect is a variation of the non-linear coefficient of order 2 (Kerr effect) induced by the introduction of He instead of air within the filament.

Region 3

Observations : When the helium flow is located after the plasma filament ($z \geq 24$ mm), the THz signal is no longer modified relatively to the reference signal (*i.e.* $|E_{THz}| = 1$ and $\theta = 0$).

Analysis : The observations corroborate the phenomenological analyses described in regions 1 and 2. Indeed, the presence of He systematically generates a relative phase shift between the two optical pulses by linear and non-linear effect, to which is added a modification of the carrier density at the level of the filament from which the THz pulse is generated. If the He is located after the sources, the induced modifications are still present but no longer impact the generation. Moreover, since no modulations are observed when He nozzle is placed after filament, this means that THz field does not interacts with He.

6.3 Model description

We consider a linear distribution of THz sources N along the optical axis z. Each of the infinitesimal sources radiates with an efficiency ρ, a linearly polarized THz field oriented with an angle θ in the proper reference of the ZnTe <111> EO crystal used. Since N, ρ and θ vary along the optical axis, the total THz signal generated by breakdown results from the integral sum of these infinitesimal THz fields. The transverse components of the total THz field are therefore :

$$E_x \propto \int_{-\infty}^{+\infty} N(z) \times \rho\ (z) \times \cos(\theta(z))\ dz, \tag{6.4a}$$

$$E_y \propto \int_{-\infty}^{+\infty} N(z) \times \rho\ (z) \times \sin(\theta(z))\ dz. \tag{6.4b}$$

The modulus $|E_{THz}|$ and the orientation θ_{THz} of the total THz field, are then defined as follows :

$$|E_{THz}| = \sqrt{E_x^2 + E_y^2}, \tag{6.5}$$

$$\theta_{THz} = \arctan\left(\frac{E_y}{E_x}\right). \tag{6.6}$$

6.3.1 Linear distribution of THz sources : z-scan

We consider that plasma filament generates a linear Gaussian distribution of THz sources :

$$N(z) = N_0 \, e^{-\left(\frac{z - z_p}{\sigma_p}\right)^2}, \tag{6.7}$$

where z_p is the position of the center of the distribution and σ_p its the half-width at $1/e$ (see Figure 6.8). z_p and σ_p were obtained experimentally using a $z-scan$.

The $z-scan$ technique, described by Chizhov *et al.* [242], consists in partially blocking the THz signal emitted by the filament using a diaphragm centered on the optical axis and whose diameter ϕ is known. As shown in Figure 6.8, the THz signal emitted by the sources located upstream of the diaphragm is partially shielded by this latter. By moving the diaphragm along the filament, the THz signal measured with our EO detection is more or less blocked. If we know the transverse profile of the THz radiation emitted by each of the sources, we are able to correlate the variation of THz field measured to the linear distribution of THz sources.

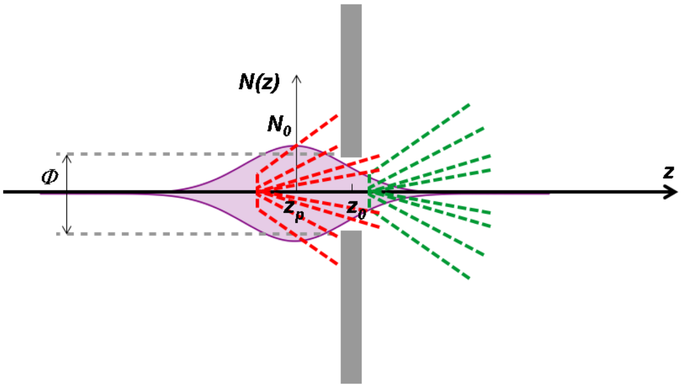

Figure 6.8: Diagram of the z-scan. The THz radiation in red is located upstream of the hole (in gray) and is only partially obstructed, the THz radiation in green, downstream of the hole, is totally detected.

Figure 6.9 shows the experimental result obtained with this technique. Thus, according to a theoretical model developed in our lab [243] to calculate the THz power passing through the diaphragm, which takes into account the "donut" like transverse profile of the emitted THz field and the diameter ϕ of the pinhole, one adjusts the parameters of the Gaussian distribution of the THz sources along the filament. The good agreement of this model with the experimental points leads to these parameters : (with z_p = 22 mm and σ_p = 1 mm)

$$N(z) \propto e^{-(z-22)^2}. \tag{6.8}$$

6.3.2 Study of the efficiency of THz generation

The generation efficiency or optical-to-THz conversion efficiency, ρ, is related to the characteristics of the plasma acting as a non-linear medium for the FWM process, on the one hand, and to the spatial and temporal overlaps of the pump pulses (fundamental and harmonic) in this plasma. By locally replacing the air by He, we modify on the one hand the optical characteristics of the propagation medium, and on the other hand the atomic composition of the ionized gas when the He flow is positioned at the filament. The ρ conversion efficiency must take into account these two effects which coexist when the He flux is placed at the level of the filament (region 2). In order to understand these two processes linked to the atomic and optical characteristics of the gases

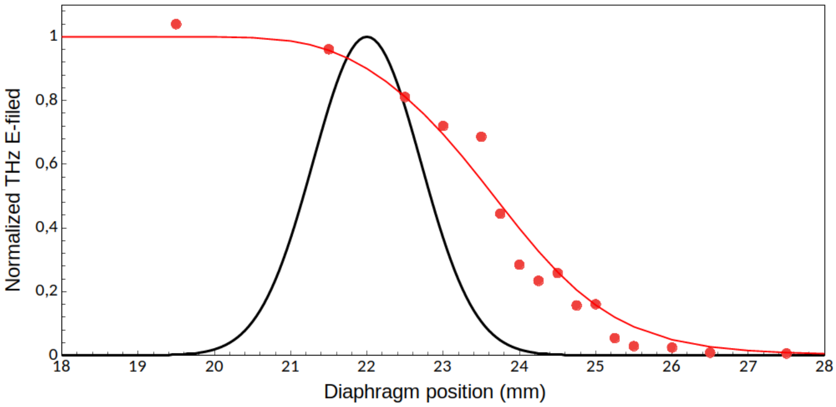

Figure 6.9: THz power detected and normalized relatively to the one measured in absence of diaphragm, for different position of this latter (red dots). The diaphragm is a 1-mm wide pinhole. The red curve is the theoretical model whose fitting parameters are the position z_p and the width at 1/e σ_p of the Gaussian distribution represented by the black curve.

involved (He and air in our case), we have decoupled the studies which are presented in the two following parts.

Influence of the atomic characteristics of the gas

The THz pulse is generated by a four-wave mixing process (3rd order non linear effect) along the plasma, which constitutes the optical filament. "ρ" depends on the density of carriers within the filament whose presence also causes an absorption of the generated THz signal. These two effects depend on the density of photo-generated carriers, and thus on the power of the optical pump. In this part, we are not interested in the dependence of ρ on the power of the pump, but rather in its dependence on the composition of the ionized gas.

Without considering the differential equations, which model the dynamics of the photo-created carriers within the plasma (justified approximation if the carrier lifetime is large compared to the pulse duration), the generation efficiency will only depend, for a given optical power and gas pressure, on the ionization efficiency.

Here we define the ionization yield as the number of ionized molecules per incident photon. This yield is proportional to the ratio between the photon energy and the ionization energy E_i^g needed to remove the primary electron from the gas molecules. It also depends on the "collision probability" between the photons and the unionized molecules whose value is proportional to their effective cross section S_{eff}^g, and to their volume density, considered as homogeneous in the volume of the filament of length l.

Neglecting the phenomena of multiple ionization of molecules (very unlikely in view of the much higher ionization energies they require), we therefore expect the THz generation efficiency to depend on the composition of the g gas considered and its physical characteristics, as follows :

$$\rho_g \propto \frac{S_{eff}^g \, \mathcal{N}_a \, l \, h\nu}{V_{mol}^g \, E_i^g}, \tag{6.9}$$

where $\mathcal{N}_a$ is the Avogadro number, V_{mol}^g the molar volume of the gas. Note that the effective cross section is directly related to the Van der Waals radius r_w of the atoms constituting the gas. If the gas is monoatomic (e.g. He), we model each particle by a sphere of radius r_w whose effective cross section seen by an incident photon is r_w :

$$S_{eff} = \pi r_w^2. \tag{6.10}$$

If the gas is diatomic (e.g. O_2 and N_2), we model the molecule by a "rod" crowned at each extremity by a hemisphere of radius r_w and whose length d corresponds to the interatomic distance. Thus, the average effective cross section of diatomic molecules is :

$$S_{eff} = \pi r_w^2 + r_w d, \tag{6.11}$$

the ratio in amplitude of the THz field radiated by breakdown in helium relative to that radiated by a diazote filament :

$$\frac{E_{THz}^{He}}{E_{THz}^{N_2}} = \frac{\rho_{He}}{\rho_{N_2}} = \frac{V_{mol}^{N_2}\, E_i^{N_2}\, S_{eff}^{He}}{V_{mol}^{He}\, E_i^{He}\, S_{eff}^{N_2}}. \tag{6.12}$$

According to the literature values reported in Table 6.1, the equation (6.12) predicts a THz signal generated in He half as intense as in diazote. This ratio is in perfect agreement with the experimental results presented in Figure 6.10.

	O_2	**N_2**	**Air**	**He**
r_w (Å)	2,06	2,25	2,12	2,11
d (Å)	1,21	1,10	1,12	X
S_{eff} (Å^2)	15,82	18,40	17,88	14,00
E_i (eV)	12,07	15,58	14,88	24,59
V_{mol} (mm^3/mol)	2,36 . 10^7	2,35 . 10^7	2,364 . 10^7	2,241 . 10^7

Table 6.1: Physical characteristics of oxygen, nitrogen and helium from the literature [244].

Figure 6.10 shows the amplitude of the THz field generated by breakdown in different gases as a function of the pump optical power. These curves were obtained by placing the gas nozzle at the plasma filament. This gas nozzle was not moved throughout the measurement campaign, only the blown gas was changed. We did these experiments first in air and then by adding a gas flow of either nitrogen (N_2) or helium (He) perpendicularly to the optical pump at the focal point, in order to change the gas mixture from which the plasma is photo-generated.

Results are presented in Figure 6.10, and clearly show that the THz generated carries information about the plasma properties (composition and density). Quadratic fitting curves (dashed line in Figure 6.10) are in good agreement with experimental measurements (dots in Figure 6.10). This is true up to a fluence of about 0.9 MW/cm^2 above which a saturation is observed regardless the gas mixture. This is partially explained by the defocusing effect induced by the plasma. We can also see that the THz generation efficiency depends on the gas photo ionised by the laser pulses. The N_2 flow (red curve in Figure 6.10) improves slightly the THz E-field in comparison to the reference curve (blue curve), which has been obtained without any added gas flow to the air. This is in accordance with the fact that the flow enriches in nitrogen a medium naturally made of 80% N_2, by replacing O_2 molecules whose ionization energy is equivalent. In these both cases, plasmas are close in composition and in density, which is not the case when purging the air with a He flow. In this case we replace N_2 and O_2 molecules by a monoatomic gas whose ionization energy is almost twice bigger. The addition of He flow clearly minimizes the amplitude of the THz generated (see green curve in Figure 6.10).

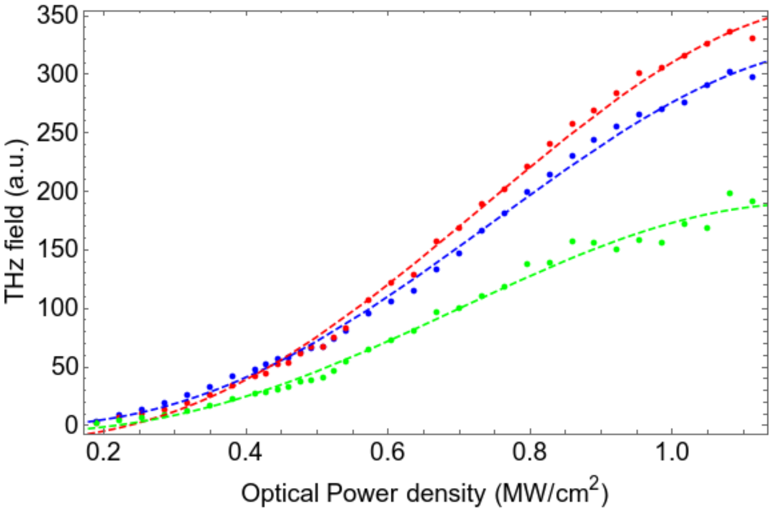

Figure 6.10: THz E-field generated by two-colors air breakdown process in air (in blue), in nitrogen (in red), and in helium (in green) as a function of the pump optical power density, and their associated quadratic fitting curves including saturation process (dashed lines) fitted by the equation $y = a x^2 e^{-\alpha x^2}$ *with* α *is the saturation coefficient.*

To conclude on the dependence of the optical/THz conversion efficiency on the atomic characteristics of the ionized gas in the filament, despite a simple model, the experimental validation of the relation (6.9) allows us to assert that this efficiency is proportional to the effective section of the ionized gas and inversely proportional to its ionization energy :

$$\rho_g \propto \frac{S^g_{eff}}{E^g_i}. \tag{6.13}$$

This approximation remains true as long as the ionized gases follow the law of perfect gases, resulting in a constant molar volume at a given pressure and temperature, and this independently of the nature of the gas, as confirmed by the values given in the table 6.1.

Influence of the optical characteristics of the gas

If the efficiency of THz generation by filamentation depends, as we have just seen, on the density of photo-created carriers whose value is governed by the atomic characteristics of the ionized gas (cf. part 6.3.2), it also depends on the temporal overlap of the pump pulse with its second harmonic at the filament. Thus, as experimentally shown by Dai *et al.* [229, 245], the conversion efficiency is the convolution product of the optical carriers of each of the two pulses, to give :

$$\rho \propto \left|\cos\left(2\omega\,\delta t + \varphi_0\right)\right|, \tag{6.14}$$

φ_0 corresponds to the relative phase shift between the ω and 2ω pulses in the absence of helium (reference measurement) due to the chromatic dispersion of the air along the optical path between the β-BBO crystal and the filament. $\delta\varphi$ $(= 2\omega\,\delta t)$ corresponds to the relative phase shift induced by the addition of helium instead of air and can be written :

$$\delta\varphi = \frac{2\,\omega\,l\,\Delta D}{c}, \tag{6.15}$$

where l is the thickness of the "slice" of air that has been replaced by He upstream of the considered source point, and ΔD the chromatic dispersion variation. If the He nozzle is completely upstream of the filament (region 1), l is equal to the inner diameter ϕ_{tube} of the nozzle that blows the He flux. Approaching the filament (region 2), the nozzle overlaps the THz sources, which consequently do not all see the same upstream He thickness. This is taken into account later in the theoretical development.If the He nozzle is completely upstream of the filament (region 1), l is equal to the inner diameter ϕ_{tube} of the nozzle that blows the He flux. Approaching the filament (region 2), the nozzle overlaps the THz sources, which consequently do not all see the same upstream He thickness. This is taken into account later in the theoretical development.

In an experiment of the type THz generation by breakdown, the peak optical intensities at the filament are enormous (of the order of 10^{16} W/cm^2). It is therefore undoubtedly necessary to consider the non-linear response of gases, which is taken into account in the variation of chromatic dispersion ΔD. As the beam is focused, the optical intensity I_{opt} evolves along the optical axis and we obtain :

$$\Delta D(z) = \Delta D_0 + \Delta D_2 \times I_{opt}(z), \tag{6.16}$$

$$\text{with : } \Delta D_0 = \underbrace{\left[n_0^{He}(@800\,nm) - n_0^{He}(@400\,nm)\right]}_{\text{Chromatic dispersion in He}} - \underbrace{\left[n_0^{air}(@800\,nm) - n_0^{air}(@400\,nm)\right]}_{\text{Chromatic dispersion in air}}$$

the chromatic dispersion variation involving the values of the refractive indices n_0 of air and helium at the optical pump frequencies and its second harmonic, and :

$$\Delta D_2 = \underbrace{\left[n_2^{He}(@800\,nm) - n_2^{He}(@400\,nm)\right]}_{\text{Non-linear chromatic dispersion in He}} - \underbrace{\left[n_2^{air}(@800\,nm) - n_2^{air}(@400\,nm)\right]}_{\text{Non-linear chromatic dispersion in air}}$$

the nonlinear dispersion variation involving the nonlinear coefficients of order 2 of air and helium. According to the ref. [246], Sellmeier's formula gives :

$$\begin{cases} n_{He}(@800\,nm) = 1{,}00003235 \\ n_{He}(@400\,nm) = 1{,}00003269 \end{cases} \quad \text{and} \quad \begin{cases} n_{air}(@800\,nm) = 1{,}00026989 \\ n_{air}(@400\,nm) = 1{,}00027718 \end{cases}$$

From these values and in agreement with the relation (6.15), the addition of the helium flux injected at the level of the optical axis upstream of the filament by a 2 mm nozzle generates a time shift $\delta t \approx -0.046\,\text{fs}$. The associated phase advance is $\delta\varphi \approx 0{,}217$ radian, and can alone explain the relative variation of the THz field modulus of 10% observed in region 1 of Figure 6.7.
Finally,

$$\rho(z,z_0) = \frac{S_{eff}(z,z_0)}{E_i(z,z_0)} \left|\cos\left(\delta\varphi(z,z_0) + \varphi_0\right)\right|, \tag{6.17}$$

If the ionization energy and the effective cross section are values depending on the local composition of the gas, the phase shift at z is related to the delay accumulation taken by one pulse relative to the other throughout their copropagation from the β-BBO crystal to z. The phase shift induced by the He flux at $z = z_0$ is thus written :

$$\delta\varphi(z,z_0) = \frac{4\pi}{\lambda} \int_{-\infty}^{z} \Pi\left(\frac{z - z_0}{\phi_{tube}}\right) \times \left[\Delta D_0 + \Delta D_2\, I_{opt}(z)\right]\, dz, \tag{6.18}$$

with I_{opt} the peak optical intensity depending on the average optical pump power $\langle P_{opt}\rangle$ (at $\lambda = 800$ nm), the repetition rate t_x of the amplified laser chain, the duration at $1/e$ of the Gaussian pulse σ_t, and the waist ω at $1/e$ of the Gaussian beam :

$$I_{opt}(z) = \frac{4 < P_{opt} >}{t_x\, \sigma_t\, \pi^{3/2}\, \omega^2(z)} = \frac{\gamma}{\omega^2(z)}. \tag{6.19}$$

According to this last expression, the evolution of the pump optical intensity along the propagation axis z is inversely proportional to the square of the power waist of the beam whose profile is supposed to be Gaussian. Modeling the phase shift induced by the addition of a He flux (cf. equation (6.18)), therefore requires modeling the evolution of the waist of the optical pump along the optical axis.

To do this, let's use the matrix formalism of geometric optics (ABCD matrix) generalized to the complex rays of Gaussian beams, also called Kogelnik transformation [247].
By writing the waist as :

$$\omega^2(z) = az^2 + bz + c, \qquad \text{with} \quad \begin{cases} a = \dfrac{d^2}{4f'^2} + \left(\dfrac{2\lambda}{\pi d}\right)^2, \\[2ex] b = -\dfrac{d^2}{2f'}, \\[2ex] c = \left(\dfrac{d}{2}\right)^2, \end{cases} \tag{6.20}$$

and from equation (6.18), we show that the relative phase shift between the optical pulses, induced by the He located at $z = z_0$, at the level of a THz source located at z in the frame of reference centered at the filament (i.e. at a distance $f' + z_s$ from the lens), is worth :

$$\delta\varphi\,(z_s, z_0) = \underbrace{\frac{4\pi\;\Delta D_0\;(\chi_2 - \chi_1)}{\lambda}}_{\text{Linear contribution}} + \underbrace{\frac{4\pi\;\Delta D_2\;\gamma}{\lambda}\int_{\chi_1}^{\chi_2}\frac{dz}{a\,(z+f')^2 + b\,(z+f') + c}}_{\text{Non-linear contribution }\delta\varphi_{NL}} \tag{6.21}$$

with $\chi_1 = \min\,(z_s, z_0 - \phi_{tube}/2)$ and $\chi_2 = \min\,(z_s, z_0 + \phi_{tube}/2)$ which are the limits of integration imposed by the respective positions of the He flux (z_0), of the considered THz source (z_s).
After a decomposition into simple elements of $\dfrac{1}{aZ^2 + bZ + c}$, we obtain :

$$\delta\varphi_{NL}\,(z_s, z_0) = \frac{4\pi\;\Delta D_2\;\gamma}{\lambda\;(Z_1 - Z_2)}\left[\ln\left(\frac{Z - Z_1}{Z - Z_2}\right)\right]_{\chi'_1}^{\chi'_2} \tag{6.22}$$

with Z_1 and $Z_2 = Z_1^*$ are the complex conjugate solutions of the binomial equation $aZ^2 + bZ + c = 0$, with a, b, and c the coefficients defined in (6.20) :

$$\begin{cases} Z_1 = f'\,\dfrac{1 + ix}{1 + x^2}, \\ \\ x = \dfrac{4\lambda\, f'}{\pi\, d^2}, \end{cases} \tag{6.23}$$

Since $Z_2 = Z_1^*$ and $Z \in \Re$, we show that :

$$\begin{cases} Z_1 - Z_2 = 2i\,\mathscr{I}m\,(Z_1)\,, \\ \\ \ln\left(\dfrac{Z - Z_1}{Z - Z_2}\right) = 2i\arg\,(Z - Z_1)\,, \end{cases} \tag{6.24}$$

where the imaginary part $\mathscr{I}m\,(Z_1) = \dfrac{f'\,x}{1 + x^2}$ and

the argument $\arg\,(Z - Z_1) = \arctan\left(\dfrac{f'\,x}{f' - Z\,(1 + x^2)}\right)$.

From the relations (6.24), and remembering that $Z = z + f'$, the equation (6.22) becomes after simplification :

$$\delta\varphi_{NL}\,(z_s, z_0) = \frac{4\sqrt{\pi}\;\langle P_{opt}\rangle\;\left(1 + x^2\right)\;d^2\;\Delta D_2}{t_x\;\sigma_t\;\lambda^2\;f'^2}\left[\arctan\left(\frac{f' x}{f' x^2 + z\,(1 + x^2)}\right)\right]_{\chi_1}^{\chi_2}. \tag{6.25}$$

To summarize

Amplitude of the transverse components E_x and E_y of the THz field radiated by a filament centered at $z = z_p$, are altered by a He flux located at $z = z_0$, according to the proposed model :

$$\begin{cases} E_x(z_0) = \int_{-\infty}^{+\infty} N(z)\ \rho(z, z_0)\ \cos(\theta(z, z_0))\ dz, \\ \\ E_y(z_0) = \int_{-\infty}^{+\infty} N(z)\ \rho(z, z_0)\ \sin(\theta(z, z_0))\ dz, \end{cases}$$

N, ρ, and θ are respectively the linear distribution of THz sources along the optical filament, the THz generation efficiency of these sources, and the orientation of the generated THz signal, defined as follows :

$$\begin{cases} N(z) = N_0\, e^{-\left(\dfrac{z - z_p}{\sigma_p}\right)^2}, \\ \\ \rho(z, z_0) = \dfrac{S_{eff}(z, z_0)}{E_i(z, z_0)}\ |\cos(\delta\varphi(z, z_0) + \varphi_0)|, \\ \\ \theta(z, z_0) = \delta\varphi(z, z_0) + \varphi_0. \end{cases}$$

The effective cross section S_{eff}, and the ionization energy E_i appearing in the expression of the conversion efficiency are specific to the molecules which constitute the ionized gas :

$$\begin{cases} E_i(z, z_0) = E_i^{air} + \Delta E_i \times \Pi\left(\dfrac{z - z_0}{\phi_{tube}}\right), \\ S_{eff}(z, z_0) = S_{eff}^{air} + \Delta S_{eff} \times \Pi\left(\dfrac{z - z_0}{\phi_{tube}}\right), \end{cases}$$

and the relative phase shift $\delta\varphi$ induced by the presence of He, is related to the linear and non linear optical characteristics of order 2 :

$$\delta\varphi\ (z_s, z_0) = \underbrace{\frac{4\pi\ \Delta D_0\ (\chi_2 - \chi_1)}{\lambda}}_{\text{Linear contribution}} + \underbrace{\frac{4\sqrt{\pi}\ \langle P_{opt}\rangle\ \left(1 + x^2\right)\ d^2\ \Delta D_2}{t_x\ \sigma_t\ \lambda^2\ f'^2}\left[\arctan\left(\frac{f'\,x}{f'x^2 + z\,(1 + x^2)}\right)\right]_{\chi_1}^{\chi_2}}_{\text{Non linear contribution } \delta\varphi_{NL}}$$

All these equations allow to compute the modulus of the THz field as well as its orientation in all regions :

$$|E_{THz}| = \sqrt{E_x^2 + E_y^2}, \tag{6.26}$$

$$\theta_{THz} = \arctan\left(\frac{E_y}{E_x}\right).$$

This model is compared with our measurements in the next section.

6.3.3 Results and interpretations

In order to analyze the temporal evolution of the vectorial E-field, a polarimetric study of the THz radiation was performed. A polarization sensitive electro-optical detection is set up according to the scheme described in Figure 3.11. It has allowed the simultaneous measurement of both transverse THz field components.

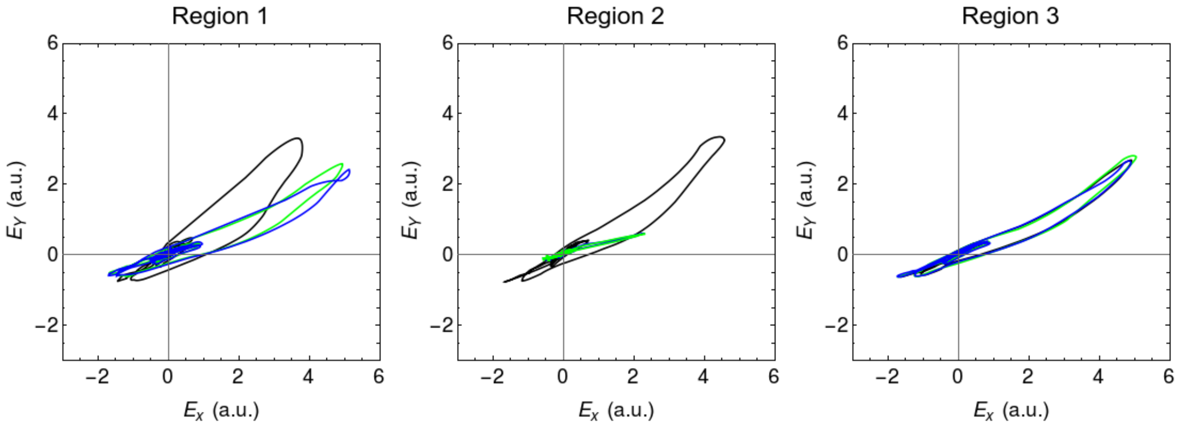

Figure 6.11: Projection of the polarization state on E_x and E_y of THz radiation propagating in the z-direction with helium flux in green, with jet plasma in blue and without any of them in black (reference measurement), as a function of the position of the helium flux (region 1 = befor the plasma filament, region 2 = in the plasma filament, region 3 = after the plasma filament).

Figure 6.11 shows the projection of the polarization state onto E_x and E_y of the THz waves with the helium flux in green, with the jet plasma in blue and without addition in black (reference measurement), as a function of the region of the helium flux. It can be seen that depending on the position of the He flux, the THz pulse is modulated in amplitude and/or orientation. This will be explained in the next two sections.

Regarding the modulus of the THz field

Using equation (6.1), THz pulse amplitude was calculated from the E_x and E_y components measured for each of the pulse time points. The modulus of the THz field then corresponds to the maximum value of the field amplitude. Figure 6.12 shows the calculated modulus (blue dots) for the different positions of the helium flow.

The solid line curve corresponds to the proposed model (see summary on page 107) for the following measured experimental parameters :

- an average optical power $\langle P_{opt} \rangle = 1$ W,
- a convergent lens of focal $f' = 200$ mm,
- a collimated pump beam of diameter $d = 7$ mm (waist at $1/e$ in field),
- an optical wavelength $\lambda = 800$ nm,
- a repetition rate $t_x = 1000$ Hz,
- a pulse duration $\sigma_t = 45$ fs,
- and a chromatic dispersion difference from the literature $\Delta D_0 = -6,95.10^{-6}$ [248].

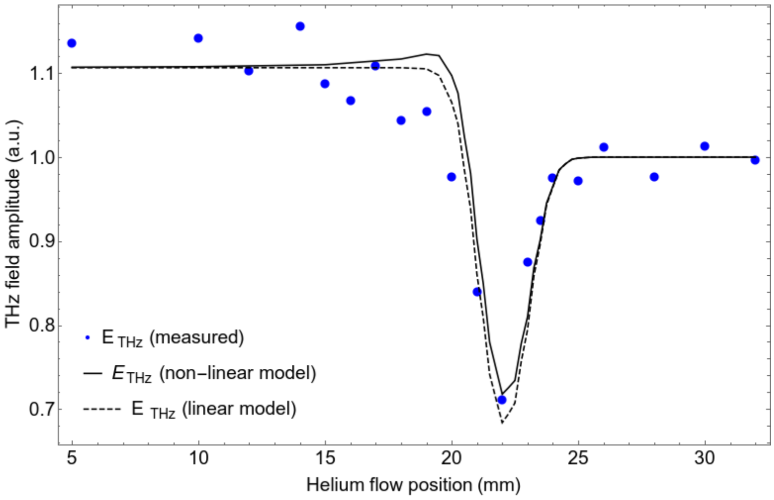

Figure 6.12: The amplitude of the THz field measured (blue points) as a function of the position of the helium flow. The curves correspond to the physical model with nonlinear contribution of order 2 (solid line), and without (dotted line).

The very good agreement between the measurements and the model was obtained by fitting the equivalent thickness ϕ_{tube} of the He jet, the phase shift at the origin φ_0 induced by the linear chromatic dispersion of the air between the β-BBO crystal and the filament, and the nonlinear second-order dispersion variation ΔD_2. The squared error between the measurements and the model was minimized for the following fitting parameters :

- $\phi_{tube} = 2$ mm,
- $\varphi_0 = 0{,}56$ radian modulo π,
- $-10^{-17} \leq \Delta D_2 \leq 10^{-18}$ cm^2/W.

He thickness (ϕ_{tube}) corresponds, as a first approximation, to the inner diameter of the nozzle, which was measured with a vernier caliper. On the other hand, the value of φ_0 adjusted was compared to the value calculated from the chromatic dispersion of air [248], and this for a distance of 6 cm between the β-BBO crystal and the filament. This calculated value is 6.87 radians, corresponding to the nearest 0.03 radian to 0.56+2π. On the other hand, the modulus predicted by the model is too insensitive to the nonlinear chromatic dispersion variation of the second order ΔD_2. This result was to be expected because, as we will see in the rest of this chapter, the relative phase shift induced by the presence of the He flux generates mostly a rotation of the polarization state, which, consequently, impacts to a lesser extent the amplitude of the radiated THz field. The latter is on the other hand sensitive to the nature of the ionized gas, which, through the effective section of the molecules which compose it and their ionization energy, changes the carrier density necessary for the THz generation. Finally, the precise extraction of ΔD_2 can only be done through the study of the $\Delta\theta_{THz}$ rotation of the THz field induced by the He flow, which is done in the following section.

Regarding the polarization orientation of the THz field

THz pulse orientation was calculated using the equation (6.2) from the E_x and E_y components measured at the time point for which the THz field amplitude is maximum. The figure 6.13 presents the orientations thus calculated (blue points) for the various positions of the He flux.

Regardless of the region considered, the model (in solid line) agrees with the measurements (see figure 6.13). This is no longer true if one neglects the non-linear response of the gases by

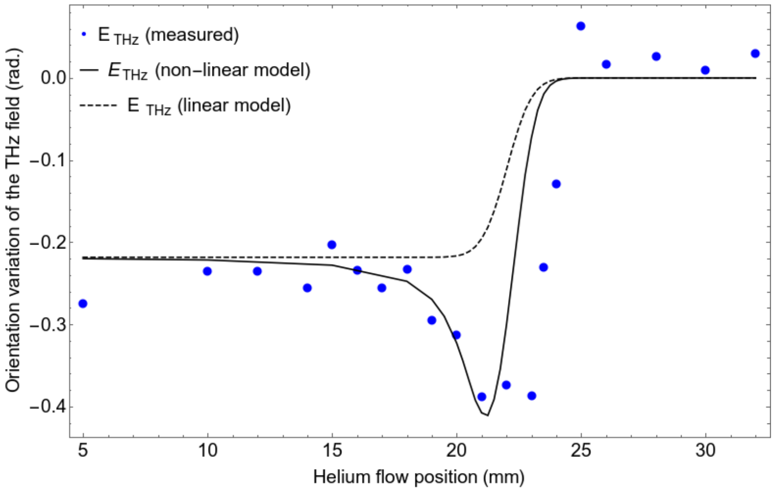

Figure 6.13: The variation of the THz field orientation measured between the measurements with helium and the reference measurements, as a function of the position of the helium flux. The blue dots are the measurement points, the dotted curve represents the linear model and the solid curve is from the non-linear model.

fixing $\Delta D_2 = 0$. Indeed, if this approximation almost impacts the modulus of the field, it is quite different for the orientation of the radiated field. This observation is even more true when we approach the He flow of the optical filament (region 2). Logically, the peak optical intensity is strongest in this region and nonlinear effects cannot be omitted in this region.

As expected, the orientation of the THz pulse is much more sensitive to the nonlinear gas response than to the modulus. Indeed, the modulus is sensitive to the gas composition through S_{eff} and E_i. Thus, the fitting of the model to the measurements allowed to extract with much more accuracy the difference of nonlinear index between air and He :

$$\Delta D_2 = -6.10^{-18}\,\text{cm}^2/\text{W}.$$

This value is negative because helium is less dispersive than air. Indeed, the value of the nonlinear coefficient of order 2 of the refractive index of helium is $D_2^{He} = 0.048.10^{-19}$ cm^2/W [249] and that of air $D_2^{air} = 5.7\pm\, 2.5.10^{-19}$ cm^2/W [250]. The expected nonlinear dispersion difference is thus of the order of -5.10^{-19} cm^2/W, which is one order of magnitude smaller than the one extracted from our model.

The overestimation of ΔD_2 is probably due to the approximations of the model. First of all, the model does not take into account the self-focusing phenomenon which drives the filament generation. This non-linear phenomenon induced by the Kerr effect leads to a stronger focusing of the pump beam, whose size at the filament is logically smaller in reality than the one calculated with the Kogelnik transform when considering a Gaussian tranverse profile of the optical pump. Our model therefore underestimates the optical intensity in region 2, whose effect is compensated in the equation (6.18) by the overestimation of the non-linear dispersion ΔD_2. On the other hand, note that the references [249] and [250] give the values of the second-order nonlinear index of He and air molecular gases. In our case, the indices to consider are those of partially ionized gases with plasma frequencies of the order of 10 THz (carrier density $\approx 10^{18}\text{cm}^{-3}$): the nonlinear dispersion coefficient ΔD_2 integrates the plasma dispersion which is overestimated.

On the other hand, we note that the model does not perfectly predict the polarization rotations induced by a He flux located at the end of region 2 (22 mm $\leq z \leq$ 25 mm). This can be explained by the fact that we considered a linear distribution of THz sources of Gaussian form (cf. relation (6.7)). This simple form allowed us to exploit z-scan measurements (see section 6.3.1) but does not perfectly reflect the filament distribution governed by known but much more complicated phenomena. However, fitting the model in this region would allow us to deduce the shape of the linear distribution.

6.4 Conclusion

This chapter seeks to show an interaction between a photo generated plasma (optical filament) and a plasma jet produced by the ionization of a helium gas. The plasma jet does not show any interaction of more than Helium when measuring the THz field generated in the plasma filament. Instead, in this chapter, we proposed a physical model to explain the modulation of the polarization state (amplitude and orientation) of the THz pulse generated by the four-wave mixing in an optical filament, induced by the presence of He. This model has been experimentally validated by a polarimetric study of the THz pulse using an innovative EO detection. We were able to extract the chromatic dispersion variation induced by the replacement of an air slice by helium. Similarly, by taking into account the non-linear response of air and helium, we were able to extract the non-linear index difference of order 2 between these two gases. The extracted value is an order of magnitude larger than the one found in the literature, probably due to the approximations of the model which does not take into account the self-focusing phenomenon, nor the optical characteristics of the photo generated plasma. Such a model, coupled with a polarization sensitive EO detection system, opens the doors to a new type of nonlinear gas spectroscopy. By changing the wavelength of the optical pump pulse, it would be possible to perform the analysis of the linear and nonlinear dispersion response of a gas.

General conclusion & Perspectives

Conclusions

Among all the relevant characteristics of a plasma, the spatio-temporal distribution of their associated electric fields is one of the critical parameters to be analyzed. The main objectives of this thesis work were to study and analyze the field associated to plasmas and voltage source. To measure the E-field, we have equipped our experimental bench with an electro-optical probe to perform a complete analysis of the E-field induced by a filament discharge in a DBD configuration or by a plasma jet of ionized helium gas.

The first part of this thesis was devoted to the history of plasma and terahertz waves. A focus was given on the "dielectric barrier discharge" (DBD) and the "cold atmospheric pressure plasma jet" (CAPPJ). We represented and compared the different methods used to measure E-fields in the literature. There are few methods to directly measure the electric field strength in DBD and atmospheric pressure plasma jet, which are based on optical emission spectroscopy. But in recent years, two other methods dedicated to the characterization of the E-field have appeared. A first optical method based on pulsed laser relies on the quantification of the optical response of the second harmonic to an externally applied E-field, called E-field-induced second harmonic generation (E-FISH). The other method is the electro-optical (EO) method, based on the pockels effect, which has shown great potential. It is the electro-optical method that was used in this work. The performances of this technique are in perfect agreement with the requirements of plasma analysis. It has a bandwidth ranging from 30 Hz to several GHz, a dynamic range greater than 130 dB, a sensitivity much better than 1 V/m, a compression point at 1 dB exceeding several 1 MV/m, and a spatial resolution of less than 1 mm^3.

The second part of this thesis was dedicated to the characterization of two types of plasma. The E-field was investigated in the close vicinity of a filamentary microplasma produced with a DBD configuration. We demonstrated the ability of these EO transducers to provide a complete vectorial analysis of the E-field induced by the high voltage source that initiates the ionization process, on the one hand, and by the plasma itself, on the other hand. The measured threshold for the generation of the discharge breakdown was determined (17 kVrms) and it is in good agreement with the electrostatic simulation performed on the basis of the finite element method. The model predicts an appearance of the plasma when the E-field value is greater than the breakdown value in the air. The performance of the EO probe allows the vectorial and real time analysis of the electric field induced by the plasma sources. The properties of the field was extracted in the linear regime as well as in the non-linear region. A quantitative evaluation of the nonlinear behavior between the field and the applied voltage was demonstrated. Furthermore, the real-time evolution of the two components of the eigenfield vector induced by the high voltage source and the ionization waves propagating in the space between the electrodes of the DBD reactors has been performed. A specific polarimetric signature of the filamentary discharge has been identified.
Indeed, we also studied the temporal evolution and the polarimetric signature of the field for a cold atmospheric helium plasma jet. The focus of this work was on the spatially and temporally resolved measurements of the E-field associated to a plasma working under atmospheric pressure condition inside long insulating quartz tube through the EO method. Well-resolved maps in time and space for both components of the field have been made to determine the velocity of the ion-

ization wavefront.

Finally, in last chapter, we have studied the interaction between a photo generated plasma (optical filament) and a plasma jet produced by the ionization of a helium gas. The plasma jet has not shown any interaction of more than gaseous helium when measuring the THz field generated in the plasma filament. Instead, we proposed a physical model to explain the modulation of the polarization state (amplitude and orientation) of the THz pulse generated by a four-wave mixing non-linear process in an optical filament, induced by the presence of He. This model has been experimentally validated by a polarimetric study of the THz pulse using an innovative EO detection.

Perspectives and future work

Several avenues can be explored to pursue this thesis work and thus improve some of the results obtained or the experimental benches themselves.
First of all, improvements could be made on the electro-optical sensors in order to improve their performances (in particular i mean their spatial resolution) by playing on the size of the BSO crystal inside the probe for example.

To complement our jet plasma work, time and space resolved voltage mapping can be performed for all possible electrode configurations. In addition, a polarimetric study using targets has shown the deformation of the longitudinal component. It is also possible to consider a study on the effect of the electrical properties of these targets and also while changing the thermodynamic properties in the measurement medium (humidity, temperature and also the gas..)

Concerning the influence of a gas flow on the THz generation by breakdown in air, the studies can be carried out according to two axes. Concerning the gas/filament interaction itself, it would be interesting to study the influence of other gases than helium. For example, it has been demonstrated that it is possible to generate stronger THz fields by replacing air with a rare gas such as Xenon. This would also be an opportunity to test the robustness of our theoretical model.

Bibliography

[1] P. Bohm, M. Kettlitz, R. Brandenburg, H. Hoft, and U. Czarnetzki, “Determination of the electric field strength of filamentary dbds by cars-based four-wave mixing,” *Plasma Sources Science and Technology*, vol. 25, no. 5, p. 054002, 2016.

[2] W. H. Brock, *William Crookes (1832-1919) and the commercialization of science*. Ashgate Publishing, Ltd., 2008.

[3] M. J. Pinheiro, “Plasma: the genesis of the word,” *arXiv preprint physics-0703260*, 2007.

[4] I. Langmuir, “Oscillations in ionized gases,” *Proceedings of the National Academy of Sciences of the United States of America*, vol. 14, no. 8, p. 627, 1928.

[5] C. Douat, *Etude dun micro-jet de plasma a pression atmospherique*. PhD thesis, Paris 11, 2014.

[6] A. M. Ali, M. A. Hassan, and B. I. Abdulkarim, “Thermal plasma: a technology for efficient treatment of industrial and wastewater sludge,” *J. Environ. Sci. Toxicol. Food. Technol*, vol. 10, pp. 63–75, 2016.

[7] S. Eliezer and Y. Eliezer, *The fourth state of matter: an introduction to plasma science*. CRC Press, 2001.

[8] K. Burm, “Plasma: The fourth state of matter,” *Plasma Chemistry and Plasma Processing*, vol. 32, no. 2, pp. 401–407, 2012.

[9] F. Kamenetsii and D. A. bertovich, *Plasma: the fourth state of matter*. Macmillan International Higher Education, 1972.

[10] Y. P. Raizer and J. E. Allen, *Gas discharge physics*, vol. 2. Springer Berlin, 1997.

[11] G. Bonizzoni and E. Vassallo, “Plasma physics and technology; industrial applications,” *Vacuum*, vol. 64, no. 3-4, pp. 327–336, 2002.

[12] F. F. Chen, “Industrial applications of low-temperature plasma physics,” *Physics of Plasmas*, vol. 2, no. 6, pp. 2164–2175, 1995.

[13] N. Venkatramani, “Industrial plasma torches and applications,” *Current Science*, pp. 254–262, 2002.

[14] R. Suchentrunk, G. Staudigl, D. Jonke, and H. Fuesser, “Industrial applications for plasma processes examples and trends,” *Surface and Coatings Technology*, vol. 97, no. 1-3, pp. 1–9, 1997.

[15] K. S. Park, S. K. Kim, S. G. Lee, H. J. Lee, and J. K. Kwon, “Application of plasma lighting for growth and flowering of tomato plants,” *Horticulture, Environment, and Biotechnology*, vol. 59, no. 6, pp. 827–833, 2018.

[16] L. Audin, “Plasma lighting, fiber optics, and daylight collectors: toward the next revolution in high-efficiency illumination,” *Strategic planning for energy and the environment*, vol. 14, no. 4, 1995.

[17] A. Morell and N. El Khiati, “Green phosphors for large plasma tv screens,” *Journal of the Electrochemical Society*, vol. 140, no. 7, p. 2019, 1993.

[18] R. Hischier and I. Baudin, “Lca study of a plasma television device,” *The International Journal of Life Cycle Assessment*, vol. 15, no. 5, pp. 428–438, 2010.

[19] J. R. Hollahan, A. T. Bell, *et al.*, “Techniques and applications of plasma chemistry,” 1974.

[20] H. Rishbeth, *Book Review: The environment of the earth. F. DELOBEAU*, vol. 20. 1972.

[21] J. Boeuf, “Applications and modeling of non-equilibrium plasmas,” *Mathematical Modeling and Computational Challenges in Plasma Physics*, 2004.

[22] N. S. J. Braithwaite, “Introduction to gas discharges,” *Plasma sources science and technology*, vol. 9, no. 4, p. 517, 2000.

[23] J. Kriegseis, “Performance characterization and quantification of dielectric barrier discharge plasma actuators,” 2011.

[24] B. M. Smirnov, *Physics of ionized gases*. John Wiley and Sons, 2008.

[25] Z. Donko, *Free-space coherent broadband terahertz time-domain spectroscopy*. 2013.

[26] J.-M. Rax, *Physique des plasmas: cours et applications*. Dunod, 2005.

[27] U. Kogelschatz, B. Eliasson, W. Egli, *et al.*, “From ozone generators to flat television screens: history and future potential of dielectric-barrier discharges,” *Pure and Applied Chemistry*, vol. 71, no. 10, pp. 1819–1828, 1999.

[28] U. Kogelschatz, “Applications of microplasmas and microreactor technology,” *Contributions to Plasma Physics*, vol. 47, no. 1-2, pp. 80–88, 2007.

[29] B. A. Niemira, “Cold plasma decontamination of foods,” *Annual review of food science and technology*, vol. 3, pp. 125–142, 2012.

[30] A. Grill, *Cold plasma in materials fabrication*, vol. 151. IEEE Press, New York, 1994.

[31] R. Thirumdas, C. Sarangapani, and U. S. Annapure, “Cold plasma: a novel non-thermal technology for food processing,” *Food biophysics*, vol. 10, no. 1, pp. 1–11, 2015.

[32] S. K. Pankaj, C. Bueno-Ferrer, N. Misra, V. Milosavljevic, C. Odonnell, P. Bourke, K. Keener, and P. Cullen, “Applications of cold plasma technology in food packaging,” *Trends in Food Science and Technology*, vol. 35, no. 1, pp. 5–17, 2014.

[33] D. Salzmann, *Atomic physics in hot plasmas*. No. 97, Oxford University Press on Demand, 1998.

[34] M. I. Boulos, P. Fauchais, and E. Pfender, *Thermal plasmas: fundamentals and applications*. Springer Science and Business Media, 2013.

[35] B. De Pontieu, S. McIntosh, M. Carlsson, V. Hansteen, T. Tarbell, P. Boerner, J. Martinez-Sykora, C. Schrijver, *et al.*, “The origins of hot plasma in the solar corona,” *Science*, vol. 331, no. 6013, pp. 55–58, 2011.

[36] P. J. Pointu Anne-Marie and J. Jacques, “Plasmas froids de decharge proprietes electriques,” *Techniques de lingenieur Materiaux conducteurs et plasmas*, vol. base documentaire : TIB251DUO., 1998.

[37] B. Ruj and S. Ghosh, “Technological aspects for thermal plasma treatment of municipal solid waste-a review,” *Fuel processing technology*, vol. 126, pp. 298–308, 2014.

[38] N. R. Council, P. S. Committee, *et al.*, *Plasma Processing of Materials: Scientific Opportunities and Technological Challenges*. National Academies Press, 1991.

[39] A. Bogaerts, E. Neyts, R. Gijbels, and J. Van der Mullen, “Gas discharge plasmas and their applications,” *Spectrochimica Acta Part B: Atomic Spectroscopy*, vol. 57, no. 4, pp. 609–658, 2002.

[40] A. Fridman, A. Chirokov, and A. Gutsol, “Non-thermal atmospheric pressure discharges,” *Journal of Physics D: Applied Physics*, vol. 38, no. 2, p. R1, 2005.

[41] F. Judee, S. Simon, C. Bailly, and T. Dufour, “Plasma-activation of tap water using dbd for agronomy applications: Identification and quantification of long lifetime chemical species and production/consumption mechanisms,” *Water research*, vol. 133, pp. 47–59, 2018.

[42] I. Adamovich, S. D. Baalrud, A. Bogaerts, P. Bruggeman, M. Cappelli, V. Colombo, U. Czarnetzki, U. Ebert, J. G. Eden, P. Favia, *et al.*, “The 2017 plasma roadmap: Low temperature plasma science and technology,” *Journal of Physics D: Applied Physics*, vol. 50, no. 32, p. 323001, 2017.

[43] T. Andrews and P. G. Tait, “Vii. on the volumetric relations of ozone, and the action of the electrical discharge on oxygen and other gases,” *Philosophical Transactions of the Royal Society of London*, no. 150, pp. 113–131, 1860.

[44] K. Buss, “Die elektrodenlose entladung nach messung mit dem kathodenoszillographen,” *Archiv fur Elektrotechnik*, vol. 26, no. 4, pp. 261–265, 1932.

[45] U. Kogelschatz, “Filamentary, patterned, and diffuse barrier discharges,” *IEEE Transactions on plasma science*, vol. 30, no. 4, pp. 1400–1408, 2002.

[46] H.-E. Wagner, R. Brandenburg, K. Kozlov, A. Sonnenfeld, P. Michel, and J. Behnke, “The barrier discharge: basic properties and applications to surface treatment,” *Vacuum*, vol. 71, no. 3, pp. 417–436, 2003.

[47] M. Xi, Y.-L. Li, S.-y. Shang, D.-H. Li, Y.-X. Yin, and X.-Y. Dai, “Surface modification of aramid fiber by air dbd plasma at atmospheric pressure with continuous on-line processing,” *Surface and Coatings Technology*, vol. 202, no. 24, pp. 6029–6033, 2008.

[48] L. Wei, T. Xiaodong, L. Dongping, L. Yanhong, F. Zhiqing, and C. Baoxiang, “Growth of fluorocarbon films by low-pressure dielectric barrier discharge,” *Plasma Science and Technology*, vol. 10, no. 1, p. 74, 2008.

[49] F. Massines, N. Gherardi, and F. Sommer, “Silane-based coatings on polypropylene, deposited by atmospheric pressure glow discharge plasmas,” *Plasmas and polymers*, vol. 5, no. 3-4, pp. 151–172, 2000.

[50] G.-M. Xu, Y. Ma, and G.-J. Zhang, “Dbd plasma jet in atmospheric pressure argon,” *IEEE transactions on plasma science*, vol. 36, no. 4, pp. 1352–1353, 2008.

[51] Z. Navratil, R. Brandenburg, D. Trunec, A. Brablec, P. Stahel, H.-E. Wagner, and Z. Kopecky, “Comparative study of diffuse barrier discharges in neon and helium,” *Plasma Sources Science and Technology*, vol. 15, no. 1, p. 8, 2005.

[52] P. Rajasekaran, P. Mertmann, N. Bibinov, D. Wandke, W. Viol, and P. Awakowicz, “Filamentary and homogeneous modes of dielectric barrier discharge (dbd) in air: investigation through plasma characterization and simulation of surface irradiation,” *Plasma Processes and Polymers*, vol. 7, no. 8, pp. 665–675, 2010.

[53] T. Shao, K. Long, C. Zhang, J. Wang, D. Zhang, P. Yan, and S. Zhang, “Electrical characterization of dielectric barrier discharge driven by repetitive nanosecond pulses in atmospheric air,” *Journal of Electrostatics*, vol. 67, no. 2-3, pp. 215–221, 2009.

[54] Y.-M. Sung and T. Sakoda, “Optimum conditions for ozone formation in a micro dielectric barrier discharge,” *Surface and Coatings Technology*, vol. 197, no. 2-3, pp. 148–153, 2005.

[55] J. M. Williamson, D. D. Trump, P. Bletzinger, and B. N. Ganguly, “Comparison of high-voltage ac and pulsed operation of a surface dielectric barrier discharge,” *Journal of Physics D: Applied Physics*, vol. 39, no. 20, p. 4400, 2006.

[56] A. Khacef, J. M. Cormier, and J. M. Pouvesle, “Nox remediation in oxygen-rich exhaust gas using atmospheric pressure non-thermal plasma generated by a pulsed nanosecond dielectric barrier discharge,” *Journal of Physics D: Applied Physics*, vol. 35, no. 13, p. 1491, 2002.

[57] M. Magureanu, N. Mandache, E. Gaigneaux, C. Paun, and V. Parvulescu, “Toluene oxidation in a plasma-catalytic system,” *Journal of applied physics*, vol. 99, no. 12, p. 123301, 2006.

[58] R. P. Mildren, R. J. Carman, and I. S. Falconer, “Visible and vuv emission from a xenon dielectric barrier discharge using pulsed and sinusoidal voltage excitation waveforms,” *IEEE transactions on plasma science*, vol. 30, no. 1, pp. 192–193, 2002.

[59] R. Carman, R. Mildren, B. Ward, and D. Kane, “High-pressure (> 1 bar) dielectric barrier discharge lamps generating short pulses of high-peak power vacuum ultraviolet radiation,” *Journal of Physics D: Applied Physics*, vol. 37, no. 17, p. 2399, 2004.

[60] S. Beleznai, G. Mihajlik, I. Maros, L. Balazs, and P. Richter, “Improving the efficiency of a fluorescent xe dielectric barrier light source using short pulse excitation,” *Journal of Physics D: Applied Physics*, vol. 41, no. 11, p. 115202, 2008.

[61] S. Ishikawa, K. Yukimura, K. Matsunaga, and T. Maruyama, “Surface modification of poly (tetrafluoroethylene) film using dielectric barrier discharge of intermittent pulse voltage,” *Japanese Journal of Applied Physics*, vol. 39, no. 9R, p. 5223, 2000.

[62] A. N. Bhoj and M. J. Kushner, “Repetitively pulsed atmospheric pressure discharge treatment of rough polymer surfaces: I. humid air discharges,” *Plasma Sources Sci. Technol*, vol. 17, no. 3, pp. 0963–0252, 2008.

[63] J. L. Walsh, J. Shi, and M. G. Kong, “Contrasting characteristics of pulsed and sinusoidal cold atmospheric plasma jets,” *Applied Physics Letters*, vol. 88, no. 17, p. 171501, 2006.

[64] P. Magnier, B. Dong, D. Hong, and J. Hureau, “Action of a pulsed dbd actuator on a slow jet,” *Journal of Electrostatics*, vol. 66, no. 7-8, pp. 369–374, 2008.

[65] B. L. Sands, B. N. Ganguly, and K. Tachibana, “A streamer-like atmospheric pressure plasma jet,” *Applied Physics Letters*, vol. 92, no. 15, p. 151503, 2008.

[66] X. Lu, Z. Jiang, Q. Xiong, Z. Tang, and Y. Pan, "A single electrode room-temperature plasma jet device for biomedical applications," *Applied Physics Letters*, vol. 92, no. 15, p. 151504, 2008.

[67] J. H. Choi, I. Han, H. K. Baik, M. H. Lee, D.-W. Han, J.-C. Park, I.-S. Lee, K. M. Song, and Y. S. Lim, "Analysis of sterilization effect by pulsed dielectric barrier discharge," *Journal of electrostatics*, vol. 64, no. 1, pp. 17–22, 2006.

[68] M. Laroussi, "Low temperature plasma jets: characterization and biomedical applications," *MDPI*, pp. 54–58, 2020.

[69] B. Gellert and U. Kogelschatz, "Generation of excimer emission in dielectric barrier discharges," *Applied Physics B*, vol. 52, no. 1, pp. 14–21, 1991.

[70] P. Bruggeman, M. J. Kushner, B. R. Locke, J. G. Gardeniers, W. Graham, D. B. Graves, R. Hofman-Caris, D. Maric, J. P. Reid, E. Ceriani, *et al.*, "Plasma–liquid interactions: a review and roadmap," *Plasma sources science and technology*, vol. 25, no. 5, p. 053002, 2016.

[71] P. Vanraes, H. Ghodbane, D. Davister, N. Wardenier, A. Nikiforov, Y. P. Verheust, S. W. Van Hulle, O. Hamdaoui, J. Vandamme, J. Van Durme, *et al.*, "Removal of several pesticides in a falling water film dbd reactor with activated carbon textile: energy efficiency," *Water research*, vol. 116, pp. 1–12, 2017.

[72] E. Marotta, E. Ceriani, M. Schiorlin, C. Ceretta, and C. Paradisi, "Comparison of the rates of phenol advanced oxidation in deionized and tap water within a dielectric barrier discharge reactor," *Water research*, vol. 46, no. 19, pp. 6239–6246, 2012.

[73] N. Korichi, O. Aubry, H. Rabat, B. Cagnon, and D. Hong, "Paracetamol degradation by catalyst enhanced non-thermal plasma process for a drastic increase in the mineralization rate," *Catalysts*, vol. 10, no. 9, p. 959, 2020.

[74] M. Magureanu, N. B. Mandache, and V. I. Parvulescu, "Degradation of pharmaceutical compounds in water by non-thermal plasma treatment," *Water research*, vol. 81, pp. 124–136, 2015.

[75] E. Stoffels, A. Flikweert, W. Stoffels, and G. Kroesen, "Plasma needle: a non-destructive atmospheric plasma source for fine surface treatment of (bio) materials," *Plasma Sources Science and Technology*, vol. 11, no. 4, p. 383, 2002.

[76] A. V. Nastuta, I. Topala, C. Grigoras, V. Pohoata, and G. Popa, "Stimulation of wound healing by helium atmospheric pressure plasma treatment," *Journal of Physics D: Applied Physics*, vol. 44, no. 10, p. 105204, 2011.

[77] S. Forster, C. Mohr, and W. Viol, "Investigations of an atmospheric pressure plasma jet by optical emission spectroscopy," *Surface and Coatings Technology*, vol. 200, no. 1-4, pp. 827–830, 2005.

[78] H. Koinuma, H. Ohkubo, T. Hashimoto, K. Inomata, T. Shiraishi, A. Miyanaga, and S. Hayashi, "Development and application of a microbeam plasma generator," *Applied physics letters*, vol. 60, no. 7, pp. 816–817, 1992.

[79] M. Laroussi and T. Akan, "Arc-free atmospheric pressure cold plasma jets: A review," *Plasma Processes and Polymers*, vol. 4, no. 9, pp. 777–788, 2007.

[80] M. Teschke, J. Kedzierski, E. Finantu-Dinu, D. Korzec, and J. Engemann, “High-speed photographs of a dielectric barrier atmospheric pressure plasma jet,” *IEEE Transactions on Plasma Science*, vol. 33, no. 2, pp. 310–311, 2005.

[81] M. Laroussi and X. Lu, “Room-temperature atmospheric pressure plasma plume for biomedical applications,” *Applied Physics Letters*, vol. 87, no. 11, p. 113902, 2005.

[82] P. Cools, N. De Geyter, and R. Morent, “Pla enhanced via plasma technology: a review,” *New Developments in Polylactic Acid Research*, p. 218, 2014.

[83] F. Ibrahim, “Design and construction of low-pressure dc-sputtering plasma system for preparing gas sensors,” *University of Baghdad, PhD. Thesis*, 2013.

[84] A. Schutze, J. Y. Jeong, S. E. Babayan, J. Park, G. S. Selwyn, and R. F. Hicks, “The atmospheric-pressure plasma jet: a review and comparison to other plasma sources,” *IEEE transactions on plasma science*, vol. 26, no. 6, pp. 1685–1694, 1998.

[85] J. Hopwood, C. Guarnieri, S. Whitehair, and J. Cuomo, “Langmuir probe measurements of a radio frequency induction plasma,” *Journal of Vacuum Science and Technology A: Vacuum, Surfaces, and Films*, vol. 11, no. 1, pp. 152–156, 1993.

[86] R. Piejak, V. Godyak, and B. Alexandrovich, “The electric field and current density in a low-pressure inductive discharge measured with different b-dot probes,” *Journal of applied physics*, vol. 81, no. 8, pp. 3416–3421, 1997.

[87] D. Vender and R. W. Boswell, “Numerical modeling of low-pressure rf plasmas,” *IEEE Transactions on Plasma Science*, vol. 18, no. 4, pp. 725–732, 1990.

[88] R. J. Mason, “An electromagnetic field algorithm for 2d implicit plasma simulation,” *Journal of Computational Physics*, vol. 71, no. 2, pp. 429–473, 1987.

[89] E. Wagenaars, M. Bowden, and G. Kroesen, “Measuring electric fields with laser-induced fluorescence-dip stark spectroscopy,” *High Temperature Material Processes: An International Quarterly of High-Technology Plasma Processes*, vol. 11, no. 3, 2007.

[90] M. de la Rosa, C. Perez, K. Grutzmacher, A. Gonzalo, and A. Steiger, “Electric field measurements in a hollow cathode discharge by two-photon polarization spectroscopy of atomic deuterium,” *Plasma Sources Science and Technology*, vol. 15, no. 1, p. 105, 2006.

[91] T. L. Chng, A. Brisset, P. Jeanney, S. Starikovskaia, I. Adamovich, and P. Tardiveau, “Electric field evolution in a diffuse ionization wave nanosecond pulse discharge in atmospheric pressure air,” *Plasma Sources Science and Technology*, vol. 28, no. 9, p. 09LT02, 2019.

[92] M. S. Simeni, E. Baratte, Y.-C. Hung, K. Frederickson, and I. Adamovich, “Ps four-wave mixing measurements of electric field in a ns pulse discharge in a hydrogen diffusion flame,” *Proceedings of the Combustion Institute*, vol. 37, no. 2, pp. 1497–1504, 2019.

[93] H. A. Bethe and E. E. Salpeter, *Quantum mechanics of one-and two-electron atoms*. Springer Science and Business Media, 2012.

[94] H. Haken and H. C. Wolf, *The physics of atoms and quanta: introduction to experiments and theory*, vol. 1439. Springer Science and Business Media, 2005.

[95] I. I. Sobelman, *Atomic spectra and radiative transitions*, vol. 12. Springer Science and Business Media, 2012.

[96] M. Hofmans, *Experimental characterization of helium plasma jets*. PhD thesis, Institut Polytechnique de Paris -Eindhoven, Pays-Bas, 2020.

[97] U. Czarnetzki, D. Luggenholscher, and H. Dobele, “Sensitive electric field measurement by fluorescence-dip spectroscopy of rydberg states of atomic hydrogen,” *Physical review letters*, vol. 81, no. 21, p. 4592, 1998.

[98] T. Freegarde and G. Hancock, “A guide to laser-induced fluorescence diagnostics in plasmas,” *Le Journal de Physique IV*, vol. 7, no. C4, pp. C4–15, 1997.

[99] D. Riès, G. Dilecce, E. Robert, P. Ambrico, S. Dozias, and J. M. Pouvesle, “Lif and fast imaging plasma jet characterization relevant for ntp biomedical applications,” *Journal of Physics D: Applied Physics*, vol. 47, no. 27, p. 275401, 2014.

[100] W. R. Lempert, S. P. Kearney, and E. V. Barnat, “Diagnostic study of four-wave-mixing-based electric-field measurements in high-pressure nitrogen plasmas,” *Applied optics*, vol. 50, no. 29, pp. 5688–5694, 2011.

[101] V. Gavrilenko, E. Kupriyanova, D. Okolokulak, V. Ochkin, and S. SAVINOV, “Generation of coherent ir light on a dipole-forbidden molecular transition with nbiharmonic puming in a static electric field,” *JETP letters*, vol. 56, no. 1, pp. 1–4, 1992.

[102] M. S. Simeni, B. M. Goldberg, C. Zhang, K. Frederickson, W. R. Lempert, and I. V. Adamovich, “Electric field measurements in a nanosecond pulse discharge in atmospheric air,” *Journal of Physics D: Applied Physics*, vol. 50, no. 18, p. 184002, 2017.

[103] T. Hoder, D. Loffhagen, J. Voráč, M. Becker, and R. Brandenburg, “Analysis of the electric field development and the relaxation of electron velocity distribution function for nanosecond breakdown in air,” *Plasma Sources Science and Technology*, vol. 25, no. 2, p. 025017, 2016.

[104] S. Muller, T. Ito, K. Kobayashi, D. Luggenholscher, U. Czarnetzki, and S. Hamaguchi, “Electric field measurements in near-atmospheric pressure nitrogen and air based on a four-wave mixing scheme,” *Journal of Physics: Conference Series*, vol. 227, no. 1, p. 012040, 2010.

[105] B. M. Goldberg, T. L. Chng, A. Dogariu, and R. B. Miles, “Electric field measurements in a near atmospheric pressure nanosecond pulse discharge with picosecond electric field induced second harmonic generation,” *Applied Physics Letters*, vol. 112, no. 6, p. 064102, 2018.

[106] Y. Cui, C. Zhuang, and R. Zeng, “Electric field measurements in plasma based on electric field induced second harmonic generation (e-fish) with nanosecond/picosecond laser,” *IEEE*, pp. 1–5, 2020.

[107] K. Orr, Y. Tang, M. S. Simeni, D. Van Den Bekerom, and I. V. Adamovich, “Measurements of electric field in an atmospheric pressure helium plasma jet by the e-fish method,” *Plasma Sources Science and Technology*, vol. 29, no. 3, p. 035019, 2020.

[108] K. Hidaka, “Electric field and voltage measurement by using electro-optic sensor,” *High Voltage Engineering Symposium*, vol. 2, 1999.

[109] J. C. Santos, M. C. Taplamacioglu, and K. Hidaka, “Optical high voltage measurement using pockels microsingle crystal,” *Review of scientific instruments*, vol. 70, no. 8, pp. 3271–3276, 1999.

[110] G. Gaborit, J.-L. Coutaz, and L. Duvillaret, “Vectorial electric field measurement using isotropic electro-optic crystals,” *Applied physics letters*, vol. 90, no. 24, p. 241118, 2007.

[111] G. Gaborit, P. Jarrige, Y. Gaeremynck, A. Warzecha, M. Bernier, J.-L. Lasserre, and L. Duvillaret, “Pockels effect-based probe for uwb and hpem measurements,” pp. 411–421, 2014.

[112] F. Behague, V. Calero, A. Coste, A. Godet, M. Suarez, G. Gaborit, L. Duvillaret, F. I. Baida, M.-P. Bernal, and N. Courjal, “Minimally invasive optical sensors for microwave-electric-field exposure measurements,” *Journal of Optical Microsystems*, vol. 1, no. 2, p. 020902, 2021.

[113] G. Gaborit, P. Jarrige, F. Lecoche, J. Dahdah, E. Duraz, C. Volat, and L. Duvillaret, “Single shot and vectorial characterization of intense electric field in various environments with pigtailed electrooptic probe,” *IEEE Transactions on Plasma Science*, vol. 42, no. 5, pp. 1265–1273, 2014.

[114] G. Gaborit, “Mesure vectorielle de champ electrique dc-thz par voie optique,” *HDR, Universite de Savoie Mont Blanc*, 2014.

[115] G. Gaborit, J. Dahdah, F. Lecoche, P. Jarrige, Y. Gaeremynck, E. Duraz, and L. Duvillaret, “A nonperturbative electrooptic sensor for in situ electric discharge characterization,” *IEEE Transactions on Plasma Science*, vol. 41, no. 10, pp. 2851–2857, 2013.

[116] F. Aljammal, G. Gaborit, G. Revillod, S. Iséni, and L. Duvillaret, “Optical probe for the real time and vectorial analysis of the electric field induced by ionized gazes,” *24th International Symposium on Plasma Chemistry Conference*, 2019.

[117] F. Aljammal, G. Gaborit, L. Galtier, G. Revillod, S. Iseni, R. Dussart, and L. Duvillaret, “Vectorial electric field characterization of plasmas using an optical probe,” *APS Annual Gaseous Electronics Meeting Abstracts, Conference GEC*, pp. LW1–085, 2018.

[118] J.-L. Coutaz, *Opto electronique terahertz.* EDP Sciences, 2012.

[119] P. G. de Alaiza Martinez, *Generation of intense terahertz sources by ultrashort laser pulses*. PhD thesis, Universite Paris-Saclay, 2016.

[120] G. P. Williams, “High–power terahertz synchrotron sources,” *Philosophical Transactions of the Royal Society of London. Series A: Mathematical, Physical and Engineering Sciences*, vol. 362, no. 1815, pp. 403–414, 2004.

[121] A. Al-Ibadi, *Terahertz imaging and spectroscopy of biomedical tissues: application to breast cancer detection*. PhD thesis, Bordeaux, 2018.

[122] S. Dhillon, M. Vitiello, E. Linfield, A. Davies, M. C. Hoffmann, J. Booske, C. Paoloni, M. Gensch, P. Weightman, G. Williams, *et al.*, “The 2017 terahertz science and technology roadmap,” *Journal of Physics D: Applied Physics*, vol. 50, no. 4, p. 043001, 2017.

[123] P. Han and X. Zhang, “Free-space coherent broadband terahertz time-domain spectroscopy,” *Measurement Science and Technology*, vol. 12, no. 11, p. 1747, 2001.

[124] B. Ferguson and X.-C. Zhang, “Materials for terahertz science and technology,” *Nature materials*, vol. 1, no. 1, pp. 26–33, 2002.

[125] P. G. Kryukov, “Continuous-wave femtosecond lasers,” *Physics-Uspekhi*, vol. 56, no. 9, p. 849, 2013.

[126] W. Ghann and J. Uddin, “Terahertz (thz) spectroscopy: A cutting-edge technology,” *Terahertz Spectroscopy-A Cutting Edge Technology*, 2017.

[127] J. Bourdet *Le journal CNRS, link: https://lepetitjournal.com/metro-shanghai-modifications-chinese-new-year*, 2018.

[128] K. Ahi, N. Jessurun, M.-P. Hosseini, and N. Asadizanjani, “Survey of terahertz photonics and biophotonics,” *Optical Engineering*, vol. 59, no. 6, p. 061629, 2020.

[129] X. Ropagnol, *Developpement dune source de radiation terahertz (THz) intense et mise en forme dimpulsions THz a partir dune antenne de grande ouverture de ZnSe.* PhD thesis, Université du Québec, Institut national de la recherche scientifique, 2013.

[130] E. Berry, G. C. Walker, A. J. Fitzgerald, N. Zinovev, M. Chamberlain, S. W. Smye, R. E. Miles, and M. A. Smith, “Do in vivo terahertz imaging systems comply with safety guidelines,” *Journal of Laser Applications*, vol. 15, no. 3, pp. 192–198, 2003.

[131] R. A. Lewis, “A review of terahertz sources,” *Journal of Physics D: Applied Physics*, vol. 47, no. 37, p. 374001, 2014.

[132] C. Thacker, A. Cooray, J. Smidt, F. De Bernardis, K. Mitchell-Wynne, A. Amblard, R. Auld, M. Baes, D. Clements, A. Dariush, *et al.*, “H-atlas: the cosmic abundance of dust from the far-infrared background power spectrum,” *The Astrophysical Journal*, vol. 768, no. 1, p. 58, 2013.

[133] A. Maestrini, J. S. Ward, J. J. Gill, C. Lee, B. Thomas, R. H. Lin, G. Chattopadhyay, and I. Mehdi, “A frequency-multiplied source with more than 1 mw of power across the 840–900-ghz band,” *IEEE transactions on microwave theory and techniques*, vol. 58, no. 7, pp. 1925–1932, 2010.

[134] X. Wu, S. Xiong, Z. Liu, J. Chen, J. Shen, T. Li, P. Wu, and P. K. Chu, “Green light stimulates terahertz emission from mesocrystal microspheres,” *Nature Nanotechnology*, vol. 6, no. 2, pp. 103–106, 2011.

[135] W. He, C. Donaldson, L. Zhang, K. Ronald, P. McElhinney, and A. Cross, “High power wideband gyrotron backward wave oscillator operating towards the terahertz region,” *Physical Review Letters*, vol. 110, no. 16, p. 165101, 2013.

[136] Y. Chassagneux, R. Colombelli, W. Maineult, S. Barbieri, H. Beere, D. Ritchie, S. Khanna, E. Linfield, and A. G. Davies, “Electrically pumped photonic-crystal terahertz lasers controlled by boundary conditions,” *Nature*, vol. 457, no. 7226, pp. 174–178, 2009.

[137] D. Cortie and R. Lewis, “Terahertz surfoluminescence,” *Surface science*, vol. 606, no. 21-22, pp. 1573–1576, 2012.

[138] D. Auston, “Subpicosecond electro-optic shock waves,” *Applied Physics Letters*, vol. 43, no. 8, pp. 713–715, 1983.

[139] P. R. Smith, D. H. Auston, and M. C. Nuss, “Subpicosecond photoconducting dipole antennas,” *IEEE Journal of Quantum Electronics*, vol. 24, no. 2, pp. 255–260, 1988.

[140] C. Fattinger and D. Grischkowsky, “Terahertz beams,” *Applied Physics Letters*, vol. 54, no. 6, pp. 490–492, 1989.

[141] C. Fattinger and D. Grischkowsky, “Point source terahertz optics,” *Applied Physics Letters*, vol. 53, no. 16, pp. 1480–1482, 1988.

[142] X. Ropagnol, R. Morandotti, T. Ozaki, and M. Reid, “Thz pulse shaping and improved optical to thz conversion efficiency using a binary phase mask,” *Optics letters*, vol. 36, no. 14, pp. 2662–2664, 2011.

[143] E. Isgandarov, X. Ropagnol, M. Singh, and T. Ozaki, “Intense terahertz generation from photoconductive antennas,” *Frontiers of Optoelectronics*, pp. 1–30, 2021.

[144] M. C. Hoffmann and J. A. Fülöp, “Intense ultrashort terahertz pulses: generation and applications,” *Journal of Physics D: Applied Physics*, vol. 44, no. 8, p. 083001, 2011.

[145] S. V. Sazonov, “Optical methods for the generation of terahertz radiation and subterahertz acoustics of solids,” *JETP letters*, vol. 96, no. 4, pp. 263–274, 2012.

[146] X.-C. Zhang, X. Ma, Y. Jin, T.-M. Lu, E. Boden, P. Phelps, K. Stewart, and C. Yakymyshyn, “Terahertz optical rectification from a nonlinear organic crystal,” *Applied Physics Letters*, vol. 61, no. 26, pp. 3080–3082, 1992.

[147] M. Bass, P. Franken, J. Ward, and G. Weinreich, “Optical rectification,” *Physical Review Letters*, vol. 9, no. 11, p. 446, 1962.

[148] P. E. Powers and J. W. Haus, *Fundamentals of nonlinear optics*. 2017.

[149] L. Gillette, *Systeme de mesure de champ electrique pour la caracterisation sans contact, vectorielle et a grande dynamique de la tension basse frequence en environnement industriel*. PhD thesis, Universite Grenoble Alpes (ComUE), 2016.

[150] “Znte crytsal,” *website: https://www.webelements.com/compounds/zinc/zinc*$_t$*elluride.html*.

[151] S. Vidal, *Etude theorique et experimentale de la generation et de la mise en forme d’impulsions terahertz*. PhD thesis, Universite Sciences et Technologies Bordeaux I, 2009.

[152] K. K. Kohli, A. Vaupel, S. Chatterjee, and W. W. Rühle, “Adaptive shaping of thz-pulses generated in< 110> znte crystals,” *JOSA B*, vol. 26, no. 9, pp. A74–A78, 2009.

[153] D. Li and G. Ma, “Pump-wavelength dependence of terahertz radiation via optical rectification in (110)-oriented znte crystal,” *Journal of Applied Physics*, vol. 103, no. 12, p. 123101, 2008.

[154] S. Gupta, J. Pamulatpati, J. Chwalek, P. Bhattacharya, G. Mourou, C. Harris, E. Ippen, G. Mourou, and A. Zewail, “Ultrafast phenomena vii.,” *Springer Series in Chemical Physics*, vol. 53, 1990.

[155] H. Hamster, A. Sullivan, S. Gordon, W. White, and R. Falcone, “Subpicosecond, electromagnetic pulses from intense laser-plasma interaction,” *Physical review letters*, vol. 71, no. 17, p. 2725, 1993.

[156] H. Hamster, A. Sullivan, S. Gordon, and R. Falcone, “Short-pulse terahertz radiation from high-intensity-laser-produced plasmas,” *Physical Review E*, vol. 49, no. 1, p. 671, 1994.

[157] D. Auston and P. Smith, “Generation and detection of millimeter waves by picosecond photoconductivity,” *Applied Physics Letters*, vol. 43, no. 7, pp. 631–633, 1983.

[158] S. Wunderlich, “Electro-optic sampling of thz pulses at the ctr source at flash,” 2012.

[159] W. L. Chan, J. Deibel, and D. M. Mittleman, “Imaging with terahertz radiation,” *Reports on progress in physics*, vol. 70, no. 8, p. 1325, 2007.

[160] Y.-S. Lee, *Principles of terahertz science and technology*, vol. 170. Springer Science & Business Media, 2009.

[161] D. H. Auston, K. Cheung, J. Valdmanis, and D. Kleinman, "Cherenkov radiation from femtosecond optical pulses in electro-optic media," *Physical Review Letters*, vol. 53, no. 16, p. 1555, 1984.

[162] N. F. Scherer, R. J. Carlson, A. Matro, M. Du, A. J. Ruggiero, V. Romero-Rochin, J. A. Cina, G. R. Fleming, and S. A. Rice, "Fluorescence-detected wave packet interferometry: Time resolved molecular spectroscopy with sequences of femtosecond phase-locked pulses," *The Journal of chemical physics*, vol. 95, no. 3, pp. 1487–1511, 1991.

[163] G. Soylu, *Sub-wavelength microscopy techniques in the TeraHertz frequency range*. PhD thesis, Université Grenoble Alpes, 2020.

[164] N. Karpowicz, J. Dai, X. Lu, Y. Chen, M. Yamaguchi, H. Zhao, X.-C. Zhang, L. Zhang, C. Zhang, M. Price-Gallagher, *et al.*, "Coherent heterodyne time-domain spectrometry covering the entire terahertz gap," *Applied Physics Letters*, vol. 92, no. 1, p. 011131, 2008.

[165] J. Dai, X. Xie, and X.-C. Zhang, "Detection of broadband terahertz waves with a laser-induced plasma in gases," *Physical review letters*, vol. 97, no. 10, p. 103903, 2006.

[166] T. Wang, K. Iwaszczuk, E. A. Wrisberg, E. V. Denning, and P. U. Jepsen, "Linearity of air-biased coherent detection for terahertz time-domain spectroscopy," *Journal of Infrared, Millimeter, and Terahertz Waves*, vol. 37, no. 6, pp. 592–604, 2016.

[167] A. Nahata and T. F. Heinz, "Detection of freely propagating terahertz radiation by use of optical second-harmonic generation," *Optics letters*, vol. 23, no. 1, pp. 67–69, 1998.

[168] Z. Lü, D. Zhang, C. Meng, L. Sun, Z. Zhou, Z. Zhao, and J. Yuan, "Polarization-sensitive air-biased-coherent-detection for terahertz wave," *Applied Physics Letters*, vol. 101, no. 8, p. 081119, 2012.

[169] F. Treussart, *Cours optique anisotrope*. 2008.

[170] A. Yariv, *Optical electronics*. Saunders College Publishing, 1991.

[171] L. Duvillaret, S. Rialland, and J.-L. Coutaz, "Electro-optic sensors for electric field measurements. ii. choice of the crystals and complete optimization of their orientation," *JOSA B*, vol. 19, no. 11, pp. 2704–2715, 2002.

[172] G. Gaborit, A. Biciunas, M. Bernier, and J.-L. Coutaz, "Emitting and receiving terahertz vectorial antennas based on cubic electro-optic crystals," *IEEE Transactions on Terahertz Science and Technology*, vol. 5, no. 5, pp. 828–835, 2015.

[173] S. Wakana, T. Ohara, M. Abe, E. Yamazaki, M. Kishi, and M. Tsuchiya, "Fiber-edge electrooptic/magnetooptic probe for spectral-domain analysis of electromagnetic field," *IEEE Transactions on Microwave Theory and Techniques*, vol. 48, no. 12, pp. 2611–2616, 2000.

[174] U. Srico company *website: https://www.srico.com/*.

[175] L. Duvillaret and G. Gaborit, "Kapteos company," *website: https://www.kapteos.com/*.

[176] M. Bernier, G. Gaborit, L. Duvillaret, A. Paupert, and J.-L. Lasserre, "Electric field and temperature measurement using ultra wide bandwidth pigtailed electro-optic probes," *Applied optics*, vol. 47, no. 13, pp. 2470–2476, 2008.

[177] Y. Gaeremynck, G. Gaborit, L. Duvillaret, M. Ruaro, and F. Lecoche, "Two electric-field components measurement using a 2 port pigtailed electro-optic sensor," *Applied Physics Letters*, vol. 99, no. 14, p. 141102, 2011.

[178] Y. Gaeremynck, G. Gaborit, L. Duvillaret, M. Ruaro, and F. Lecoche, "Two electric-field components measurement using a 2-port pigtailed electro-optic sensor," *Applied Physics Letters*, vol. 99, no. 14, p. 141102, 2011.

[179] J. Jarrige, M. Laroussi, and E. Karakas, "Formation and dynamics of plasma bullets in a non-thermal plasma jet: influence of the high-voltage parameters on the plume characteristics," *Plasma Sources Science and Technology*, vol. 19, no. 6, p. 065005, 2010.

[180] "Altechna company," *website: https://www.altechna.com/*.

[181] Z. Navratil, R. Brandenburg, D. Trunec, A. Brablec, P. Stahel, H.-E. Wagner, and Z. Kopecky, "Comparative study of diffuse barrier discharges in neon and helium," *Plasma Sources Science and Technology*, vol. 15, no. 1, p. 8, 2005.

[182] F. Aljammal, G. Gaborit, M. Bernier, S. Iseni, L. Galtier, G. Revillod, and L. Duvillaret, "Pigtailed electro-optic sensor for time and space resolved dielectric barrier discharges analysis," *IEEE Transactions on Instrumentation and Measurement*, 2021.

[183] K. H. Becker, U. Kogelschatz, K. Schoenbach, and R. Barker, *Non-equilibrium air plasmas at atmospheric pressure*. CRC press, 2004.

[184] D. B. Graves, "Low temperature plasma biomedicine: A tutorial review," *Physics of Plasmas*, vol. 21, no. 8, p. 080901, 2014.

[185] T. Von Woedtke, S. Reuter, K. Masur, and K.-D. Weltmann, "Plasmas for medicine," *Physics Reports*, vol. 530, no. 4, pp. 291–320, 2013.

[186] M. Laroussi, X. Lu, and M. Keidar, "Perspective: The physics, diagnostics, and applications of atmospheric pressure low temperature plasma sources used in plasma medicine," *Journal of Applied Physics*, vol. 122, no. 2, p. 020901, 2017.

[187] E. Martines, "Plasma technology for biomedical applications," *Multidisciplinary Digital Publishing Institute*, 2020.

[188] J. Shen, C. Cheng, S. Fang, H. Xie, Y. Lan, G. Ni, Y. Meng, J. Luo, and X. Wang, "Sterilization of bacillus subtilis spores using an atmospheric plasma jet with argon and oxygen mixture gas," *Applied Physics Express*, vol. 5, no. 3, p. 036201, 2012.

[189] J.-P. Lim, H. S. Uhm, and S.-Z. Li, "Influence of oxygen in atmospheric-pressure argon plasma jet on sterilization of bacillus atrophaeous spores," *Physics of plasmas*, vol. 14, no. 9, p. 093504, 2007.

[190] K. Lotfy, "The impact of the carrier gas composition of non-thermal atmospheric pressure plasma jet for bacteria sterilization," *AIP Advances*, vol. 10, no. 1, p. 015303, 2020.

[191] X. Lu, M. Laroussi, and V. Puech, "On atmospheric-pressure non-equilibrium plasma jets and plasma bullets," *Plasma Sources Science and Technology*, vol. 21, no. 3, p. 034005, 2012.

[192] X. Lu, Z. Jiang, Q. Xiong, Z. Tang, and Y. Pan, "A single electrode room-temperature plasma jet device for biomedical applications," *Applied Physics Letters*, vol. 92, no. 15, pp. 151–504, 2008.

[193] G. Park, S. Park, M. Choi, I. Koo, J. Byun, J. Hong, J. Sim, G. Collins, and J. Lee, "Atmospheric-pressure plasma sources for biomedical applications," *Plasma Sources Science and Technology*, vol. 21, no. 4, p. 043001, 2012.

[194] P. Attri, K. Ishikawa, T. Okumura, K. Koga, and M. Shiratani, "Plasma agriculture from laboratory to farm: A review," *Processes*, vol. 8, no. 8, p. 1002, 2020.

[195] U. M. Ekanayake, D. H. Seo, K. Faershteyn, A. P. O Mullane, H. Shon, J. MacLeod, D. Golberg, and K. K. Ostrikov, "Atmospheric-pressure plasma seawater desalination: Clean energy, agriculture, and resource recovery nexus for a blue planet," *Sustainable Materials and Technologies*, vol. 25, p. e00181, 2020.

[196] B. Surowsky, O. Schluter, and D. Knorr, "Interactions of non-thermal atmospheric pressure plasma with solid and liquid food systems: a review," *Food Engineering Reviews*, vol. 7, no. 2, pp. 82–108, 2015.

[197] A. Maroofi, N. N. Safa, and H. Ghomi, "Atmospheric air plasma jet for improvement of paint adhesion to aluminium surface in industrial applications," *International Journal of Adhesion and Adhesives*, vol. 98, p. 102554, 2020.

[198] T. Mui, L. Silva, V. Prysiazhnyi, and K. Kostov, "Polyurethane paint adhesion improvement on aluminium alloy treated by plasma jet and dielectric barrier discharge," *Journal of adhesion science and Technology*, vol. 30, no. 2, pp. 218–229, 2016.

[199] A. Sobota, O. Guaitella, and A. Rousseau, "The influence of the geometry and electrical characteristics on the formation of the atmospheric pressure plasma jet," *Plasma sources science and technology*, vol. 23, no. 2, p. 025016, 2014.

[200] Z.-S. Chang, G.-J. Zhang, X.-J. Shao, and Z.-H. Zhang, "Diagnosis of gas temperature, electron temperature, and electron density in helium atmospheric pressure plasma jet," *Physics of Plasmas*, vol. 19, no. 7, p. 073513, 2012.

[201] M. Ghasemi, P. Olszewski, J. Bradley, and J. Walsh, "Interaction of multiple plasma plumes in an atmospheric pressure plasma jet array," *Journal of Physics D: Applied Physics*, vol. 46, no. 5, p. 052001, 2013.

[202] C. Douat, G. Bauville, M. Fleury, M. Laroussi, and V. Puech, "Dynamics of colliding microplasma jets," *Plasma Sources Science and Technology*, vol. 21, no. 3, p. 034010, 2012.

[203] T. Gerling, T. Hoder, R. Brandenburg, R. Bussiahn, and K. Weltmann, "Influence of the capillary on the ignition of the transient spark discharge," *Journal of Physics D: Applied Physics*, vol. 46, no. 14, p. 145205, 2013.

[204] Q. Xiong, A. Y. Nikiforov, M. A. Gonzalez, C. Leys, and X. P. Lu, "Characterization of an atmospheric helium plasma jet by relative and absolute optical emission spectroscopy," *Plasma Sources Science and Technology*, vol. 22, no. 1, p. 015011, 2012.

[205] T. Murakami, K. Niemi, T. Gans, D. OConnell, and W. G. Graham, "Chemical kinetics and reactive species in atmospheric pressure helium–oxygen plasmas with humid-air impurities," *Plasma Sources Science and Technology*, vol. 22, no. 1, p. 015003, 2012.

[206] R. P. Guragain, S. Gautam, D. P. Subedi, and R. Shrestha, "Effect of plasma treatment on the surface of polyethylene terephthalate with 50hz dielectric barrier discharge at near-atmospheric pressure," *International Journal of Recent Research and Review*, vol. 9, no. 4, pp. 34–37, 2016.

[207] V. V. Kovacevic, G. B. Sretenovic, E. Slikboer, O. Guaitella, A. Sobota, and M. M. Kuraica, "The effect of liquid target on a nonthermal plasma jetimaging, electric fields, visualization of gas flow and optical emission spectroscopy," *Journal of Physics D: Applied Physics*, vol. 51, no. 6, p. 065202, 2018.

[208] G. B. Sretenovic, O. Guaitella, A. Sobota, I. B. Krstic, V. V. Kovacevic, B. M. Obradovic, and M. M. Kuraica, "Electric field measurement in the dielectric tube of helium atmospheric pressure plasma jet," *Journal of Applied Physics*, vol. 121, no. 12, p. 123304, 2017.

[209] T. Darny, J.-M. Pouvesle, J. Fontane, L. Joly, S. Dozias, and E. Robert, "Plasma action on helium flow in cold atmospheric pressure plasma jet experiments," *Plasma Sources Science and Technology*, vol. 26, no. 10, p. 105001, 2017.

[210] J. L. Walsh, F. Iza, N. B. Janson, V. Law, and M. G. Kong, "Three distinct modes in a cold atmospheric pressure plasma jet," *Journal of Applied Physics*, vol. 43, no. 7, p. 075201, 2010.

[211] A. Shrestha, R. Shrestha, H. Baniya, R. Tyata, D. Subedi, and C. Wong, "Influence of discharge voltage and pressure on the plasma parameters in a low pressure dc glow discharge," *relation*, vol. 2, p. 1, 2014.

[212] E. Robert, T. Darny, S. Dozias, S. Iseni, and J.-M. Pouvesle, "New insights on the propagation of pulsed atmospheric plasma streams: From single jet to multi jet arrays," *Physics of plasmas*, vol. 22, no. 12, p. 122007, 2015.

[213] R. Rutkowski, G. Daeschlein, T. von Woedtke, R. Smeets, M. Gosau, and H.-R. Metelmann, "Long-term risk assessment for medical application of cold atmospheric pressure plasma," *Diagnostics*, vol. 10, no. 4, p. 210, 2020.

[214] G. B. Sretenovic, I. B. Krstic, V. V. Kovacevic, B. M. Obradovic, and M. M. Kuraica, "Spatio-temporally resolved electric field measurements in helium plasma jet," *Journal of Physics D: Applied Physics*, vol. 47, no. 10, p. 102001, 2014.

[215] H. B. Baniya, R. P. Guragain, B. Baniya, and D. P. Subedi, "Cold atmospheric pressure plasma jet for the improvement of wettability of polypropylene," *International Journal of Polymer Science*, 2020.

[216] A. Sobota, O. Guaitella, and E. Garcia-Caurel, "Experimentally obtained values of electric field of an atmospheric pressure plasma jet impinging on a dielectric surface," *Journal of Physics D: Applied Physics*, vol. 46, no. 37, p. 372001, 2013.

[217] E. Slikboer, O. Guaitella, and A. Sobota, "Time-resolved electric field measurements during and after the initialization of a khz plasma jetfrom streamers to guided streamers," *Plasma Sources Science and Technology*, vol. 25, no. 3, p. 03LT04, 2016.

[218] E. Robert, T. Darny, S. Dozias, S. Iseni, and J.-M. Pouvesle, "New insights on the propagation of pulsed atmospheric plasma streams: From single jet to multi jet arrays," *Physics of plasmas*, vol. 22, no. 12, p. 122007, 2015.

[219] M. Jinno, Y. Ikeda, H. Motomura, Y. Kido, and S. Satoh, "Investigation of plasma induced electrical and chemical factors and their contribution processes to plasma gene transfection," *Archives of biochemistry and biophysics*, vol. 605, pp. 59–66, 2016.

[220] S. A. Norberg, E. Johnsen, and M. J. Kushner, "Helium atmospheric pressure plasma jets interacting with wet cells: delivery of electric fields," *Journal of Physics D: Applied Physics*, vol. 49, no. 18, p. 185201, 2016.

[221] S. Iséni, "Mapping the electric field vector of guided ionization waves at atmospheric pressure," *Plasma Research Express*, vol. 2, no. 2, p. 025014, 2020.

[222] G. Gaborit, J. Dahdah, F. Lecoche, P. Jarrige, Y. Gaeremynck, E. Duraz, and L. Duvillaret, "A nonperturbative electrooptic sensor for in situ electric discharge characterization," *IEEE Transactions on Plasma Science*, vol. 41, no. 10, pp. 2851–2857, 2013.

[223] G. Gaborit, P. Jarrige, F. Lecoche, J. Dahdah, E. Duraz, C. Volat, and L. Duvillaret, "Single shot and vectorial characterization of intense electric field in various environments with pigtailed electrooptic probe," *IEEE Transactions on Plasma Science*, vol. 42, no. 5, pp. 1265–1273, 2014.

[224] R. Wang, H. Xu, Y. Zhao, W. Zhu, C. Zhang, and T. Shao, "Spatial–temporal evolution of a radial plasma jet array and its interaction with material," *Plasma Chemistry and Plasma Processing*, vol. 39, no. 1, pp. 187–203, 2019.

[225] X. Lu and M. Laroussi, "Dynamics of an atmospheric pressure plasma plume generated by submicrosecond voltage pulses," *Journal of applied physics*, vol. 100, no. 6, p. 063302, 2006.

[226] G. V. Prakash, K. Patel, N. Behera, and A. Kumar, "Expansion dynamics of atmospheric pressure helium plasma jet in ambient air," *Physics Letters A*, vol. 384, no. 19, p. 126497, 2020.

[227] T. Darny, J. M. Pouvesle, V. Puech, C. Douat, S. Dozias, and E. Robert, "Analysis of conductive target influence in plasma jet experiments through helium metastable and electric field measurements," *Plasma Sources Science and Technology*, vol. 26, no. 4, p. 045008, 2017.

[228] S. A. Norberg, E. Johnsen, and M. J. Kushner, "Helium atmospheric pressure plasma jets touching dielectric and metal surfaces," *Journal of Applied Physics*, vol. 118, no. 1, p. 013301, 2015.

[229] J. Dai, N. Karpowicz, and X.-C. Zhang, "Coherent polarization control of terahertz waves generated from two-color laser-induced gas plasma," *Physical Review Letters*, vol. 103, no. 2, p. 023001, 2009.

[230] B. Muller, F. Aljammal, G. Gaborit, M. Bernier, E. Hérault, and J.-L. Coutaz, "Femtosecond laser driven plasma for terahertz generation," *24th International Symposium on Plasma Chemistry Conference*, 2019.

[231] D. Cook and R. Hochstrasser, "Intense terahertz pulses by four-wave rectification in air," *Optics letters*, vol. 25, no. 16, pp. 1210–1212, 2000.

[232] K.-Y. Kim, J. H. Glownia, A. J. Taylor, and G. Rodriguez, "Terahertz emission from ultrafast ionizing air in symmetry-broken laser fields," *Optics express*, vol. 15, no. 8, pp. 4577–4584, 2007.

[233] G. V. Naidis, "Modelling of plasma bullet propagation along a helium jet in ambient air," *Journal of Physics D: Applied Physics*, vol. 44, no. 21, p. 215203, 2011.

[234] S. Yonemori, Y. Nakagawa, R. Ono, and T. Oda, "Measurement of OH density and air–helium mixture ratio in an atmospheric-pressure helium plasma jet," *Journal of Physics D: Applied Physics*, vol. 45, no. 22, p. 225202, 2012.

[235] K. Urabe, T. Morita, K. Tachibana, and B. N. Ganguly, “Investigation of discharge mechanisms in helium plasma jet at atmospheric pressure by laser spectroscopic measurements,” *Journal of Physics D: Applied Physics*, vol. 43, no. 9, p. 095201, 2010.

[236] S. Hübner, J. S. Sousa, V. Puech, G. M. W. Kroesen, and N. Sadeghi, “Electron properties in an atmospheric helium plasma jet determined by Thomson scattering,” *Journal of Physics D: Applied Physics*, vol. 47, no. 43, p. 432001, 2014.

[237] F. Théberge, W. Liu, P. T. Simard, A. Becker, and S. L. Chin, “Plasma density inside a femtosecond laser filament in air: Strong dependence on external focusing,” *Physical Review E*, vol. 74, no. 3, p. 036406, 2006.

[238] J. Papeer, M. Botton, D. Gordon, P. Sprangle, A. Zigler, and Z. Henis, “Extended lifetime of high density plasma filament generated by a dual femtosecond–nanosecond laser pulse in air,” *New Journal of Physics*, vol. 16, no. 12, p. 123046, 2014.

[239] K.-Y. Kim, J. H. Glownia, A. J. Taylor, and G. Rodriguez, “Terahertz emission from ultrafast ionizing air in symmetry-broken laser fields,” *Optics Express*, vol. 15, no. 8, p. 4577, 2007.

[240] T. I. Oh, Y. S. You, N. Jhajj, E. W. Rosenthal, H. M. Milchberg, and K. Y. Kim, “Scaling and saturation of high-power terahertz radiation generation in two-color laser filamentation,” *Applied Physics Letters*, vol. 102, no. 20, p. 201113, 2013.

[241] K. Y. Kim, A. J. Taylor, J. H. Glownia, and G. Rodriguez, “Coherent control of terahertz supercontinuum generation in ultrafast laser–gas interactions,” vol. 2, pp. 605–609, Oct. 2008.

[242] P. Chizhov, A. Ushakov, V. Bukin, and S. Garnov, “Terahertz radiation from extended two-colour air filaments,” *Laser Physics Letters*, vol. 16, no. 7, p. 075301, 2019.

[243] B. Muller, *Génération de rayonnements térahertz par plasma photo-généré dans les gaz et à la surface de métaux*. PhD thesis, Université de Grenoble Alpes, 2021.

[244] D. R. Lide, “Crc handbook of chemistry and physics crc,” *Boca Raton*, 2008.

[245] J. Dai, J. Liu, and X.-C. Zhang, “Terahertz wave air photonics: terahertz wave generation and detection with laser-induced gas plasma,” *IEEE Journal of selected topics in Quantum Electronics*, vol. 17, no. 1, pp. 183–190, 2010.

[246] A. Börzsönyi, Z. Heiner, M. Kalashnikov, A. Kovács, and K. Osvay, “Dispersion measurement of inert gases and gas mixtures at 800 nm,” *Applied optics*, vol. 47, no. 27, pp. 4856–4863, 2008.

[247] H. Kogelnik and T. Li, “Laser beams and resonators,” *Applied optics*, vol. 5, no. 10, pp. 1550–1567, 1966.

[248] A. Börzsönyi, Z. Heiner, M. Kalashnikov, A. Kovács, and K. Osvay, “Dispersion measurement of inert gases and gas mixtures at 800 nm,” *Applied optics*, vol. 47, pp. 4856–63, Oct. 2008.

[249] C. Brée, A. Demircan, and G. Steinmeyer, “Saturation of the all-optical Kerr effect,” *Physical review letters*, vol. 106, no. 18, p. 183902, 2011.

[250] Á. Börzsönyi, Z. Heiner, A. P. Kovács, M. P. Kalashnikov, and K. Osvay, “Measurement of pressure dependent nonlinear refractive index of inert gases,” *Optics Express*, vol. 18, no. 25, pp. 25847–25854, 2010.

[251] G. Soylu, *Techniques de microscopie sous-longueur d'onde aux fréquences térahertz.* PhD thesis, Université Grenoble Alpes, 2020.

[252] P. M. Davulis, B. T. Sturtevant, S. L. Duy, and M. P. da Cunha, "P1f-4 revisiting lgt dielectric constants and temperature coefficients up to 120ř c," *2007 IEEE Ultrasonics Symposium Proceedings*, pp. 1397–1400, 2007.

[253] A. Khan and A. Ballato, "Lateral field excitation predictions for plates of langasite and isomorphs driven in simple thickness modes," *Proceedings of the 2000 IEEE EIA International Frequency Control Symposium and Exhibition (Cat. No. 00CH37052)*, pp. 180–185, 2000.

[254] J. Imbaud, G. Douchet, and F. Sthal, "Passive noise analyses on langatate crystal resonators," *2010 IEEE International Frequency Control Symposium*, pp. 419–424, 2010.

[255] B. V. Mifdouatll and Y. V. Pisarevsky, "Langasite-type materials: from discovery to present state," *Proceedings of the 2000 IEEE EIA International Frequency Control Symposium and Exhibition (Cat. No. 00CH37052)*, pp. 133–144, 2000.

[256] P. M. Davulis and M. P. Da Cunha, "High-temperature langatate elastic constants and experimental validation up to 900 degree c," *IEEE transactions on ultrasonics, ferroelectrics, and frequency control*, vol. 57, no. 1, pp. 59–65, 2009.

[257] P. M. Davulis, B. T. Sturtevant, S. L. Duy, and M. P. da Cunha, "P1f-4 revisiting lgt dielectric constants and temperature coefficients up to 120 degree c," pp. 1397–1400, 2007.

[258] Y. V. Pisarevsky, P. Senyushenkov, B. Mill, and N. Moiseeva, "Elastic, piezoelectric, dielectric properties of la sub 3 ga sub 5.5 ta sub 0.5 o sub 14 single crystals," *Proceedings of the 1998 IEEE International Frequency Control Symposium (Cat. No. 98CH36165)*, pp. 742–747, 1998.

[259] J. Bohm, R. Heimann, M. Hengst, R. Roewer, and J. Schindler, "Czochralski growth and characterization of piezoelectric single crystals with langasite structure: La3ga5sio14 (lgs), la3ga5. 5nb0. 5o14 (lgn), and la3ga5. 5ta0. 5o14 (lgt): Part i," *Journal of crystal growth*, vol. 204, no. 1-2, pp. 128–136, 1999.

[260] I. Kaurova, G. Kuzmicheva, V. Rybakov, A. Dubovski, and A. Cousson, "Composition, structural parameters, and color of langatate," *Inorganic Materials*, vol. 46, no. 9, pp. 988–993, 2010.

[261] E. Boursier, P. Segonds, B. Boulanger, C. Felix, J. Debray, D. Jegouso, B. Menaert, D. Roshchupkin, and I. Shoji, "Phase-matching directions, refined sellmeier equations, and second-order nonlinear coefficient of the infrared langatate crystal la 3 ga 5.5 ta 0.5 o 14," *Optics letters*, vol. 39, no. 13, pp. 4033–4036, 2014.

[262] E. Boursier, G. M. Archipovaite, J.-C. Delagnes, S. Petit, G. Ernotte, P. Lassonde, P. Segonds, B. Boulanger, Y. Petit, F. Legarze, *et al.*, "Study of middle infrared difference frequency generation using a femtosecond laser source in lgt," *Optics letters*, vol. 42, no. 18, pp. 3698–3701, 2017.

[263] E. Boursier, G. M. Archipovaite, J.-C. Delagnes, S. Petit, G. Ernotte, P. Lassonde, Y. Petit, P. Segonds, B. Boulanger, F. Legare, *et al.*, "Femtosecond nonlinear interactions in the langatate lgt: Characterization of a new middle infrared nonlinear crystal," *Mid-Infrared Coherent Sources*, pp. MT2C–4, 2018.

[264] J. Stade, L. Bohatỳ, M. Hengst, and R. Heimann, “Electro-optic, piezoelectric and dielectric properties of langasite (la3ga5sio14), langanite (la3ga5. 5nb0. 5o14) and langataite (la3ga5. 5ta0. 5o14),” *Crystal Research and Technology: Journal of Experimental and Industrial Crystallography*, vol. 37, no. 10, pp. 1113–1120, 2002.

Part IV

Appendix

A

Data sheet EO probe

eoProbe™

Patents EP2035845 EP2035846
US7769250 US8264685
CA2655034 CA2655447

MAIN FEATURES

- Electric field probes without any metal and perturbation-free
- Absolute vector E-field measurement from mV/m up to MV/m
- For single shot, repetitive and CW signals from 50 Hz to 60 GHz and +
- For time-domain and frequency-domain measurements
- Ultra harsh environment compatibility like pressure, temperature, X rays and gamma rays
- 5 m optical fiber cord as standard
- For all media like plasma, liquids, biological tissues...
- Ultra high damage threshold (> 10 MV/m and 10 W/cm^2 permanent power density)
- Equivalent to UWB, EMI-free, ultra small antenna (λ/10 @ 60 GHz) with real time compensation of IL variations when used with optoelectronic converter eoSense™
- Intended for use with optoelectronic converters eoSense™

TYPICAL APPLICATIONS

- Antennas characterization
- SAR assessment in phantoms
- Plasma characterization
- MRI compliance for electronic implants
- Field mapping of high voltage devices
- EMC malfunction diagnosis
- EMP measurement

Health
Science
Defence
Aerospace
Telecommunications

PRODUCTS LINE

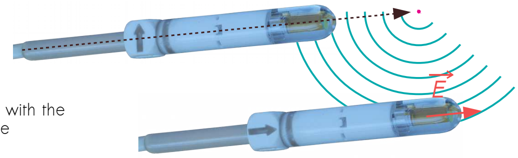

Transverse probes ETX-xxx
- easy to point the source
- easy access to main & cross polarizations

Longitudinal probes ELX-xxx
- perfect for precise alignment with the E field component to measure

Types of probe:
- air probes → measurements in plasma, gases and low κ liquids,
- bio probes for measurements in high κ liquids,
- vac probes for ultra low and high pressure measurements in low κ media.

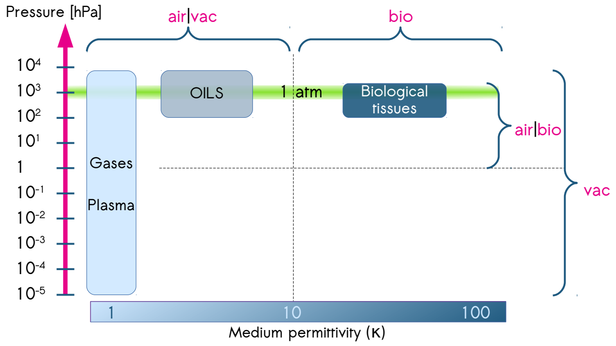

Your **key partner** for **electromagnetism**
in **harsh environment**

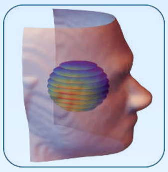

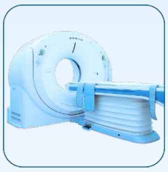

PERFORMANCE SPECIFICATIONS

		Min	Typical	Max	Unit
Frequency bandwidth	**EL5** & **ET5** line	10	12		GHz
	EL1 & **ET1** line	50	60		
Dynamic range		130	135		dB.Hz
Sensitivity in **Time Domain** (E_{min}^{TD}) for f ≥ 3 kHz	**EL5** line		16	20	$\mathrm{mV_{rms}/m.\sqrt{Hz}}$
	ET5-bio probe		25	32	
	EL1 line		64	80	
	ET5-air|vac probe		80	100	
	ET1-bio probe		100	125	
	ET1-air|vac probe		320	400	
Sensitivity in **Frequency Domain** (E_{min}^{FD}) for f ≥ 3 kHz	**EL5** line		40	50	$\mathrm{mV_{rms}/m.\sqrt{Hz}}$
	ET5-bio probe		64	80	
	EL1 line		160	200	
	ET5-air|vac probe		200	250	
	ET1-bio probe		250	320	
	ET1-air|vac probe		800	1 000	
Phase noise	@ 10 Hz from carrier			-70	dBc/Hz
Selectivity (orthog. components rejection)		50	60		dB
Isotropy defined from HPBW	below 100 MHz	300			°
	@ 20 GHz for ET5-air	70	80		
Damage threshold in terms of	E field strength	10			$\mathrm{MV_{rms}/m}$
	perm. power density	10			$\mathrm{W/cm^2}$
Measurement repeatability	for E ≥ 100 x E_{min}		0.15	0.2	dB
Measurement voxel (cylinder)	diameter		0.5	1	mm
	length for **EX5** probe	4.8	5	5.2	
	length for **EX1** probe	0.8	1	1.2	
P1dB (1-dB compression point)	**EL5** line	50			$\mathrm{kV_{rms}/m}$
	ET5-bio probe	80			
	EL1 line	200			
	ET5-air|vac probe	250			
	ET1-bio probe	320			
	ET1-air|vac probe	1 000			
Lower cut-off frequency	**air|vac** probe line		32	40	Hz
	bio probe line		25	32	kHz
Effective relative permittivity (@ 10 MHz)	**air|vac** probe line	3.2	3.6	4.0	
	bio probe line	26	30	34	
Insertion Loss			4.0	6	dB
Antenna factor ***AF*** (@ 500 MHz when probe used directly in combination with optoelectronic converter eoSense MF or HF0.1-XX)	**EL5** line		100	110	dB/m
	ET5-bio probe		105	115	
	EL1 line		110	120	
	ET5-air|vac probe		115	125	
	ET1-bio probe		115	125	
	ET1-air|vac probe		125	135	

---

[1] Half Power Beam Width. HPBW is decreasing with frequency.

USEFUL EQUATIONS

	Equation[2]
Frequency domain	E [dBV$_{rms}$/m] = AF [dB/m] + $P_{eoSense}$ [dBm] - 13.01
Time domain	E [V/m] = AF [m^{-1}] x $V_{eoSense}$ [V]
Conversion of units	AF [dB/m] = 20 log$_{10}$(AF [m^{-1}])
	E [V$_{rms}$/m] = 10^(E [dBV$_{rms}$/m] / 20)

[2] $P_{eoSense}$: power delivered by optoelectronic converter - $V_{eoSense}$: voltage at output of optoelectronic converter

MECHANICAL SPECIFICATIONS

		Min	Typical	Max	Unit
Optical fiber cord length		4.5	**5**	5.5	m
Transducer weight			**2**		g
Overall weight	**air**|**bio** probe line	100	**110**	120	g
	vac probe line	120	**140**	160	
Probe axis marker (ETX)	angular deviation |**δθ**|		2	5	°
	selectivity versus axis marker	20	**27**		dB
Ingress Protection rating[3]	except optical connector		IP67		

[3] Max. 4h in a row in pure water and 1h in salty water

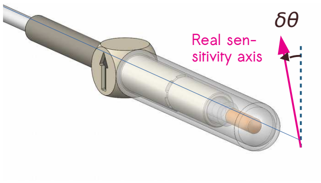

TRANSDUCER - Drawings at scale 1:1 - Dimensions in mm (± 0.1 mm on diameters unless otherwise noted) - Arrow indicating the measured E field component

air line

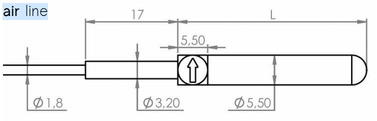

bio line

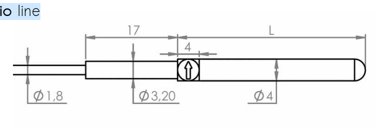

Transducer length (mm)	1	5
Overall length L ± 0.25 (mm)	31.75	34.75

vac line

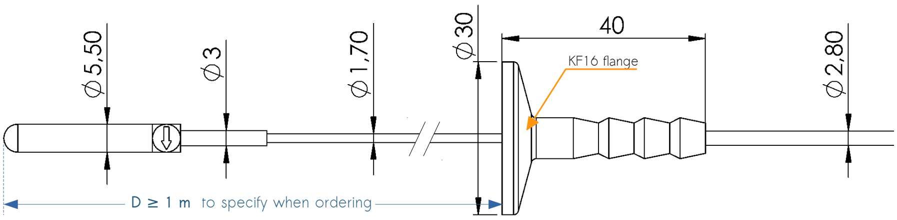

For use in vacuum chamber or in high pressure enclosure

- ultra low out-gassing properties
- down to 1 mPa (10^{-5} mbar)
- up to 700 kPa (7 bar or 100 psig)

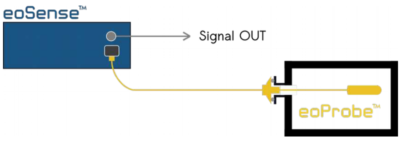

OPTICAL CONNECTOR - Drawings true to scale - Dimensions in mm (± 0.25 mm on diameters unless otherwise noted)

connector-to-eoSense™ front view

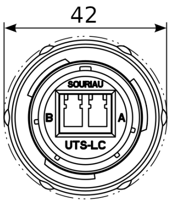

connector-to-eoSense™ side view

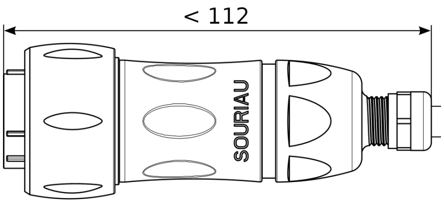

PROBE TAG

for pairing with eoPod™ holder
letter A → E

for pairing with eoSense™ converter
number 1 → 3

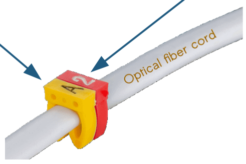

ENVIRONMENTAL SPECIFICATIONS

		Min	Typical	Max	Unit
Fiber bending radius	operating	40			mm
	storage	50			
Temperature	operating	10		50	°C
	storage	10		40	
Pressure	**air**|**bio** line	1		2 000	hPa
	vac line	10^{-5}		7 000	
Out-gassing properties (**vac** line with **PEEK sheath** option: ECSS-Q-70-71A compliant)	CVCM[4]			0.1	%
	RML[5]			1	%
Relative humidity (non-condensing)				90	%
Storage pressure		690		1 075	hPa
Optical connector durability		500			mating
Storage	only in its original case in a clean, dry environment				
Probe cleaning	use cloth lightly moistened with isopropyl alcohol				

[4] Collected Volatile Condensable Material
[5] Recovered Mass Loss

PACKAGING INFORMATION

	Contents
eoProbe™ E-field probe	delivered with a routine test report
Probe protection for handling	protective foam
USB key	probe calibration file, eoSystem software, user guide & routine test report
Transport case (up to 3 probes)	drip-proof and dust-proof case (W x D x H = 430 x 330 x 110 mm - Weight: 2.2 kg)
Other parts (for **vac** line only)	1 KF16 O ring, 1 KF16 clamp
User guide	cf. eoSystem User Guide PDF file GU-eoSystem

COMPATIBLE DEVICES & ACCESSORIES

	Device-related data sheet	Use	Outline schematic
Optoelectronic converter eoSense™	FT20-eoSense-05.pdf	Recommended setup in most cases	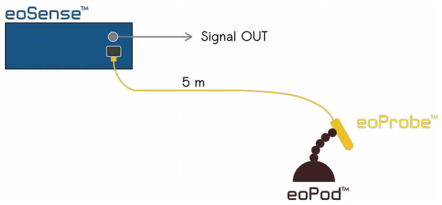
Probe holder eoPod™	FT20-eoPod-05.pdf		
Optical fiber extension cord eoLink™	FT20-eoLink-05.pdf	Required setup for measurements over great distances, like outdoor conditions	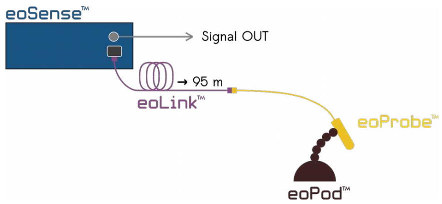
Probe calibration cell eoCal™	FT20-eoCal-05.pdf	Required setup for probe calibration in air or in any fluid	
Probe vacuum feed-through eoVac™	FT20-eoVac-05.pd	Required setup to use air|bio probe line for measurements down to 1 hPa	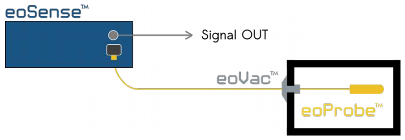

OPTIONS AND CUSTOMIZATION FOR SPECIFIC APPLICATIONS		
Application	Issue	Solution
EMP generation by laser-plasma interaction using PW lasers in vacuum chamber	intense UV, X and γ rays	Additional protective sheath for vac probe 
Measurement of the 3 E-field components in a pressurized hot gases environment	temperature T > 100°C	Water-cooled device for vac probes 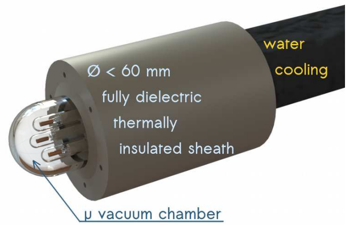 Low | high pressure feed-through 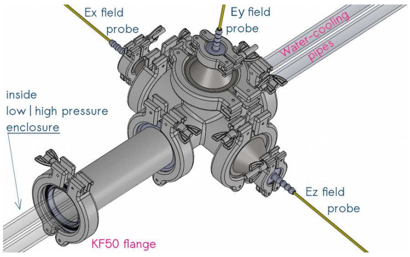
E-field mapping in phantoms for MRI applications and SAR assessment	permittivity matching	Underwater high κ holder for bio probes 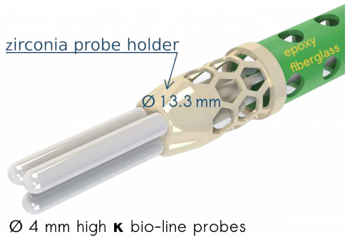
RF measurement of the 3 E-field components in small enclosures	high spatial resolution interference-free	Ultra low κ packaging incorporating 3 probes Dimensions: 12 x 12 x 36 mm 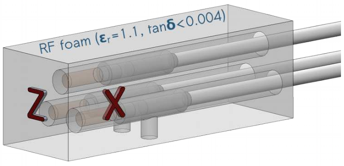

TYPICAL CHARACTERISTICS		
Probe response	DUT and Conditions[7]	Measurement
Spectral purity	probe **eoProbe EL5-air** converter **eoSense MF** E-field applicator **eoCal HF-10**	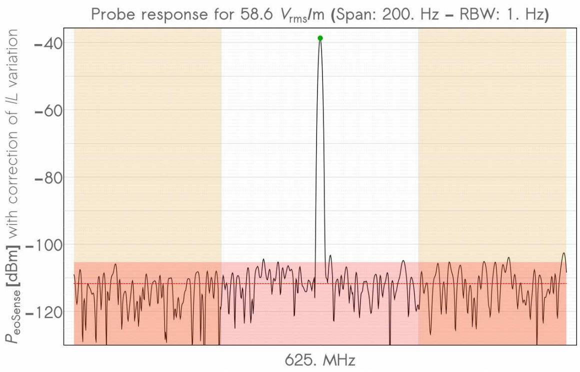
E-field strength	probe **eoProbe EL5-air** converter **eoSense MF** E-field applicator **eoCal HF-10**	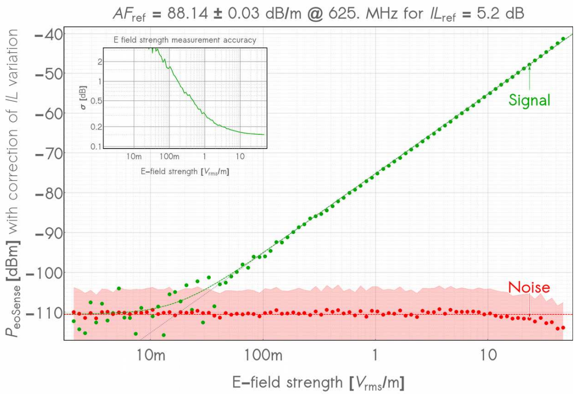
E-field polarization	probe **eoProbe ET5-air** converter **eoSense LF** E-field applicator **eoCal LF-θ**	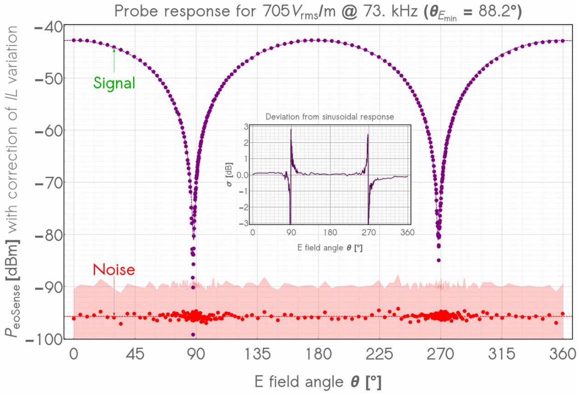

Low-Frequency		
Stationary piezoelectric resonances around 1 MHz	probe **eoProbe EL5-air** converter **eoSense LF** @ high gain (restricted BW) E-field applicator **eoCal HF-10**	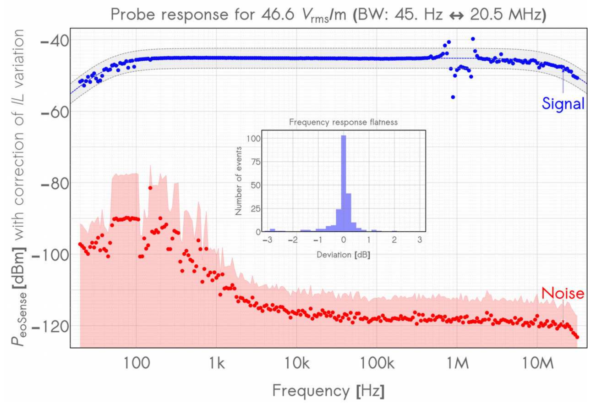

---

[7] All measurements provided above were performed at the following conditions:

- Temperature of 22 ± 2 °C
- Pressure of 985 ± 15 hPa
- Relative humidity of 55 ± 20 %
- DUT warm up time of 30 min
- Test equipment warm up time of 1 hour

🟥 Area corresponding to power values < noise PSD[8] + 3 σ(noise PSD)[9]
Area above which a measuring point has a probability of 0.56% of being noise

[8] Power Spectral Density [dBm/Hz] (red points)

[9] Standard deviation

Kapteos SAS
Bâtiment Cleanspace
354 voie Magellan
73800 Sainte-Hélène du Lac
FRANCE

Email: contact@kapteos.com
☎ +33 (0)4 79 62 88 34

Follow us on

SCAN ME
www.kapteos.com

B

Data sheet eoCal

eoCal™

MAIN FEATURES

- Adiabatic TEM (ATEM) cell with suppression of first higher-order modes
- Operating frequency from DC to 6 GHz
- Electric field strength up to 15 kV_{rms}/m
- 50 Ω characteristic impedance
- Mean VSWR of 1.2
- SMA female connectors
- Ideal for use with electric field probes eoProbe™ with specific holders

TYPICAL APPLICATIONS

- Electric field probe calibration
- SAR studies in Petri dishes
- Exposure of biological media to EM waves
- EMC pre compliance for electronic boards
- HPEM exposure of integrated circuits

Health
Science
Defence
Aerospace
Telecommunications

PRODUCTS LINE

Single model:
- HF6

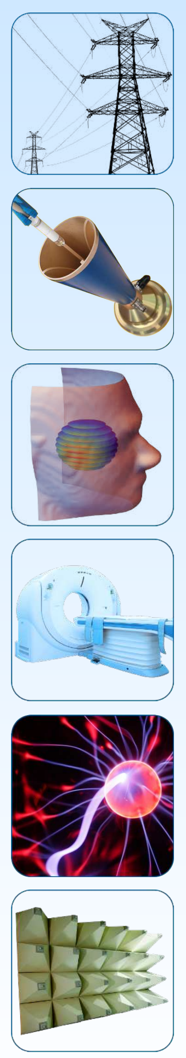

Your **key partner** for **electromagnetism**
in **harsh environment**

PERFORMANCE SPECIFICATIONS

		Min	Typical	Max	Unit
Frequency bandwidth	DC to	6	6.4		GHz
Characteristic impedance			50		Ω
Insertion loss				1	dB
Return loss		12			dB
VSWR[1]			1.20	1.65	
E field strength				2	kV_{rms}/m
Input power				44	dBm
EFSWR[2] (measured inside ATEM cell) @	100 MHz		1.03	1.10	
	126 MHz		1.03	1.10	
	158 MHz		1.03	1.10	
	200 MHz		1.03	1.10	
	251 MHz		1.04	1.10	
	316 MHz		1.04	1.10	
	398 MHz		1.03	1.10	
	501 MHz		1.03	1.10	
	631 MHz		1.03	1.10	
	794 MHz		1.04	1.10	
	1000 MHz		1.03	1.10	
	1260 MHz		1.05	1.20	
	1580 MHz		1.24	1.30	
	2000 MHz		1.07	1.40	
	2510 MHz		1.23	1.45	
	3160 MHz		1.07	1.50	
	3980 MHz		1.17	1.55	
	5010 MHz		1.53	1.60	
	6310 MHz		1.25	1.65	

[1] Voltage Standing Wave Ratio defined by ratio |Vmax|/|Vmin|

[2] Electric Field Standing Wave Ratio defined by ratio |Emax|/|Emin| in the quiet zone of ATEM cell (H ∊ {6.25,11.25} mm and D ∊ {-20,+20} mm)

USEFUL EQUATIONS

	Equation[3]
Electric field strength	E_{ATEM} [dBV_{rms}/m] = P_{ATEM} [dBm] + 22.18
	E_{ATEM} [V_{rms}/m] = 12.85 x 10^(P_{ATEM} [dBm] / 20)

[3] P_{ATEM}: ATEM cell input power - E_{ATEM}: E field strength between ground planes and septum in the central zone of ATEM cell

MECHANICAL SPECIFICATIONS

		Min	Typical	Max	Unit
Overall dimensions	width		108.9		mm
	depth		269.3		
	height		47.3		
Weight			1		kg

ATEM CELL - Drawings at scale 1:2 - Dimensions in mm (± 0.1 mm unless otherwise noted)

front view

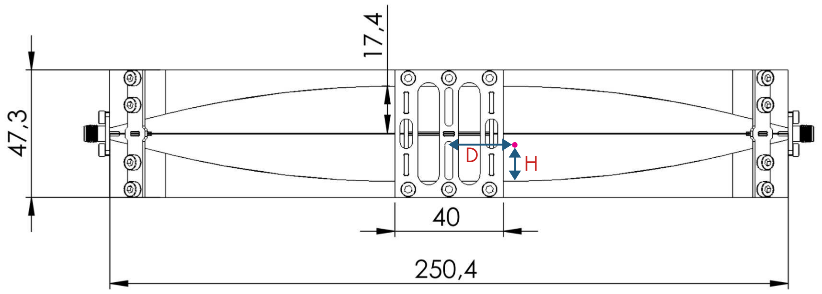

top view

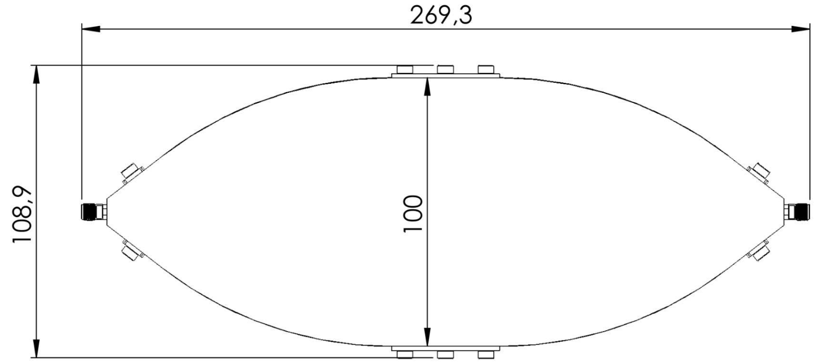

ENVIRONMENTAL SPECIFICATIONS

	Min	Typical	Max	Unit
Temperature	10		50	°C
Pressure	690		2 000	hPa
Relative humidity (non-condensing)			90	%
RF connector durability	500			mating
Storage	only in its original case in a clean, dry environment			
ATEM cell cleaning	use cloth lightly moistened with isopropyl alcohol			

PACKAGING INFORMATION

	Contents
ATEM cell	delivered with a routine test report
Transport case	cardboard with protective foam (W x D x H = 385 x 275 x 80 mm)
User guide	cf. eoSystem User Guide PDF file GU-eoSystem

COMPATIBLE DEVICES & ACCESSORIES

	Device-related data sheet	Use	Outline schematic
Probe calibration cell eoCal™	FT20-eoProbe-09.pdf	Required setup for probe calibration in air or in any fluid	

TYPICAL CHARACTERISTICS		
ATEM cell	DUT and Conditions[4]	Measurement
S parameter	VNA[5] **Anritsu 37 397 C** Calibration **SOLT**	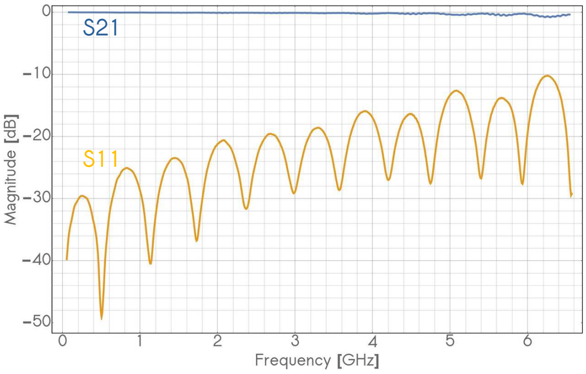
E-field map ✦ 10 points/decade ✦ contour lines every 0.2 dB ✦ 1-mm sampling step	Probe **eoProbe ET5-air** Conv. **eoSense HF-0.1-6.4-1S** Source **Agilent 83640B** Digitizer **Keysight N9030A** see front view for D & H definitions	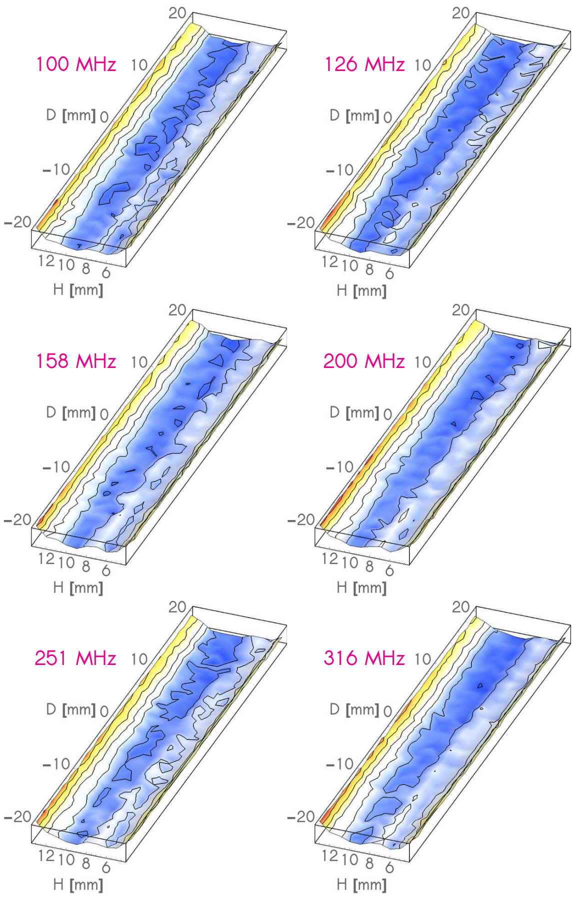

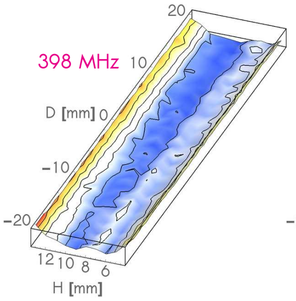
398 MHz
20
10
D [mm] 0
-10
-20
12 10 8 6
H [mm]

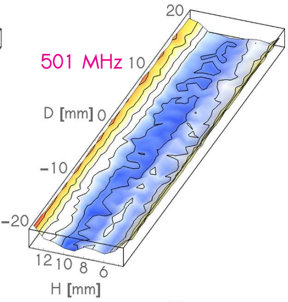
501 MHz
20
10
D [mm] 0
-10
-20
12 10 8 6
H [mm]

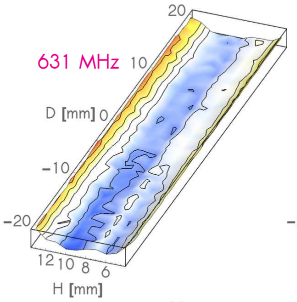
631 MHz
20
10
D [mm] 0
-10
-20
12 10 8 6
H [mm]

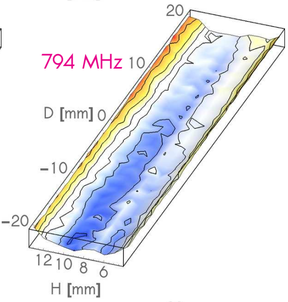
794 MHz
20
10
D [mm] 0
-10
-20
12 10 8 6
H [mm]

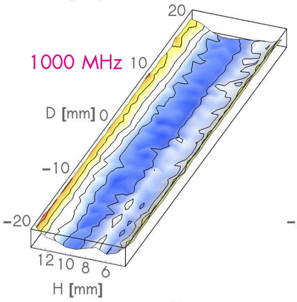
1000 MHz
20
10
D [mm] 0
-10
-20
12 10 8 6
H [mm]

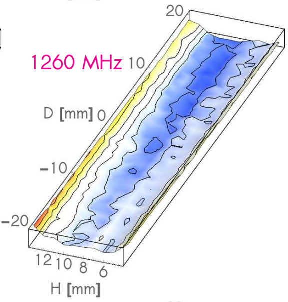
1260 MHz
20
10
D [mm] 0
-10
-20
12 10 8 6
H [mm]

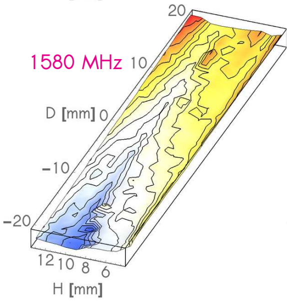
1580 MHz
20
10
D [mm] 0
-10
-20
12 10 8 6
H [mm]

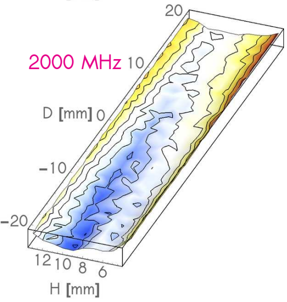
2000 MHz
20
10
D [mm] 0
-10
-20
12 10 8 6
H [mm]

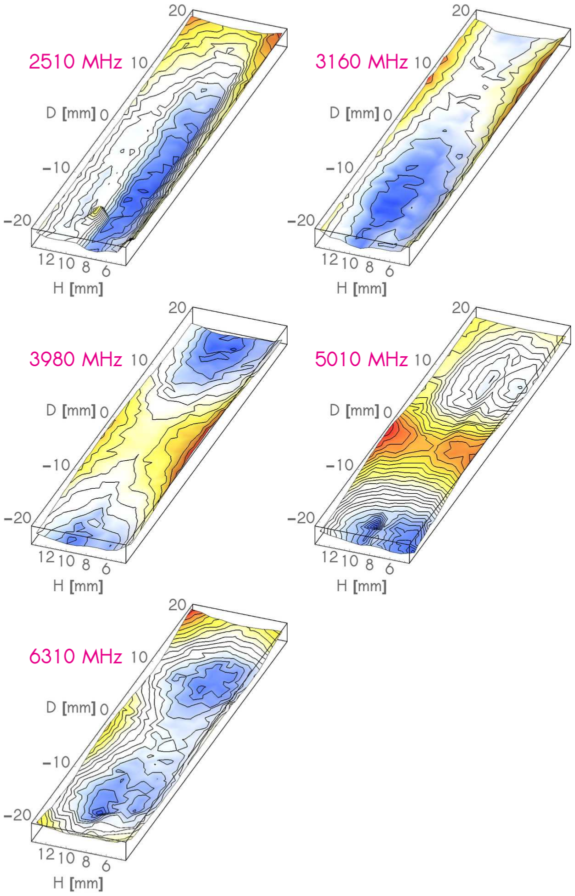

---

[4] All measurements provided above were performed at the following conditions:
- Temperature of 22 ± 2 °C
- Pressure of 985 ± 15 hPa
- Relative humidity of 55 ± 20 %
- Test equipment warm up time of 1 hour

[5] Vector Network Analyzer

C

Optical rectification in a langatate crystal for THz generation

In this chapter we exploit the nonlinear optical behavior of a Langatate crystal (LGT) to generate THz waves by optical rectification of a femtosecond laser pulse. In section C.1 we will recall the definition and the various properties of the LGT crystal. Section C.2 deals with a brief theoretical calculation to estimate the THz E-field generated by optical rectification (OR) in LGT, while Section C.3 presents the experiemntal setup used. A Z-cut crystal is here studied, leading to the emission of THz whatever the impinging polarization state (Section C.4). Also we explore the absorption coefficient and refractive index in the THz range and we investigate quantitatively the damage threshold of the crystal. At long last, the LGT will be discussed as a possible THz emitter by comparing with one of the most used crystals for generating THz waves the "Zinc telluride" (ZnTe). Note that this work has been made in collaboration with Gizem Soylu, a doctor that used to study as a PhD studient in the laboratory [251] and the plateform Crystal Innov.

C.1 Langatate crystal

Definition and properties

Lanthanum Gallium Tantalate is a crystal with the structure of calcium-gallogermanate with chemical formula : (LGT, $La_3Ga_5.5Ta_0.5O_{14}$), which belongs to the langasite family of crystals (LGX) [252–254]. It has been grown for the first time at the University of Moscow, and characterized more intensively in the past decade. These LGX crystals are mainly used for sensors applications due to their piezoelectric properties [255,256], which present no hysteresis, pyroelectric and ferroelectric effects. For those reasons, family of crystals is considered for variety of sound wave applications, including acousto-optic devices, physical, chemical, and biological sensors, filters for wireless and mobile communication, and high-temperature applications [257,258]. Indeed, they present certain advantages compared to traditional piezoelectric materials (piezoceramics and quartz): the phase transition occurs at the melting point (1470°C) [259] and they do not exhibit pyroelectric effect or hysteresis. Moreover, the value of piezoelectric constant d_{11} remains stable in a temperature range up to 600°C and their electrical resistivity is rather high (about 108 Ohm.m). LGT optical properties have also been investigated. This crystal is transparent from a wavelength of 600 nm up to the infrared and its damage threshold is at least six times higher than $LiNbO_3$ [260]. The associated

nonlinear properties demonstrates the possibility to perform second harmonic generation (SHG), sum frequency generation (SFG) and difference frequency generation (DFG) with an efficiency very close to KTP crystal [261–263].
Although LGT crystal has not been considered as possible THz source, it constitutes a good candidate for terahertz (THz) generation using OR of a femtosecond laser pump beam. Thus, we here investigate and demonstrate theoretically and experimentally the possibility to exploit LGT crystal as a THz emitter. Nevertheless, to the best of our knowledge, no value of d_{11} and damage threshold have been reported.

C.2 Theoretical analysis

LGT owns to the trigonal crystal family and belongs to symmetry group 32 [259]. It exhibits second order nonlinear effect. OR within zinc-blend crystals involves the following non-linear susceptibility tensor $\overleftrightarrow{d}$, in which only two coefficients d_{11} and d_{14} contribute:

$$\overleftrightarrow{d} = \begin{bmatrix} d_{11} & d_{11} & 0 & d_{14} & 0 & 0 \\ 0 & 0 & 0 & 0 & -d_{14} & d_{11} \\ 0 & 0 & 0 & 0 & 0 & 0 \end{bmatrix} \tag{C.1}$$

The emitted THz E-field $\vec{E}_\Omega$ is proportional to the nonlinear polarization $\vec{P}$ and varies as the square of the optical E-field $\vec{E}_\omega$. In the crystal referential $\Re_{crystal} = (X,Y,Z)$, the $\vec{E}_\Omega$ field writes:

$$\vec{E}_\Omega \propto \begin{bmatrix} P_X \\ P_Y \\ P_Z \end{bmatrix} = \overleftrightarrow{d} : \vec{E}_\omega \vec{E}_\omega = \overleftrightarrow{d} : \begin{bmatrix} E^2_{\omega,X} \\ E^2_{\omega,Y} \\ E^2_{\omega,Z} \\ 2E_{\omega,Y}E_{\omega,Z} \\ 2E_{\omega,X}E_{\omega,Z} \\ 2E_{\omega,X}E_{\omega,Y} \end{bmatrix} \tag{C.2}$$

Taking the nonlinear value from ref. [264], $\vec{E}_\Omega$ can be written as a function of the optical field and the nonlinear coefficients of LGT, in the laboratory refential (x,y,z). Thus, one can extract the maximum achievable efficiency of OR for each spherical angle between the optical wave vector relatively to the crystal referential.

A Z-cut crystal is here chosen, which means that the optical wave vector is along the Z axis (see Figure C.1), not only to reach the greatest THz generation, but also because in this configuration, $\vec{E}_{\Omega,Z-cut}$ depends only on d_{11}. Assuming the optical polarization state perpendicular to the Z axis with an azymuthal angle ψ, $E_\omega = E_0(\cos\Phi, \sin\Phi, 0)$, the emitted THz field writes:

$$\vec{E}_{\Omega,Z-cut} \propto E_0^2 \begin{bmatrix} d_{11} \\ d_{11}\sin 2\Phi \\ 0 \end{bmatrix} \tag{C.3}$$

Eq.C.3 demonstrates that THz wave can be generated whatever the orientation of the impinging polarization state of the laser beam with a minimum amplitude of $d_{11}E_0^2$.

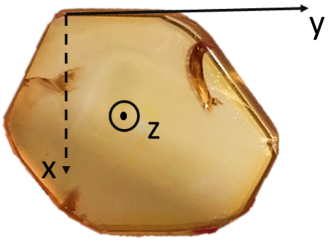

Figure C.1: The Z-cut LGT crystal used.

C.3 Measurement protocol and experimental setup

C.3.1 Sample preparation

The preparation of the sample is a very important step. In order to clean impurities from the LGT crystal, we clean it with acetone. The crystal is placed at the sample location in the experimental setup in Figure C.2.

C.3.2 THz generation setup

In this work, 3-mm thick *Z*-cut crystal was pumped under normal incidence by a Ti:sapphire amplified mode-locked laser system (Coherent Libra) that delivers pulses of 45 fs duration, 5 mJ of energy at 800 nm, and at a 1 kHz repetition rate.

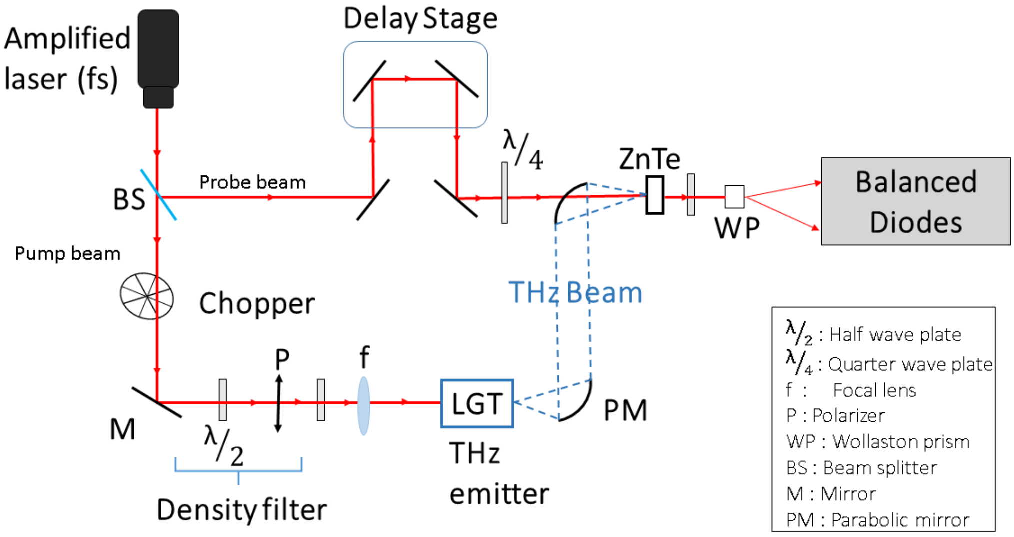

Figure C.2: Typical THz-TDs system

The pump laser beam is modulated at 160 Hz by a mechanical chopper, which triggers the detection lock-in amplifier. A half wave plate (HWP) is used to rotate the angle of the polarization state of impinging optical pump. A wave plate rotation of ψ leads to a rotation of 2ψ of the linear polarization state. The detection has been performed and recorded thanks to an electro optic setup: the use of a quarter wave plate generates circular polarization in the probe beam. Thus, the THz signal induces a birefringence in a 1-mm thick <111> ZnTe crystal, which modifies the probe polarization state to be elliptical. This birefringence is read with a Wollaston prism and two balanced photodiodes. In particular, we used <111> cubic crystal because it is isotropic and exhibits a transverse isotropy for second-order nonlinear phenomena [172]. Therefore, the rotation of the ZnTe crystal is not required for optimizing the detection. A half wave plate permits to select initially the referential orientation of the balanced detection. The obtained differential signal is directly proportional to one component of the THz field vector (see Figure C.2).

C.4 Experimental results

C.4.1 Temporal waveform of the optical rectification signal

The THz signal for LGT crystal was recorded under different average laser powers. A measured waveform with a thickness of 3 mm *Z*-cut LGT crystal is given in Figure C.3 with a laser average 285 mW on the crystal.

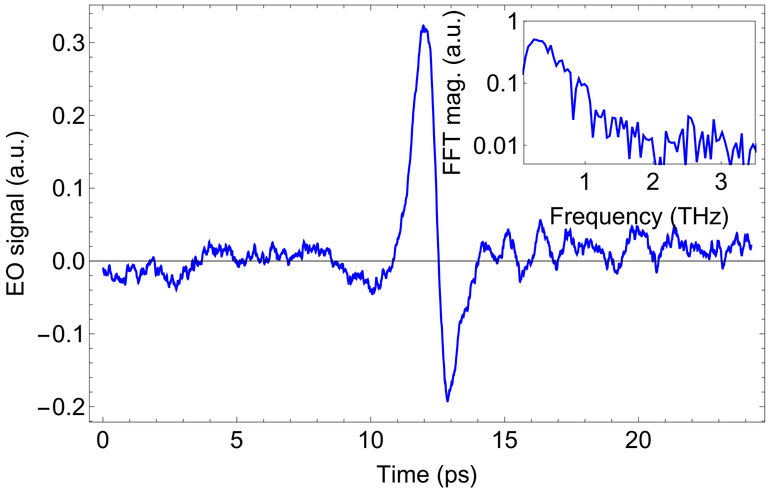

Figure C.3: Temporal waveform of the obtained OR signal. The inset shows the frequency distribution of the transient signal.

Figure C.3 shows the temporal waveform and its spectrum generated by OR. The obtained OR signal demonstrates the possibility to generate THz wave with the LGT crystal. The inset of Figure C.3 shows the generated THz frequency, which ranges from 0.04 THz to 1.5 THz with a 40 dB dynamic range, and the maximum of the spectrum is around 0.3 THz.

In order to determine the relationship of THz signal and the crystal azimuthal angle (crystal orientation), another experiment was performed by rotating HWP to obtain different laser polarization angles. Figure C.4 shows the THz signal versus the polarization angle of the pumping laser beam for four different azimuthal angle of the crystal (0°, 22.5°, 45° and 67.5°).

As seen in Figure C.4, there is always same maximum THz peak value regardless the crystal azimuthal angle. By using expression (17) from [172], the experimental results of obtained THz peak values for four different azimuthal angles were fitted nicely with equation C.4. The THz

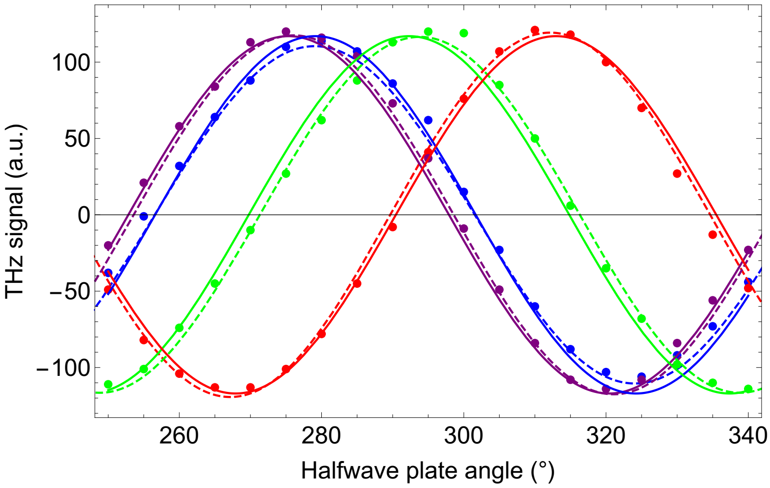

Figure C.4: HWP versus THz signal for four different azimuthal angle of the crystal with their fitting curves.

electric field is :

$$E_{THz} = sin(\psi - 3\theta + 4\gamma) \tag{C.4}$$

Here ψ is the angle of THz E-field, θ is the azimuthal angle of the crystal and γ is the angle of half wave plate.

C.4.2 Index of refraction and absorption coefficient

Additionally, index of refraction and absorption coefficient spectra were determined in the 0.01-1 THz frequency range by a means of a classic THz time domain spectroscopy setup (THz-TDS). This setup is just used for this measurement. In the setup, LTG-GaAs photo-conductive antennas (PCAs) from Teravil company were used as THz emitter and detector. The LGT crystal was placed between the PCAs separated at a distance of 12 cm.

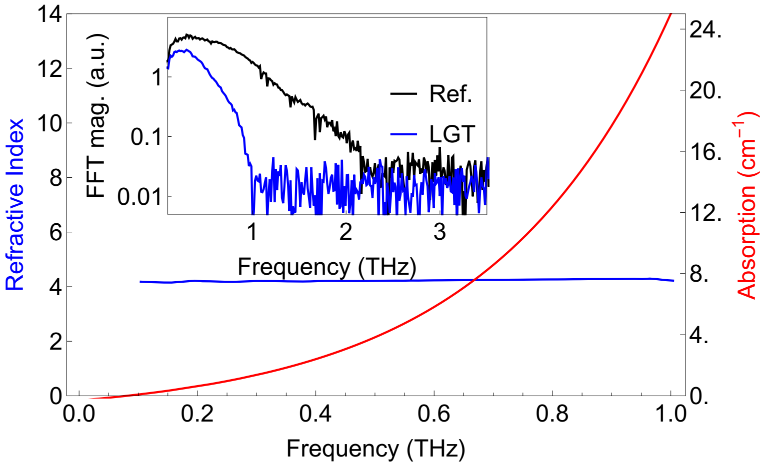

Figure C.5: Measured refractive indices and the absorption coefficients between 0.04 THz and 1 THz for LGT crystal (THz-TDS set up using photoconductive antennas). The inset shows measured THz waves with and without the LGT crystal.

In the inset of Figure C.3, the black curve gives the reference intensity spectrum of the THz pulse obtained without the crystal, and the blue one gives the spectrum of pulse transmitted through the LGT crystal. The refractive index and absorption coefficients were measured for two axes of

LGT by rotating the sample 90 °. As expected, the crystal shows an isotropic behavior with an optical index (black line in Figure C.5) and absorption coefficient (red line in Figure C.5) on both x and y axis for each frequency.

C.4.3 Damage threshold and comparison with ZnTe

Another experiment was performed to compare the efficiency in LGT with a 4-mm thick ZnTe crystal. For both crystals, the beam waist at the crystal is 0.735 mm, and the peak power densities on the crystals were varied from 0.03 TW/cm^2 to 0.37 TW/cm^2. The power of the incoming laser beam was varied by rotating a half-wave plate before a polarizer, which is in front of the crystals. The emitted THz field versus the peak power density is shown in Figure C.6. As the results are seen in Figure C.6, ZnTe crystal generates more THz signal than LGT crystal, it starts to saturate over 0.1 TW/cm^2. However, a good linearity was obtained fot the LGT crystal and no saturation was observed until 0.37 TW/cm^2 which is the maximum value delivered by our setup.

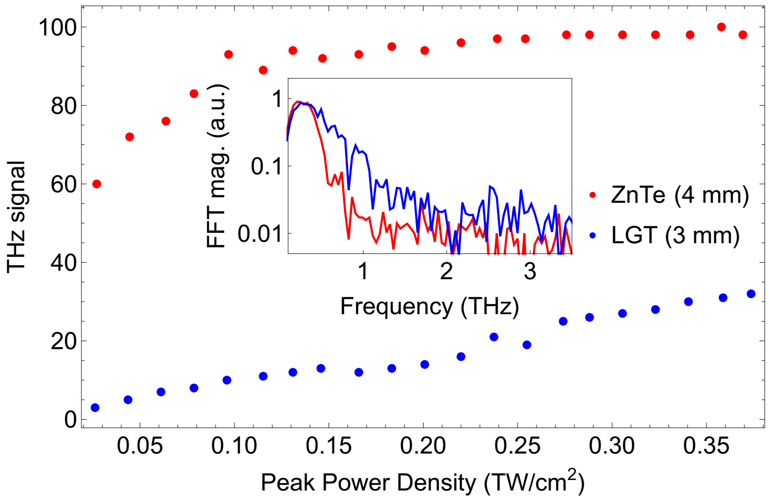

Figure C.6: THz emitted signal versus peak power density for ZnTe (red dots and line) and LGT (blue dots and line) crystals. The inset shows the spectrum for these crystals.

We also compared ZnTe crystal and LGT crystal damage threshold. The experiment was performed with an equivalent average laser power (282 mW, the utmost laser power in our setup) but the spot size of the laser beam on the crystals differed. After the samples were damaged, we measured the dimensions of the damaged areas employing a commercial microscope available in our laboratory. Pictures of damaged crystal areas and therefore the crystal damage threshold values are given in Figure C.7. As a result, the peak power density applied to the LGT crystal is above that of the ZnTe crystal, i.e. the damage threshold of the LGT crystal is above that of the ZnTe crystal (15 times higher).

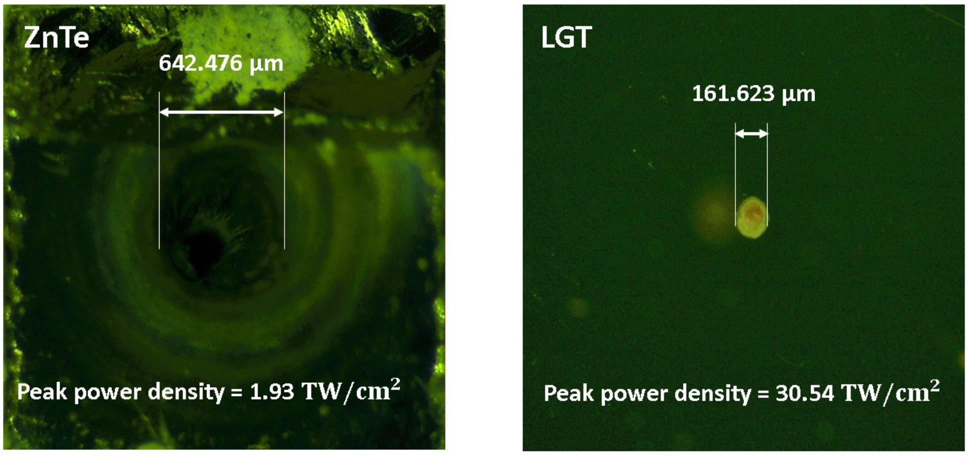

Figure C.7: Representative photograph showing the photos of damaged area with the applied peak power density on crystals (ZnTe and LGT).

Conclusion

We investigated for the first time THz generation by optical rectification in LGT crystal. We report that the THz generation efficiency within LGT crystal is independent of the crystal orientation. The crystal is compared with one among the foremost common crystals used for the THz generation, ZnTe. In spite of the fact that the THz signal in ZnTe is generated more than the LGT crystal, it is observed that the generated THz field is saturated in ZnTe crystal. However, no saturation is observed for the LGT crystal. Lastly, the damage threshold of both crystals was compared, and therefore the LGT features a 15 times higher damage threshold than the ZnTe.

D

Publications and conferences

Publications in peer-reviewed international journals

[1] F. Aljammal, G. Gaborit, M. Bernier, L. Galtier, G. Revillod, S. Iséni and L. Duvillaret,*"Pigtailed Electrooptic Sensor for Time-and Space-Resolved Dielectric Barrier Discharges Analysis"*, IEEE Transactions on Instrumentation and Measurement, 2021 [182].

[2] F. Aljammal, G. Gaborit, M. Bernier, S. Iséni and L. Duvillaret,*"Electric Field Measurements Using an eoProbe for Cold Atmospheric Plasma Jet: a High-Resolution Analysis"*, Plasma journal. (to be submitted)

[3] F. Aljammal, G. Soylu, G. Gaborit, M. Dumortier, H. Cabane, E. Herault and J.-L. Coutaz ,*"Optical rectification in a langatate crystal for terahertz generation"*, Optics Letters journal. (to be submitted)

Peer-reviewed international conference with proceedings

Oral:

[1] F. Aljammal, G. Gaborit, M. Bernier, S. Iséni, G. Revillod and L. Duvillaret, *"Real time and polarimetric analysis of intense electric field using electro-optic probe*, **Invited paper**, 8th Euro-Asian Pulsed Power Conference & 23th International Conference on High-Power Particle Beams & 17th International Conference on Megagauss Magnetic Field Generation and Related Topics, Biarritz, France, August, 2021.

[2] M. Bernier, B. Muller, E. Hérault, F. Aljammal, G. Gaborit and J-L. Coutaz, *Extraction of non linear coefficient of gaz from polarization state modulation of THz pulse generated by filament*, **Invited paper**, International conference on Advanced Laser Technologies ALT21, Moscou, Russie, September, 2021.

[3] B. Muller, M. Bernier, E. Hérault, F. Aljammal, G. Gaborit and J-L. Coutaz, *Influence of a gas flow on THz generation from optical air-breaking filament*, International Conference on Infrared, Millimeter, and Terahertz Waves, Chengdu, China, September, 2021.

[4] J.-M. Leveque, N. Gondrexon, S. Baup, S. Molina-Boisseau, R. Vibert, A. Perrier, G. Gaborit, F. Aljammal and S. Labouret, *"Physical and chemical characterization of a combined 20 / 500 kHz ultrasonic reactor"*, **Invited paper**, 4th Meeting of the Asia-Oceania Society of Sonochemistr, Nanjing, China, September, 2019.

[5] F. Aljammal, G. Gaborit, L. Galtier, S. Iséni, R. Dussart, G. Revillod and L. Duvillaret, *"Electro-optical probe for dielectric barrier discharge analysis"*, The 45th IEEE International Conference on Plasma Science, Denver, CO, USA, June, 2018.

Poster:

[1] F. Aljammal, G. Gaborit, S. Iséni, G. Revillod and L. Duvillaret, *"Optical Probe for the Real Time and Vectorial Analysis of the Electric Field Induced by Ionized Gazes"*, 24th International Symposium on Plasma Chemistry, Naples, Italy, June, 2019.

[2] B. Muller, F. Aljammal, G. Gaborit, M. Bernier, E. Herault and J.-L. Coutaz, *"Femtosecond Laser Driven Plasma for Terahertz Generation"*, 24th International Symposium on Plasma Chemistry, Naples, Italy, June, 2019.

[3] G. Soylu, F. Aljammal, G. Gaborit, E. Herault, M. Dumortier, H. Cabane and J.-L. Coutaz, *"Terahertz generation in langatate crystal by optical rectification"*, French-German THz conference, Kaiserslautern, Germany, April, 2019.

[4] F. Aljammal, G. Gaborit, L. Galtier, S. Iséni, R. Dussart, G. Revillod and L. Duvillaret, *"Vectorial Electric Field Characterization Of Plasmas Using An Optical Probe"*, 71st Annual Gaseous Electronics Conference, Portland, Oregon, USA, November, 2018.

Peer-reviewed national conference with proceedings

[1] F. Aljammal, G. Gaborit, M. Bernier, S. Iséni and L. Duvillaret, *"Analyse polarimétrique de plasmas à laide dune sonde électro-optique"*, 1^{eres} Rencontres Scientifiques Plasmas Froids et Lasers, Toulouse, France, November, 2019.

[2] F. Aljammal, G. Gaborit, M. Bernier, S. Iséni, G. Revillod and L. Duvillaret, *"Analyse et caractérisation vectorielle de champ électrique à l'aide dune sonde électro-optique dédiée aux diagnostiques de plasmas froids"*, 25eme Congrès Général de la SFP, Nantes, France, July, 2019.

Optique non-linéaire et plasma: caractérisation du champ électrique et génération des ondes THz

Résumé

En raison de la large gamme d'applications des décharges et des plasmas, leurs caractérisations ont reçu un regain d'intérêt ces dernières années. Parmi toutes les caractéristiques pertinentes d'un plasma, la distribution spatio-temporelle du champ électrique (E) qui leur est associé est un sujet d'intérêt majeur et l'un des paramètres critiques à analyser. Ce travail de thèse concerne d'abord la caractérisation vectorielle non invasive du champ électrique associé aux plasmas froids (décharge à barrière diélectrique, jet de plasma à pression atmosphérique, ...). L'autre partie est consacrée à l'interaction non linéaire entre un plasma froid et une onde impulsionnelle optique pour la génération paramétrique d'ondes Térahertz. Dans les deux cas (plasma généré avec une source haute tension et plasma dû à un claquage de l'air), nous avons détecté un champ électrique (de l'ordre du MV/m pour l'analyse du plasma et de quelques V/m pour la génération haute fréquence) soit avec une sonde électro-optique (EO) fibrée (développée à Kapteos), soit en utilisant un banc expérimental en espace libre faisant appel là aussi à une détection EO (développé à l'IMEP-LAHC). Nous avons réalisé une étude polarimétrique complète du champ E généré par des électrodes ponctuelles ou par ionisation d'un gaz comme l'hélium. En particulier, nous nous sommes intéressés au comportement en polarisation des phénomènes observés. Nous avons également étudié la possibilité d'améliorer l'efficacité de génération d'une impulsion teraHertz (THz) par claquage dans l'air en ajoutant un jet de plasma d'hélium. Une étude complète du signal généré (en module et en orientation) a été menée, et les résultats obtenus sont parfaitement décrits par un modèle que nous avons développé. Ce modèle a été validé expérimentalement par une étude polarimétrique de l'impulsion THz en utilisant une détection EO innovante.

Mots-clés : Haute tension, Décharges à barrière diélectrique (DBD), Mesure du champ électrique, Mesure électro-optique (EO), Capteur optique, Jet de plasma d'hélium, Génération de térahertz

Abstract

Due to the wide range of applications of discharges and plasmas, their characterizations have been receiving a revival of interest these last couple of years. Among all the relevant characteristics of a plasma, the spatial distribution and the temporal evolution its associated electric field (E-field) is a subject of major interest and one of the more critical parameters to be analyzed. Firstly, this thesis work concerns the non-invasive vector characterization of the electric field associated to cold plasmas (dielectric barrier discharge, atmospheric plasma jet, ...). The other part is devoted to the nonlinear interaction between a cold plasma and an optical pulse wave for the parametric generation of Terahertz (THz) waves. In both cases (plasma generated with a high voltage source and plasma due to air breakdown), we have detected an electric field (of the order of MV/m for plasma analysis and of a few V/m for high frequency generation) either with a pigtailed electro-optical probe (developped at Kapteos), or by using an experimental free space EO bench (developped at IMEP-LAHC). We have carried out a complete polarimetric study of the E-field generated by electrodes or by ionization of a gas like helium. In particular, we have been interested in the polarization behavior of the observed phenomena. We also studied the possibility to improve the efficiency of the THz generation by adding a helium plasma jet or the gas alone. We have performed a complete characterization of the generated THz signal (in modulus and orientation). The obtained results are perfectly described by a model that we have developed. This model has been experimentally validated by a polarimetric study of the THz pulse using an innovative EO detection.

Keywords : High voltage, Dielectric barrier discharges (DBDs), Electric field measurement, Electrooptic (EO) measurement, Optical sensor, Helium plasma jet, Terahertz generation